

**Imperial College**  
London

**TOUGHENING MECHANISMS OF SILICA  
NANOPARTICLE-MODIFIED EPOXY POLYMERS**

A thesis submitted for the degree of Doctor of Philosophy of Imperial College London  
and the Diploma of Imperial College

April 2010

By Kunal Masania

Department of Mechanical Engineering

Imperial College London

## Abstract

The present work investigates the ability of several different epoxies to be toughened with the addition with 20 nm silica nanoparticles (nanosilica). The formation of 'hybrid' epoxy polymers, containing both silica nanoparticles and carboxyl-terminated butadiene-acrylonitrile (CTBN) rubber micro-particles, is also discussed. The structure/property relationships are considered, with an emphasis on the toughness and the toughening mechanisms. Particular attention was given to an anhydride cured diglycidyl ether of bisphenol-A (DGEBA) system where the fracture energy increased from 83 to 204 J/m<sup>2</sup> with the addition of 20 wt. % of silica nanoparticles. Plastic shear bands followed by debonding of the matrix from the silica nanoparticles, and subsequently plastic void growth of the epoxy were found to be the operative toughening mechanisms. The largest increases in toughness observed were for the 'hybrid' materials where a synergistic behaviour on the fracture energy. A maximum fracture energy of 1051 J/m<sup>2</sup> was measured for a 'hybrid' epoxy polymer containing 10 wt. % silica nanoparticles and 9 wt. % rubber micro-particles. The toughening mechanisms for such systems were postulated to be rubber-particle cavitation, shear band yielding and void growth and debonding and plastic void growth of the nanosilica necklaces.

Ultimately, these polymers are intended to be used as matrices in fibre-reinforced composites. Therefore, resistance to delamination as fibre-composites has been examined for such modified epoxies. The interlaminar fracture energies for the fibre-composite materials were found to increase even further by a fibre bridging toughening mechanism. However, the fibre-matrix adhesion is shown to be an important parameter.

The present work has extended an existing model to predict the toughening effect of the nanoparticles in the epoxy polymer. There was excellent agreement between the predictions and the experimental data for epoxy containing the silica nanoparticles, and for epoxy polymers containing rubber or coreshell particles. Inferences have been made about the toughenability of the epoxy being sensitive to particle-matrix adhesion and the ability for the matrix to shear yield.

## Acknowledgments

I cannot begin to express enough gratitude to my supervisors, Dr Ambrose Taylor and Professor Tony Kinloch for their help with this project. Ambrose has been a fantastic mentor through the course of this PhD and has been a genuine pleasure and privilege to work with. My thanks also to Tony for all of his help and suggestions during the course of this project and for the encouragement towards the latter part of writing up. I would like to thank Dr S. Sprenger (Nanoresins) for his supply of materials and the EPSRC for DTA funding. Without either of these, this study would not have been possible.

It is a pleasure to thank the many people who have helped me during the PhD. I would like to give a special thanks to Dr M. Ardakani for his help with the microscopy, Mr A. Choda for his help with machining, Mr T.H. Hsieh for his help with the compressive testing, Dr R.D. Brooker for kindly sharing her data and Dr Y. Patel for his help in producing this thesis.

I would also like to thank: Ms P. Carry of Analytical Services, Department of Chemical Engineering; Mr G. Senior and The Composites Centre; and Mr H. MacGillivray for their help with the mechanical testing and use of equipment.

For the friendly co-operation and useful discussions, the author wishes to express his gratitude to Mr H. Arora, Ms Cook, Dr C.M. Davies, Dr S. Frenz, Mr I. Giannakopoulos, Mr T. Hault, Mr P. Hooper, Dr B. Johnsen, Dr S. Lamorinière, Dr S. Rodriguez-Sanchez, Ms M. Skea, Dr J. Sohn Lee and Mr K. Zuo to name a few.

It is only fitting for me to also acknowledge the many friends who have shared my success and failures with me. This has been a true test of mental endurance, the best Alpine training ever!

Please be assured, if your name is not listed, my gratitude is no less for the help you have given me.

Last but not least, I would like to thank my family for their support and patience, not just through the PhD, but up until now. Thank you for being so encouraging and always allowing me to pursue my interests and passions. I would not have got this far without you.

**Thanks!**

# Table of Contents

Title Page .....	1
Abstract .....	2
Acknowledgments .....	3
Table of Contents .....	4
List of Figures .....	8
List of Tables .....	18
Nomenclature .....	21
Abbreviations .....	21
English Alphabet .....	22
Greek Alphabet .....	24
1 Introduction .....	25
1.1 Background .....	25
1.2 Aims and objectives .....	26
1.3 Thesis outline .....	27
2 Literature Review .....	29
2.1 Introduction .....	29
2.2 Rigid particle toughening .....	30
2.2.1 Yield behaviour .....	31
2.2.2 Fracture behaviour .....	33
2.2.3 Toughening mechanisms .....	34
2.3 Rubber toughening .....	36
2.3.1 Yield behaviour .....	37
2.3.2 Fracture behaviour .....	38
2.3.3 Toughening mechanisms .....	39
2.4 Hybrid toughening .....	41
2.4.1 Yield behaviour .....	42
2.4.2 Fracture behaviour .....	42
2.4.3 Toughening mechanisms .....	43
2.5 Composite materials .....	44
2.5.1 Fracture behaviour .....	45
2.5.2 Toughening mechanisms .....	46
2.6 Chapter summary .....	47
3 Materials and Manufacturing .....	48
3.1 Introduction .....	48
3.2 Silica nanoparticles .....	49
3.3 Rubber particles .....	50
3.4 Amine cured TGMDA (Ch. 5) .....	54
3.5 Polyether-amine cured DGEBA/F (Ch. 6) .....	54
3.6 Polyether-amine cured DGEBA (Ch. 7) .....	54
3.7 Amine cured multifunctional epoxy (Ch. 8) .....	55
3.8 Anhydride cured DGEBA (Ch. 9) .....	55
3.9 Manufacturing .....	55
3.9.1 Bulk epoxies .....	55
3.9.2 Single-fibre composites .....	57
3.9.3 Continuous-fibre composites .....	58

4	Experimental Methods .....	61
4.1	Introduction.....	61
4.2	Determination of density .....	61
4.3	Determination of glass transition temperature .....	61
4.4	Determination of viscosity .....	62
4.5	Atomic force microscopy .....	62
4.6	Transmission electron microscopy.....	63
4.7	Scanning electron microscopy .....	63
4.8	Optical microscopy.....	64
4.9	Image analysis .....	64
4.9.1	Determination of volume fraction from AFM images .....	64
4.9.2	Determination of percentage of void growth .....	65
4.10	Tensile properties.....	66
4.11	Compressive properties .....	67
4.12	Bulk fracture properties .....	68
4.12.1	Sub-critically loaded crack-tips .....	69
4.13	Fibre-matrix interfacial tests .....	71
4.14	Composite short beam shear strength.....	72
4.15	Composite flexural properties .....	72
4.16	Composite mode I fracture energy.....	73
5	Amine cured TGMDA Epoxy Properties.....	74
5.1	Introduction.....	74
5.2	Glass transition temperature .....	75
5.3	Morphology.....	76
5.3.1	Nanosilica-modified formulations .....	76
5.3.2	Rubber-modified formulations .....	78
5.3.3	Fibre-reinforced composite .....	79
5.4	Tensile properties.....	81
5.5	Compressive properties .....	82
5.6	Fracture properties .....	83
5.6.1	Nanosilica-modified formulations .....	84
5.6.2	Rubber-modified formulations .....	84
5.6.3	Toughening mechanisms of the nanosilica-modified formulations.....	85
5.6.4	Toughening mechanisms of the rubber-modified formulations .....	86
5.7	Composite properties .....	87
5.7.1	Composite flexural modulus.....	87
5.7.2	Composite mode I fracture.....	88
5.8	Chapter summary.....	93
6	Polyether-amine Cured DGEBA/F Epoxy Properties .....	95
6.1	Introduction.....	95
6.2	Glass transition temperature .....	96
6.3	Morphology.....	96
6.4	Tensile properties.....	98
6.5	Compressive properties .....	99
6.6	Fracture properties.....	100
6.6.1	Toughening mechanisms .....	101
6.7	Chapter summary.....	102
7	Polyether-amine Cured DGEBA Epoxy Properties .....	103
7.1	Introduction.....	103
7.2	Glass transition temperature .....	104
7.3	Morphology.....	104
7.4	Tensile properties.....	106
7.5	Compressive properties .....	108

7.6	Fracture properties .....	109
7.6.1	Toughening mechanisms .....	110
7.7	Chapter summary .....	112
<b>8</b>	<b>Amine Cured Multifunctional Epoxy Properties .....</b>	<b>114</b>
8.1	Introduction .....	114
8.2	Glass transition temperature .....	114
8.3	Morphology .....	115
8.4	Tensile properties .....	117
8.5	Compressive properties .....	118
8.6	Fracture properties .....	119
8.6.1	Toughening mechanisms .....	120
8.7	Chapter summary .....	121
<b>9</b>	<b>Anhydride Cured DGEBA Epoxy Properties .....</b>	<b>123</b>
9.1	Introduction .....	123
9.2	Glass transition temperature .....	124
9.3	Morphology .....	125
9.3.1	Nanosilica-modified formulations .....	125
9.3.2	Rubber-modified formulations .....	128
9.3.3	Fibre-reinforced composites .....	131
9.4	Rheological properties .....	135
9.5	Tensile properties .....	137
9.6	Compressive properties .....	138
9.6.1	Nanosilica-modified formulations .....	139
9.6.2	Rubber-modified formulations .....	140
9.7	Fracture properties .....	143
9.7.1	Nanosilica-modified formulations .....	143
9.7.2	Rubber-modified formulations .....	143
9.7.3	Toughening mechanisms of the nanosilica-modified formulations .....	145
9.7.4	Toughening mechanisms of the rubber-modified formulations .....	147
9.8	Composite properties .....	152
9.8.1	Single-fibre properties .....	153
9.8.2	Short beam shear properties .....	154
9.8.3	Flexural modulus .....	155
9.8.4	Composite mode I fracture .....	155
9.8.5	Composite toughening mechanisms .....	158
9.9	Chapter summary .....	163
<b>10</b>	<b>System Comparisons and Toughening Mechanisms .....</b>	<b>167</b>
10.1	Introduction .....	167
10.2	Morphology .....	168
10.2.1	Nanosilica-modified epoxies .....	168
10.2.2	Rubber-modified epoxies .....	169
10.3	The effect of cross-link density .....	172
10.3.1	Nanosilica-modified epoxies .....	172
10.3.2	Rubber-modified epoxies .....	175
10.4	Stiffness behaviour .....	175
10.4.1	Nanosilica-modified epoxies .....	177
10.4.2	Rubber-modified epoxies .....	178
10.5	Yield behaviour .....	180
10.5.1	Nanosilica-modified epoxies .....	180
10.5.2	Rubber-modified epoxies .....	185
10.6	Fracture behaviour .....	185
10.6.1	Nanosilica-modified epoxies .....	185
10.6.2	Rubber-modified epoxies .....	192

10.7	Chapter summary.....	196
11	Analytical Modelling of Toughening Mechanisms.....	198
11.1	Introduction.....	198
11.2	Shear band yielding due to nanosilica, $\Delta G_s$ .....	199
11.3	Debonding of nanosilica, $\Delta G_{db}$ .....	202
11.4	Plastic void growth in the epoxy, $\Delta G_v$ .....	202
11.5	Modelling nanosilica toughening.....	203
11.5.1	The effect of particle size.....	210
11.5.2	Optimal particle size for rigid particle toughening.....	211
11.6	Modelling coreshell particle toughening.....	213
11.7	Modelling rubber toughening.....	215
11.8	Modelling hybrid toughening.....	216
12	Concluding Remarks and Future Work.....	220
12.1	Conclusions.....	220
12.1.1	Nanosilica-modified epoxies.....	220
12.1.2	Rubber-modified epoxies.....	222
12.1.3	Fibre-Composites.....	224
12.1.4	Analytical Modelling.....	225
12.2	Recommendations for future work.....	226
12.2.1	Nanosilica toughening.....	226
12.2.2	Hybrid toughening.....	228
12.2.3	Continuous-fibre composites.....	228
	References.....	230
	Appendix I. List of Publications.....	248
	Conference Papers.....	248
	Journal Papers.....	249

# List of Figures

Figure 2.1. The characteristic types of crack growth in epoxies with respect to the tensile yield strength [16]. .....	30
Figure 2.2. The Young's modulus is independent of (a) particle size [24] and (b) particle-matrix adhesion [34] (original work from [35]). .....	31
Figure 2.3. The yield strength versus volume fraction for (a, b) different particle sizes of chalk-filled polypropylenes [26, 36]. .....	32
Figure 2.4. The debonding stress at the interface is generally regarded to be inversely proportional to the square root of particle radius [50]. .....	33
Figure 2.5. The mechanisms (a-d) that are widely regarded to toughen rigid particle-modified epoxy polymers [46, 67, 75, 76]. .....	35
Figure 2.6. Images of nanosilica-modified epoxies from (a) the fracture surface with evidence of void growth and (b) sub-critically loaded crack-tips to show shear banding [7, 61]. .....	36
Figure 2.7. Fracture energy as a function of monomer molecular weight [86]. .....	37
Figure 2.8. The ability for the epoxy to plastically deform is an important parameter for large toughening effects with rubber particles [88]. .....	38
Figure 2.9. Zhang and Berglund [89] showed the effect of rubber-modification on the yield behaviour in (a) tension and (b) compression. ....	38
Figure 2.10. Polished sections of sub-critically loaded crack-tips show extensive shear banding in rubber-modified epoxies [89, 97]. .....	39
Figure 2.11. Images from (a) a sample cross section of a rubber-modified epoxy and (b) the fracture surface for the same formulation [101]. .....	40
Figure 2.12. Schematic of rubber bridging shown (a) initially and (b) with continued loading, the larger bridged particles fail [105]. .....	40
Figure 2.13. Shows (a-c) morphologies of (nanosilica and rubber) hybrid-modified epoxies [59, 135]. Note that images from [59] have been stained with osmium tetroxide. ....	42
Figure 2.14. Fracture energy versus rigid particle content for hybrid-modification using CTBN and (a) micron-sized glass beads [113] or (b) nanosilica [134]. .....	43
Figure 2.15. Sub-critically loaded crack-tips show shear banding between the rubber particles and shear band yielding (due to stress field interactions) from the glass particles [72, 89]. .....	43
Figure 2.16. Fracture surface images for CTBN and (a) glass- or (b) nanosilica-containing hybrid-modified epoxies [60, 72]. .....	44
Figure 2.17. Specific stiffness and strength for various structural materials, recreated from [139]. .....	45

Figure 3.1. Representation of the silane treatment process to produce dispersed nanosilica particles in the epoxy [162]. .....	49
Figure 3.2. The particle number density versus the particle size for the nanosilica particles used in this study [162]. .....	50
Figure 3.3. Optical micrographs of a sample from the 9R anhydride cured DGEBA epoxy during curing. Selected images (a-h) show how the morphology of the rubber-modified epoxy varies with respect to temperature and time.....	51
Figure 3.4. Variation of epoxy and oven temperatures during the anhydride cured DGEBA epoxy cure cycle. ....	57
Figure 3.5. Schematic shows the preparation technique for single-fibre pull-out specimens.....	58
Figure 3.6. Shows (a) a side view of fibre stack for RIFT to produce continuous fibre-reinforced polymer composites and (b) how the resin flow front progresses with time. ....	60
Figure 4.1. Heat flow versus temperature for the unmodified anhydride cured DGEBA epoxy shows the glass transition temperature, $T_g$ , region.....	62
Figure 4.2. Sample SEM images (a-d) during the procedure to measure the percentage of particles that debond with subsequent void growth with some shown circled in (d). The original image is from [182]......	65
Figure 4.3. The type 1BA geometry that was used for tensile tests [183, 184]. ....	66
Figure 4.4. Geometry for the plane strain compression specimens, compressed along the long length of the specimen with 12 mm platens.....	67
Figure 4.5. Standard specimen geometry that was employed for single edge notched bend (SENB) tests. ....	68
Figure 4.6. Standard geometry that was used to conduct the double-notched four point-bend (DN4PB) tests. ....	69
Figure 4.7. Cross-polarised light optical images of the 10N anhydride cured DGEBA (a) before applying a load and (b) imminent fracture in one of the cracks (noted as the right crack). .....	70
Figure 4.8. Load-displacement trace from a typical single-fibre pull-out test. ....	71
Figure 5.1. Shows (a) phase and (b) height images of the unmodified amine cured TGMDA epoxy. The cut direction is shown in the height image. ....	76
Figure 5.2. Shows (a, c) phase and (b, c) height images of amine cured TGMDA with 10N. The cut direction is shown in (b) and (c, d) shows some of the 20 nm nanosilica particles (arrows). 77	77
Figure 5.3. Shows (a) phase and (b) height images of the 20N amine cured TGMDA epoxy. ...	78
Figure 5.4. Shows (a) phase and (b) height images of the 9R amine cured TGMDA with spherical, phase separated, 1 $\mu\text{m}$ CTBN particles (arrows) in the epoxy.....	79

Figure 5.5. Shows (a) phase and (b) height images of the 10N9R amine cured TGMDA epoxy. Some CTBN particles (blue) and nanosilica necklaces (white) are identified. ....	79
Figure 5.6. Optical micrographs show (a) the fibre architecture in the CFRP and (b, c) the inter-ply region. The fracture plane (blue) and a resin rich pocket (red) are identified. ....	80
Figure 5.7. Height images of the 10N amine cured TGMDA CFRP with (a) showing the carbon-fibre matrix morphology and (b) showing the inter-space region at high magnification. ....	81
Figure 5.8. Tensile true stress versus tensile true strain for the unmodified and modified amine cured TGMDA epoxies. ....	82
Figure 5.9. Compressive true stress versus compressive true strain for unmodified and nanosilica modified amine cured TGMDA from plane strain compression tests. ....	83
Figure 5.10. Polished cross section of the unmodified amine cured TGMDA that was loaded to the strain softening region shows extensive shear banding in the compressed region. ....	83
Figure 5.11. The (a) fracture toughness and (b) fracture energy versus nanosilica content for the unmodified and modified amine cured TGMDA epoxies. A linear fit shows the general trend in the fracture properties for the nanosilica-modified epoxies. ....	84
Figure 5.12. Shows (a, b), FEGSEM micrographs of 20N amine cured TGMDA. The 20 nm nanosilica particles are indentified with arrows. Little evidence of debonding was observed and is shown as circled, noting that no evidence of void growth was identified. ....	86
Figure 5.13. A FEGSEM micrograph from the fracture surface of 9R amine cured TGMDA shows evidence of toughening by rubber micro-particle cavitation to create voids in the epoxy. ....	87
Figure 5.14. A FEGSEM micrograph of the fracture surface from the 10N9R amine cured TGMDA with evidence of toughening by rubber-particle cavitation in the epoxy (indicated). ....	87
Figure 5.15. Mode I fracture energy for the unmodified and modified amine cured TGMDA CFRPs. ....	89
Figure 5.16. The mode I CFRP fracture initiation and propagation energies versus the bulk fracture energy for the unmodified and modified amine cured TGMDA epoxies. ....	89
Figure 5.17. An SEM image of the mode I fracture surface in the steady state propagation region for the unmodified amine cured TGMDA CFRP. ....	90
Figure 5.18. Images (a, b) of the mode I fracture surface in the steady state propagation region of the 10N amine cured TGMDA CFRP. ....	91
Figure 5.19. Shows (a, b) SEM images of the mode I fracture surface in the steady state propagation region of the rubber-modified (9R) amine cured TGMDA CFRP with some cavitated rubber particles indicated in the image. ....	92
Figure 5.20. The mode I fracture surface in the steady state propagation region from the 10N9R hybrid-modified amine cured TGMDA CFRP. ....	93

Figure 6.1. Shows (a) phase and (b) height images of the unmodified polyether-amine cured DGEBA/F epoxy. The cut direction is shown in the height image. ....	97
Figure 6.2. Shows (a, c) phase and (b, d) height images of the 20N polyether-amine cured DGEBA/F epoxy. The 20 nm nanosilica particles are indicated with arrows. ....	97
Figure 6.3. Tensile true stress versus tensile true strain for the unmodified and nanosilica-modified polyether-amine cured DGEBA/F epoxies. ....	98
Figure 6.4. Compressive true stress versus compressive true strain for the unmodified and nanosilica-modified polyether-amine cured DGEBA/F epoxies. ....	100
Figure 6.5. Optical section of the unmodified polyether-amine cured DGEBA/F shows extensive shear banding in the compressed region when viewed using cross-polarised light microscopy. ....	100
Figure 6.6. The (a) fracture toughness, $K_{IC}$ , and (b) fracture energy, $G_C$ , versus nanosilica content for the unmodified and nanosilica-modified polyether-amine cured DGEBA/F epoxies. A linear fit shows the general trend. ....	101
Figure 6.7. A FEGSEM image of the fracture surface for the 20N amine cured polyether-amine cured DGEBA/F epoxy. The nanosilica particles are identified with arrows and evidence of plastic void growth around debonded particles is shown circled. ....	102
Figure 7.1. Shows (a) phase and (b) height images of the unmodified polyether-amine cured DGEBA. The cut direction is shown in the height image. ....	104
Figure 7.2. Shows (a, c) phase and (b, d) height images of the 10N polyether-amine cured DGEBA epoxy. The white arrows identify the nanosilica on the surface and the blue arrows indicate sub-surface particles. ....	105
Figure 7.3. Shows (a, c) phase and (b, d) height images of polyether-amine cured DGEBA with 20N. The nanosilica remains dispersed; some of the 20 nm particles are indicated with arrows. ....	106
Figure 7.4. Tensile true stress versus tensile true strain for the unmodified and nanosilica-modified polyether-amine cured DGEBA epoxies. ....	107
Figure 7.5. Compressive true stress versus compressive true strain for unmodified and nanosilica-modified polyether-amine cured DGEBA epoxies. ....	109
Figure 7.6. Optical section of the unmodified polyether-amine cured DGEBA shows extensive shear banding in the gauge area when viewed with cross-polarised light. ....	109
Figure 7.7. The (a) fracture toughness, $K_{IC}$ , and (b) fracture energy, $G_C$ , versus nanosilica content for the unmodified and nanosilica-modified polyether-amine cured DGEBA epoxies. A linear fit shows the general trend. ....	110
Figure 7.8. Shear bands in the process zone region of the 20N polyether-amine cured DGEBA epoxy. ....	111

Figure 7.9. A FEGSEM micrograph of the process zone region of a 20N polyether-amine cured DGEBA sample. The hackle and mist regions are identified at low magnification. ....	112
Figure 7.10. A FEGSEM micrograph from the fracture surface of the 20N polyether-amine cured DGEBA. Some debonded nanosilica particles are identified with arrows. ....	112
Figure 8.1. Shows (a) phase and (b) height images of the unmodified amine cured multifunctional epoxy [79]. The cut direction is shown in the height image. ....	116
Figure 8.2. Shows (a, c) phase and (b, d) height images of the 15N amine cured multifunctional epoxy [211]. The dispersed 20 nm nanosilica particles are indicated with arrows. ....	116
Figure 8.3. Tensile true stress versus tensile true strain for the unmodified and 20N amine cured multifunctional epoxies. ....	117
Figure 8.4. Compressive true stress versus compressive true strain for the unmodified and nanosilica-modified amine cured multifunctional epoxies. ....	119
Figure 8.5. Polished section of the unmodified amine cured multifunctional epoxy shown with cross-polarised light optical microscopy. ....	119
Figure 8.6. The (a) fracture toughness, $K_{IC}$ , and (b) fracture energy, $G_C$ , versus nanosilica content for the unmodified and nanosilica-modified amine cured multifunctional epoxies. A linear fits shows the general trend. ....	120
Figure 8.7. Shows a FEGSEM image of the fracture surface for the 20N amine cured multifunctional epoxy. Some nanosilica particles are shown with arrows. ....	121
Figure 9.1. Shows (a) phase and (b) height images of the unmodified anhydride cured DGEBA epoxy. The cut direction is shown in the height image. ....	125
Figure 9.2. Shows (a, c) phase and (b, d) height images of the 10N anhydride cured DGEBA epoxy. Some of the nanosilica particles are identified in (c ,d). ....	126
Figure 9.3. Shows (a, c) phase and (b, d) height images of the 20N anhydride cured DGEBA epoxy. Some of the nanosilica particles are identified with arrows in (c ,d). ....	127
Figure 9.4. Shows TEM images of the (a) 10N anhydride cured DGEBA and (b) 20N anhydride cured DGEBA. Some of the nanosilica particles are identified with arrows. ....	127
Figure 9.5. Shows (a, c) phase and (b, d) height images of the 9R anhydride cured DGEBA epoxy. Spherical, particles up to 1 $\mu\text{m}$ in diameter are formed in the epoxy (white arrows). ...	128
Figure 9.6. Shows (a, c) phase and (b, d) height images of the 10N9R anhydride cured DGEBA epoxy. Some rubber particles are indicated with white arrows and the nanosilica necklace structures are shown with blue. ....	129
Figure 9.7. Shows TEM images of the 10N9R anhydride cured DGEBA. Some rubber particles are indicated with white arrows and the nanosilica necklaces are shown with blue. ....	130

Figure 9.8 Shows (a) phase and (b) height images of the 15N9R anhydride cured DGEBA epoxy [182]. Some rubber particles are indicated with white arrows and the nanosilica necklace structures are shown with blue. ....	130
Figure 9.9. Shows (a) phase and (b) height images of the 20N9R anhydride cured DGEBA epoxy. Some rubber particles are indicated with white arrows and the nanosilica necklace structures are shown with blue. ....	131
Figure 9.10. Optical cross-sectional micrographs of the UD GFRP show (a) the composite beam, and (b) a high magnification micrograph of the individual glass-fibres in the fracture plane (blue). ....	132
Figure 9.11. Optical cross-sectional micrographs from the QI GFRP showing (a) the composite beam, (b) a micrograph through the thickness of the GFRP and (c) a micrograph of the individual glass-fibres in the interlaminar fracture plane (blue). ....	133
Figure 9.12. Height images (a, b) of the 10N anhydride cured DGEBA UD GFRP. The nanosilica particles (white arrows) are well dispersed up to the fibre-matrix interface. ....	134
Figure 9.13. A TEM image of the fibre-matrix interface in the 10N9R anhydride cured DGEBA QI GFRP. The nanosilica necklaces are indicated with white arrows and a single rubber particle is identified with blue. ....	135
Figure 9.14. A FEGSEM from the fracture surface of the 10N9R anhydride cured DGEBA UD GFRP. The rubber particles are identified with arrows. The nanosilica particles cannot be seen at this magnification. ....	135
Figure 9.15. Viscosity versus time for the unmodified, 10N, 9R and 10N9R anhydride cured DGEBA epoxies as the samples went through the cure cycle. ....	137
Figure 9.16. Tensile true stress versus tensile true strain for the unmodified and modified anhydride cured DGEBA epoxies. ....	138
Figure 9.17. Compressive true stress versus compressive true strain for the unmodified and nanosilica-modified anhydride cured DGEBA epoxies. ....	139
Figure 9.18. Images from compressed samples of the unmodified and modified anhydride cured DGEBA epoxies. The images show extensive shear banding in the compressed region. ....	140
Figure 9.19. Compressive true stress versus compressive true strain for the rubber- and hybrid-modified anhydride cured DGEBA epoxies. ....	141
Figure 9.20. Images from compressed samples of the rubber- and hybrid-modified anhydride cured DGEBA epoxies. ....	142
Figure 9.21. A TEM image from the shear band yielded region of the 15N9R anhydride cured DGEBA epoxy. The rubber particles appear elongated (arrows), parallel to the shear direction and the nanosilica necklaces have debonded (circled). ....	143

Figure 9.22. The (a) fracture toughness and (b) fracture energy for the unmodified and modified anhydride cured DGEBA. The general trends in the nanosilica-modified epoxies are shown with a linear fit (blue) and the rubber-modified epoxies with a quadratic fit (red).....	144
Figure 9.23. Cross-polarised light microscopy images (a, b) of 10N sub-critically loaded crack-tips. The two images are from different samples. ....	145
Figure 9.24. A FEGSEM micrograph of the fracture surface for the unmodified anhydride cured DGEBA epoxy [224]. ....	146
Figure 9.25. A FEGSEM micrograph of 20N anhydride cured DGEBA shows evidence of toughening. Some nanosilica particles are identified with arrows. Void growth was observed around some of the nanosilica particles, shown as circled [224]......	147
Figure 9.26. Images of a sub-critically loaded crack-tip for the 9R anhydride cured DGEBA. Shows the crack-tip with (a) transmission light- and (b) cross-polarised light microscopy. Evidence feathering shear band yielding in the epoxy was obtained. ....	148
Figure 9.27. Images of a sub-critically loaded crack-tip for the 10N9R anhydride cured DGEBA epoxy. Shows the plane strain plastic zone ahead of the crack-tip with (a, b) transmitted light and (c) cross-polarised light microscopy.....	149
Figure 9.28. A FEGSEM micrograph of the fracture surface for the 9R anhydride cured DGEBA [224]. Some of the voids created by cavitation of the rubber particles are indicated. ....	150
Figure 9.29. A FEGSEM image of the fracture surface for the 10N9R anhydride cured DGEBA epoxy [224]. A composite image shows extensive deformation in the process zone region. The rubber micro-particles are shown with arrows. ....	151
Figure 9.30. High magnification FEGSEM images of the 10N9R epoxy fracture surface [224], showing (a) in-lens and (b) SE2 lens images of a single rubber particle and deformation around the agglomerated nanosilica particles.....	151
Figure 9.31. A FEGSEM image of the fracture surface for the 15N9R anhydride cured DGEBA epoxy [224]. A composite image identifies some cavitated rubber micro-particles. ....	152
Figure 9.32. High magnification FEGSEM images of the 15N9R epoxy fracture surface [224], showing (a) in-lens and (b) SE2 lens images of a single rubber particle and deformation around the agglomerated nanosilica particles.....	152
Figure 9.33. Pull-out shear strength versus embedded length for the unmodified and modified anhydride cured DGEBA single-fibre GFRPs. ....	154
Figure 9.34. Mode I UD GFRP fracture energy versus crack length, $a$ , for unmodified and modified anhydride cured DGEBA UD GFRPs. ....	156
Figure 9.35. Mode I UD GFRP fracture energy versus bulk fracture energy for unmodified and modified anhydride cured DGEBA epoxies.....	156

Figure 9.36. Mode I QI GFRP fracture energy versus crack length, $a$ , for unmodified and modified anhydride cured DGEBA epoxies.....	157
Figure 9.37. Mode I QI GFRP fracture energy versus bulk fracture energy for the unmodified and modified anhydride cured DGEBA epoxies. ....	158
Figure 9.38. Shows (a, b), FEGSEM images of the fracture surface for the anhydride cured DGEBA QI GFRP, taken in the steady state propagation region of crack propagation. ....	159
Figure 9.39. Shows (a-c) FEGSEM images of the mode I fracture surface for the 10N anhydride cured DGEBA QI GFRP. The nanosilica particles are indicated in the fracture surface (arrows) and some plastic void growth in the 10N epoxy is shown circled.....	160
Figure 9.40. Shows (a, b) FEGSEM images of the mode I fracture surface for the 9R anhydride cured DGEBA QI GFRP with some cavitated rubber particles shown with arrows. ....	161
Figure 9.41. Shows (a-d) FEGSEM images of the mode I fracture surface from the steady state propagation region of the 10N9R anhydride cured DGEBA QI GFRP. Some rubber particles are indicated with arrows and plastic void growth around agglomerated nanosilica is circled. ....	163
Figure 10.1. Shows (a, b) AFM phase images and (c, d) TEM micrographs of the 20N anhydride cured DGEBA epoxy. The particles remain well dispersed (white arrows) at 20 wt. % addition of nanosilica to the epoxy.....	169
Figure 10.2. Shows (a-d) AFM phase images of the rubber- and hybrid-modified anhydride cured DGEBA epoxies. The spherical rubber particles are indicated with white arrows and the nanosilica-necklaces/agglomerates with blue.....	171
Figure 10.3. Fracture energy versus glass transition temperature, $T_g$ for the nanosilica-modified epoxies that were studied. ....	174
Figure 10.4. Compressive yield strength, $\sigma_{yc}$ , versus glass transition temperature, $T_g$ for the unmodified and nanosilica modified epoxies in this study. ....	174
Figure 10.5. Normalised Young's modulus versus nanosilica content for the nanosilica-modified epoxies that were studied are compared to Halpin-Tsai [241, 245] and Nielson [247] and rule of mixtures analytical modulus models. ....	178
Figure 10.6. Normalised tensile Young's modulus versus nanosilica content for the rubber- and hybrid-modified epoxies. The results from the present study and Hsieh et al. [61] are compared to the Halpin-Tsai [241, 245] and Neilson [247] and Rule of mixtures analytical models.....	180
Figure 10.7. Normalised yield strength versus nanosilica content for the nanosilica-modified epoxies. The experimental results are compared to Pukánszky and Vörös' model [36, 37] in order to quantify the particle-matrix interfacial adhesion. ....	184
Figure 10.8. Fracture energy, $G_C$ , versus compressive true yield strength, $\sigma_{yc}$ , for the nanosilica-modified epoxies. ....	184

Figure 10.9. Low magnification FEGSEM image of the fracture surface for the 20N polyether-amine cured DGEBA epoxy shows crack forking due to the relatively large release of energy at fracture. No evidence of crack pinning mechanisms were indentified.....	187
Figure 10.10. The crack opening displacement for the nanosilica-modified epoxies that were studied. The values are shown for the 20N anhydride cured DGEBA epoxy.....	187
Figure 10.11. Cross-polarised light microscopy images (a, b) of a 10N sub-critically loaded crack-tip. The images are taken of polished sections from the edge of the DN4PB sample, thus under plane stress conditions. (The two images are from different samples).....	188
Figure 10.12. Cross-polarised light microscopy images (a-e) of polished cross-sections from unmodified epoxies loaded to within the compressive strain softening region.....	189
Figure 10.13. Fracture surfaces for the 20N (a) polyether-amine cured DGEBA and (b) the polyether-amine cured DGEBA/F epoxy. The arrows show some nanosilica particles and debonding is circled, (blue) showing no void growth and (white) showing void growth. ....	190
Figure 10.14. Normalised fracture energy versus nanosilica content for the nanosilica-modified epoxies that were studied. The linear fits show the general trend in the fracture energies.....	191
Figure 10.15. Fracture surface of rubber-modified (9R) epoxy. Internal cavitation of the CTBN and subsequent plastic void growth was observed. Some of the rubber particles are indicated with arrows.....	193
Figure 10.16. A FEGSEM image of the 10N9R anhydride cured DGEBA epoxy fracture surface [224]. A composite shows extensive deformation in the process zone region and the rubber micro-particles are shown identified.....	193
Figure 10.17. Normalised fracture energy versus nanosilica content for the rubber- and hybrid-modified epoxies that were studied. The quadratic fit shows the general trend in the fracture energy for the anhydride cured DGEBA epoxy.....	194
Figure 10.18. High magnification FEGSEM images of the 10N9R epoxy fracture surface [224], show (a) in-lens and (b) SE2 lens images of a single rubber particle and deformation around the agglomerated nanosilica particles.....	195
Figure 10.19. Schematic representation of the mechanisms that are expected to occur in the 10N9R anhydride cured DGEBA hybrid-toughened epoxy.....	196
Figure 11.1. Schematic representation of a single particle with the maximum void size that can form in the epoxy.....	203
Figure 11.2. Fracture energy and $\Delta G_s$ (inset) for the amine cured TGMDA epoxy versus nanosilica content. The experimental results from the present study are compared to the predicted fracture energy. ....	205
Figure 11.3. Fracture energy for the polyether-amine cured DGEBA/F epoxy versus nanosilica content for is compared to the predictive model. The individual contributions $\Delta G_s$ and $0.15\Delta G_v$ are shown in the inset. ....	206

Figure 11.4. Fracture energy for the polyether-amine cured DGEBA versus nanosilica content. The experimental results and [65] are compared to the predicted fracture energy and $\Delta G_s$ is shown in the inset. ....	207
Figure 11.5. Fracture energy for the amine cured multifunctional epoxy versus nanosilica content. The experimental results from [79] did not vary with nanosilica content. ....	208
Figure 11.6. Fracture energy for the anhydride cured DGEBA epoxy versus nanosilica content. The contributions $\Delta G_s$ and $0.15\Delta G_v$ are shown inset. The experimental data from this study and [61] compare very well to the predictive model.....	209
Figure 11.7. Fracture energy versus nanosilica content for piperidine cured DGEBA/F epoxy from [52] (20 nm silica particles) is compared to the predictive model. The inset shows contributions $\Delta G_s$ and $0.15\Delta G_v$ . ....	210
Figure 11.8. Fracture energy for piperidine cured DGEBA epoxy versus nanosilica content from [52] (80 nm silica particles) is compared to the predictive model. The contributions of $\Delta G_s$ , $0.15\Delta G_v$ and $0.3\Delta G_v$ shown in the inset. ....	211
Figure 11.9. The shear band yielding term, $\Delta G_s$ versus nanosilica-particle radius (at 10 and 20 vol. %) for the anhydride cured DGEBA epoxy. There is little variation for small changes in particle size (inset). ....	212
Figure 11.10. The debonding stress, $\sigma_{db}$ , as a function of particle radius at the particle-matrix interface. The inset focuses on small particle radii in the range 0-200 nm.....	213
Figure 11.11. The fracture surfaces for 9 wt. % coreshell particle-modified anhydride cured DGEBA epoxies with (a) 100 nm particles and (b) 300 nm particles.....	214
Figure 11.12. Fracture energy for anhydride cured DGEBA epoxy versus CSR content from [262]. The experimental values of $G_c$ are compared to the predictive models for 100 nm and 300 nm particles. The contributions of $\Delta G_s$ and $\Delta G_v$ are shown in the inset.....	215
Figure 11.13. Fracture energy for the rubber-modified anhydride cured DGEBA epoxy versus phase separated rubber content. The present work is compared to the predicted fracture energy. The individual contributions of $\Delta G_s$ , $\Delta G_v$ and $\Delta G_b$ are shown (inset). ....	216
Figure 11.14. Fracture energy for the rubber- and hybrid-modified epoxies anhydride cured DGEBA epoxy versus nanosilica content. The experimental study from [61] is compared to the predicted fracture energy for different degrees of void growth. ....	219

# List of Tables

Table 3.1. The constituent resins and curing agents that were used in this study. ....	52
Table 5.1. Formulations of amine cured TGMDA epoxies that were studied. ....	74
Table 5.2. Mean glass transition temperatures of unmodified and modified amine cured TGMDA epoxies, measured using DSC. ....	75
Table 5.3. Young's modulus, $E_t$ , ultimate tensile true stress, $\sigma_{UTS}$ , and ultimate tensile true strain, $\epsilon_{UTS}$ , for unmodified and modified amine cured TGMDA epoxies. ....	81
Table 5.4. Compressive Young's modulus, $E_c$ , compressive true yield strength, $\sigma_{yc}$ , and compressive true yield strain, $\epsilon_{yc}$ , for the unmodified and nanosilica-modified amine cured TGMDA epoxies. ....	82
Table 5.5. Fracture toughness, $K_C$ , and fracture energy, $G_C$ , for the unmodified and modified amine cured TGMDA epoxies. ....	84
Table 5.6. Flexural modulus, $E_f$ , and fracture initiation energy, $G_{IC INT}$ , and fracture propagation energy, $G_{IC PROP}$ , for the unmodified and nanosilica-modified amine cured TGMDA epoxies. ...	88
Table 6.1. Formulations of the unmodified and nanosilica-modified polyether-amine cured DGEBA/F epoxies. ....	95
Table 6.2. Glass transition temperatures, $T_g$ , of the unmodified and nanosilica-modified polyether-amine cured DGEBA/F epoxies. ....	96
Table 6.3. Young's modulus, $E_t$ , tensile true yield strength, $\sigma_{yt}$ , and tensile true strain at yield, $\epsilon_{yt}$ , for the unmodified and nanosilica-modified polyether-amine cured DGEBA/F epoxies. ....	98
Table 6.4. Compressive Young's modulus, $E_c$ , compressive true yield strength, $\sigma_{yc}$ , and compressive true yield strain, $\epsilon_{yc}$ , for the unmodified and nanosilica-modified polyether-amine cured DGEBA/F epoxies. ....	99
Table 6.5. Fracture toughness, $K_C$ , and fracture energy, $G_C$ , from SENB tests for unmodified and nanosilica-modified polyether-amine cured DGEBA/F. ....	101
Table 7.1. Formulations of the unmodified and nanosilica-modified polyether-amine cured DGEBA epoxies. ....	103
Table 7.2. Glass transition temperatures, $T_g$ , of the unmodified and nanosilica-modified polyether-amine cured DGEBA epoxies. ....	104
Table 7.3. Young's modulus, $E_t$ , tensile true yield strength, $\sigma_{yt}$ , and tensile true yield strain, $\epsilon_y$ , for the unmodified and nanosilica-modified polyether-amine cured DGEBA epoxies. ....	107
Table 7.4. Compressive Young's modulus, $E_c$ , compressive true yield strength, $\sigma_{yc}$ , and compressive true yield strain, $\epsilon_{yc}$ , for the unmodified and nanosilica-modified polyether-amine cured DGEBA epoxies. ....	108

Table 7.5. Fracture toughness, $K_C$ , and fracture energy, $G_C$ , for the unmodified and nanosilica-modified polyether-amine cured DGEBA epoxies. ....	110
Table 8.1. Formulations of unmodified and nanosilica-modified amine cured multifunctional epoxies. ....	114
Table 8.2. Glass transition temperatures, $T_g$ , of the unmodified and nanosilica-modified amine cured multifunctional epoxies. ....	115
Table 8.3. Young's modulus, $E_t$ , ultimate tensile true strength, $\sigma_{UTS}$ , and ultimate tensile true strain, $\epsilon_{UTS}$ , for the unmodified and nanosilica-modified amine cured multifunctional epoxies [79]. ....	117
Table 8.4. Compressive Young's modulus, $E_c$ , compressive true yield strength, $\sigma_{yc}$ , and compressive true yield strain, $\epsilon_{yc}$ , for the unmodified and nanosilica-modified amine cured multifunctional epoxies. ....	118
Table 8.5. Fracture toughness, $K_C$ , and fracture energy, $G_C$ , for the unmodified and nanosilica-modified amine cured multifunctional epoxies [79]. ....	120
Table 9.1. Formulations of anhydride cured DGEBA epoxies that were studied. ....	123
Table 9.2. Mean glass transition temperature, $T_g$ , of unmodified and modified anhydride cured DGEBA epoxies. ....	125
Table 9.3. Morphologies in the rubber- and hybrid-modified anhydride cured DGEBA epoxies. ....	131
Table 9.4. Young's modulus, $E_t$ , tensile yield strength, $\sigma_{yt}$ , and tensile fracture strain, $\epsilon_{yt}$ , for unmodified and modified anhydride cured DGEBA epoxies. ....	138
Table 9.5. Compressive Young's modulus, $E_c$ , compressive true yield strength, $\sigma_{yc}$ , and compressive true yield strain, $\epsilon_{yc}$ , for the unmodified and nanosilica modified anhydride cured DGEBA epoxies. ....	139
Table 9.6. Compressive Young's modulus, $E_c$ , compressive true yield strength, $\sigma_{yc}$ , and compressive true yield strain, $\epsilon_{yc}$ , for rubber- and hybrid- modified anhydride cured DGEBA epoxies. ....	141
Table 9.7. Fracture toughness, $K_C$ , and fracture energy, $G_C$ , for the unmodified and modified anhydride cured DGEBA epoxies. ....	144
Table 9.8. Pull-out shear strength, $\tau_{max}$ , from single-fibre pull-out tests for the unmodified and modified anhydride cured DGEBA single-fibre GFRPs. ....	153
Table 9.9. Interlaminar shear strength, $\sigma_{SBS}$ , for the unmodified and modified anhydride cured DGEBA UD GFRPs. ....	154
Table 9.10. Flexural Modulus, $E_f$ , and fracture initiation energy, $G_{IC INT}$ , and fracture propagation energy, $G_{IC PROP}$ , for the unmodified and nanosilica-modified anhydride cured DGEBA UD GFRPs. ....	155

Table 9.11. Flexural Modulus, $E_f$ , and fracture initiation energy, $G_{IC\ INT}$ , and fracture propagation energy, $G_{IC\ PROP}$ , for the unmodified and nanosilica-modified anhydride cured DGEBA QI GFRPs.....	155
Table 10.1. Morphologies of the nanosilica-modified epoxies that were studied. ....	168
Table 10.2. Morphologies of the rubber- and hybrid-modified epoxies that were studied. The inter-particle distance, $D_{IP}$ was calculated for the rubber particles and measured for the nanosilica necklaces/agglomerates. ....	170
Table 10.3. Glass transition temperatures, $T_g$ , for the unmodified and nanosilica-modified epoxies from this study. ....	173
Table 10.4. Glass transition temperature, $T_g$ , for the rubber- and hybrid-modified epoxies from this study. ....	175
Table 10.5. Tensile and compressive Young's moduli for the unmodified and nanosilica-modified epoxies. ....	177
Table 10.6. Tensile and compressive Young's moduli that were measured for the rubber- and hybrid-modified epoxies. ....	179
Table 10.7. Yield strengths for the unmodified and nanosilica-modified systems. Some values of $\sigma_{yt}$ were calculated using Equation (10.7) (italicised).....	181
Table 10.8. Yield strengths that were measured for the rubber- and hybrid-modified epoxies. ....	185
Table 10.9. Fracture energy, $G_C$ , and $T_g$ for the unmodified and nanosilica-modified epoxies. The toughenability is shown as a function of the unmodified epoxy.....	186
Table 10.10. Fracture toughness, $K_C$ , and fracture energy, $G_C$ , for the rubber- and hybrid-modified epoxies from this study and toughenability with respect to the rubber-modified epoxy. ....	192
Table 11.1. The epoxy systems that were analytically modelled. The material properties for the unmodified epoxies are listed, and the individual contributions of shear band yielding and plastic void growth are indentified as toughening observations for each epoxy polymer. ....	204

# Nomenclature

## Abbreviations

AFM	Atomic force microscopy	ISO	International standards organisation
ASTM	American society for testing materials	LEFM	Linear elastic fracture mechanics
CBT	Corrected beam theory	QI	Quasi-isotropic
CFRP	Carbon-fibre reinforced polymer	M-CDEA	4,4'-methylenebis-(3-chloro 2,6-diethylaniline)
Ch.	Chapter	M-DEA	4, 4'-methylenebis (2, 6-diisopropylaniline)
CSR	Coreshell rubber	M-DIPA	4, 4'-methylenebis (2, 6-diisopropylaniline)
CTBN	Carboxyl-terminated butadiene-acrylonitrile	NCF	Non-crimp fabric
DCB	Double cantilever beam	PTFE	Poly(tetrafluoroethylene)
DGEBA	Diglycidyl ether of bisphenol A	RIFT	Resin infusion under flexible tooling
DGEBA/F	Diglycidyl ether of bisphenol A and F	SANS	Small angle neutron scattering
DGEBF	Diglycidyl ether of bisphenol F	SAXS	Small angle X-ray scattering
DMA	Dynamic mechanical analysis	SBT	Simple beam theory
DN4PB	Double-notched four-point bend	SEM	Scanning electron microscopy
DSC	Differential scanning calorimetry	SENB	Single-edge notched bend
ECM	Experimental compliance method	TEM	Transmission electron microscopy
E-glass	Electrical glass	TGAP	Triglycidyl amino phenol
FIB	Focused ion beam	TGMDA	Tetra-glycidyl methylenedianiline
FEGSEM	Field emission gun scanning electron microscopy	UD	Uni-directional
GFRP	Glass-fibre reinforced polymer	VARTM	Vacuum assisted resin transfer moulding
HBP	Hyper-branched polymer	vol. %	Volume fraction
		wt. %	Weight fraction
		xN	Nanosilica content (by wt.)
		xNyR	Nanosilica content and CTBN content (by wt.)
		yR	CTBN content (by wt.)

## English Alphabet

		$G_{LEFM}$	Fracture energy from LEFM
$a$	Crack length	$k$	Proportionality constant for stress transfer
$B$	Thickness	$k'$	Proportion of void growth in the hybrid epoxies
$B_c$	Compressed thickness	$k_E$	Generalised Einstein coefficient
$d$	Fibre diameter	$K$	Stress intensity factor
$d_p$	Particle diameter	$K_C$	Fracture toughness or critical stress intensity factor
$D_{IP}$	Inter-particle distance	$K_{Cu}$	Fracture toughness for the unmodified epoxy
$E$	Young's modulus	$K_p$	von Mises stress concentration factor for a rigid particle
$E_c$	Compressive Young's modulus	$K_V$	von Mises stress concentration factor for a void
$E_f$	Young's modulus of filler	$L$	Embedded length
$E_m$	Young's modulus of the matrix	$m$	Gradient of load/displacement
$E_p$	Young's modulus of particle	$M_{nc}$	Cross-link density or molecular weight between cross-links
$E_t$	Tensile Young's modulus	$N$	Correction for end block stiffening
$E_u$	Young's modulus of the unmodified epoxy	$N_V$	Number of particles
$f(x)$	SENB Shape factor as a function of $x$	$P$	Load
$f'(x)$	DN4PB Shape factor as a function of $x$	$P_{max}$	Maximum load
$F$	Correction for large displacements	$P_Q$	5 % offset load
$F'(r_y)$	Modified function with respect to $r_p$ and $r_y$	$r$	Radial distance from the crack-tip
$G_C$	Fracture energy or critical strain energy release rate	$r_p$	Particle radius
$G_{Cu}$	Fracture energy for the unmodified epoxy	$r_{pz}$	Radius of the plastic zone
$G_{IC}$	Composite mode I fracture energy or critical strain energy release rate	$r_{pzu}$	Radius of the plastic zone for the unmodified epoxy
$G_{IC INT}$	Composite mode I fracture initiation energy	$r_y$	Radius of the plastic zone ahead of the crack-tip
$G_{IC PROP}$	Composite mode I fracture propagation energy		

$R$	Correlation coefficient
$S$	Support span
$t$	<i>Thickness</i>
$T_g$	Glass transition temperature
$T_{go}$	Glass transition temperature of the linear polymer
$U_s(r)$	Dissipated strain energy density function
$v_f$	volume fraction
$v_{fv}$	Volume fraction of voids
$v_{sb}(r)$	Volume fraction of shear yielded material
$v_{sb/p}$	Volume fraction of shear yielded material per particle
$W$	Width
$w_d(r)$	Plastic strain energy density
$x$	$a/W$
$\bar{x}$	Arithmetic mean
$\pm$	Standard deviation

## Greek Alphabet

$\alpha(r)$	Scaling factor for the strain field in the process zone	$\mu$	Material constant
$\beta$	Material constant	$\mu_m$	Material constant for pressure dependency
$\Gamma(T)$	Tearing energy as a function of temperature	$\nu$	Poisson's ratio
$\gamma_d$	Specific debonding energy for two newly created surfaces	$\nu_{max}$	Material constant for particle type and arrangement
$\gamma_{fu}$	True fracture strain for the unmodified epoxy	$\sigma_{db}$	Critical debonding stress
$\delta$	Displacement	$\sigma_c$	Compressive true stress
$\delta_c$	Crack opening displacement	$\sigma_e$	External stress for the modified matrix
$\Delta$	Crack length correction	$\sigma_E$	Engineering stress
$\epsilon_E$	Engineering strain	$\sigma_m$	Matrix stress
$\epsilon_t$	Tensile true strain	$\sigma_t$	Tensile true stress
$\epsilon_c$	Compressive true strain	$\sigma_{UTS}$	Ultimate true tensile strength
$\epsilon_{UTS}$	Ultimate tensile true strain	$\sigma_{yc}$	Compressive true yield stress
$\epsilon_{yc}$	Compressive true yield strain	$\sigma_{ycu}$	Compressive true yield stress for the unmodified epoxy
$\epsilon_{yt}$	Tensile true yield strain	$\sigma_{yt}$	Tensile true yield stress
$\Delta G_b$	Toughening increment from rubber bridging	$\sigma_{ytu}$	Tensile true yield stress for the unmodified epoxy
$\Delta G_{db}$	Toughening increment from particle debonding	$\tau_{max}$	Pull-out shear strength
$\Delta G_s$	Toughening increment from shear band yielding	$\phi$	Energy calibration factor
$\Delta G_v$	Toughening increment from plastic void growth	$\psi_H$	Toughening increment due to hybrid-modification
$\zeta$	Shape factor	$\psi_N$	Toughening increment due to rigid (nanosilica) particles
$\eta$	Material constant as a function of $\zeta$ , $E_p$ and $E_u$	$\psi_R$	Toughening increment due to phase separated rubber

## Introduction

### 1.1 Background

The use of epoxy polymers is extensive in engineering applications such as coatings, adhesives and matrices in composite materials. As coatings, such resins are used widely for applications requiring UV light protection or high scratch resistance. Their insulating properties, good temperature resistance and ease of processing allow epoxies to be used heavily in the electronics industry for applications in printed circuit boards and encapsulated electrical components [1].

As adhesives, epoxies possess many advantages over mechanical fastening techniques. Their relatively high Young's modulus and chemical resistance make them ideal for stress distribution across bonded joints including joining of dissimilar materials [2]. This has been used by industry to produce more efficient structures with greater tolerance in design methods due better distribution of stresses between components.

By definition a composite is a combination of two distinct phases, which, when mixed to a reasonable proportion, exhibit properties that far exceed those of the components. In the case of fibre-reinforced composites, the fibre phase, typically carbon, glass or aramid, is supported by a matrix material [3]. The primary functions of the matrix material in a fibre-reinforced composite are to distribute stress between the fibres and provide rigid structural support to prevent the load carrying fibres from buckling or distorting. Secondary functions include a high service temperature range and toughness and durability; increasing both the component life and performance envelope. Importantly, the fibre-reinforcement can be tailored specifically for the required loading situation, making them extremely efficient. This feature provides ever increasing and exciting applications of composite materials as better constituent phases are designed.

The highly cross-linked nature of these epoxies which makes them so favourable for stress transfer applications also means that the epoxy is inherently brittle with poor resistance to crack initiation and propagation. The addition of rubber and rigid particles

can vastly improve the fracture properties by enhancing crack-tip deformation processes [4-6]. However, the addition of these micron-sized particles results in difficulties with processing, particularly when considering infusion based manufacturing techniques. Thus, the general theme of this study was to examine the effect of silica nanoparticle-modification (referred to as nanosilica here on in) on the stress-strain and yield behaviour with particular interest on the fracture energy,  $G_C$ .

The use of nano-sized modification has been shown to vastly improve these properties without altering the thermo-mechanical properties of the epoxy which made them so favourable to begin with [4-6]. Furthermore, the particles are small enough, that they are not impeded by the fibre performs for the case of fibre-reinforced composite materials. For this study, rigid, amorphous nanosilica particles were used to modify the epoxy polymers.

## 1.2 Aims and objectives

The primary objective of this work was to investigate and identify the toughening mechanisms that exist in nanosilica-modified epoxies. When phase separating rubber has been introduced, interesting synergistic behaviour of  $G_C$  has been obtained. Little understanding exists for the exact toughening mechanisms that are occurring and these will be explored.

Furthermore, the toughening mechanisms were hoped to be modelled analytically and coupled with the experimental data. This was to verify that the correct controlling parameters for the toughening effect were identified. Of particular interest is that previous work has identified that nanosilica particle debonding with subsequent plastic void growth plays a vital role to the improved fracture properties that have been recorded [7]. This was examined in greater detail, and the extent by which the void growth process plays on the improvements in  $G_C$  were determined.

This is to be achieved by correlating the mechanical properties to the microstructure and examining the effect of particle size, distribution and adhesion. Five different epoxy systems are to be compared using their thermo-mechanical properties and overall nanosilica-toughenability.

The transfer of toughness to the continuous fibre-reinforced composite materials is to be examined. Qualitative work will explain the importance of fibre-matrix adhesion and stress transfer across the fibre-matrix interface and this will be used to explain the toughening mechanisms that are observed.

## 1.3 Thesis outline

This thesis is structured by epoxy system. Each system was characterised by morphology, thermal, tensile and compressive and fracture properties. The fractured samples are examined using various microscopy techniques to verify the presence of toughening mechanisms.

Each Chapter (Ch.) in this thesis can be summarised as follows:

Ch. 2 is a review of literature regarding previous studies that examined the effect of particle modification (both hard and soft), on the toughening of epoxy polymers. The effects of particle size, adhesion and overall yield behaviour, and their effect on the fracture energy are reviewed.

Ch. 3 specifies the materials that were used in this study. The constituents that were used to produce the epoxy polymers are listed with the individual mix ratios and the cure regimes that were applied.

Ch. 4 describes the experimental procedures that were followed to obtain the various material properties. Also detailed, are the data reduction methods that were used and information regarding the microscopy that was conducted.

Ch. 5 presents the first of the experimental results; for the amine cured tetra-glycidyl methylenedianiline (TGMDA) epoxy. This system was examined in bulk and as a fibre-composite. This epoxy system possesses relatively high Young's modulus and glass transition temperature. Similar epoxies are generally used for infusion based manufacturing of high performance components, often with complex geometries in the aerospace and motorsport sectors. Thus, this system was examined as a composite material with continuous carbon-fibre reinforcement. Nanosilica-modified epoxies and nanosilica-modified and rubber-modified (hybrid-modified) epoxies were used.

Chs. 6, 7 and 8 report on the bulk epoxy properties for nanosilica-modified (i) polyether-amine cured di-glycidyl ether of bisphenol A & F (DGEBA/F), (ii) polyether-amine cured di-glycidyl ether of bisphenol A (DGEBA) and (iii) an amine cured multifunctional epoxy. This section of work focuses on the effect of nanosilica-modification on the pure epoxy, i.e. rubber-modification was not considered for these systems.

Ch. 9 describes the results that were obtained for an anhydride cured DGEBA. This system was the main focus of this study and was examined as a bulk epoxy and as a

fibre-reinforced composite. The anhydride cured DGEBA epoxy is a low cost and low viscosity system. It is ideally suited to infusion based manufacturing of large structures and intermediate performance applications, such as those in the wind and marine sectors. This epoxy is examined with continuous glass-fibre reinforcement. Furthermore, the epoxy polymer was examined as a nanosilica-modified epoxy and as a hybrid-modified epoxy.

Ch. 10 reviews the results from the previous Chapters. A detailed comparison of the material properties and stress-strain relationships was conducted for the various nanosilica-modified and hybrid-modified epoxies. The variations in these properties were compared to nanosilica content with particular emphasis on the fracture energy. Some hypotheses are made regarding particle-matrix adhesion and evidence to support these are discussed.

Once the toughening mechanisms are established, analytical models are developed in Ch. 11 to examine the relative contributions of each of these mechanisms and their relative importance to the overall toughenability of the epoxies.

Lastly, Ch. 12 presents the conclusions of this project, and provides recommendations regarding potential areas for future work and interesting avenues that were identified during the course of this study.

The following Chapter, Ch. 2, provides some background of literature pertaining to toughening of epoxies using particle inclusions and their effect on the yield and fracture behaviour. The transfer of toughness that has been reported with matrix modification to fibre-reinforced composite materials is also reviewed.

## Literature Review

### 2.1 Introduction

This chapter focuses on literature related to epoxies with respect to (i) their toughening with nanosilica and (ii) their use as matrices in continuous fibre reinforced composites. The general theme of this work was to focus on the effect that matrix modification has on the fracture properties. This chapter discusses published work related to epoxy modification, the effect this has on the fracture energy and the toughening mechanisms that were reported for such systems.

The epoxy polymers used in this work are commonly used as clearcoats, adhesives and matrices in fibre-composite materials [8]. The use of bonded joints and composites materials is ever increasing in areas such as the aerospace and wind sectors due to their structural efficiency [2, 9]. Epoxies are amorphous, highly cross-linked, thermosetting polymers which exhibit good elevated temperature resistance and low creep. However, their high cross-link density causes them to be relatively brittle polymers. This limits their application as structural materials, as they have a poor resistance to the initiation and growth of cracks. Thus, any improvements in fracture or fatigue performance are highly sought after by industry.

This chapter is separated into four sections that detail the published works of rigid particle-, rubber- and hybrid toughening and then the use of such modified-epoxies as a matrix in fibre composites. This literature survey aims to provide a modern review in order to put this study into context.

The yield and fracture behaviour of epoxies has been shown to be sensitive to pressure and strain rate and can be described using a modified von Mises criterion [10, 11]. The yield behaviour of bulk glassy polymers was examined in detail by Bowden and co-workers [12-15]. Their works showed that strain inhomogeneities act as initiation sites for yield and this forms a negative slope on the true stress-true strain curve after the yield strength, i.e. strain softening occurs. They used this work to describe the formation of shear bands during strain softening in the polymer. It was

noted that the inclination of these bands was not always measured at 45° due to elastic recovery in the polymer.

Vakil and Martin [16] reported fracture and yield data for their epoxies and correlated their results to Kinloch and Williams [17] and Yamini and Young [18]. They characterised types of crack growth in the epoxy polymers with respect to the tensile yield strength and relative initiation/propagation fracture toughness, shown in Figure 2.1. The ductile epoxies general possessed the lowest tensile yield strength. The epoxies with relatively high tensile yield strength were found to fail in a brittle manner.

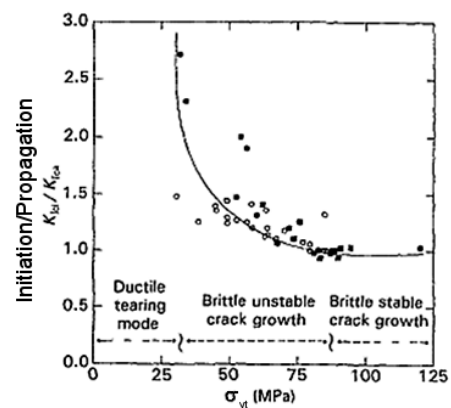


Figure 10 Correlation between  $K_{Ia}/K_{Pa}$  and true tensile yield stress, (●) Kinloch and Williams [21], (■) Yamini and Young [13]; (○) present work.

Figure 2.1. The characteristic types of crack growth in epoxies with respect to the tensile yield strength [16].

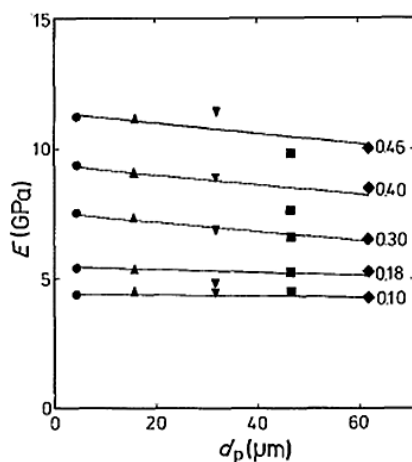
## 2.2 Rigid particle toughening

The addition of micron-sized rigid particles is widely regarded as a less effective toughener compared to rubber particles. However, useful properties such as increased Young's modulus, reduced cure shrinkage and maintained thermo-mechanical properties can be achieved in addition to a toughening effect [19, 20]. The incorporation of a readily available filler particle can also reduce the overall cost of such polymer systems. Different types of such particles have been reported in the literature e.g. glass/silica, alumina and chalk [21-26]. This review focuses on silica particles with particular attention to the nano-size range although larger particles are explored to provide a size comparison.

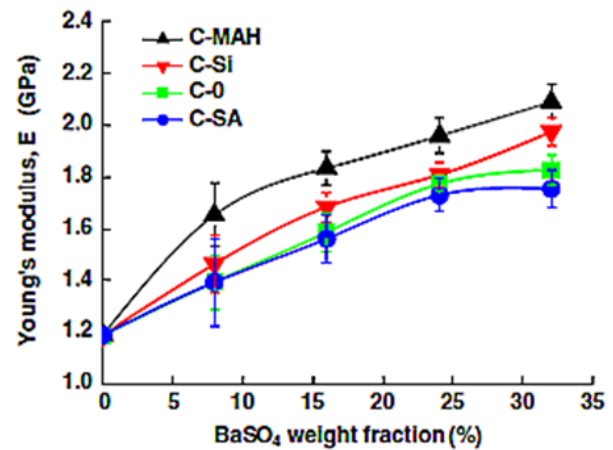
Vollenberg and Heikens [26-28] have reported particle size dependence on the Young's modulus due to variable inter-phase properties in the polymer. However, the Young's modulus is generally regarded to be unaffected by particle-matrix adhesion [29-32]. The Young's modulus is measured at low intrinsic strains and interfacial

separation would not be expected to occur [29, 30, 32, 33]. Figure 2.2 shows that the Young's modulus is independent of particle size (*left*) and adhesion (*right*). Spanoudakis and Young's work [24] concentrates on the effect of Young's modulus for different particle sizes,  $d_p$ , at different volume fractions of glass particle in epoxy, as indicated to the right of the data.

Wang et al. [35] varied the surface modification of their  $1.29 \mu\text{m}$   $\text{BaSO}_4$  particles in polypropylene and compared a copolymer (0.66 wt. %), C-MAH, 1 wt. % silane treated particles, C-Si an unmodified control, C-O, and lastly, 1 wt. % steric acid treated particles, C-SA. No difference in the Young's modulus was obtained with particle adhesion for the varying particle contents.



(a) Spanoudakis and Young [24]



(b) Fu et al. [34] from Wang et al. [35]

Figure 2.2. The Young's modulus is independent of (a) particle size [24] and (b) particle-matrix adhesion [34] (original work from [35]).

## 2.2.1 Yield behaviour

Pukánsky and Vörös [36-38] were able to show that very different levels of particle-matrix adhesion could be obtained with particle filled polymers (including glass-filled epoxy) and the adhesion has a marked effect on the yield strength at different volume fractions, as also shown by Dekkers and Heikens [39]. Their work was focused on using stress averaging principles to form predictive models for the variation of yield strength with different volume fractions of glass (e.g. Figure 2.3(a)). The general trend in their work was in good agreement to that of Vollenberg and Heikens [26-28, 40]. Their studies showed that smaller particles generate higher yield strengths for a given particle-matrix adhesion. An energy based analysis showed that the relationship between the yield stress of the matrix and the debonding stress determines the mechanism of deformation. Strong adhesion leads to matrix yielding, while decreased

particle-matrix interaction leads to debonding, with a corresponding dependence of yield strength on the filler content.

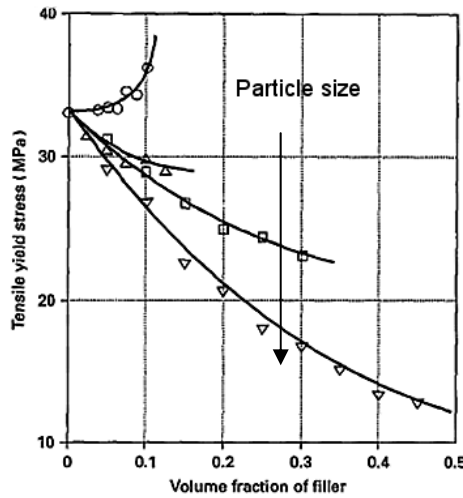


Figure 1 Tensile yield stress of particulate filled PP composites plotted against filler content. Effect of filler particle size: ( $\nabla$ ) 58.0  $\mu\text{m}$ , ( $\square$ ) 3.6  $\mu\text{m}$ , ( $\Delta$ ) 0.08  $\mu\text{m}$ , ( $\circ$ ) 0.01  $\mu\text{m}$ .

(a) Pukánsky and Vörös [36]

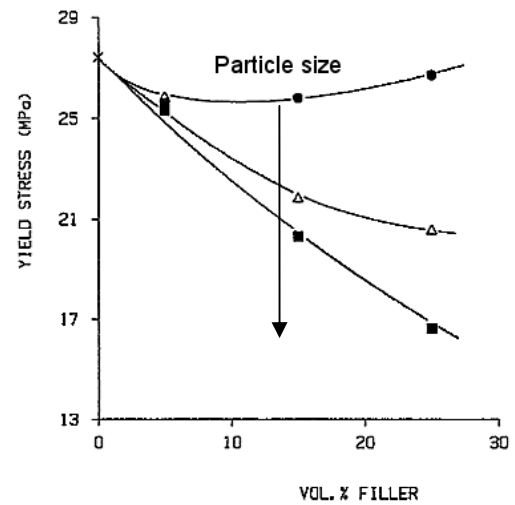


Figure 4 The yield stress as a function of the volume fraction of the filler for 3.5  $\mu\text{m}$  ( $\bullet$ ), 30  $\mu\text{m}$  ( $\Delta$ ) and 130  $\mu\text{m}$  ( $\blacksquare$ ) chalk particles.

(b) Vollenberg and Heikens [26]

Figure 2.3. The yield strength versus volume fraction for (a, b) different particle sizes of chalk-filled polypropylenes [26, 36].

It was reported that particle size, interaction and the inter-phase properties determine the stress necessary to separate the particle-matrix interface. The thickness of the inter-phase depends on the strength of the interaction; a linear correlation was found between the thickness of interlayer and the reversible work of adhesion. They have been extending their work to include the inter-phase properties that surround the particles [41], recently reviewed in [42]. Zhang et al. [43] predicted the formation of an inter-phase in nanosilica-modified epoxies but were not able to support it with experimental evidence. Sen et al. [44] reported the formation of an inter-phase around nanosilica particles in their modified polystyrene using small angle neutron scattering experiments.

Kawaguchi and Pearson [45, 46] varied the interfacial adhesion in glass bead filled epoxies using aminopropyltrimethoxysilane and found that better adhesion resulted in higher yield strengths in their epoxies. Many researchers, for example the works of Gent [47], Nicholson [48] and more recently, Chen [49, 50] and Williams [51] have reported the strong dependence of debonding stress on the particle size with other notable studies in [33, 34, 36, 37]. Figure 2.4 is extracted from Chen's recent work and shows that the debonding stress is very high for particles in the nanometre size range, where  $E_p/E$  is approximately 50 for nanosilica particles in epoxy.

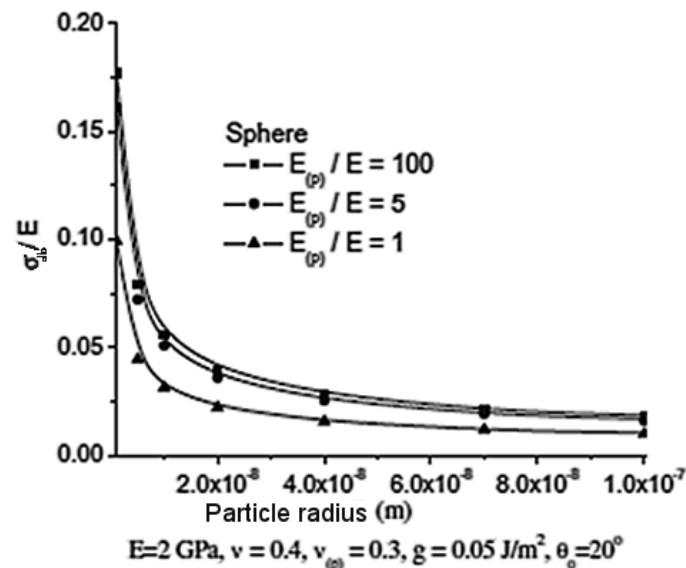


Figure 2.4. The debonding stress at the interface is generally regarded to be inversely proportional to the square root of particle radius [50].

Recently, Pearson and co-workers [52, 53] reported data for their nanosilica-modified epoxies and found no change in the yield strength for varying nanosilica content, suggesting that yield in the epoxy initiates prior to debonding of the particle-matrix interface for particles in this size range.

### 2.2.2 Fracture behaviour

A detailed review of energy absorption capabilities of nanocomposites has been reported recently in [54, 55] with a fatigue specific review in [56]. The studies detailed relevant references in the subjects of particle size, stiffness, dispersion, interfacial effects and the overall toughening effects that have been reported for various types of nano-particle e.g. silica, carbon nanotubes and nanoclays.

Lee and Yee [57] examined the effect of matrix toughness on the overall toughenability of glass bead-modified epoxies. Their work was able to show that the fracture energy of the glass-bead modified epoxy scales with epoxide molecular weight because matrix shear yielding is the major energy dissipation mechanism. Kawaguchi and Pearson [45, 46] were able to induce ductility (using moisture) in their glass bead epoxies and reported that improved fracture energies could be obtained. Liang and Pearson [52] have been able to do this with their nanosilica-modified epoxies (by varying cure temperature) and reported similar trends. This would suggest that these epoxies are toughened by matrix dominated matrix yield processes.

From the literature, the fracture energy seems to pass through a maximum value with subsequent decreases at higher particle volume fractions, e.g. [24]. The optimal volume fraction is dependent on many factors such as particle size, particle-matrix adhesion and yield behaviour of the epoxy. Therefore, no single volume fraction can be deemed to be optimal from the documented studies.

Spanoudakis and Young [23, 24] showed that the effect of particle matrix adhesion only had a small effect on the fracture toughness,  $K_{IC}$ . However, much higher values of fracture energy,  $G_C$ , could be obtained for poorly bonded particles where large amounts of shear yielding and plastic void growth occurred. Kawaguchi and Pearson [45, 46] also found that with poor adhesion, they could obtain higher values of  $G_C$  in their glass bead-modified epoxies.

Previous work from Kinloch, Taylor and co-workers has shown that nanosilica particles can be used increase the bulk fracture- [7, 58-61] and fatigue-performance [60, 62, 63]. Johnsen et al. [7], Zhang et al. [43, 64], Ma et al. [65] and Liang and Pearson [52] have reported roughly linear increases in the fracture energy with the addition of 20 nm nanosilica up to contents of about 14-18 vol. %.

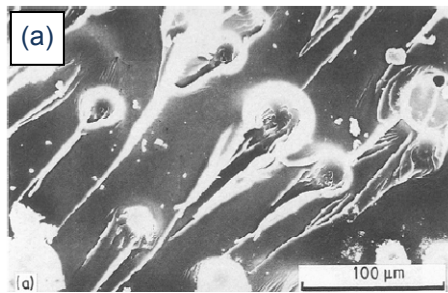
The effect of particle size was examined by Lee and Yee [66] and Kawaguchi and Pearson [45, 46]. No notable effect on the fracture energy was noted for particles in the 3-24  $\mu\text{m}$  or 4-42  $\mu\text{m}$  ranges respectively. Liang and Pearson reported fracture properties for their 20 and 80 nm nanosilica-modified epoxies with their results suggesting very little difference in toughenability between the two [52]. Interestingly, they reported that the nanosilica-modified epoxies were more toughenable than the micron-size equivalent that was reported by Kawaguchi and Pearson [45, 46] (having worked with the same epoxy system).

### 2.2.3 Toughening mechanisms

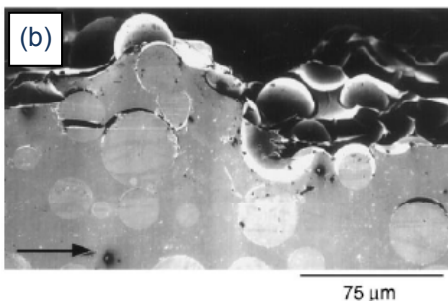
Toughening mechanisms for micron-sized glass particles have been well reported in the literature. Particular works of interest include those by Spanoudakis and Young [23, 24], Kawaguchi and Pearson [45, 46] and Lee and Yee [57, 67]. For the nano-size range; Johnsen et al. [7], Liang and Pearson [52] and Hsieh et al. [61] are the most pertinent.

Rigid (micro) particle-modified epoxies have been toughened through mechanisms such as (a) crack pinning [19, 68-72], (b) deflection [23, 73], (c) shear band yielding in the epoxy [57] and (d) particle debonding and with subsequent plastic void growth [45,

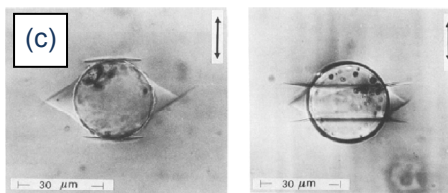
46, 57, 74]. Figure 2.5 shows examples and provides brief descriptions of the processes that take place.



Crack pinning [75], whereby tails form from the interaction of the crack path as the two arms of the crack intersect on different planes.



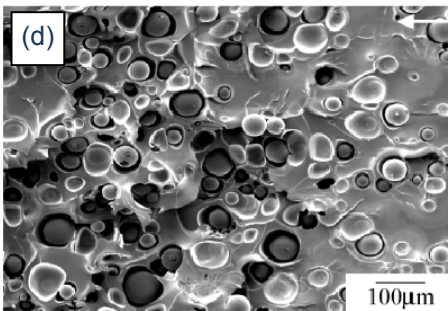
Crack deflection occurs when the crack path is attracted to the poles of the particles for the case of well bonded particles, or has to navigate around the particle-matrix interface with poorly bonded particles [67].



Shear band yielding can be shown to occur for both well and poorly bonded glass particles in the plane of highest shear stress [76].

Figure 1 Combined craze and shear band pattern at an excellently adhering glass bead in a SAN matrix. The arrow indicates the direction of the applied tension.

Figure 3 Combined craze and shear band pattern at a poor adhering glass bead in a SAN matrix. The arrow indicates the direction of the applied tension.



Plastic void growth occurs when the particles debond, crack-tip stress triaxiality is lost and the epoxy can plastically deform to form voids surrounding the debonded particles [46].

Figure 2.5. The mechanisms (a-d) that are widely regarded to toughen rigid particle-modified epoxy polymers [46, 67, 75, 76].

The first two mechanisms (a and b) have been shown by Johnsen et al. [7] to be trivial for the case of nanosilica particles in epoxy because the particles are many orders of magnitude smaller than the crack opening displacement. Their work comprehensively explored the effects of surface roughness to show that the mechanisms of crack deflection, pinning and immobilised polymer in the inter-phase layer do not directly contribute to a toughening effect. Thus, these mechanisms are not reported further,

although the reader can obtain a comprehensive background from the referenced studies.

Dekkers and Heikens [76, 77] and Lee and Yee [45, 57] noted shear band yielding with micron glass particles for both well bonded and debonded particles. They were able to show that shear banding initiates near the poles (highest stress concentration) for the well bonded or debonded glass beads.

Due to the very small size of the nanosilica particles, low volume fractions can induce very large amounts of toughening if the mechanisms are based on epoxy deformation. Johnsen et al. [7] were among the first to report that plastic void growth mechanisms may be leading to the toughening effect, see Figure 2.6(a). Liang and Pearson [52] extended this theory to show that shear band yielding must also contribute to toughening mechanisms that were being observed (Figure 2.6(b) from Hsieh et al. [61]). These mechanisms were recently implemented into mathematical models by Hsieh et al. [61] (based on this study) that can successfully predict the fracture energy of such epoxies.

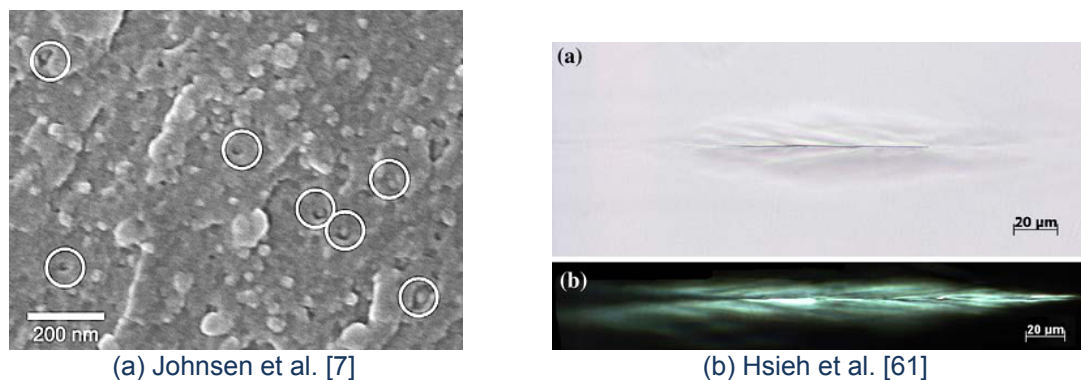


Figure 2.6. Images of nanosilica-modified epoxies from (a) the fracture surface with evidence of void growth and (b) sub-critically loaded crack-tips to show shear banding [7, 61].

## 2.3 Rubber toughening

Toughening epoxy polymers using a rubbery phase has been investigated extensively in the past [78], and can be characterised into two distinct categories. The first being the incorporation of a solute phase that separates upon curing and the second being a direct homogenisation of the rubber phase using for example, a thermoplastic additive [79].

Solute carboxyl-terminated butadiene-acrylonitrile (CTBN) adducts were used in this work, creating phase separated micron-sized particles upon curing. Sultan and McGarry [10] first applied this technique to toughen epoxies. This method is preferred

as the rubber particles are formed as a well-dispersed phase without any processing complexities. As CTBN rubbers were used in this study, they will be the sole focus of this review with regard to rubber toughening. Modern and comprehensive reviews of rubber toughened epoxies can be obtained from [80, 81] and with particular attention to CTBN modified-epoxies in [2].

The inevitable effect of adding rubber to epoxies is the resulting loss of glass transition temperature, compromising their high temperature performance [82]. This was attributed to the rubber that does not phase separate upon curing. Huang et al. [83] were able to show that particle-matrix adhesion had little effect on the fracture properties.

### 2.3.1 Yield behaviour

Kinloch et al. [84, 85] and Pearson and Yee [86] showed that higher molecular weight epoxies are more toughenable than low molecular weight (high glass transition temperature epoxies). Figure 2.7 shows that there is little variation in  $G_C$  with monomer molecular weight for the unmodified epoxies. However, increasing the molecular weight between cross-links can enhance the toughening effect due to rubber particles considerably [86].

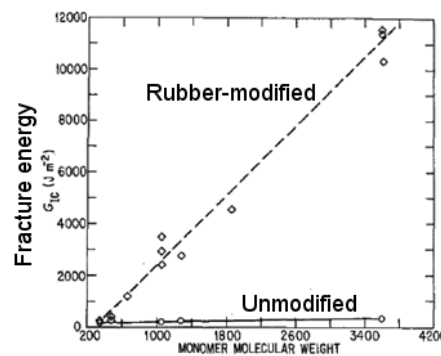


Figure 5 Fracture toughness increases modestly with increasing monomer molecular weight for neat epoxies. However, the fracture toughness of the rubber-modified epoxies increases dramatically with increasing epoxide monomer molecular weight. ( $\diamond$ ) Elastomer-modified resins; ( $\circ$ ) neat resins.

Figure 2.7. Fracture energy as a function of monomer molecular weight [86].

Meeks [87] also showed that tightly cross-linked epoxies are not toughenable because the epoxy is not able to plastically deform. The major toughening mechanisms for the rubber-modified epoxies are dependent on deformation within the epoxy polymer; hence this section briefly explains some of the yield properties that have been reported.

Arias et al. [88] reported that the yield stress is lowered when a dispersed rubber phase is added to a rigid polymer. Their work showed (Figure 2.8) that epoxies that can strain

soften exhibit more toughening effects because the yield stress is maintained at low magnitude during deformation. With their unmodified epoxies in uniaxial compression, they showed that the generation of significant toughening mechanisms may be related to the ability of the epoxy matrix to undergo strain softening followed by large deformation at relatively low stress. It was postulated that strain softening enables the formation of dilatation bands that extend in area and lead to massive shear band yielding of the material located in the region close to the crack-tip, absorbing strain energy.

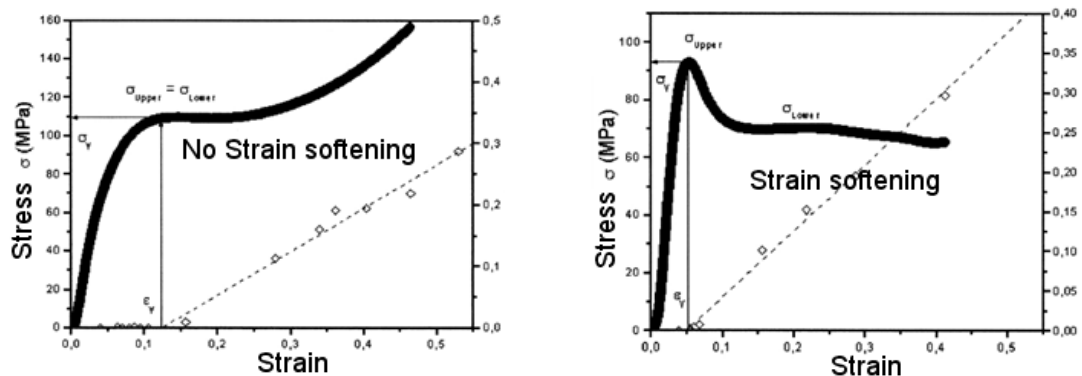


Figure 2.8. The ability for the epoxy to plastically deform is an important parameter for large toughening effects with rubber particles [88].

Zhang and Berglund's work showed the effect of volume fraction of rubber on the yield behaviour in tension and compression, reproduced in Figure 2.9 [89]. The addition of rubber leads to lower yield strengths and vastly increased strains to failures.

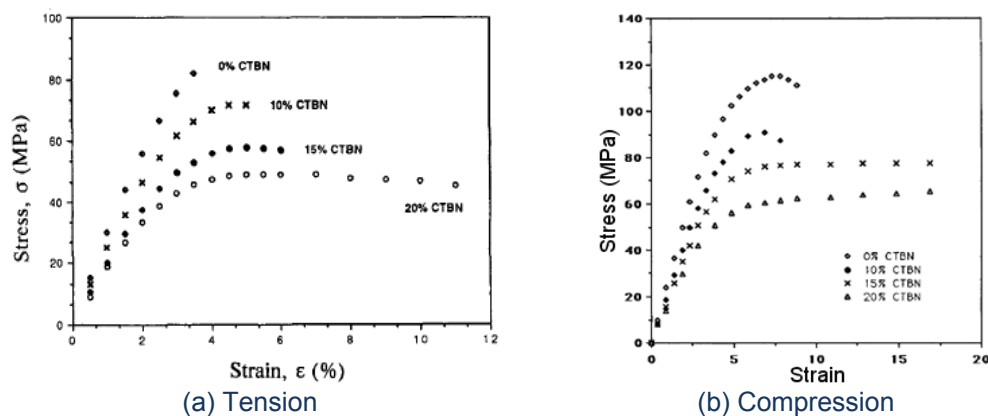


Figure 2.9. Zhang and Berglund [89] showed the effect of rubber-modification on the yield behaviour in (a) tension and (b) compression.

### 2.3.2 Fracture behaviour

A linear trend in the value of  $G_C$  can be attained up to about 10-20 vol. % of rubber i.e. [90-92]. Further addition of rubber to the epoxy tends to result in stabilisation or

decrease in  $G_C$  due to the formation of co-continuous or phase inverted morphologies in the epoxy [82].

No variation in the fracture properties was been reported for rubber particles of the range 1-5  $\mu\text{m}$  [91]. Sultan and McGarry [10] did examine 40 nm rubber particles and found the micron sized particles to be more efficient at toughening. This lack of efficiency at low particle sizes is believed to be due to the relatively high cavitation stresses that are required by the smaller particles. Guild et al. [93] were able to show that particles smaller than 0.25  $\mu\text{m}$  require very high strains to induce cavitation and would seem to agree with Sultan and McGarry's work.

### 2.3.3 Toughening mechanisms

Localised shear band yielding between the rubber particles is widely regarded as the major toughening mechanism in rubber-modified epoxies [85, 91, 94-96] as shown in Figure 2.10. The rubber micro-particles have been shown to act as stress concentrations which initiate localised yielding, often between the rubber particles. This deformation absorbs strain energy and incorporates larger deformation zones in the epoxy, and delays the onset of failure.

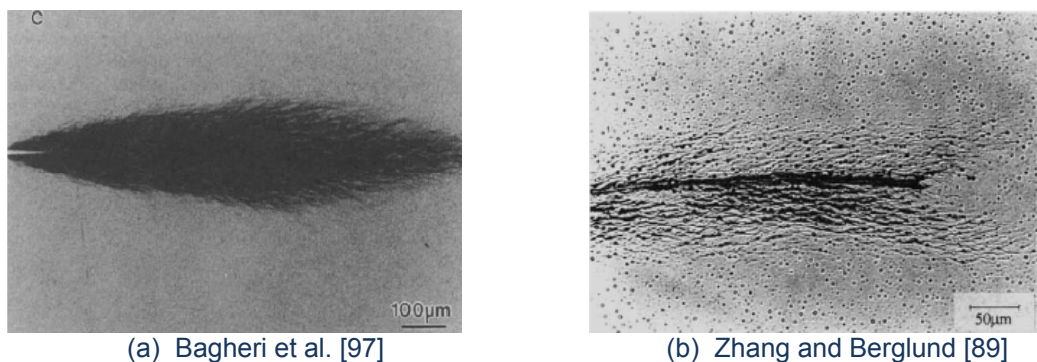


Figure 2.10. Polished sections of sub-critically loaded crack-tips show extensive shear banding in rubber-modified epoxies [89, 97].

The rubber particles are believed to cavitate at relatively low stress, which precedes localised shear yielding [98]. Huang and Kinloch [99] were able to show that cavitation can occur either before or after shear banding. The high bulk modulus of the rubber particles prohibits any volumetric deformation until the rubber particles either cavitate internally or debond from the matrix, and this process is based on an energy balance [100]. This has the effect of absorbing a little strain energy, but also the role of cavitation is to allow plastic void growth to occur in the epoxy matrix and this process is independent of shear banding [85, 101]. Furthermore, the release of stress triaxiality

during the plastic void growth process will enhance the plane stress shear banding process. Figure 2.11 shows images of a rubber-modified epoxy before loading and the fracture surface. Prior to loading, the rubber rich regions are spherical and can be seen to contain rubber. Post-fracture, the rubber domains now appear as voids, notably much bigger than previously due to the plastic void growth processes that have occurred.

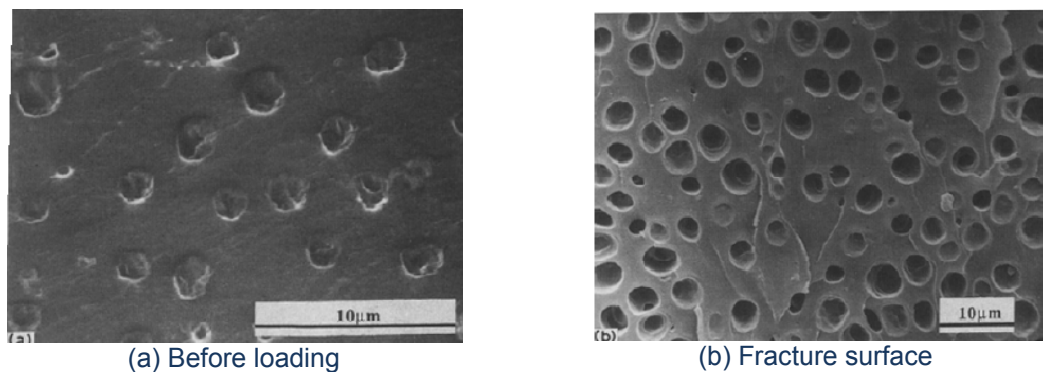


Figure 2.11. Images from (a) a sample cross section of a rubber-modified epoxy and (b) the fracture surface for the same formulation [101].

Bagheri and Pearson [102] were able to show that that the cavitation resistance of rubber particles should not play a major role in toughening. Many studies have shown that toughening can also be achieved with micro-voids [95, 102, 103] although this is not quite as efficient as rubber toughening [104].

Huang and Kinloch [94] attributed this additional toughening effect to rubber bridging mechanisms and expected it to contribute to about 10 % of the overall fracture energy at room temperature as originally proposed by Kunz-Douglas et al. [105]. Moreover, crazing based toughening mechanisms are not generally regarded as pertinent mechanisms in such epoxies due to their cross-linked nature [91].

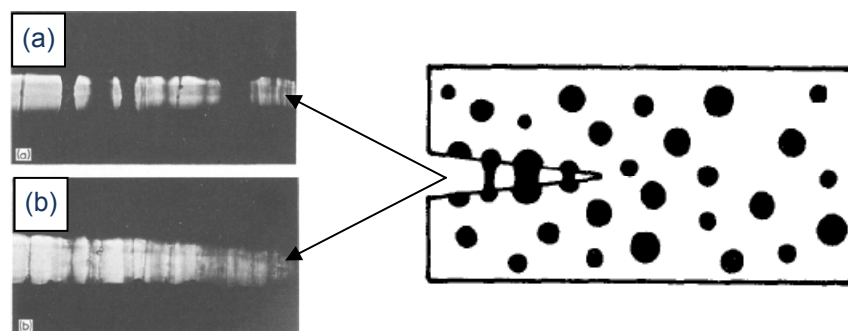


Figure 2.12. Schematic of rubber bridging shown (a) initially and (b) with continued loading, the larger bridged particles fail [105].

Numerical and analytical models to explain and predict rubber toughening are well documented in the literature, for example [85, 94, 96, 105-112]. The most pertinent to this work being Huang and Kinloch's models that predict the relative toughening increments of void growth, shear band yielding and rubber bridging as independent mechanisms [85, 94].

## 2.4 Hybrid toughening

This section focuses on the published work regarding a combination of two or more types of toughener in the epoxy, referred to as hybrid toughening. Often the combination of two or more types of toughening results in synergistic behaviour, whereby the sum of the toughening contributions due each type of particle alone are exceeded by the  $G_C$  for the hybrid-modified epoxy. Many researchers have reported the synergistic behaviour of glass and CTBN in epoxy, e.g. [72, 89, 113-120]. Historically, this combination was sought to try and restore the loss of Young's modulus that occurs with rubber-modification and was first examined in detail by Kinloch, Maxwell and Young [72, 113-115].

Synergistic effects have also been reported for other systems with the combination of CTBN using particles such as nanoclays, bimodal rubber, zirconia and carbon nanotubes [118, 121-131]. Unconventional forms of hybrid-modified synergy for  $G_C$  have been reported for rubber coated glass beads by Lee and Yee [132] and Amdouni [75], and bimodal-size glass particles by Dittanet and Pearson [53].

Hybrid morphologies have been reported for nanosilica with phase separable rubbers (such as CTBN) in the literature, i.e. [4, 59, 61, 133-136]. Interestingly, Tsai et al. [135] has been the only study to report good dispersion in the hybrid form at such high concentrations of rubber. Mohammed [59] found that above rubber concentrations of more than about 5-7 wt. % of CTBN rubber, the nanosilica particles agglomerated into necklace-like structures as shown in Figure 2.13.

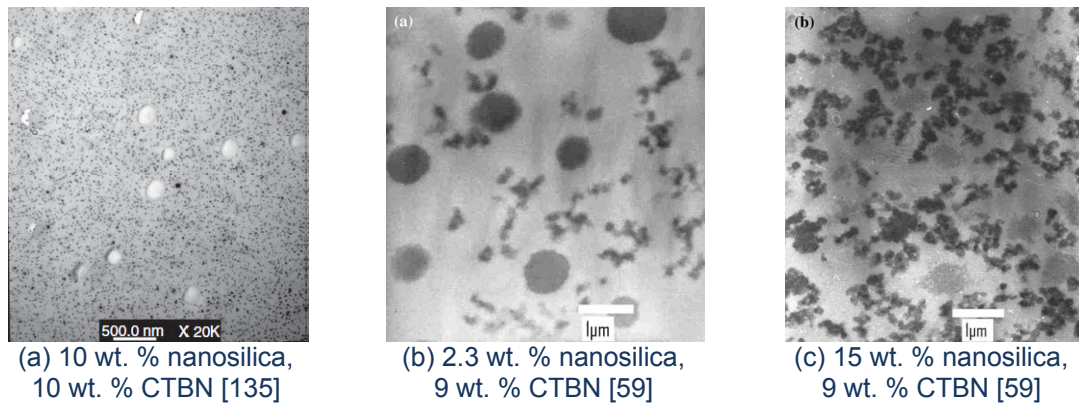


Figure 2.13. Shows (a-c) morphologies of (nanosilica and rubber) hybrid-modified epoxies [59, 135]. Note that images from [59] have been stained with osmium tetroxide.

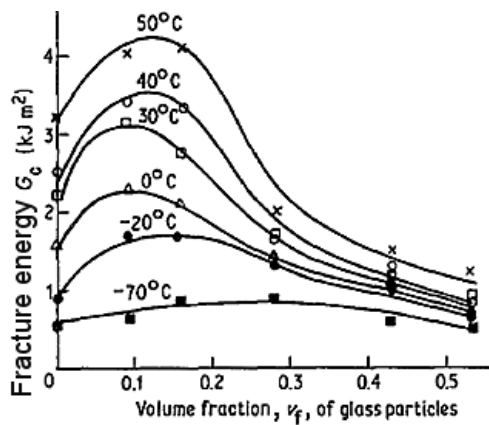
It is of note that a synergistic behaviour is not always obtained, for example Tsai et al. [135], Lee [58] and Mohammed [59] have reported hybrid-modified epoxies for which  $G_C$  remained the same as the rubber-modified equivalent for certain amine cured epoxies.

#### 2.4.1 Yield behaviour

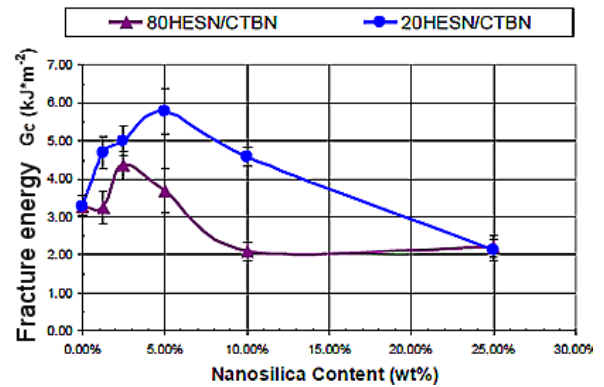
Zhang and Berglund [89] examined the yield behaviour of a hybrid-modified epoxy with glass particles. They found no difference in the yield behaviour of the modified epoxy compared to the rubber-modified epoxy (assumed as the baseline value). Young et al. [115] and Liu et al. [137] also reported yield data for hybrid-modified epoxies and showed no increase in yield strength from the value of the rubber-modified epoxy. This would suggest that yielding initiates due to the rubber particles rather than due to debonding of the glass particles.

#### 2.4.2 Fracture behaviour

Kinloch et al. [113] and Liang and Pearson [134] both reported hybrid-modification of a piperidine cured DGEBA with similar amounts of rubber (15 or 18 wt. % respectively). It is of note that for micron-sized or nano-sized particles, an optimal volume fraction exists. Beyond this concentration, the fracture energy is lower than that of the rubber-modified epoxy. It is of note that the two sets of data in Figure 2.14 are for the same epoxy polymer. Thus, it would seem that nanosilica particles provide a higher synergistic behaviour to  $G_C$  than the glass beads. For micron-sized glass particle containing hybrids, the effect of particle-matrix adhesion on  $G_C$  was reported as negligible [72]. However, it is unclear if this is the case for nano-sized rigid reinforcements with CTBN rubber.



(a) Kinloch et al. 15 wt. % CTBN with glass particles (30 °C of interest) [113]

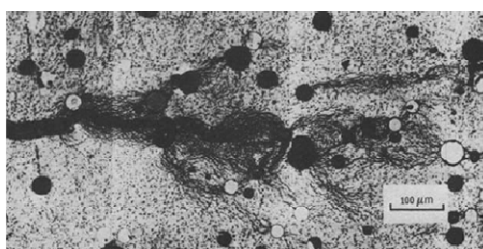


(b) Liang and Pearson, 18 wt. % CTBN with nanosilica (blue) [134]

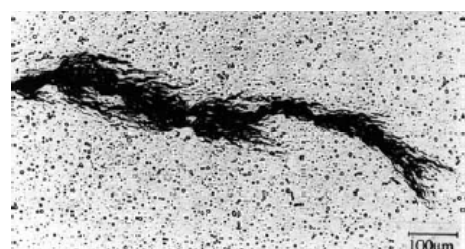
Figure 2.14. Fracture energy versus rigid particle content for hybrid-modification using CTBN and (a) micron-sized glass beads [113] or (b) nanosilica [134].

### 2.4.3 Toughening mechanisms

With glass bead reinforced hybrid polymers, mechanisms of pinning, deflection, and debonding with void growth are generally considered to toughen the epoxy polymer. The presence of the rubber particles, which cavitate at relatively low stress will have the effect of initiating yield at a lower stress, enhancing localised plastic deformation ahead of the crack-tip and increasing the efficiency of the toughening effects of the rigid filler particles [89, 115, 117, 119, 120, 132]. The improved fracture properties have also been described as interactions of overlapping stress fields, [72, 116] which again result in enhanced localised plastic deformation ahead of the crack-tip. Figure 2.15 shows two sub-critically loaded crack-tips [72, 89].



(a) Kinloch et al. 10 wt.% glass, 15 wt.% CTBN [72]

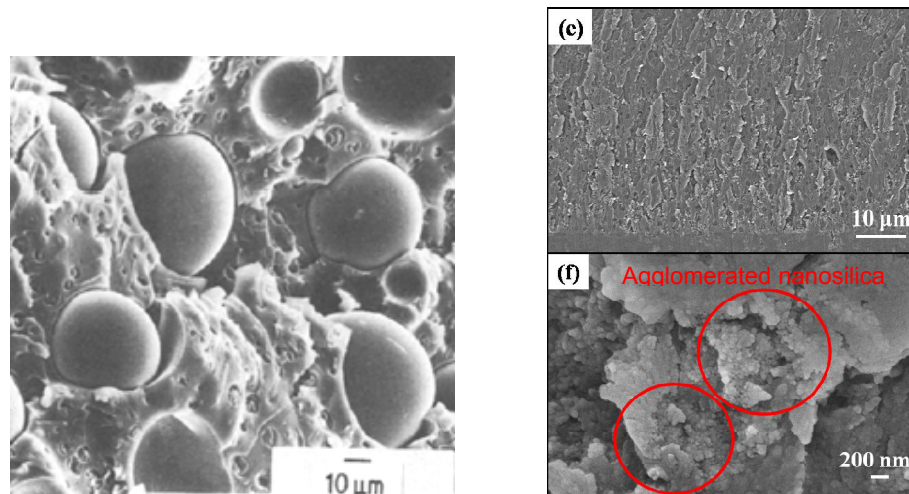


(b) Zhang and Berglund, 5 vol. % glass, 10 vol. % CTBN [89]

Figure 2.15. Sub-critically loaded crack-tips show shear banding between the rubber particles and shear band yielding (due to stress field interactions) from the glass particles [72, 89].

The images show the stress field interactions between the rubber and the glass particles. The enhanced plastic deformation can be compared to the rubber toughened epoxies that were shown previously. Figure 2.16 shows SEM images of fractures of the micron- and nano-sized silica particle hybrid-modified epoxies [60, 72]. It is clear that there is a large difference in the particle size, thus many more particles may exist in the

plastic zone of the nanosilica and rubber hybrid-modified epoxy and contribute to the toughening processes.



(a) 10 wt.% glass, 15 wt.% CTBN [72] (b) 4.5 wt.% nanosilica, 9 wt.% CTBN [60]

Figure 2.16. Fracture surface images for CTBN and (a) glass- or (b) nanosilica-containing hybrid-modified epoxies [60, 72].

## 2.5 Composite materials

Epoxies have limited use in structural applications because their mechanical properties are much lower than most metals. However, they have desirable properties, most notably their ability to be easily formed into complex shapes. Materials such as glass, aramid and carbon have extremely high tensile and compressive strengths. When stressed, random surface flaws will cause the material to fracture prematurely. However, if the material is produced in fibre form, although the same number of random flaws exist, only very few fibres will fail, giving the fibres collectively, a supreme stress carrying capability [138]. A bundle of fibres will require a matrix to prevent the fibres from buckling or distorting, for example a polymer. Greater specific stiffness and strength properties can be exhibited for such systems, shown in Figure 2.17, and the properties can be tailored for specific applications.

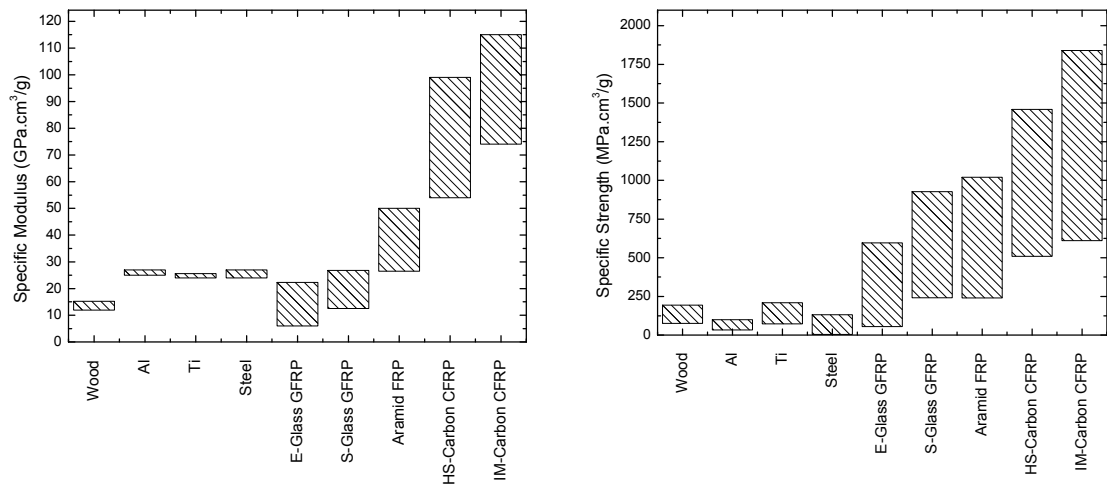


Figure 2.17. Specific stiffness and strength for various structural materials, recreated from [139].

Due to the stiffness mismatch that exists between the fibres and matrix (80 or 300 GPa compared to  $\sim 3$  GPa) the fibre-matrix interface can be a potential site for failure to occur. Therefore for the best structural properties, the matrix requires very good adhesion to the fibres and as close a stiffness to the fibre as possible [140]. Moreover, if fatigue related degradation of the interface is going to occur over time, then high fracture resistance is desirable.

A novel characteristic of using phase separable or nano-size fillers are that such particles are not filtered out during infusion processes [141-143]. These tougheners can be employed as modified matrices for continuous fibre composites using such processes. Interesting enhancements have been reported in the literature, for example, improved flame retardancy [144] and electrical conductivity [145].

### 2.5.1 Fracture behaviour

Scott and Philips [141] reported the addition of rubber to the matrix of a carbon-fibre reinforced composite. They noted improvements in toughness without compromising the modulus. However, they also suggested that the fibres may be suppressing the toughening effect of the rubber particles.

Vlasveld et al. [146] examined the effect of layered silicates on the fibre-matrix adhesion in glass-fibre reinforced nano-composites and found that their interface degraded with the addition of silicate. This was attributed this to the leaching of surfactants from their layered silicates to the interface. Improvements in the fibre-matrix interfacial behaviour have however, been noted in the literature, e.g. [147, 148].

Caccavale et al. [133] employed the same nanosilica particles as those from this study to create continuous carbon-fibre reinforced epoxies. They examined the effect of

matrix modification on the overall fracture properties using mode I double cantilever beam tests. By employing a control formulation, 3.7 wt. % nanosilica and a 3.7 wt. % nanosilica plus 7.3 wt. % CTBN hybrid, they reported a 123 % increase when compared to the neat epoxy, suggesting good transfer of toughness from the bulk properties. They reported a small decrease in the short beam shear strength for the hybrid-modified composite, but could not explain this observation.

Tsai et al. [135] examined the effect of coreshell or CTBN rubber with nanosilica particles to form hybrid matrices with glass-fibre reinforcement. The morphology of the cycloaliphatic amine cured DGEBA showed well-dispersed nanosilica with a micron sized rubber phase in the hybrid epoxies. This is interesting because more commonly, the nanosilica particles are reported to agglomerate upon curing with such formulations, e.g. [6]. A 50 % increase in  $G_C$  was reported for the nanosilica and CTBN hybrid whilst their coreshell only system was reported to provide a 100 % increase in the mode I fracture energy with no improvement in the nanosilica and coreshell hybrid.

Kinloch, Taylor and co-workers [4, 5, 143, 149-151] have previously shown that fibre-composites may be successfully manufactured using 20 nm diameter silica nanoparticles, and that these particles increase the toughness of the composite material. Moreover, the particles are not filtered out during the infusion process and fibre-composites may be manufactured using resin infusion techniques with good transfer of toughness to a composite material [6]. Manjunatha et al. [152-154] conducted a tensile fatigue study on the nanosilica- and hybrid-modified composite materials. It was reported that the addition of nanosilica could suppress micro-cracking and increase the fatigue threshold by 15 % for the nanosilica-modified epoxy or 25 % for the hybrid-modified epoxy.

## 2.5.2 Toughening mechanisms

Compston et al. [155] investigated brittle matrix and rubber-toughened glass-fibre reinforced composites. They reported that the matrix fracture energy was completely transferred to the composite initiation energy in the brittle-matrix composites, but in the toughened composites transfer was only partial due to the presence of fibres. They showed that the enhancing effect of fibre bridging was greater in the toughened composites. The enhancement was related to a larger deformation zone in the toughened matrices.

Bradley [156] reported that the resin toughness plays a dominant role in the interlaminar fracture of composite materials. By employing tougher matrices, the size of

the plastic zone ahead of the crack-tip could be enhanced. The low efficiency of translation of bulk fracture properties into composite fracture properties was the result of constraint provided by the fibres in the adjacent plies, hindering the development of a larger plastic zone. Due to the close packed nature of the fibres in the matrix, the inter-fibre distance may be relatively small. By nature of the fibres being significantly stiffer than the matrix, the fibres may constrain the plastic zone in an analogous manner to thin bond lines in adhesive joints and limit the amount of plastic deformation that occurs [157, 158].

Fibre related mechanisms such as pull-out, fracture and deflection are widely associated with the elevated fracture energies that are present in the composite materials. Employing tougher matrices simply enhances this effect due to the larger damage zone that can encompass more fibres [3]. Huang and Hull [159] reported that for fibre-bridging greater than 5 mm behind the crack front, deviations from linear elastic fracture mechanics occurs and this results in over-prediction of the mode I fracture energy with such bridging phenomena.

## **2.6 Chapter summary**

The present chapter has reviewed previous studies regarding the toughening of epoxies using rigid particles and CTBN rubber. The interactions of these particles with the epoxy govern the toughening effect that can be achieved.

For rigid particle toughening, the particle-matrix adhesion seems to play a vital role in determining the overall yield and fracture behaviour and this will be explored further. Interesting inferences have been made with regard to the very high stresses for particle debonding at such small particle sizes and this will be explored further.

Rubber toughening is well established as a method of toughening epoxies. However, little work has been reported for hybrid-modified epoxies with nanosilica particles and this will be explored further.

Exciting new applications are arising for nanosilica-modified matrices in fibre-composites. These will be manufactured and the degree of transfer of toughness explored. The next chapters will detail the materials that were used along with the manufacturing techniques that were employed to produce bulk and composite specimens.

## Materials and Manufacturing

### 3.1 Introduction

This chapter describes formulating the epoxy polymers that were used in this study. The manufacturing techniques that were employed to produce the unmodified and modified-matrix bulk polymers and fibre-composites are also explained. The epoxy polymers can be separated into five systems that were examined, viz (i) an amine cured tetra-glycidyl methylenedianiline (TGMDA) (see Chapter (Ch.) 5), (ii) a polyether-amine cured di-glycidyl ether of bisphenol A & F (DGEBA/F) (see Ch. 6), (iii) a polyether-amine cured di-glycidyl ether of bisphenol A (DGEBA) (see Ch. 7), (iv) an amine cured multifunctional epoxy (see Ch. 8), and lastly the anhydride cured DGEBA (see Ch. 9).

All of the epoxy polymers were produced in house. They have been developed from their constituent parts and are based on reported systems from literature e.g. [1-6]. These systems have a range of different glass transition temperatures and material properties. This will allow the effect of nanosilica modification on the overall toughenability of the epoxy polymers to be examined. Different types of epoxy formulations were prepared; unmodified epoxy, epoxy with nanosilica particles (termed 'xN'), epoxy with rubber micro-particles (termed 'yR') and a hybrid-modified epoxy containing both nanosilica and rubber micro-particles (termed 'xNyR'). The magnitudes of  $x$  and  $y$  refer to the amount of modifier by percentage weight of the total formulation weight, i.e.

$$\text{wt. \%} = \frac{\text{Wt}_{\text{modifier}}}{\text{Wt}_{\text{modifier}} + \text{Wt}_{\text{epoxy}} + \text{Wt}_{\text{hardener}}} \times 100 \quad (3.1)$$

The volume fraction was calculated from the weight percentages of the system's constituents and the measured density of the bulk epoxy. The density of nanosilica was taken to be the same as bulk silica, 1,800 kg/m<sup>3</sup> [160] and the density of CTBN was known to be 948 kg/m<sup>3</sup> [161].

## 3.2 Silica nanoparticles

The approximately spherical amorphous silica particles are formed via a sol-gel technique and are treated with an epoxy-silane treatment to aid dispersion of the particles, as shown schematically in Figure 3.1 [162]. Without this treatment, agglomeration and flocculation would occur in the epoxy.

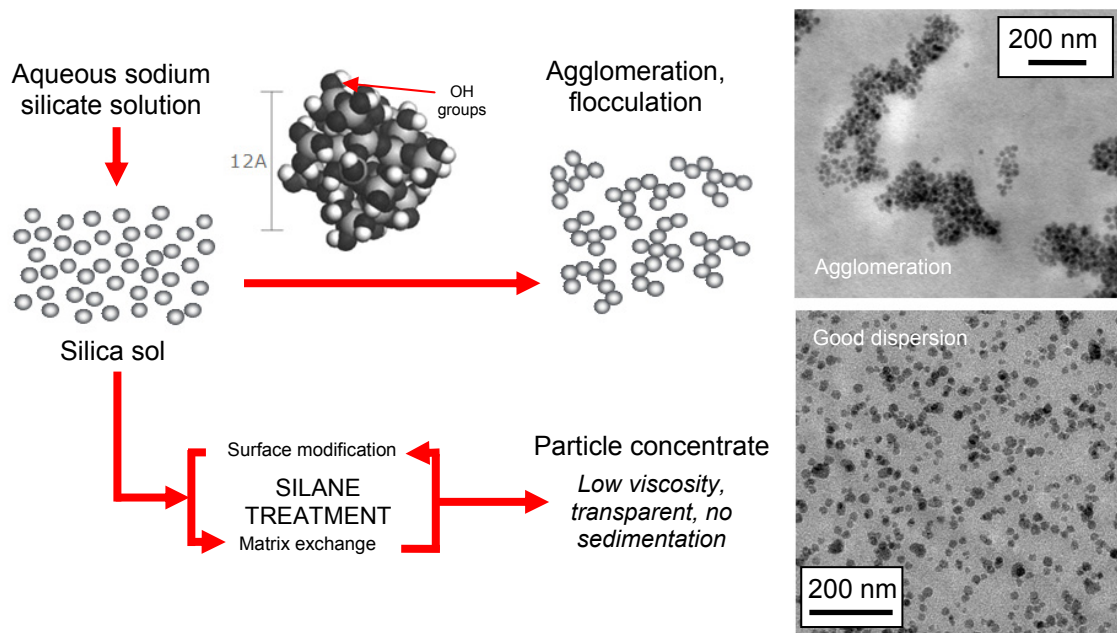


Figure 3.1. Representation of the silane treatment process to produce dispersed nanosilica particles in the epoxy [162].

Nanoresins reported small angle neutron scattering (SANS) data [162] to show the particle number density versus particle size (see Figure 3.2). There is some variation in the particle size; in the range 5-35 nm with a peak number density at 15 nm and mean particle size of about 20 nm. This SANS data was compared to experimentally measured particle distributions from atomic force microscopy (AFM) and transmission electron microscopy (TEM) images and was found to be a reasonable approximation to the actual particle size distribution that exists in the nanosilica-modified epoxies from this work, although the actual dispersion is perhaps a little broader.

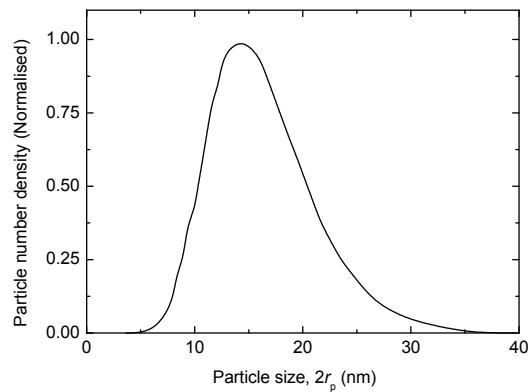


Figure 3.2. The particle number density versus the particle size for the nanosilica particles used in this study [162].

### 3.3 Rubber particles

The carboxyl-terminated butadiene-acrylonitrile (CTBN) phase used in this work was 'Hycar 1300 x 8' from Emerald Performance Materials, Cleveland, USA. It is initially dissolved and pre-reacted in the epoxy resin as an adduct. The CTBN phase-separates via a nucleation and growth process during curing to form the particulate phase of spherical CTBN rubber particles.

Extensive studies [163-166] have shown that as the epoxy cures, the molecular weight in the resin locally increases. This changes the free energy of mixing which leads to a decrease in the solubility parameter of the CTBN, the decrease of this solubility parameter drives the rubber to phase separate [167]. Spinodal decomposition mechanisms have been reported in epoxies but tend to be limited to fast reacting systems [168, 169].

In order to confirm that nucleation based phase separation had occurred in the anhydride cured DGEBA system, hot stage tests were conducted on a rubber-modified (9R) epoxy. The selected images shown in Figure 3.3(a-h) were taken periodically during curing using an optical microscope. Nucleation was found to initiate very late in the cure; at 50 mins into the cure cycle. Comparing the images in Figure 3.3(g) and (h), the maximum amount of phase separation occurs at vitrification i.e. after 70 mins and at 160 °C.

A summary of the chemicals that were used to prepare the different epoxies is shown in Table 3.1. The table provides details of the commercial name, supplier and epoxide equivalent weight (EEW) or anhydride equivalent weight (AEW). Sections 3.4 through to 3.8 specify the individual systems that were studied in this work and provide detail regarding to formulating and manufacturing each epoxy polymer.

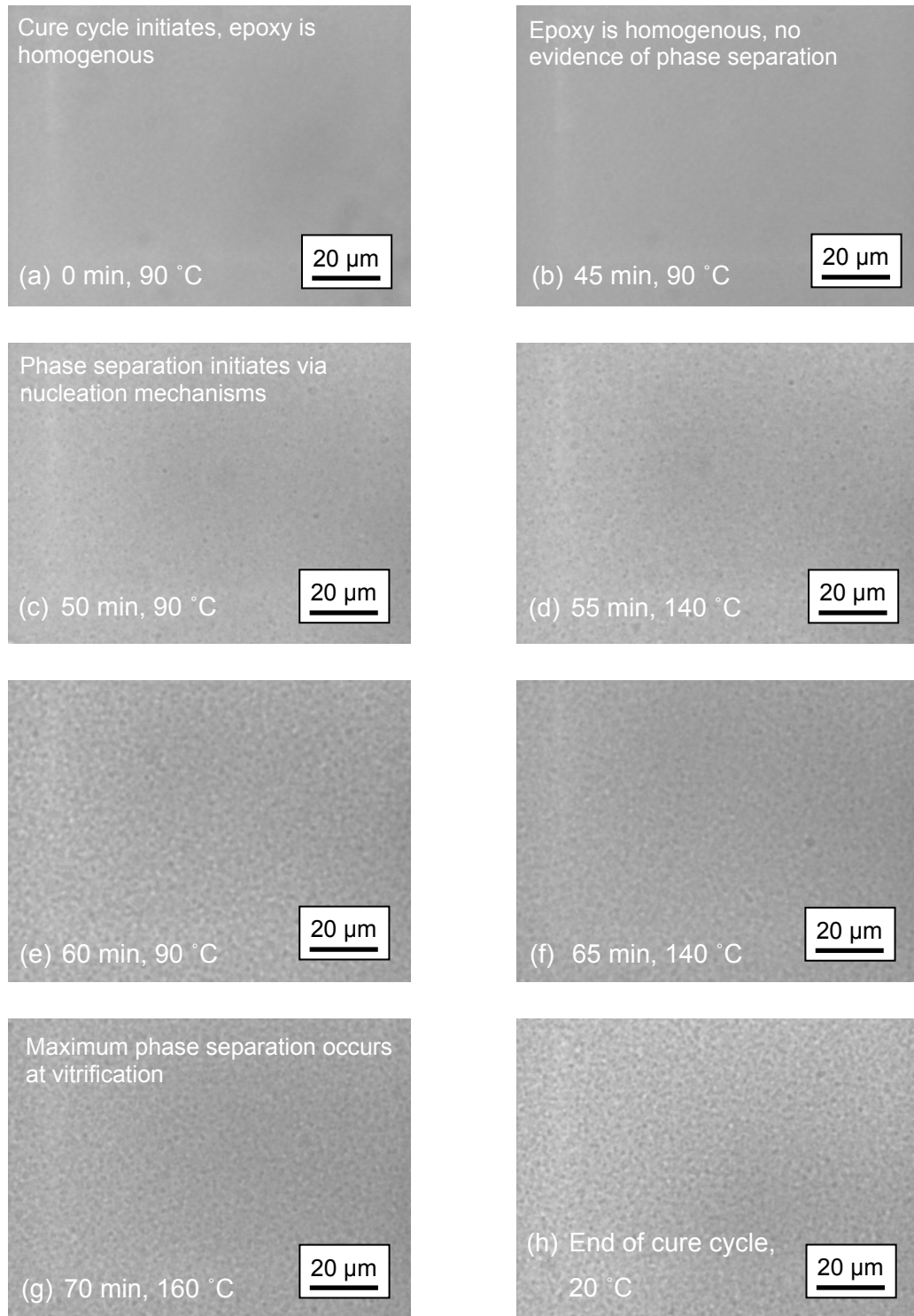


Figure 3.3. Optical micrographs of a sample from the 9R anhydride cured DGEBA epoxy during curing. Selected images (a-h) show how the morphology of the rubber-modified epoxy varies with respect to temperature and time.

Table 3.1. The constituent resins and curing agents that were used in this study.

System	Chemical	Commercial name	Supplier	EEW <sup>1</sup> (g/eq.)
Amine cured TGMDA (Ch. 5)	Tetra-glycidyl methylenedianiline (TGMDA) epoxy	Epikote 496	Hexion, Germany	115
	Epikote 496 TGMDA + 40 wt. % nanosilica	Epikote 486	Nanoresins, Germany	180
	Epikote 496 TGMDA + 40 wt. % CTBN	Albipox XP 23/0206	Nanoresins, Germany. CTBN from Emerald Performance Materials, USA	131
	4, 4'-methylenebis (2, 6-diisopropylaniline)	Lonzacure M-DIPA and M-DEA	Lonza, Switzerland	158 and 186
Polyether-amine cured DGEBA/F (Ch. 6)	Pre-blended di-glycidyl ether of bisphenol A (DGEBA) and di-glycidyl ether of bisphenol F (DGEBF)	Araldite AY 105	Huntsman, UK	173
	Bakelite EPR 164' DGEBA + 40 wt. % nanosilica	Nanopox F 400	Nanoresins, Germany	295
	Polyether-amine (otherwise known as polyoxypropylenediamine)	Jeffamine D 230	Huntsman, UK	60

*Continues onto next page*

Polyether-amine cured DGEBA (Ch. 7)	DGEBA	Araldite LY 556	Huntsman, UK	186
	DGEBA + 40 wt. % nanosilica	Nanopox F 400	Nanoresins, Germany	295
	Polyether-amine (otherwise known as polyoxypropylenediamine)	Jeffamine D 230	Huntsman, UK	60
Amine cured multifunctional Epoxy (Ch. 8)	Triglycidyl amino phenol (TGAP)	Araldite MY 0510	Huntsman, UK	97
	Diglycidyl ether of bisphenol F (DGEBF)	Araldite PY 306	Huntsman, UK	160
	50 wt. % nanosilica in 'PY 306' DGEBF	PY 306 + Nanosilica	Nanoresins, Germany	320
	4,4'-methylenebis-(3-chloro 2,6-diethylaniline)	Lonzacure M-CDEA	Lonza, Switzerland	
Anhydride cured DGEBA (Ch. 9)	DGEBA	Araldite LY 556	Huntsman, UK	186
	Bakelite EPR 164' DGEBA + 40 wt. % nanosilica	Nanopox F 400	Lonza, Switzerland	295
	Bakelite EPR 164' DGEBA + 40 wt. % CTBN	Albipox 1000	Nanoresins, Germany. CTBN from Emerald Performance Materials., USA	330
	Accelerated methylhexahydrophthalic acid anhydride	Albidur HE 600	Nanoresins, Germany	AEW <sup>2</sup> 95

<sup>1</sup>EEW - Epoxide equivalent weight, <sup>2</sup>AEW - Anhydride equivalent weight

### 3.4 Amine cured TGMDA (Ch. 5)

The nanosilica particles were obtained pre-dispersed in 'Epikote 486' epoxy and the CTBN rubber was adducted as 'Albipox XP 23/0206' TGMDA. The curing agent was a blend of 'Lonzacure M-DEA' and 'Lonzacure M-DIPA', obtained as powders and mixed to a 79/21 ratio by weight [170] and then mixed to a stoichiometric quantity with the resin. This system is similar RTM-6, a single-component epoxy system [171] and would be expected to exhibit comparable physical and chemical properties.

The hardener constituents were dissolved into the resin (already degassed to -1 atm and at 90 °C) for one hour by mechanically stirring at 200 rpm (90 °C). The resin mixture was degassed a second time and then poured into release-agent coated, (using 'Frekote 700-NC', Loctite, UK) pre-heated steel moulds and cured. The resins were cured at 160 °C for 75 mins and then post-cured at 180 °C for 2 hours (using a 10 °C/min ramp rate).

### 3.5 Polyether-amine cured DGEBA/F (Ch. 6)

This epoxy polymer comprises 'Araldite AY 105' (termed DGEBA/F) cured with 'Jeffamine D 230' polyether-amine. Table 3.1 shows that nanosilica-modification was achieved by adding 'Nanopox F 400'. This was cured to a mixing ratio of 1:0.3 epoxy to polyether-amine by weight to achieve a sub-stoichiometric composition [172].

The resin constituents and hardener were blended using a mechanical stirrer at room temperature, then degassed at 50 °C and -1 atm. These parts were then mixed for 15 mins using a mechanical stirrer (200 rpm at 50 °C) and degassed a second time. The resin mixture then was poured into release-agent coated, pre-heated steel moulds and cured for 3 hours at 75 °C followed by a post cure of 12 hours at 110 °C (ramp rate of 10°C/min) and allowed to cool to room temperature before removing the sample from the oven.

### 3.6 Polyether-amine cured DGEBA (Ch. 7)

The second polyether-amine epoxy was formulated with DGEBA, 'Araldite LY 556'. Nanosilica-modification was achieved by adding 'Nanopox F 400' and this epoxy was cured with 'Jeffamine D 230' at stoichiometric quantities. This system was cured using the same procedure as the polyether-amine cured DGEBA/F epoxy that was discussed in Section 3.5.

### 3.7 Amine cured multifunctional epoxy (Ch. 8)

A blend of epoxies was used at a ratio of 1:1.17 'Araldite MY 0510' to 'Araldite PY 306' by weight (termed multifunctional epoxy). The nanosilica-modification was achieved adding 'Araldite PY306 + Nanosilica'. This blend was cured with the amine 'Lonzacure M-CDEA' at a ratio of 1:0.65 multifunctional epoxy to M-CDEA by weight i.e. sub-stoichiometry.

The M-CDEA hardener was obtained as a powder and was dissolved into the degassed (-1 atm) resin mixture (at 120 °C) for one hour whilst mechanically stirring (200 rpm at 120 °C) and degassed again. The resin mixture was poured into release-agent coated; pre-heated steel moulds and cured for 5 hours at 180 °C.

### 3.8 Anhydride cured DGEBA (Ch. 9)

The base epoxy resin was a standard DGEBA, 'Araldite LY 556'. This was mixed with 'Nanopox F 400' and/or 'Albipox 1000' to produce the required amounts of nanosilica and CTBN in each formulation. A stoichiometric quantity of the curing agent was added to the epoxy resin. For this system, an accelerated methylhexahydrophthalic acid anhydride curing agent, 'Albidur HE 600' was used.

To produce bulk plates, the individual components were separately degassed at 50 °C and -1 atm, and then mixed for 15 mins (200 rpm at room temperature) using a mechanical stirrer and degassed a second time. The resin mixture was then poured into release-agent coated pre-heated steel moulds and cured. The specimen plates were cured at 90 °C for 1 hour then post-cured at 160 °C for 2 hours (ramp at 10 °C/min).

## 3.9 Manufacturing

The following section outlines the procedure that was followed to manufacture bulk and composite specimens.

### 3.9.1 Bulk epoxies

Bulk polymer samples were cured in gravity moulds to obtain void free epoxy plates of uniform thickness with minimal wastage of material. For this study, two mould geometries were used, (i) a 3 mm thick mould and (ii) a 5 mm thick gravity mould. The 3 mm mould was formed in picture frame arrangement and was clamped shut to utilise

the mould as a gravity mould. The 5 mm gravity mould was clamped shut with a 3 mm diameter silicone gasket to prevent any leakage.

Firstly, the moulds were cleaned with acetone and coated with release agent, 'Frekote 700-NC' from Loctite, UK and left in a fume hood for 30 mins to dry. The moulds were then assembled and placed in pre-heated ovens at their respective processing temperature, dependent on the system being prepared. Once the moulds were at temperature, and the resin prepared, the degassed resin was poured in carefully. By pouring on one side, with a continuous flow rate, aeration of the resin was minimised as the mould was filled. The resin in the mould was degassed a second time if required before curing.

For the hybrid-modified formulations, over-sized beakers (~3 x volume of the resin) were used to degas the resins due to their relatively high viscosities with respect to the unmodified epoxy. Secondly, vacuum assisted infusion techniques were utilised, to reduce the mould filling time for the high viscosity formulations.

The moulds would cool a little whilst they were out of the oven as the resin was being introduced. Therefore, a ten min delay was applied when the mould was placed to the oven to allow the mould and resin to regain the processing temperature before the cure cycle was commenced. The oven was then ramped to the cure temperature at 10 °C/min to allow the epoxy and mould to heat steadily. Thermocouple data was recorded for the anhydride cure and satisfied that the oven temperature compared well to the pre-programmed cured regime, see Figure 3.4. Initially, a 10 min hold was applied to all the plates to recoup the loss of mould and resin temperature during filling. The epoxy and mould were heated steadily to reach isothermal conditions with the oven before the cure program was commenced. As expected, a small overshoot in the temperature was observed of the epoxy because curing is an exothermic process.

The plates were allowed to cool to room temperature before being removed from the oven and de-moulded. Visual inspection was conducted to ensure that the plates were free of porosity.

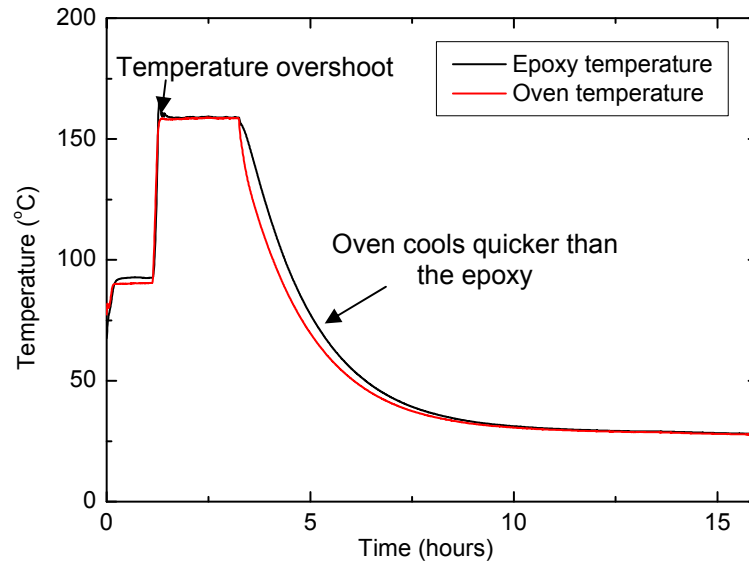


Figure 3.4. Variation of epoxy and oven temperatures during the anhydride cured DGEBA epoxy cure cycle.

### 3.9.2 Single-fibre composites

The gel time for the epoxy was required to produce single-fibre pull-out specimens. Therefore, single fibre pull out tests were conducted for the anhydride system only. The unmodified and modified-epoxies were partially cured, 45 mins into the cure cycle, in the socket-head of a M3 steel bolt. The single glass-fibres were dried in a desiccator and then mounted to 3 mm washers with self-adhesive tape. The free end was cut with a sharp razor blade, perpendicular to the axial direction. As shown schematically in Figure 3.5, the washer was then mounted on the single-fibre specimen preparation jig and the partially gelled resin-containing bolt was placed carefully into a small furnace and heated to continue the cure cycle. The fibre was then brought into contact with the surface of the resin using an optical microscope. This resulted in a large meniscus of resin to draw up the fibre, i.e. the embedded lengths were larger than 100  $\mu\text{m}$ , and so the fibre was removed slightly to provide embedded lengths in the range 10 to 100  $\mu\text{m}$ . Once gelation had occurred, the sample was removed from the jig and placed in a programmed oven to finish the cure cycle as per the bulk epoxy.

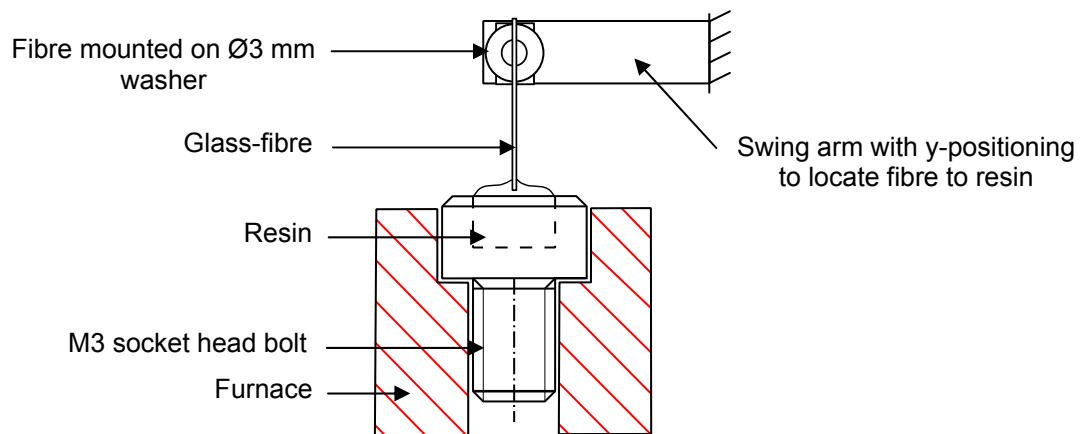


Figure 3.5. Schematic shows the preparation technique for single-fibre pull-out specimens.

### 3.9.3 Continuous-fibre composites

Resin infusion under flexible tooling (RIFT) was used to prepare continuous fibre-reinforced epoxy composites. RIFT is a process by which the dry fibre is laid up as desired and placed in a vacuum using a flexible polymeric film, shown schematically in Figure 3.6. The resin is drawn through the fibres using the vacuum to achieve a neat composite that is free of voids [173]. This method was favoured because it is a clean alternative to wet lay-up techniques and did not incur the large tooling costs associated with techniques such as vacuum assisted resin transfer moulding (VARTM) where matching moulds are required. Higher fibre volumes fractions can also be achieved using RIFT compared to VARTM [174], making it an ideal low volume composite preparation method. However, there is an inherent crimp in the fabrics because the individual tows are intermingled as the vacuum is applied to the dry pre-form. This results in a reduction in the in-plane properties of the resulting composite laminate [175].

Carbon-fibre reinforced polymer (CFRP) composites were manufactured for the amine cured TGMDA epoxy. Quasi-isotropic plates (QI), 4 mm thick, were prepared using 8 plies of a biaxial stitched non-crimp fabric, 'XC 305/1270' supplied by SP Systems, UK. The carbon-fibre fabric was cut into 330 mm by 330 mm squares and laid up into a balanced symmetric sequence i.e.  $[\pm 45, 0/90, \mp 45, 90/0]_s$  to give a '0/0' interface across the fracture plane. A 12.5  $\mu\text{m}$  thick poly(tetrafluoroethylene) (PTFE) film was inserted in the mid-plane to initiate the starter crack. The individual fabric plies were found to be handed although they are sold as non-handed. One side of the fabric was single stitched (A side) and the other being double stitched (B side). In order to prevent warping in the finished composite panels, the plies were organised such that the double stitch faces were mated, i.e.  $[AB, BA, AB, BA]_s$ . The fabric was cut into two and

one half was infused. The resulting half-sized laminate was large enough to produce 12 fracture specimens.

For the anhydride cured DGEBA system, uni-directional (UD) and quasi-isotropic (QI) glass-fibre reinforced polymer (GFRP) composite panels were manufactured. Uni-directional GFRP composites were produced using 'UT-E500' from SP Systems, UK, to produce 12-ply, 7 mm thick composites with a PTFE insert placed in the mid-plane to initiate a starter crack. Quasi-isotropic plates, 4 mm thick, were prepared using 8 plies of a biaxial stitched non-crimp fabric, 'XE 450/1200' supplied by SP Systems, UK. The E-glass fabric was cut into 330 mm by 330 mm squares and laid up into a balanced symmetric sequence i.e.  $[+/-45, 0/90, -/+45, 90/0]_s$  to give a '0/0' interface across the fracture plane. As, the individual plies were handed, the plies were arranged such that the double-stitch faces were mated, i.e.  $[AB, BA, AB, BA]_s$ . To increase the stiffness of the quasi-isotropic plates, they were backed with 2 plies of uni-directional carbon-fibre, 'RUCT500/150', SP Systems, UK in the axial direction on the outer-most faces such the modified lay-up was  $[0]_2^{Carbon-fibre} [+/-45, 0/90, -/+45, 90/0]_s^{Glass-fibre}$ . The fabric was sectioned into two, with the resulting laminate being large enough to produce 12 fracture specimens. A natural pre-crack was initiated via a PTFE insert film in the mid-plane.

To produce the laminates, a controller-monitored hot plate and oven was set to the required infusion temperature. The work station was cleaned and an infusion stack was built up, as shown in Figure 3.6(a). All the consumables for RIFT were obtained from Aerovac, UK. The infusion stack commences with a sheet of polyimide film to provide a clean base to work from which and was held in place using adhesive PTFE tape. The infusion area was masked off with 'vacuum bag sealant tape' and the inlet and outlet pipes were positioned. Layers of 'flow media', 'peel ply', the dry fibre-perform, 'peel ply', 'flow media' and a final sheet of 'peel ply' were all encased in a 'vacuum bag' and sealed using the 'vacuum bag sealant tape' to produce the closed mould. Careful placement of the peel plies and flow media were determined to optimise the RIFT process, as shown in Figure 3.6. The flow media was cut short; 20 mm from the end of the dry perform. This allowed careful control of the resin flow front and ensured that fully consolidated laminates were manufactured. This is shown schematically in Figure 3.6(b) with a through thickness projection with time.

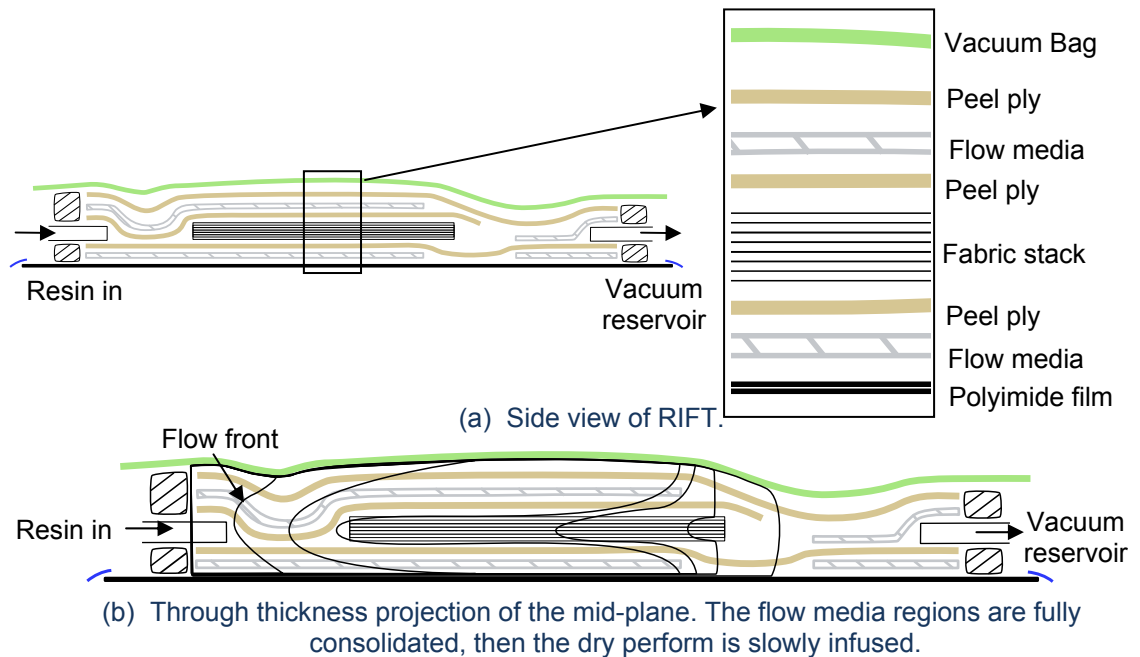


Figure 3.6. Shows (a) a side view of fibre stack for RIFT to produce continuous fibre-reinforced polymer composites and (b) how the resin flow front progresses with time.

A stable vacuum was applied to the mould using a vacuum pump connected through a reservoir chamber that was filled with desiccator to remove any moisture from the closed mould for one hour. The desired matrix was then prepared and infused until the flow front had reached 10 mm beyond the flow media. By arranging the flow media as mentioned, the flow front was found to flow very quickly through the porous flow media. With time, the resin slowly progressed through the dry perform, even after the inlet was closed, and this resulted in high fibre volume fraction composites.

Thereafter, the inlet was closed, the infused composite fabric was covered with a large steel pressure plates and the hot plate was encased with a thermally insulating material to (i) minimize the thermal gradient through the thickness of the laminate and (ii) to prevent heat loss to the atmosphere. The same cure regime as the bulk epoxy was applied to the composite panels via the hot plate and this was verified using a thermocouple.

The finished composite laminates were inspected using ultrasonic C-Scan and visual inspection to ensure that the plates were defect-free. For the glass-fibre composites, visual inspection of the finished laminate was found to be as sufficient for picking up defects or voids.

## Experimental Methods

### 4.1 Introduction

This chapter describes the procedures that were followed to obtain the various micro-structural images and material properties for this study.

### 4.2 Determination of density

Density measurements for the different epoxies were obtained as per International standards organisation (ISO) 1183 [176] using, 'method A', the immersion technique. The mass of the bulk epoxy polymer was measured using an analytical balance and the volume was obtained by immersing the epoxy samples in de-ionised water. A total of six repeat measurements were conducted using about 200 g of cured epoxy for each specimen and the density was calculated.

The density of nanosilica was taken to be the same as bulk silica, 1,800 kg/m<sup>3</sup> [160] and the density of CTBN was known to be 948 kg/m<sup>3</sup> [161].

### 4.3 Determination of glass transition temperature

Differential scanning calorimetry (DSC) was performed using a 'TA Instruments Q2000' to ensure that the epoxies were fully cured, and secondly, to obtain the glass transition temperature,  $T_g$ . Standard procedures exist for the determination of  $T_g$ , e.g. [177, 178]. The specific energy required to change the temperature of the 10 mg sample per degree was monitored using a 10 °C/min rate for heating and cooling. Each sample was heated through a range from room temperature to about 60 °C above the expected value of  $T_g$  twice and two values were obtained for each test (Figure 4.1). A point of inflexion was observed in the heat flow versus temperature plot as the sample epoxy passed through the  $T_g$  region. The value of  $T_g$  was taken as the mid-point of the inflexion curve and two repeat tests were conducted for each formulation.

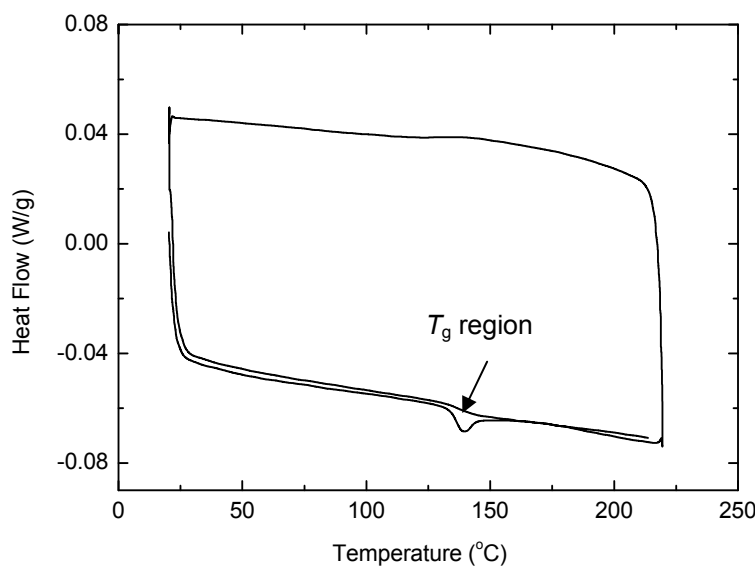


Figure 4.1. Heat flow versus temperature for the unmodified anhydride cured DGEBA epoxy shows the glass transition temperature,  $T_g$ , region.

#### 4.4 Determination of viscosity

Rheological tests were conducted to measure how the viscosity of epoxy varied as it cross-linked. Tests were conducted on degassed and pre-mixed samples of the anhydride cured di-glycidyl ether of bisphenol A (DGEBA) using a 'TA AR 2000ex' rheometer. The machine was set up with Ø25 mm disposable aluminium parallel-plates at a gap distance of 100  $\mu\text{m}$  and a constant rotational frequency of 0.01 Hz. Corrections for geometry inertia, compliance in the system and gap temperature compensation were applied to the data for viscosity versus temperature as the cure cycle progressed. Between two and four tests were performed for each formulation.

#### 4.5 Atomic force microscopy

A smooth surface was first prepared by cutting an approximately 1  $\text{mm}^2$  area using a 'RMC PowerTome XL cryo-ultramicrotome' at room temperature for the unmodified and nanosilica-modified epoxies, and at -80  $^{\circ}\text{C}$  for the rubber- and hybrid-modified epoxies. Atomic force microscopy (AFM) studies were undertaken using a 'Veeco MultiMode scanning probe microscope' equipped with a 'NanoScope IV controlled J-scanner' and 'RTESP10' silicon tips. The AFM scans were performed in the tapping mode using a silicon probe with a 5 nm tip. The phase and height images were recorded at 512  $\times$  512 pixel resolution at a 1 Hz scan speed.

At very high magnifications, the nanosilica particles appeared to be non-spherical. This was adjudged as a function of the AFM scan process because such particle shapes were not observed with transmission electron microscopy.

## 4.6 Transmission electron microscopy

Transmission electron microscopy (TEM) was also performed. The cryo-ultramicrotomy technique described previously was used to prepare slices of 80-90 nm in thickness for the TEM studies. These slices were placed on 'Agar 300 mesh' lacy-carbon filmed copper grids, and viewed using a 'JEOL JEM-2000FX II' transmission electron microscope at a 200kV accelerating voltage.

## 4.7 Scanning electron microscopy

The fracture surfaces of the bulk epoxy polymers and the fibre composites were studied using scanning electron microscopy (SEM). Specimens approximately 1-2 mm thick were extracted from the fracture surfaces by razor-tapping to provide very thin samples, making them less likely to charge upon imaging.

The surfaces were sputter-coated with a layer of (i) gold using an 'Edwards Scancoat six' coater at 40 mA for 9 sec with a target height of 50 mm or (ii) with an 'Emitech K575X Peltier cooled sputter coater' equipped with a chromium target at 60 mA for 1 min, to reduce charging of the samples. A line of electrical conductivity was obtained from the surface to the sample stub using conductive silver paint.

An 'Hitachi S-3400N' SEM was used, with typical accelerating voltages of 15 kV for low magnification imaging (up to 10 kX). High-resolution scanning electron-microscopy was performed using a scanning electron microscope equipped with a field-emission gun (FEGSEM); a 'Carl Zeiss Leo 1525' with a Gemini column was used, with a typical accelerating voltage of 5 kV.

Due the very high magnification that was used during FEGSEM imaging, the image quality was very sensitive to coating effects. Often many attempts were required to successfully coat the samples to an optimal quality in order to obtain FEGSEM images of the fracture surfaces. Too little coating was found to result in charging of the specimens, creating difficulties with beam focus and aperture or stigmation correction. With too much coating, the finer details of the fracture surface were masked.

## 4.8 Optical microscopy

The samples were prepared by polishing with a ‘Struers labopol-21’ using progressively finer grades of emery paper at intervals of 240, 800, 1200, 2400 and 4000 grit. The last stage of grinding was equivalent to 3  $\mu\text{m}$  polishing. For the samples that would be examined at high magnification, polishing was performed with 1  $\mu\text{m}$  and 0.25  $\mu\text{m}$  diamond polishing solutions on polishing ‘Multicloth’ (from Metprep, UK). The samples were mounted to standard glass slides using an optically transparent epoxy; ‘Araldite 2020’ (from Huntsman, UK) and were polished to a nominal thickness of 100  $\mu\text{m}$ .

A ‘Carl Zeiss AXIO Scope’ optical microscope was used to obtain the through transmission dark field cross-polarised and bright field reflected light microscopy images. Moreover, the microscope was coupled with a ‘Linkam THMS 600’ hot stage to observe phase separation of the carboxyl-terminated butadiene-acrylonitrile (CTBN) rubber particles during the curing process.

## 4.9 Image analysis

Images that were processed for volume fraction, particle size and distribution measurements were examined with GNU image manipulation program (GIMP) v2.6 [179] and ImageJ v1.43r [180] open source scripts. Moreover, panoramas were stitched and blended using Hugin’s GUI platform v2009.4.0 [181].

### 4.9.1 Determination of volume fraction from AFM images

The AFM phase images tended to be sharper than the height images. However, sub-surface particles of nanosilica were found to appear in the scan. The AFM phase images was analysed and the height image was used to decide which particles to include in volume fraction analysis.

The inter-particle distances,  $D_{\text{IP}}$ , for the disperse nanosilica and (particulate) rubber phases were calculated as

$$D_{\text{IP}} = \left( \left( \frac{4\pi}{3v_f} \right)^{1/3} - 2 \right) r_p \quad (4.1)$$

where  $v_f$  is the volume fraction and  $r_p$  is the particle radius [94] and assumes that the particles are perfectly dispersed with no size variation.

### 4.9.2 Determination of percentage of void growth

For the nanosilica-modified anhydride cured DGEBA epoxy, FEGSEM images from the fracture surfaces were used to study debonding and subsequent plastic void growth of the polymer.

FEGSEM images of the fracture surfaces were obtained for different weight percentages of nanosilica. To ensure that all of the nanosilica particles were included in the analysis, the images were overlaid with a grid of cells, see Figure 4.2(b). Each cell was analysed manually for debonding and plastic void growth using GIMP and ImageJ. The area fraction of all the particles was measured and compared to the volume fraction of the particles, ensuring all the particles on the fracture surface were considered in the analysis (Figure 4.2(c)). With stereology applied, the area fraction and volume fraction should be equal. Thereafter, the percentages of particles that debond with subsequent void growth were obtained by zooming into the image (i.e. Figure 4.2(d)), and the diameter of some of these voids was measured.

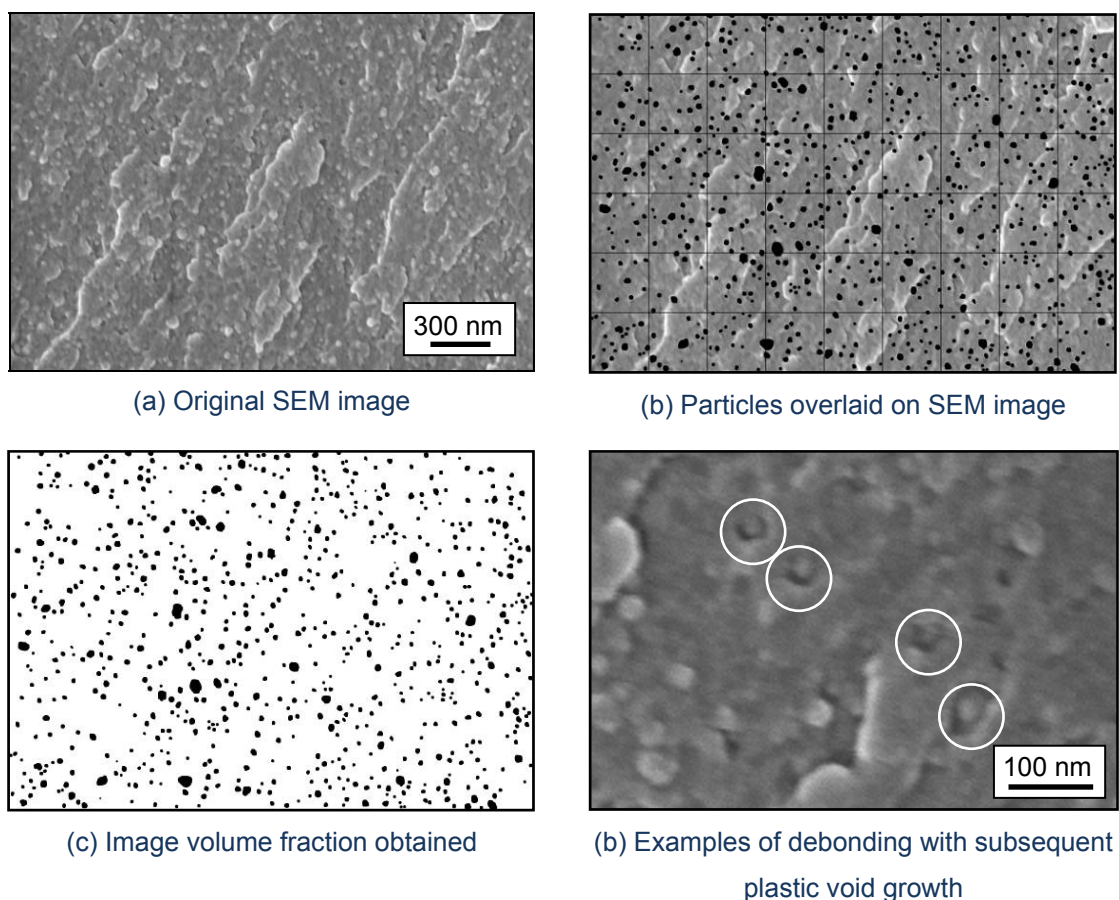


Figure 4.2. Sample SEM images (a-d) during the procedure to measure the percentage of particles that debond with subsequent void growth with some shown circled in (d). The original image is from [182].

This was conducted for several images at the different nanosilica contents. Within the experimental error, no differences were recorded in the percentage of particles that debond with respect to nanosilica content. This was calculated as  $15 \pm 5 \%$  of the nanosilica particles on the fracture surface with void diameters of the range 30-35 nm.

## 4.10 Tensile properties

Tensile tests were carried out on machined tensile dumbbell specimens of a type 1BA geometry (see Figure 4.3) in accordance to ISO 527 [183, 184]. The Young's modulus,  $E_t$ , and true yield strength,  $\sigma_{yt}$ , and true yield strain,  $\epsilon_{yt}$ , were determined for the epoxies.

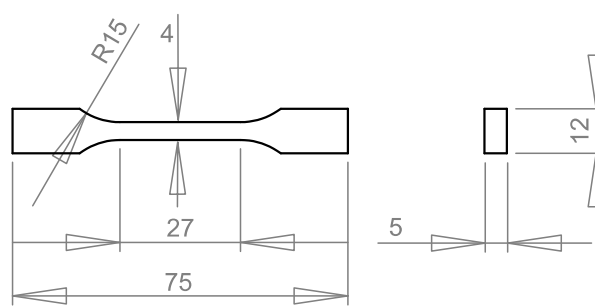


Figure 4.3. The type 1BA geometry that was used for tensile tests [183, 184].

An extensometer was attached to the specimens using knife edges to obtain accurate strains in the sample during the test making compliance correction unnecessary. Tests were carried out at a 1 mm/min displacement rate using an Instron universal testing machine. The Young's modulus was calculated using the linear portion of the stress-strain curves. This was conducted nominally in the range 0-0.01 true strain range. The tensile true stress,  $\sigma_t$  was calculated as

$$\sigma_t = \sigma_E (1 + \epsilon_E) \quad (4.2)$$

and tensile true strain,  $\epsilon_t$ , was defined as

$$\epsilon_t = \ln(\epsilon_E + 1) \quad (4.3)$$

where the subscript 'E' denotes engineering values and 'y' was used to denote the yield value for the respective material parameter. The maximum yield stress,  $\sigma_{yt}$ , was determined as the first point on the true stress-true strain curve with zero gradient. The mean values with their standard deviation are reported for a sample of six specimens.

## 4.11 Compressive properties

Plane-strain compression tests were conducted as described by Williams and Ford [185]. Figure 4.4 shows that tests were conducted using 3 × 60 × 40 mm specimens loaded in compression along the 60 mm length, between two parallel, 12 mm wide platens.

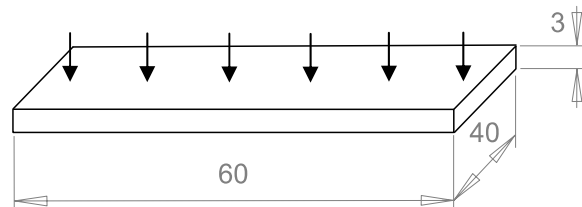


Figure 4.4. Geometry for the plane strain compression specimens, compressed along the long length of the specimen with 12 mm platens.

A set square was used to ensure the indenter was perpendicular to the specimen edge. Tests were conducted at a constant displacement rate of 0.1 mm/min to approximately match the strain rate from tensile tests. The values of Young's modulus,  $E_c$ , true yield stress,  $\sigma_{yc}$ , true yield strain,  $\epsilon_{yc}$ , and fracture strain,  $\gamma_f$ , were obtained as per the tensile tests. The results were corrected for the compliance of the machine and test rig which was verified before and after testing. The test method is highly sensitive to frictional effects; therefore the platens and specimen surfaces were ground to 4000 grit. In addition, 'Dow Corning lubricant BRZ plus multi-grease EP grease' was used to lubricate the contact surfaces. The true compressive stress,  $\sigma_c$ , was calculated as

$$\sigma_c = \left( \frac{\sqrt{3}}{2} \right) \sigma_E \quad (4.4)$$

and the true compressive strain,  $\epsilon_c$ , was calculated as

$$\epsilon_c = \left( \frac{2}{\sqrt{3}} \right) \ln \left( \frac{B_c}{B} \right) \quad (4.5)$$

where  $B_c$  is the compressed thickness and  $B$  is the initial thickness, to give modified von Mises values [186] for the compressive true stress and compressive true strain respectively [185]. The Young's modulus was taken from the linear portion of the true stress-true strain in the nominal range 0-0.02 true strain. The maximum yield stress,  $\sigma_{yc}$ , was determined as the first point on the true stress-true strain curve with zero gradient. A minimum of three specimens were tested for each formulation and their mean values are reported with the standard deviation. The specimen width was

reduced to obtain fracture strains to avoid reaching the maximum load for the universal testing machine (150 kN) prior to fracture.

## 4.12 Bulk fracture properties

Single-edge notch-bend (SENB) tests were conducted on the epoxies to obtain values for the initiation fracture energy,  $G_C$ , and fracture toughness,  $K_C$ . Tests were conducted as per ISO 13586 [187] in three-point bending.

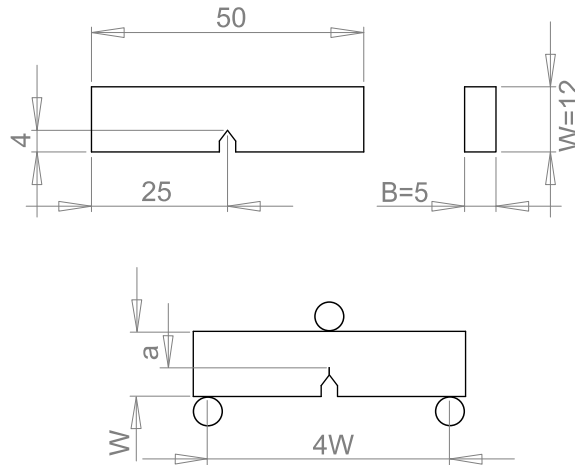


Figure 4.5. Standard specimen geometry that was employed for single edge notched bend (SENB) tests.

The specimens were tapped using liquid-nitrogen cooled razor blades to obtain sharp cracks, with crack length,  $a$ , to width,  $W$ , ratios of the order of  $a/W = 0.5$ . The crack length was measured after the test using an optical microscope.

The fracture energy,  $G_C$ , was calculated using the energy method as

$$G_C = \frac{U}{BW\phi} \quad (4.6)$$

where  $U$  is the indentation corrected energy and  $B$ ,  $W$  and  $\phi$  are the thickness, width and energy calibration factor respectively. The fracture toughness,  $K_C$ , was calculated using the fracture load as

$$K_C = \left( \frac{P}{BW^{1/2}} \right) f(x) \quad (4.7)$$

and  $P$  is either the maximum,  $P_{\max}$ , or 5% offset,  $P_Q$ , load and  $f(x)$  is a shape factor as a function of  $x$ , where  $x = a/W$ .

As a check, the fracture energy was also calculated from the measured values of  $K_C$  and  $E$  for each specimen using the linear elastic fracture mechanics (LEFM) method.

$$G_{\text{LEFM}} = \frac{(1 - \nu^2)K_C^2}{E} \quad (4.8)$$

The value of  $E$  was taken from tensile tests and  $\nu$  was taken as 0.35 [188]. Good agreement was found between the values of  $G_C$  and  $G_{\text{LEFM}}$ . The various validity checks were performed to ensure that plane strain conditions were satisfied and that LEFM was valid, for example, the size calibration

$$B, a, (W - a) > 2.5 \frac{K_C}{\sigma_{yt}} \quad (4.9)$$

and for LEFM to be valid the maximum fracture load,  $P_{\text{max}}$ , and 5 % offset load,  $P_Q$ , need to meet the criterion:

$$\frac{P_{\text{max}}}{P_Q} < 1.1 \quad (4.10)$$

A minimum of six specimens were tests for each of the formulations. Their mean values are reported with the standard deviation.

#### 4.12.1 Sub-critically loaded crack-tips

Double-notched four-point bend (DN4PB) tests were conducted to understand the toughening mechanisms in the epoxies. This method has previously been employed successfully [189-192] using the specimen geometry in Figure 4.6.

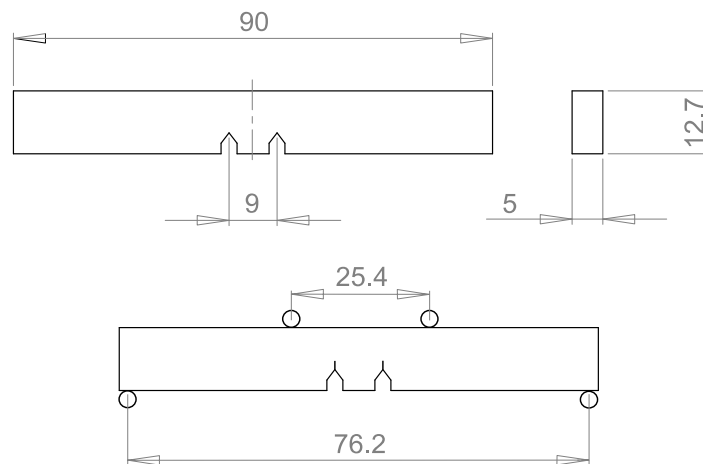


Figure 4.6. Standard geometry that was used to conduct the double-notched four point-bend (DN4PB) tests.

Tests were conducted using the same procedure to the SENB tests unless otherwise mentioned in this section. Two near-identical natural cracks were produced by tapping a nitrogen-chilled razor blade into each machined-notch, maintaining  $a/w = 0.5$  as closely as possible. The specimen was then loaded in four-point bending, resulting in two near-identical stress fields at the crack-tips, as can be shown using cross-polarised light optical microscopy in Figure 4.7(a) and (b).

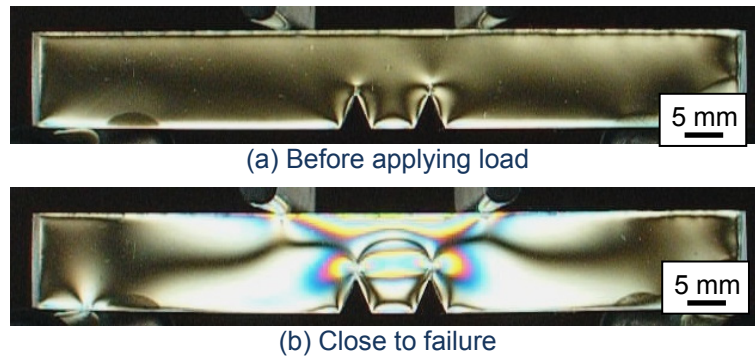


Figure 4.7. Cross-polarised light optical images of the 10N anhydride cured DGEBA (a) before applying a load and (b) imminent fracture in one of the cracks (noted as the right crack).

Upon loading, one of the cracks will propagate by virtue of being slightly longer, or providing a larger stress concentration due to crack inhomogeneities and will leave a second crack-tip that is loaded to a near-critical stress intensity factor (fracture toughness) for that material. The process-zone region directly ahead of this second crack-tip can then be examined using techniques such as polarised optical microscopy or transmission electron microscopy. AFM was also conducted on such specimens and unfortunately, no useful information about the toughening mechanisms was obtained.

The fracture toughness from these tests can be directly compared to those obtained using SENB tests to ensure that the second crack-tip was had a nearly fully-developed process zone ahead of the second crack-tip,

$$K_C = \left( \frac{P}{BW^{1/2}} \right) f'(x) \quad (4.11)$$

where  $f'(x)$  takes the modified form for this geometry, as reported in [189, 190]. Many specimens were tested. Those specimens that attained the same mean value of  $K_C$  as that from SENB tests were selected for further evaluation using microscopy.

The value of  $r_{pz}$ , the Irwin prediction of plane strain plastic zone radius for the epoxy at fracture, was calculated from [193] as

$$r_{pz} = \frac{1}{6\pi} \frac{K_C^2}{\sigma_{yt}^2} \quad (4.12)$$

where  $K_C$  is the fracture toughness and  $\sigma_{yt}$  is the tensile true yield strength for the unmodified epoxy polymer. Some systems failed prior to obtaining maximum yield strength. A relationship between the values of  $\sigma_{yt}$  and  $\sigma_{yc}$  was reported in [94] reported as

$$\sigma_{yt} = \sigma_{yc} \frac{(3^{1/2} - \mu_m)}{(3^{1/2} + \mu_m)} \quad (4.13)$$

and  $\mu_m$  was taken as 0.2 [10] to calculate a value of  $\sigma_{yt}$  for these systems.

### 4.13 Fibre-matrix interfacial tests

Single-fibre pull-out tests were conducted to specifically characterise the effect on the interfacial properties in the GFRP of nanosilica modification. The tests were conducted at a constant displacement rate of 1  $\mu\text{m/s}$ . Failure for the unmodified and modified matrices initiates at the free end of the fibre and propagate down the fibre length as matrix yielding occurs, shown in the load-displacement trace in Figure 4.8. Lastly, the end of the fibre debonds, and the reduction in load with increased displacement is the effect of friction between the fibre and matrix.

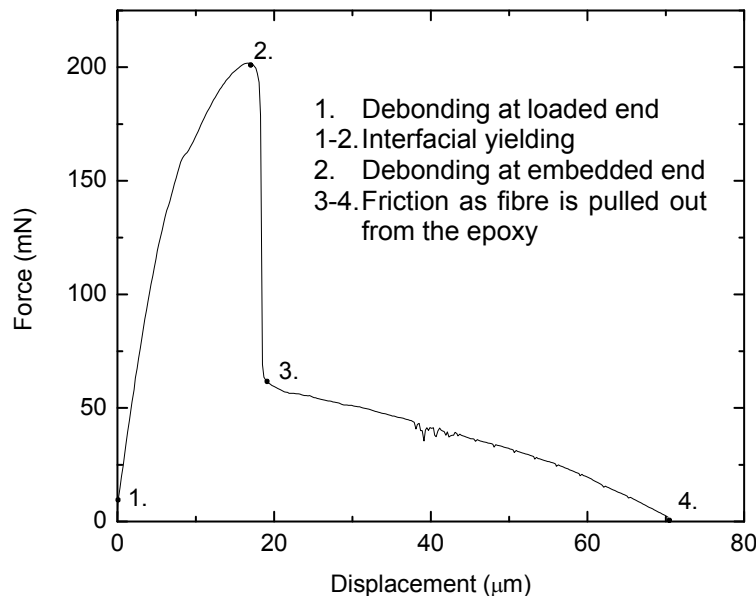


Figure 4.8. Load-displacement trace from a typical single-fibre pull-out test.

The mean pull-out shear strength,  $\tau_{max}$ , from single-fibre pull-out tests was calculated using

$$\tau_{\max} = \frac{P_{\max}}{\pi d L} \quad (4.14)$$

The fibre diameter,  $d$ , was measured using SEM images after the test and the embedded length  $L$  was confirmed to be the same value as that obtained from the pull out test, i.e. between 1 and 4.

A total of 10 specimens were produced for each formulation and were tested. Fibre fracture was a common failure in the test, hence only few valid tests were obtained for some of the modified epoxies. The strength of the fibre was calculated for these tests and agreed well with literature data (~2 GPa) [194].

#### 4.14 Composite short beam shear strength

Short beam shear tests have been conducted in accordance with ASTM D2344 [195]. Uni-directional GFRP specimens of 2 mm thickness, 10 mm by 20 mm length were tested. The uni-directional orientation was in the longitudinal direction of the specimen. Specimens were prepared as a composite plate and were milled down to give 2 mm plates.. Tests have been conducted using an 'Instron 5584' universal testing machine at a test rate of 1 mm/min. Flexure rig dimensions were controlled so that the span was set as 12 mm, and the specimen was loaded in three-point bend using 6mm diameter steel pins.

#### 4.15 Composite flexural properties

Flexural Young's modulus data was required for mode I fracture analysis. These tests were conducted in accordance with ASTM D790M [196] using 20 × 200 mm beams. The load was allowed to reach a maximum value of 300 N at a test rate of 1 mm/min to ensure that the test in the beam's elastic region. The three-point bend rig was set up such that the span was fixed at 200 mm. End supports and the loading point contact was made with 10 mm diameter steel pins. Tests were conducted using an 'Instron 5583' universal testing machine. The Young's modulus was calculated as

$$E_f = \frac{S^3 m}{4WB^3} \quad (4.15)$$

where  $S$  is the support span,  $m$  is the gradient of the load-displacement trace and  $W$  and  $B$  are the width and thickness respectively.

## 4.16 Composite mode I fracture energy

The mode I composite fracture energy was measured using the double cantilever beam (DCB) test in accordance with ASTM D5528 [197] and ISO 25217 [198].

The composites were first cut into 20 mm wide beams using a diamond wet saw (the length of the starter film was ~35 mm). The end-block surfaces were prepared for bonding by sand blasting and acetone cleaning before bonding aluminium end blocks using a two part epoxy adhesive; 'Permabond E32'. Thereafter the specimen edges were coated with white ink and marked at 1 mm intervals to facilitate detection of the crack front.

The DCB tests were conducted at a constant displacement rate of 1 mm/min. The crack length was recorded every millimetre, along with the time, load and displacement. The composite mode I fracture energies at crack initiation,  $G_{IC INT}$ , were measured by taking the minimum value from the non-linear, 5 % offset compliance and visual initiation methods [198].

The initial pre-crack was grown to a fixed crack length of 60 mm before the specimen was unloaded, and re-loaded to measure the propagation fracture energy. Results were analysed the corrected beam theory (CBT) method [199],

$$G_{IC} = \frac{3P\delta}{2W(a+|\Delta|)} \cdot \frac{F}{N} \quad (4.16)$$

where  $P$  is the load,  $\delta$  is the displacement,  $W$  is the width of the beam and  $a$  is the crack length,  $F$  is a correction for large displacements,  $N$  is a correction to account for the additional stiffness of having end loading blocks and  $\Delta$  is the crack length correction. The displacement was also corrected by performing a compliance calibration on the test rig.

Moreover, the simple beam theory (SBT) and experimental compliance method (ECM) were employed to verify the precision of the data that was obtained. The SBT method is the most basic method of calculation and assumes that the beam is perfectly built in. The ECM method compensates for human error in the measurement of crack length by using the experimental compliance from flexural tests to predict the crack length.

## Amine cured TGMDA Epoxy Properties

### 5.1 Introduction

This chapter presents the morphology and material properties of tetra-glycidyl methylenedianiline (TGMDA) epoxy cured with 4, 4'-methylenebis (2, 6-diisopropylaniline) blend, termed amine cured TGMDA. The studied system is similar in chemistry and material properties to RTM-6, a single-component epoxy based system that has been developed for aerospace applications [171]. It is used commercially as a matrix material with continuous carbon-fibre reinforcement and is suited to infusion based manufacturing techniques for high performance carbon-fibre reinforced polymer (CFRP) components.

Bulk properties were considered for epoxies modified with 10 wt. % and 20 wt. % nanosilica, 9 wt. % carboxyl terminated butadiene acrylonitrile (CTBN) rubber, and a hybrid of 10 wt. % nanosilica and 9 wt. % CTBN rubber, summarised in Figure 5.1. The volume fraction was calculated from known weight percentages of the system's constituents. The density of the unmodified epoxy was determined to be 1,140 kg/m<sup>3</sup>.

Table 5.1. Formulations of amine cured TGMDA epoxies that were studied.

Formulation	Nanosilica content		CTBN content	
	wt. %	vol. %	wt. %	vol. %
Unmodified	0	0	0	0
10N	10	6.6	-	-
20N	20	13.7	-	-
9R	-	-	9	10.6
10N9R	10	6.6	9	10.6

Differential scanning calorimetry (DSC) was conducted to examine changes in glass transition temperature with varying modification of nanosilica and rubber. Atomic force microscopy (AFM) was performed to verify the morphology of the bulk formulations and confirm good nanosilica dispersion in the manufactured carbon-fibre composite. The bulk material properties were characterised using tensile tests, plane strain compression and single edge notched bend (SENB) fracture tests. Field emission gun

scanning electron microscopy (FEGSEM) was conducted on the fractured specimens to gain an understanding of the toughening mechanisms in the bulk systems. Continuous carbon-fibre reinforced polymers (CFRPs) were manufactured using the unmodified and modified epoxies as matrix materials. Composite fracture properties were examined using double cantilever beam tests (DCB) for the unmodified, 10N, 9R and 10N9R formulations. The 10N and 10N9R formulations were identified as potential formulations to give optimal toughening for minimal filler contents, with the unmodified and 9R formulations as baselines for their respective nanosilica-modification. The 20N formulation provided little additional bulk toughening for the high nanosilica content, and therefore, was not identified as a worthwhile CFRP formulation. These tests provide insight into the transfer of toughness to a continuous fibre composite from bulk properties, and the effect that matrix modification has on the interfacial properties in the continuous-fibre composite.

## 5.2 Glass transition temperature

The glass transition temperature,  $T_g$ , was compared for the bulk formulations using DSC and summary of results is shown in Table 9.2. The  $T_g$  of the unmodified epoxy was measured to be 186 °C and agrees well with tabulated data for the  $T_g$  of RTM-6 [200]. The addition of nanosilica has no effect on the overall  $T_g$  of the epoxy. The cross-link density seems to remain unchanged. The addition of CTBN rubber to the epoxy results little or no change where  $T_g = 183$  °C. For the hybrid-modified epoxy, a reduction is also reported with  $T_g = 182$  °C. This would suggest that some of the rubber remains in solution. A quantitative analysis is discussed further when the morphologies of the rubber-modified formulations are examined in Section 5.3.2.

Table 5.2. Mean glass transition temperatures of unmodified and modified amine cured TGMDA epoxies, measured using DSC.

Formulation	$T_g$ (°C)	
	$\bar{x}$	$\pm$
Unmodified	186	2
10N	184	1
20N	186	0
9R	183	2
10N9R	182	6

## 5.3 Morphology

An atomic force micrograph of a microtome-cut surface of unmodified epoxy is shown in Figure 5.1. The phase and height images show that the sample was featureless and flat. This is typical for a homogenous thermoset polymer [59]. There are scratch marks in the surface of the polymer from microtome preparation. These are shown to be parallel to the cut direction and are therefore, discounted from being features in the epoxy polymer.

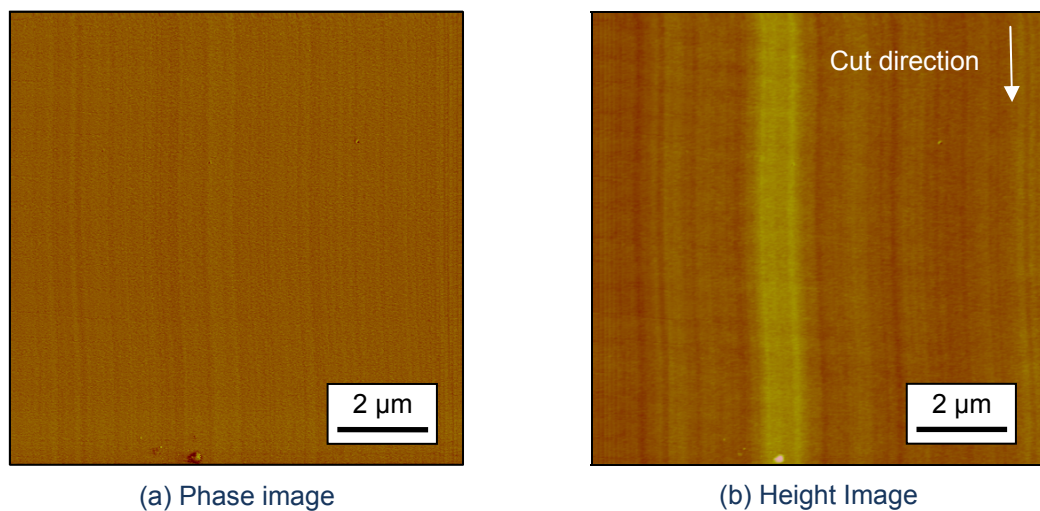


Figure 5.1. Shows (a) phase and (b) height images of the unmodified amine cured TGMDA epoxy. The cut direction is shown in the height image.

### 5.3.1 Nanosilica-modified formulations

The 20 nm nanosilica particles are dispersed in the epoxy in the 10N as shown by the AFM micrographs in Figure 5.2. The area fraction was measured using the high magnification height image in Figure 5.2(c) and a value of about 6.1 % was obtained. This compares reasonably well with the calculated volume fraction that was shown in Table 5.1 as 6.6 vol. %.

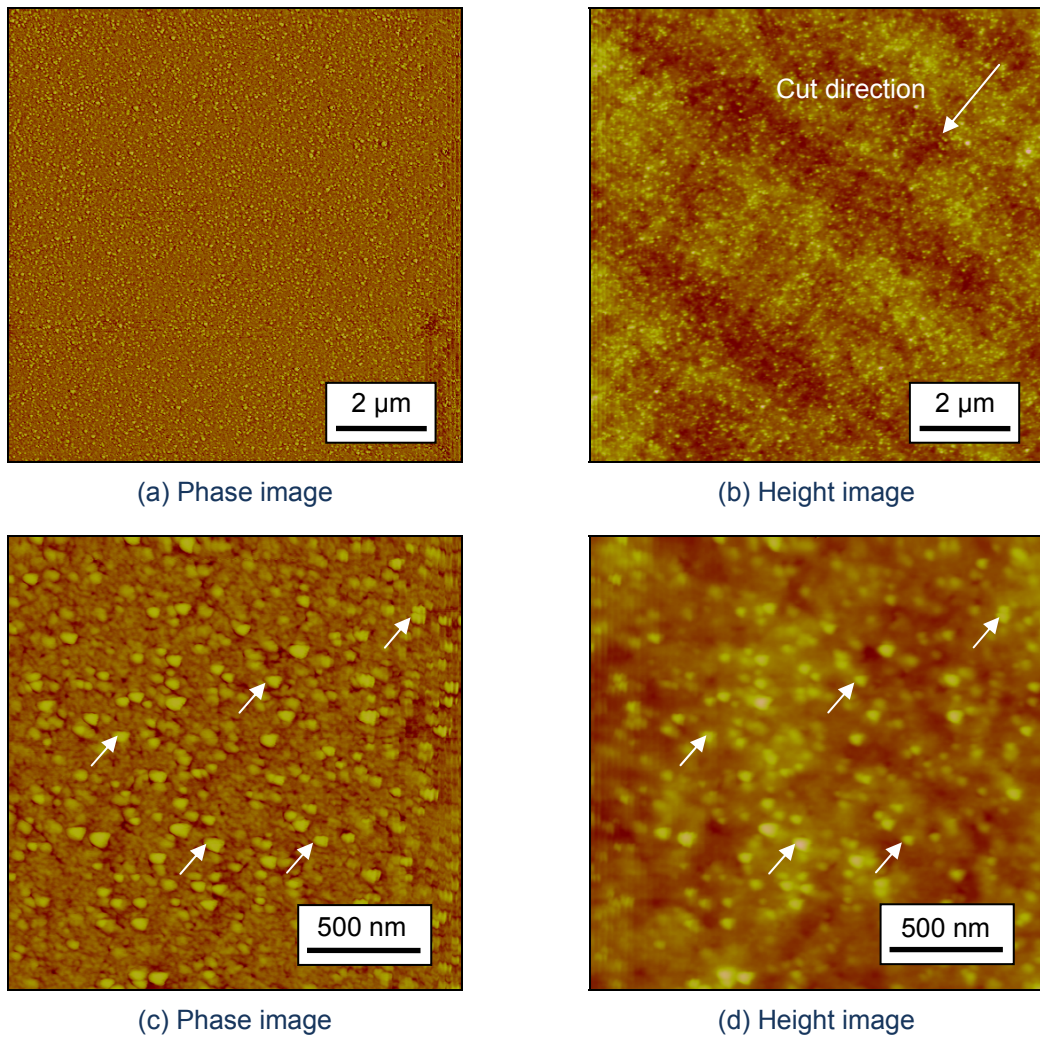


Figure 5.2. Shows (a, c) phase and (b, d) height images of amine cured TGMDA with 10N. The cut direction is shown in (b) and (c, d) shows some of the 20 nm nanosilica particles (arrows).

Good dispersion was also found at higher nanosilica content in Figure 5.3 for the 20N formulation. The inter-particle distance was calculated to be 20 nm to 11 nm for 10N and 20N respectively and based on the assumptions of perfect dispersion and no size variation in the 20 nm nanosilica particles.

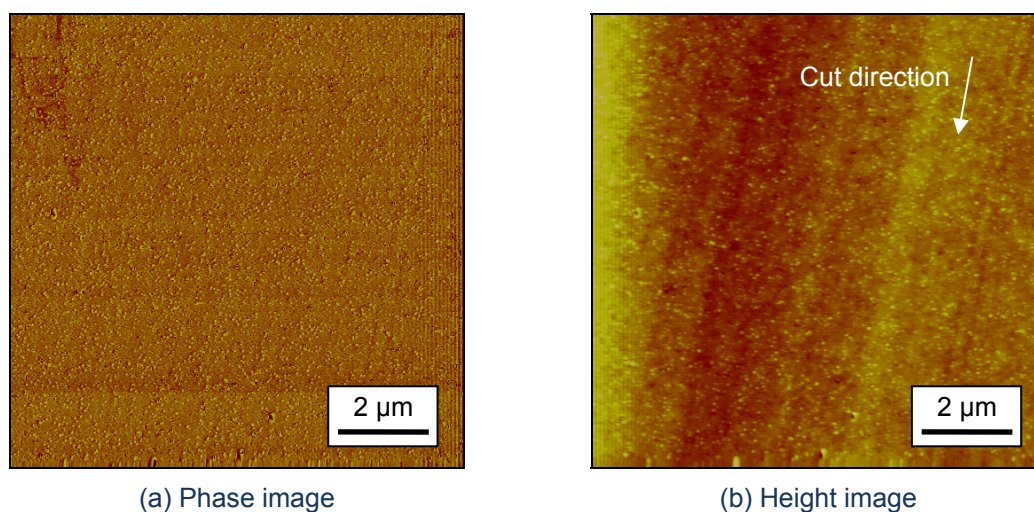


Figure 5.3. Shows (a) phase and (b) height images of the 20N amine cured TGMDA epoxy.

### 5.3.2 Rubber-modified formulations

The CTBN has phase separated out of the epoxy during curing, as shown by the AFM micrographs in Figure 5.4. Spherical rubber particles up to 1  $\mu\text{m}$  in diameter are present in the epoxy, and are shown with arrows. There is some evidence from the images to suggest that some epoxy remains in the rubber-rich domains. The area fraction was measured to be 9.1 % using low magnification micrographs. Based on the calculated volume fraction being 10.6 vol. % (Table 5.1), 1.5 vol. % would be expected to remain in solution. The Fox equation [201] was used to confirm that indeed, the small change in  $T_g$  noted in Table 5.2 can be explained by somewhere in the range of 0.2-1.2 vol. % remaining in solution. Based on a 9.1 vol. % in the epoxy, the inter-particle distance, between rubber particles was calculated as 1.6  $\mu\text{m}$ .

A rubber particle diameter up to 1.5  $\mu\text{m}$  was found in the hybrid-modified epoxy, and is shown with AFM micrographs in Figure 5.5. The CTBN particles in the image appear to be less circular than for the 9R epoxy. Based on area fraction analysis of the CTBN in the hybrid sample, 0.8 vol. % was estimated to remain in solution. Fox's equation [201] shows agreement with this measurement based on the difference in the  $T_g$  of the hybrid epoxy, with the reduction in  $T_g$  explained by 0-2.5 vol. % remaining in solution (noting the large standard deviation in the mean 10N9R  $T_g$ ). The inter-particle distance between rubber particles was calculated as 2.2  $\mu\text{m}$  (using  $v_f = 9.8\%$ ). The dispersion of nanosilica was disrupted by the phase separation of the rubber during curing. This resulted in networks of agglomerated nanosilica which are well dispersed in the epoxy. Typically, agglomerated nanosilica particles, 700 nm by 150 nm in size were

measured. The inter-particle distance between nanosilica necklaces was measured to be around  $0.8 \mu\text{m}$ .

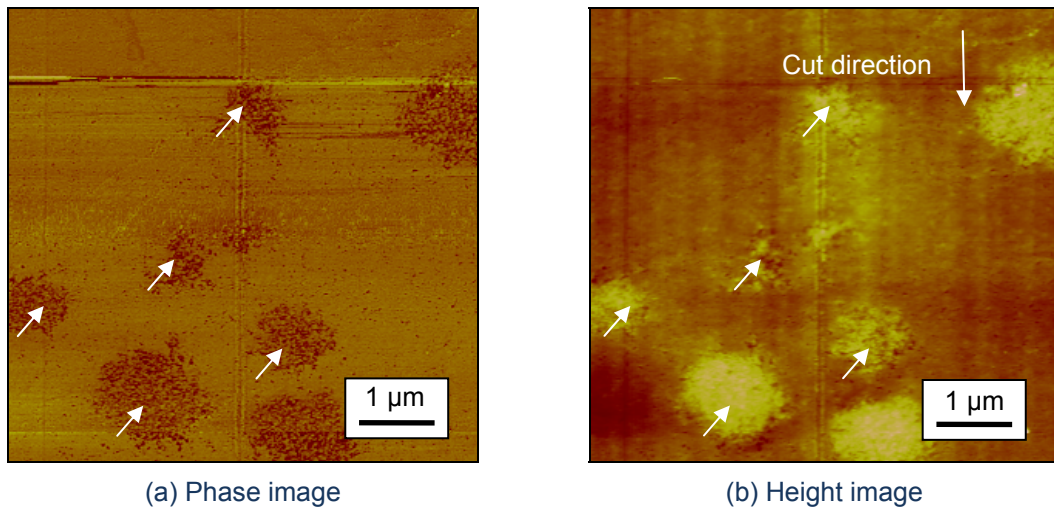


Figure 5.4. Shows (a) phase and (b) height images of the 9R amine cured TGMDA with spherical, phase separated,  $1 \mu\text{m}$  CTBN particles (arrows) in the epoxy.

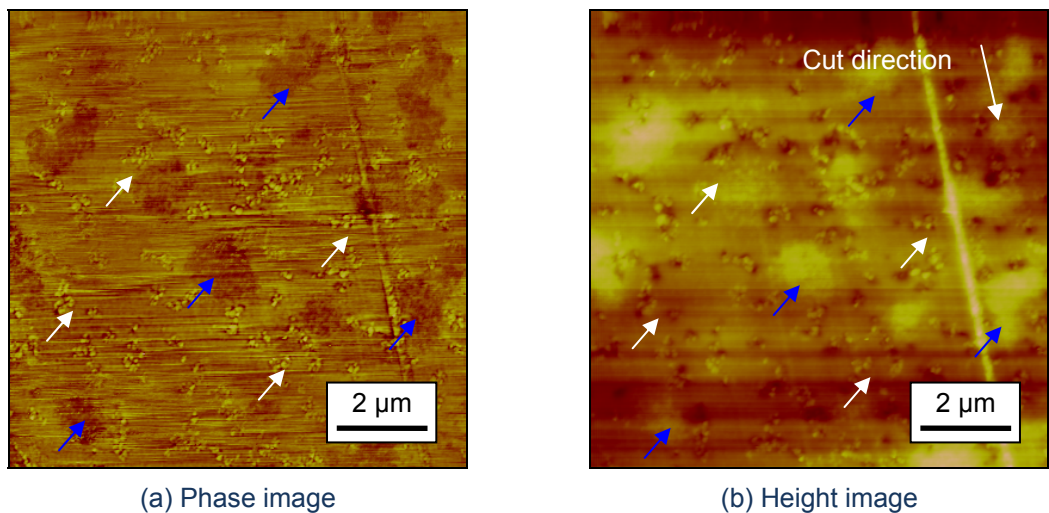
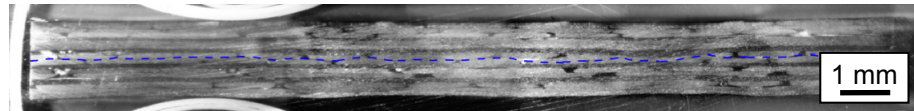


Figure 5.5. Shows (a) phase and (b) height images of the 10N9R amine cured TGMDA epoxy. Some CTBN particles (blue) and nanosilica necklaces (white) are identified.

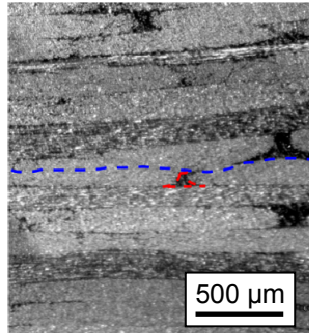
### 5.3.3 Fibre-reinforced composite

The most common application for this type of epoxy polymer are as matrices in carbon-fibre reinforced composites. These were produced from a balanced, symmetric lay-up of biaxial non-crimp fabric. This was arranged with a  $0^\circ/0^\circ$  interface to study fracture events and is indicated with the broken line in Figure 5.6(a). Individual  $7 \mu\text{m}$  diameter fibres are organised in tows measuring 1-2 mm by  $50 \mu\text{m}$ . The tows are arranged into lamina, and are bound together using a polyethylene weft stitching. The stitching is

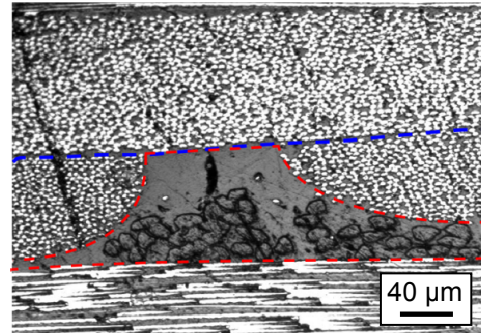
visible in the resin rich pockets of the composite and is traced with red, best shown in the high magnification micrograph in Figure 5.6(c). The morphology of the inter-space between plies is variable, the resin rich regions range from  $1 \mu\text{m}^2$  to  $100 \mu\text{m}^2$ . The mean fibre volume fraction was measured optically to be  $57 \pm 1 \%$ .



(a) The interlaminar fracture plane (blue) through the thickness of the CFRP.



(b) High magnification optical image of the fracture plane.



(c) Resin rich pocket containing some weft stitching in the fracture plane.

Figure 5.6. Optical micrographs show (a) the fibre architecture in the CFRP and (b, c) the inter-ply region. The fracture plane (blue) and a resin rich pocket (red) are identified.

AFM was conducted on the 10N CFRP in order to verify dispersion of the nanosilica particles in the fibre inter-space, as shown in Figure 5.7. It was not possible to cut a flat surface of the composite with standard microtomy techniques; therefore, a flat ground (4,000 grit) section was examined. The fibres are identified in the low magnification image and are shown in Figure 5.7(a). Closer examination verified that the nanosilica particles do remain dispersed and are not filtered, or agglomerated during the infusion process, as shown in Figure 5.7(b).

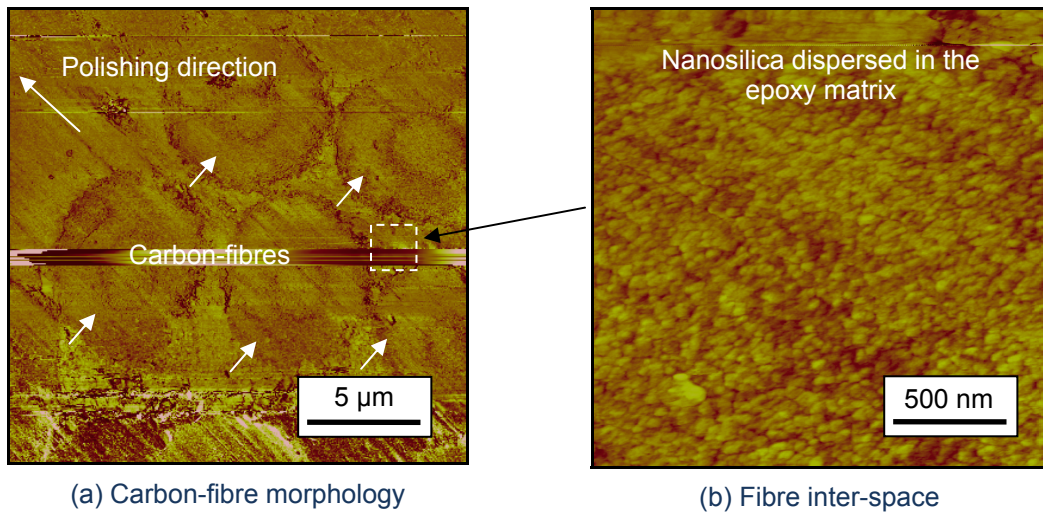


Figure 5.7. Height images of the 10N amine cured TGMDA CFRP with (a) showing the carbon-fibre matrix morphology and (b) showing the inter-space region at high magnification.

## 5.4 Tensile properties

Tensile tests were conducted on bulk polymer samples. The tensile Young's modulus,  $E_t$ , ultimate tensile true strength,  $\sigma_{UTS}$ , and ultimate tensile true strain,  $\epsilon_{UTS}$ , for the unmodified and modified amine cured TGMDA are summarised in Table 5.3 and shown graphically in Figure 5.8. The value of  $E_t$  was found to increase steadily with nanosilica content from 3.14 GPa for the unmodified epoxy to 3.97 GPa for the 20N epoxy. The addition of CTBN decreases  $E_t$  to 2.46 GPa, with some stiffness restored when nanosilica was added in the hybrid-modified (10N9R) epoxy. The values of  $E_t$  agree with reported data from Mohammed [59]. A large variation in  $\sigma_{UTS}$  was found, with brittle failure and inconsistent results in the samples (i.e. a maximum yield strength was not identified). The variation in true tensile stress also explains the scatter in the true fracture strain.

Table 5.3. Young's modulus,  $E_t$ , ultimate tensile true stress,  $\sigma_{UTS}$ , and ultimate tensile true strain,  $\epsilon_{UTS}$ , for unmodified and modified amine cured TGMDA epoxies.

Formulation	$E_t$ (GPa)		$\sigma_{UTS}$ (MPa)		$\epsilon_{UTS}$ (true strain)	
	$\bar{x}$	$\pm$	$\bar{x}$	$\pm$	$\bar{x}$	$\pm$
Unmodified	3.14	0.06	44	2	0.02	0.00
10N	3.55	0.03	77	4	0.04	0.01
20N	3.97	0.01	16	9	0.02	0.02
9R	2.46	0.03	66	1	0.05	0.00
10N9R	2.66	0.06	60	3	0.04	0.01

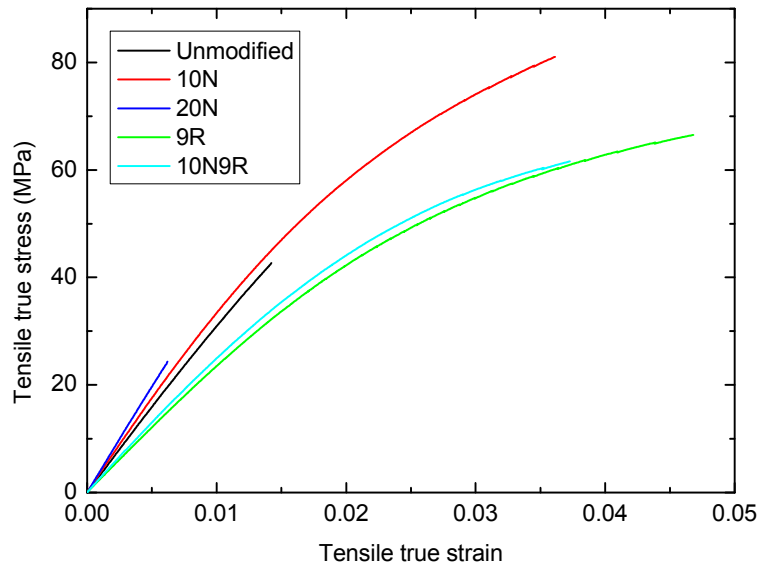


Figure 5.8. Tensile true stress versus tensile true strain for the unmodified and modified amine cured TGMDA epoxies.

## 5.5 Compressive properties

Plane strain compression tests were conducted on amine cured TGMDA modified with nanosilica. The compressive Young's modulus,  $E_c$ , compressive true yield strength,  $\sigma_{yc}$ , and compressive true yield strain,  $\varepsilon_{yc}$ , are summarised in Table 5.4. The value of  $E_c$  increases with nanosilica content and agrees well with  $E_t$  from tensile tests. The value of  $\sigma_{yc}$  was also found to increase with nanosilica content as demonstrated in the plot of compressive true stress versus compressive true strain in Figure 5.9. The curves plateau at  $\sigma_{yc}$  and then work-harden with further applied strain. This locus of zero gradient was defined as the strain softening point for this epoxy because no actual decrease in stress was observed at strain softening.

The unmodified epoxy was loaded to failure and a compressive true fracture strain of  $0.76 \pm 0.01$  was obtained.

Table 5.4. Compressive Young's modulus,  $E_c$ , compressive true yield strength,  $\sigma_{yc}$ , and compressive true yield strain,  $\varepsilon_{yc}$ , for the unmodified and nanosilica-modified amine cured TGMDA epoxies.

Formulation	$E_c$ (GPa)		$\sigma_{yc}$ (MPa)		$\varepsilon_{yc}$ (true strain)	
	$\bar{x}$	$\pm$	$\bar{x}$	$\pm$	$\bar{x}$	$\pm$
unmodified	2.85	0.52	140	1	0.14	0.01
10N	3.26	0.12	151	2	0.14	0.00
20N	4.11	0.05	162	1	0.13	0.02

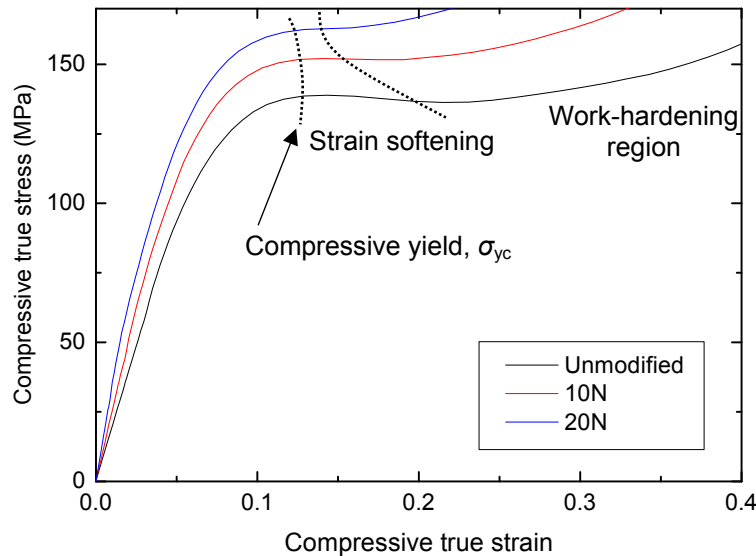


Figure 5.9. Compressive true stress versus compressive true strain for unmodified and nanosilica modified amine cured TGMDA from plane strain compression tests.

A sample of the unmodified epoxy was loaded to the strain softening region (0.23 true strain) and sectioned to be examined by optical cross-polarised light optical microscopy, shown in Figure 5.10. There was no drop in stress at  $\sigma_{yc}$ , hence the unmodified epoxy had diffuse shear bands in the compressed region of the sample. It was noted that shear yielding has occurred in this epoxy, though well defined shear bands are not present. There was a notable effect of surface asperities on the sample, with small shear bands initiating from the two compressed faces.

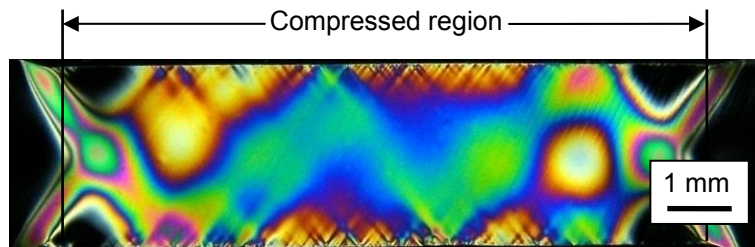


Figure 5.10. Polished cross section of the unmodified amine cured TGMDA that was loaded to the strain softening region shows extensive shear banding in the compressed region.

## 5.6 Fracture properties

Fracture tests were conducted on the unmodified and modified epoxies; namely the 10N, 20N, 9R and 10N9R formulations. The mean values of fracture toughness,  $K_C$ , and fracture energy,  $G_C$ , are summarised in Table 5.5. For the unmodified epoxy, the values of  $K_C = 0.51 \text{ MPa}\sqrt{\text{m}}$  and  $G_C = 70 \text{ J/m}^2$  and agree closely the values of  $G_C$  and  $K_C$  that were measured for the RTM-6 epoxy. Such a system was also reported by Mohammed [59] with nanosilica and rubber modification. A reasonable agreement was

found with the present study when the difference in crack preparation methods was considered.

### 5.6.1 Nanosilica-modified formulations

A two fold increase in  $G_C$  was observed with the addition of 20 wt. % nanosilica. Maximum values of  $K_C = 0.87 \text{ MPa}\sqrt{\text{m}}$  and  $G_C = 172 \text{ J/m}^2$  (Figure 5.11) were observed for the 20N formulation.

### 5.6.2 Rubber-modified formulations

There were significant gains in  $K_C$  and  $G_C$  with the addition of rubber. A six fold increase in  $G_C$  was found for 9R with  $G_C = 557 \text{ J/m}^2$ . Pearce et al. [202] also noted similar gains with CTBN in TGMDA cured with piperidine. Interestingly, there was no further increase in fracture properties when nanosilica was introduced in the hybrid epoxy, as is apparent in Figure 5.11 for  $K_C$  and for  $G_C$ . No synergy was observed between the nanosilica particles and rubber micro-particles in this epoxy system.

Table 5.5. Fracture toughness,  $K_C$ , and fracture energy,  $G_C$ , for the unmodified and modified amine cured TGMDA epoxies.

Formulation	$K_C$ (MPa $\sqrt{\text{m}}$ )		$G_C$ (J/m $^2$ )	
	$\bar{x}$	$\pm$	$\bar{x}$	$\pm$
Unmodified	0.51	0.06	70	21
10N	0.71	0.05	114	13
20N	0.87	0.08	172	18
9R	1.33	0.09	557	21
10N9R	1.42	0.11	573	52

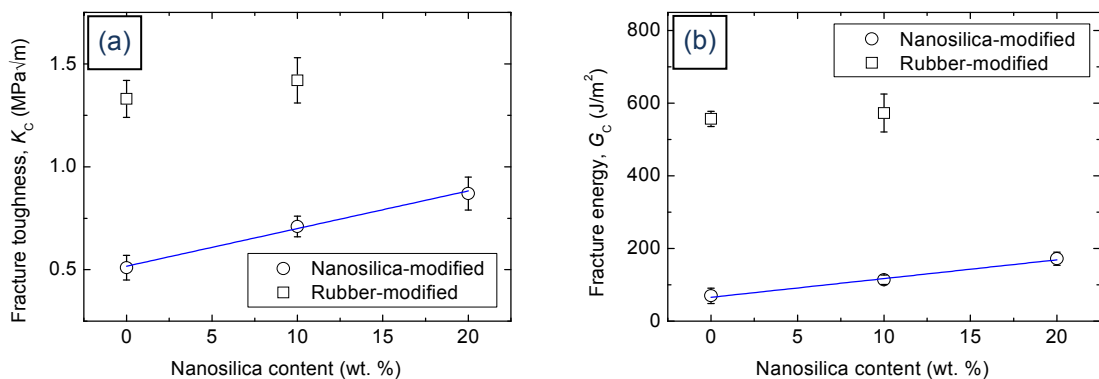


Figure 5.11. The (a) fracture toughness and (b) fracture energy versus nanosilica content for the unmodified and modified amine cured TGMDA epoxies. A linear fit shows the general trend in the fracture properties for the nanosilica-modified epoxies.

### 5.6.3 Toughening mechanisms of the nanosilica-modified formulations

The plastic zone radius,  $r_{pz}$ , was calculated for the nanosilica-modified formulations using Irwin's prediction in plane strain conditions [193]. The value of  $r_{pz}$  was found to be 1.1  $\mu\text{m}$  for the unmodified epoxy, up to 2.5  $\mu\text{m}$  for 20N. The process zone was identified on the fracture surface of the 20N SENB sample and is shown with high magnification FEGSEM in Figure 5.12(a, b). Measurement of the identified nanosilica particles (shown with arrows) yielded a mean diameter of around 35 nm. The sample was coated with approximately 5 nm of chromium. The debonding stress at the interface is proportional to  $r_p^{-1/2}$  [34, 47, 49] and so one would expect the larger particles to debond more readily. These two processes could aid explanation of why the observed nanosilica particles on the fracture surface are relatively large. Due to particle size being many orders of magnitude smaller than the crack opening displacement, crack deflection and crack pinning are discounted as toughening mechanisms [73, 203]. Some evidence of particle debonding was found, as shown circled, but no evidence of plastic void growth around debonded nanosilica particles was identified. The particles have remained well bonded to the epoxy and the dominant mechanism of energy absorption for this system seems to be shear band yielding in the epoxy.

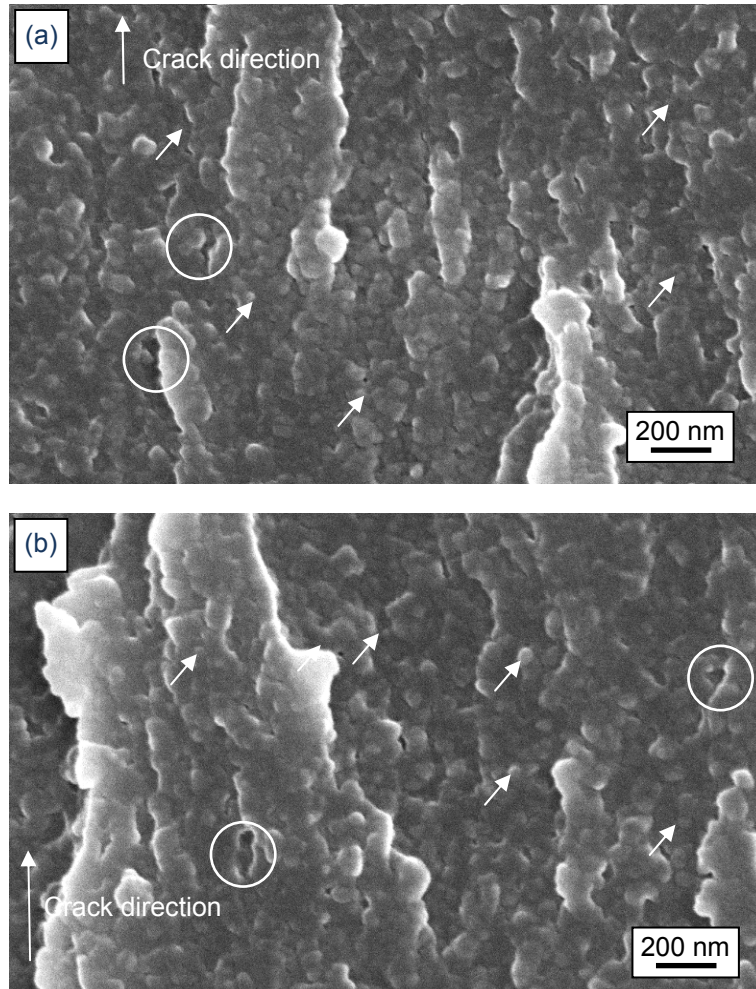


Figure 5.12. Shows (a, b), FEGSEM micrographs of 20N amine cured TGMDA. The 20 nm nanosilica particles are identified with arrows. Little evidence of debonding was observed and is shown as circled, noting that no evidence of void growth was identified.

#### 5.6.4 Toughening mechanisms of the rubber-modified formulations

The plastic zone radii,  $r_{pz}$ , for the rubber-modified formulations were calculated [193] and the values  $r_{pz} = 19 \mu\text{m}$  and  $26 \mu\text{m}$  for the 9R and 10N9R epoxies respectively. The rubber particles (9R epoxy) are shown in Figure 5.13, to internally cavitate and produce voids in the epoxy polymer. Void sizes close to  $1.5 \mu\text{m}$  were observed extensively on the fracture surface. The structured nature of the cavitated rubber particles may suggest that some epoxy polymer remains in the rubber particles. A FEGSEM image of the fracture surface for the hybrid-modified (10N9R) epoxy is shown in Figure 5.14. Unfortunately, the image was of poor quality in comparison to the 9R epoxy. Rubber cavitation was still present in the epoxy as indicated with arrows. No indication of void growth around the individual nanosilica necklaces was found in the hybrid epoxy. The fracture properties remain constant, and so the nanosilica particles would not be expected to contribute via shear deformation or debonding and void growth processes.

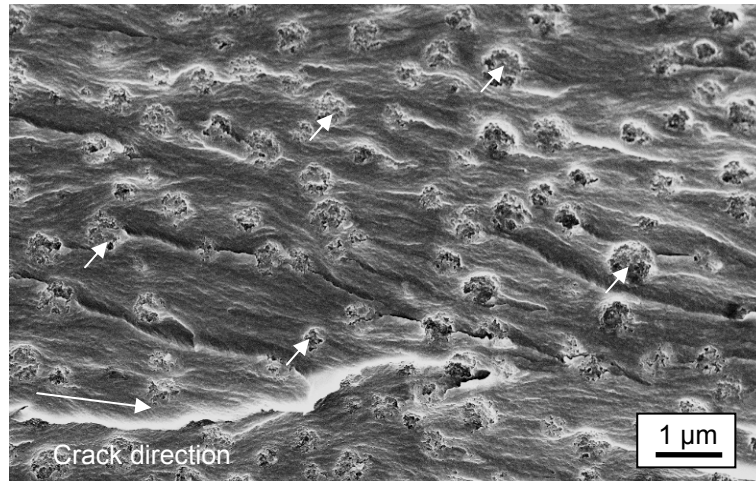


Figure 5.13. A FEGSEM micrograph from the fracture surface of 9R amine cured TGMDA shows evidence of toughening by rubber micro-particle cavitation to create voids in the epoxy.

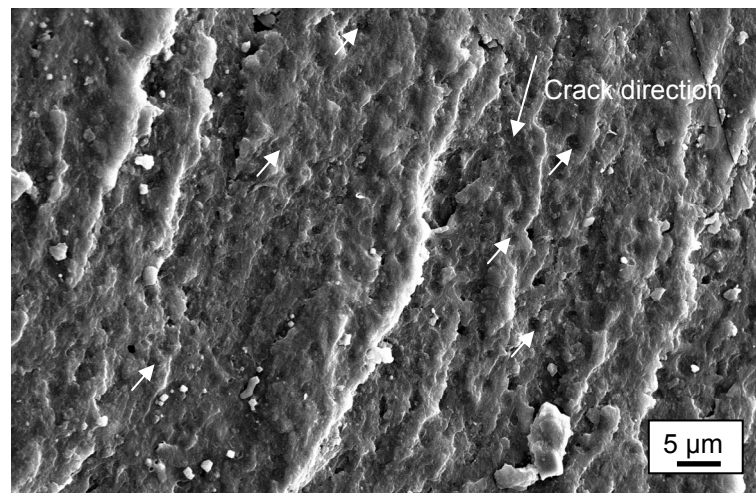


Figure 5.14. A FEGSEM micrograph of the fracture surface from the 10N9R amine cured TGMDA with evidence of toughening by rubber-particle cavitation in the epoxy (indicated).

## 5.7 Composite properties

This section details the properties that were obtained for the carbon-fibre reinforced composite with modified matrices.

### 5.7.1 Composite flexural modulus

The flexural modulus was measured under quasi-static conditions. The results summarised in Table 5.6 are used to confirm complete consolidation of void-free composite specimens and allowed calculation of a crack length independent mode I fracture energy,  $G_{IC}$ . The modulus was consistent for the different modifications of epoxy, as expected for a fibre dominant property and verifies that the composites are all correctly consolidated and void free [204].

Table 5.6. Flexural modulus,  $E_f$ , and fracture initiation energy,  $G_{IC\ INT}$ , and fracture propagation energy,  $G_{IC\ PROP}$ , for the unmodified and nanosilica-modified amine cured TGMDA epoxies.

Formulation	$E_f$ (GPa)		$G_{IC\ INT}$ (J/m <sup>2</sup> )		$G_{IC\ PROP}$ (J/m <sup>2</sup> )	
	$\bar{x}$	$\pm$	$\bar{x}$	$\pm$	$\bar{x}$	$\pm$
Unmodified	31	2	319	42	340	47
10N	33	1	144	43	196	68
9R	31	0	214	95	552	33
10N9R	31	1	483	44	714	100

### 5.7.2 Composite mode I fracture

The unmodified and modified-matrix CFRP composites were examined using mode I double cantilever beam (DCB) tests. Specimens were produced with a 40 mm insert, and fracture was analysed from the region at the end of the insert, until 20 mm of steady state crack propagation had occurred. A summary of the fracture initiation energy from the insert,  $G_{IC\ INT}$ , and the mean propagation energy,  $G_{IC\ PROP}$ , are shown in Table 5.6. Adding nanosilica has reduced the values of  $G_{IC\ INT}$  and  $G_{IC\ PROP}$  compared to the unmodified epoxy. Figure 5.15 shows values of  $G_{IC}$  for the unmodified and modified CFRPs with increasing crack length.

The extent of fibre bridging can be evaluated by observing the crack length by which a steady value of  $G_{IC}$  was attained (commonly referred to as R-curve). The unmodified and nanosilica-modified systems showed evidence of little fibre bridging occurring and steady state propagation attained at low crack lengths (43 mm). More fibre bridging occurs in the rubber and hybrid-modified formulations, and crack lengths of 50 mm were recorded before steady state propagation occurred. Therefore, fibre pull-out and crack bridging would be expected to contribute to the elevated fracture properties of the rubber-modified formulations. It is to be expected that the rubber-modified formulations would exhibit a greater degree of fibre bridging and pullout by nature of a tougher matrix in comparison to the fibre-matrix interface.

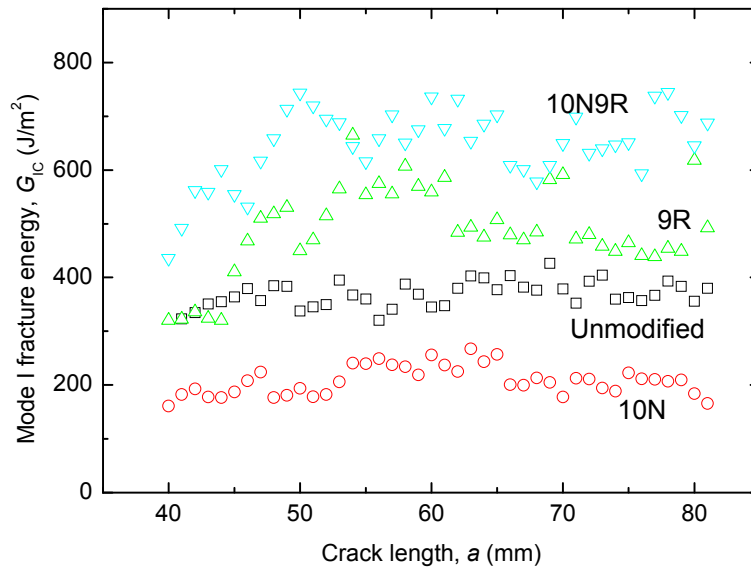


Figure 5.15. Mode I fracture energy for the unmodified and modified amine cured TGMDA CFRPs.

Figure 5.16 shows the CFRP  $G_{IC\ INT}$  and  $G_{IC\ PROP}$  versus the bulk fracture energy. The extent of fibre bridging results the different CFRP initiation and propagation values i.e. larger difference indicates more fibre bridging. The best transfer of toughness occurred in the unmodified formulation with the greatest increase in composite fracture energies from the bulk value. Apart from the 9R CFRP initiation energy, a 1:1 transfer of toughness occurred in the modified formulations. The low initiation energy of the 9R CFRP could be attributed to an interfacial failure in the fibre-matrix interface at insert initiation. Notably, improvements were seen with the hybrid formulation over the 9R baseline. This was not noted when the bulk fracture properties were examined.

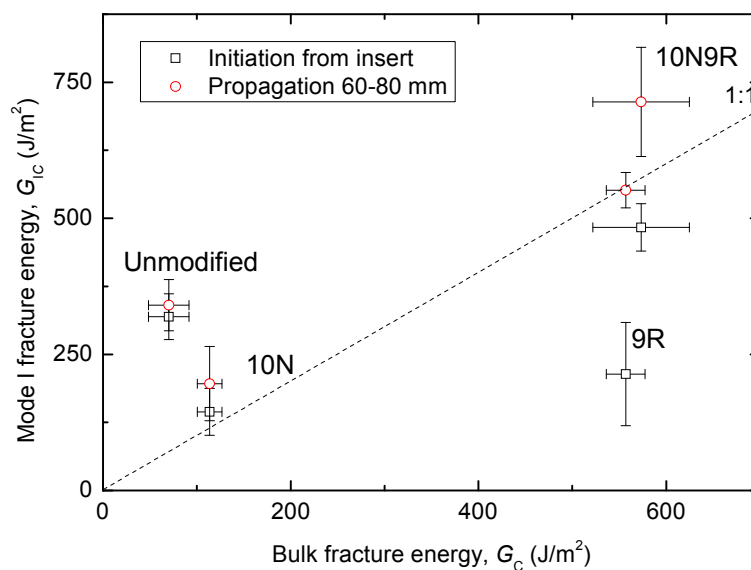


Figure 5.16. The mode I CFRP fracture initiation and propagation energies versus the bulk fracture energy for the unmodified and modified amine cured TGMDA epoxies.

### Composite mode I toughening mechanisms

The plastic zone radii,  $r_{pz}$ , were calculated for the modified-matrix CFRPs using Irwin's prediction in plane strain conditions [193]. The rule of mixtures was used to obtain a transverse Young's modulus for the CFRP [3] and  $G_C$  was assumed to be the bulk fracture energy to estimate the plastic zone radius. This would give expected  $r_{pz}$  values of 1-2.5  $\mu\text{m}$  for the unmodified and 10N formulations and about 20  $\mu\text{m}$  for the rubber- and hybrid-modified formulations. Such values would suggest that the unmodified and 10N plastic zones contain at less than the fibre diameter (7  $\mu\text{m}$ ), each side of the crack-tip. The rubber-modified systems would encompass a few fibres.

This could explain how the rubber-modified systems attain such improved toughness properties. The mode I CFRP fracture surfaces were examined using scanning electron microscopy (SEM) and to find evidence of the toughening mechanisms.

The unmodified epoxy CFRP primarily fractured with cohesive failure in the epoxy and little fibre bridging occurring as shown in Figure 5.17. The crack front was found to stabilise within 100  $\mu\text{m}$  of propagation from the insert film and to remain cohesive during propagation.

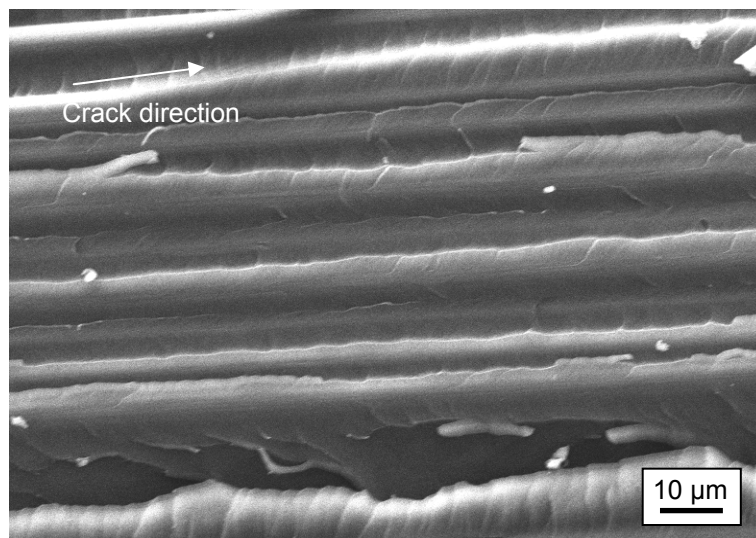


Figure 5.17. An SEM image of the mode I fracture surface in the steady state propagation region for the unmodified amine cured TGMDA CFRP.

An SEM image of the nanosilica-modified epoxy-fibre composite is shown in Figure 5.18(a). At low magnification it would appear that the fibres are clean and the interfacial adhesion was poor, however, looking closer shows that the adhesion is in fact quiet good and a reasonable amount of epoxy polymer is retained on the fibres. Little fibre bridging was shown in Figure 5.18(b) for the 10N CFRP. Better fibre-matrix interfacial

adhesion in this system could explain the poor fracture performance of the 10N modified CFRP.

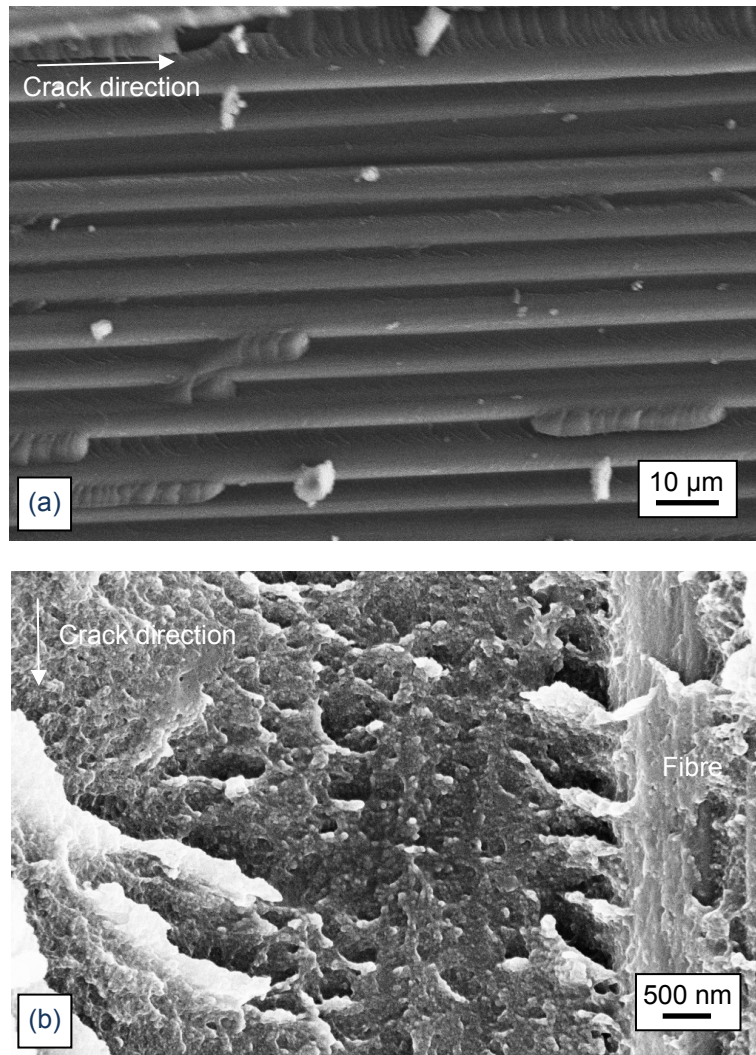


Figure 5.18. Images (a, b) of the mode I fracture surface in the steady state propagation region of the 10N amine cured TGMDA CFRP.

Micron sized voids are well defined on the fracture surface of the 9R CFRP composite, shown in Figure 5.19(a). Upon closer examination, deformed rubber was found to be present in the voids, just as with the bulk polymer in Figure 5.13. The presence of fibres has not hindered phase separation of the rubber, and internal cavitation occurs in the rubber micro-particles as shown with arrows. The SEM image shows a region of cohesive failure with extensive deformation in the matrix. However, evidence of broken and loose single fibres was also found to be present on the surface as shown Figure 5.19(b).

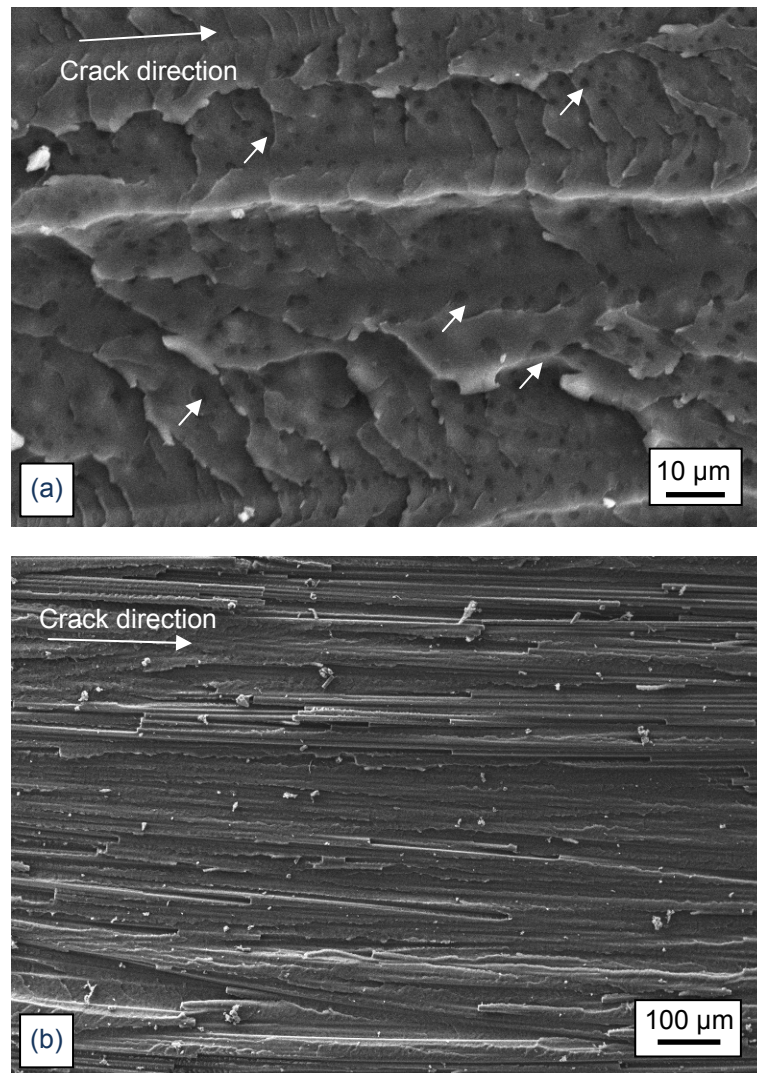


Figure 5.19. Shows (a, b) SEM images of the mode I fracture surface in the steady state propagation region of the rubber-modified (9R) amine cured TGMDA CFRP with some cavitated rubber particles indicated in the image.

As shown in Figure 5.20(a), the fracture surface of the hybrid-modified CFRP was found to be very rough in appearance. Extensive matrix deformation has occurred in this formulation. Evidence of rubber particle cavitation was present in regions when fibres had been pulled out, for example in Figure 5.20(b).

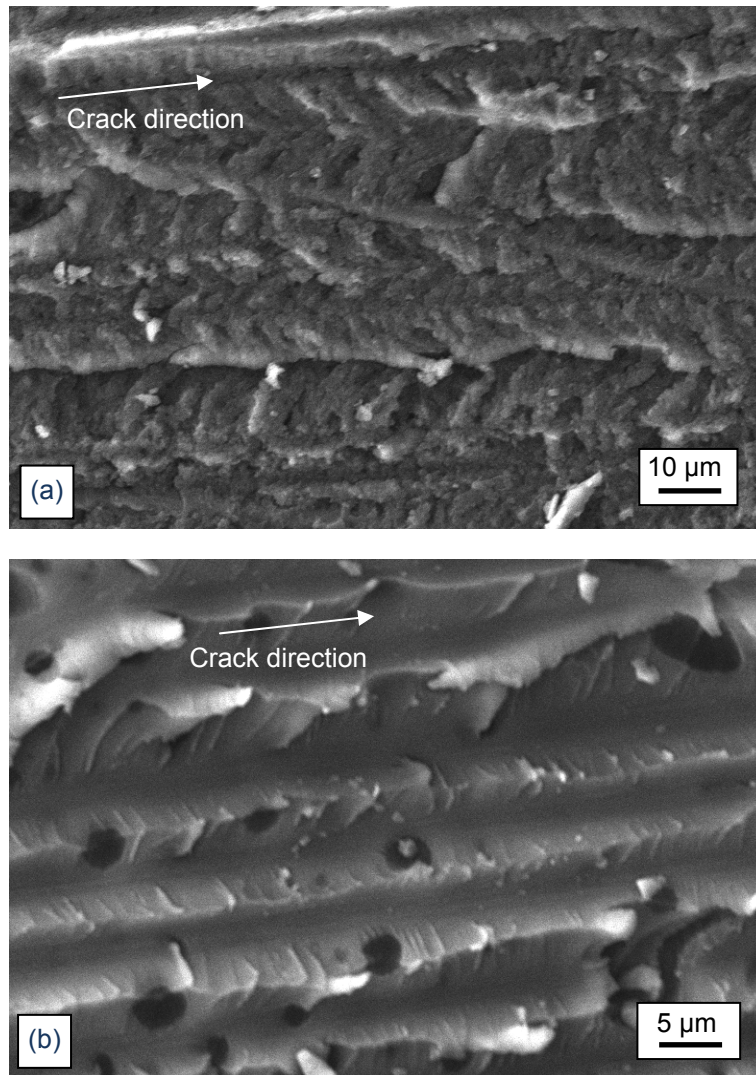


Figure 5.20. The mode I fracture surface in the steady state propagation region from the 10N9R hybrid-modified amine cured TGMDA CFRP.

## 5.8 Chapter summary

Bulk properties for amine cured TGMDA epoxy modified with nanosilica and rubber micro-particles were examined. The  $T_g$  was found to be constant with a mean value of 186 °C for the unmodified epoxy and nanosilica modifications up to 20 wt. %. The cross-link density is reported to remain unchanged when nanosilica was added to this epoxy. The 20 nm particles have been shown to remain well dispersed up to 20 wt. % using AFM. In the rubber-modified formulations, 1-1.5 vol. % of CTBN was found to remain in solution and resulted in a drop (~5 °C) in the overall  $T_g$  of the epoxy. Spherical 1 μm rubber particles were formed in the 9R epoxy. In the hybrid-modified formulation, the rubber particles were less circular, with an increase in the mean rubber particle size to 1.5 μm and agglomeration of the nanosilica particles into 700 nm by 150 nm clusters.

The tensile Young's modulus was found to increase with nanosilica content from 3.14-3.97 GPa with 20N modification. A reduction in the Young's modulus was found for the rubber-modified system to 2.46 GPa with some stiffness restored in the 10N9R hybrid epoxy. No useful data for the yield behaviour for this system was obtained, with all formulations failing prior to yield. Compression tests were utilised to obtain true stress-true strain characteristics of the unmodified and nanosilica-modified amine cured TGMDA epoxy. Good agreement was obtained between the Young's modulus measurements from compression and tensile tests. The compressive yield strength was found to increase with nanosilica content. This would suggest good particle-matrix adhesion. Interestingly, a small drop in stress was observed at the yield strength, and would suggest that a little shear banding yielding occurs in this epoxy. A strain softened sample of the unmodified epoxy was observed with cross polarised light and indeed, diffuse shear yielding was observed in the gauge area of the specimen.

A two fold increase in the fracture energy was obtained with 20N modification to the epoxy. Fracture surface imaging showed that the primary contribution of toughening in the nanosilica-modified epoxies was obtained from shear band yielding in the epoxy and no significant evidence of debonding or void growth was identified. Large gains in the fracture properties were obtained in the 9R with  $G_C = 550 \text{ J/m}^2$ . However, no further improvements were found in the 10N9R hybrid-modified epoxy. Rubber particle cavitation was successfully identified in both systems, with no evidence of plastic void growth around the nanosilica necklaces.

Resin infusion under flexible tooling was successfully used to produce consistent and void-free CFRP composites. Polished cross sections show a variable interlaminar region in the composite. The nanosilica particles are not filtered out, and do not agglomerate in the composite. For the unmodified and nanosilica-modified composites, the plastic zone region was estimated to be roughly the diameter of a single fibre. The rubber-modified formulations had a much larger interfacial region that is expected to include many tens of fibres in the process zone region. Composite fracture tests yielded variable results, but show that the interfacial properties of the modified matrix is an important parameter in determining toughenability of the fibre-composite. The nanosilica-modified CFRP performed poorly compared to the the unmodified epoxy-matrix CFRP. The rubber-modified formulations exhibited a 50 % increase in the mean propagation energy and evidence of rubber particle cavitation was observed in both the modified matrices.

## Polyether-amine Cured DGEBA/F Epoxy Properties

### 6.1 Introduction

This chapter presents the morphology and material properties of nanosilica-modified polyether-amine (Jeffamine D 230) cured blend comprising di-glycidyl ether of bisphenol A (DGEBA) and di-glycidyl ether of bisphenol F epoxy (DGEBF) termed DGEBA/F. Polyether-amine cured epoxies are suited to applications that require high toughness and high elongation applications due to their polyether backbone [205, 206]. The system considered currently is a sub-stoichiometric composition of epoxy and hardener. Conversely, Chapter 7 shows the properties for a stoichiometric polyether-amine cured DGEBA.

The unmodified epoxy and two nanosilica-modified epoxies were examined and are summarised in Table 6.1. The volume fraction was calculated from known weight percentages of the system's constituents. The density of the matrix was determined to be 1,100 kg/m<sup>3</sup>.

Table 6.1. Formulations of the unmodified and nanosilica-modified polyether-amine cured DGEBA/F epoxies.

Formulation	Nanosilica content	
	wt. %	vol. %
Unmodified	0	0
10N	10	6.4
20N	20	13.3

The effect of nanosilica content on the glass transition temperature is reported and the effect nanosilica has on the cross-link density of the epoxy was postulated. Atomic force microscopy (AFM) was used to verify the dispersion of the nanosilica particles in the epoxy. Tensile, plane strain compression and fracture tests are reported to show the effect of adding nanosilica, on the toughenability of the epoxy polymer. This system was previously examined by Stewart [207] and Kinloch and Taylor [208] with layered silicates.

## 6.2 Glass transition temperature

The glass transition temperature,  $T_g$ , of the unmodified epoxy and nanosilica-modified formulations was compared using differential scanning calorimetry (DSC). Little variation in  $T_g$  was found, as shown in Table 6.2. A mean value of  $68 \pm 1$  °C was measured, and agrees with tabulated data for polyether-amine cured with a sub-stoichiometric amount of epoxy [172]. The addition of nanosilica has no effect on the  $T_g$  of the system, thus, the cross-link density is reported to remain unchanged. This has been reported previously for nanosilica in epoxies and is widely accepted [7, 52, 65].

Table 6.2. Glass transition temperatures,  $T_g$ , of the unmodified and nanosilica-modified polyether-amine cured DGEBA/F epoxies.

Formulation	$T_g$ (°C)	
	$\bar{x}$	$\pm$
Unmodified	68	1
10N	68	1
20N	69	1

## 6.3 Morphology

Atomic force microscopy (AFM) was conducted on the unmodified and 20N modified polyether-amine DGEBA/F. As shown in Figure 6.1, the planed surface of the unmodified sample was flat and free of any features. This is typical for a homogenous thermoset polymer. Figure 6.2 shows that the nanosilica particles are dispersed in the 20N sample. The cutting direction is shown in the height image in Figure 6.2 (b) and scratch lines parallel to this are eliminated from being features in the epoxy. The area fraction of the nanosilica particles was calculated using the phase image in Figure 6.2(c). For these particles, the area fraction was measured as 13 %, and agrees well with the calculated volume fraction of 13.3 vol. % shown previously in Table 6.2. The inter-particle distance varies from 20 nm for 10N to 12 nm for the 20N. This assumes perfect dispersion and no size variation in the 20 nm diameter nanosilica particles.

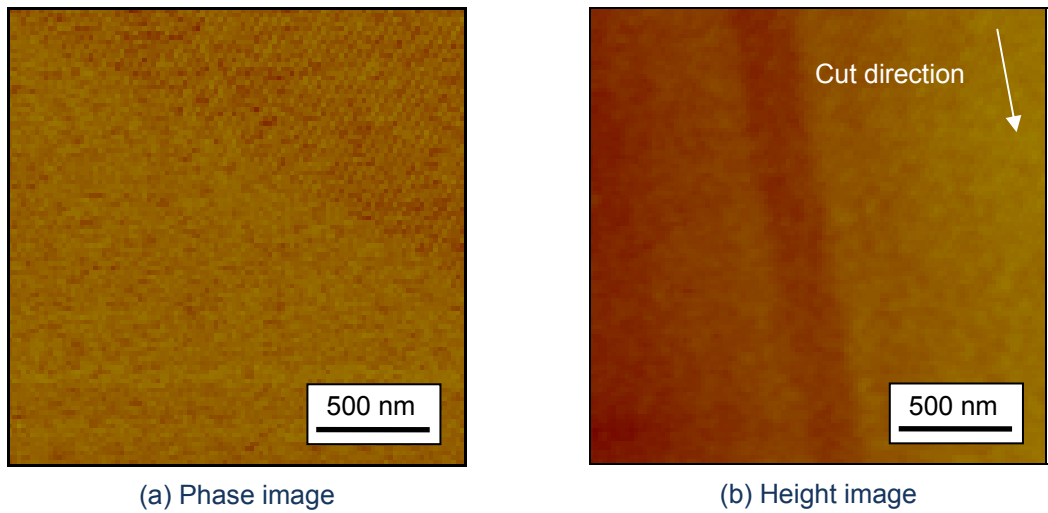


Figure 6.1. Shows (a) phase and (b) height images of the unmodified polyether-amine cured DGEBA/F epoxy. The cut direction is shown in the height image.

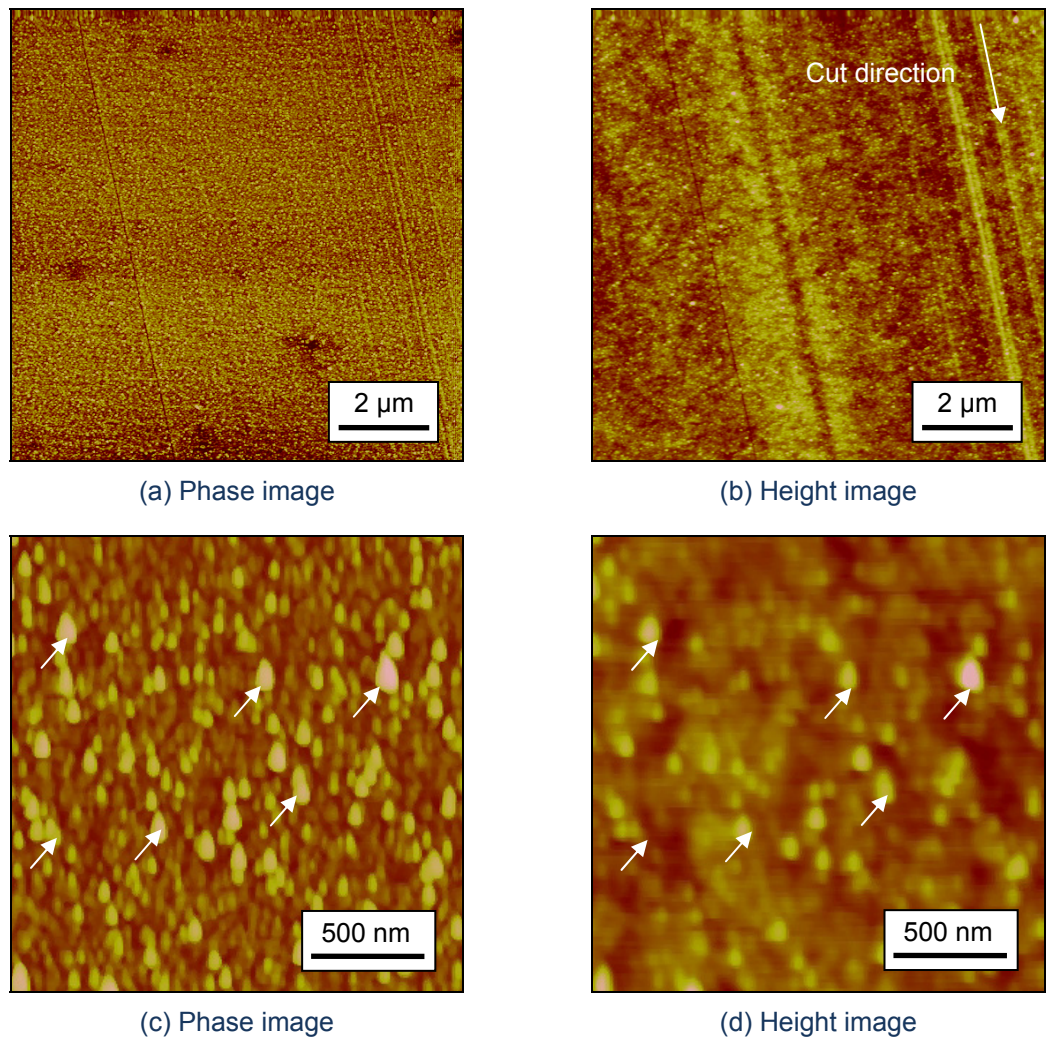


Figure 6.2. Shows (a, c) phase and (b, d) height images of the 20N polyether-amine cured DGEBA/F epoxy. The 20 nm nanosilica particles are indicated with arrows.

## 6.4 Tensile properties

Tensile tests were conducted on unmodified and nanosilica-modified polyether-amine cured DGEBA/F. Summarised in Table 6.3, are the tensile Young's modulus,  $E_t$ , and the tensile true yield strength,  $\sigma_{yt}$ , and the tensile true strain at yield,  $\epsilon_{yt}$ . The value of  $E_t$  was found to increase to a maximum of 3.48 GPa for the 20N formulation. The value of  $\sigma_{yt}$  was found to decrease slightly with the addition of nanosilica. A plot of tensile true stress versus tensile true strain is shown in Figure 6.3. Non-linearity occurred at 0.015 true strain and was independent of nanosilica content. This would suggest that the epoxy polymer yields before any deformation associated with the nanosilica particles occurs. Notably, this system was the only considered system in the present work that showed a reduction in yield strength with increasing nanosilica content. It appears that yield initiated in the polymer, and was promoted by the presence of the nanosilica particles.

Table 6.3. Young's modulus,  $E_t$ , tensile true yield strength,  $\sigma_{yt}$ , and tensile true strain at yield,  $\epsilon_{yt}$ , for the unmodified and nanosilica-modified polyether-amine cured DGEBA/F epoxies.

Formulation	$E_t$ (GPa)		$\sigma_{yt}$ (MPa)		$\epsilon_{yt}$ (true strain)	
	$\bar{x}$	$\pm$	$\bar{x}$	$\pm$	$\bar{x}$	$\pm$
Unmodified	3.16	0.07	82	1	0.03	0.00
10N	3.43	0.10	77	1	0.03	0.00
20N	3.48	0.07	73	7	0.03	0.02

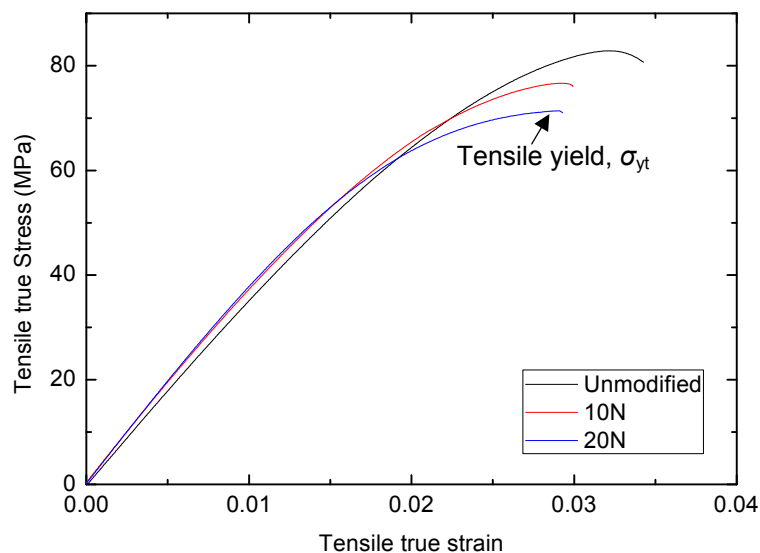


Figure 6.3. Tensile true stress versus tensile true strain for the unmodified and nanosilica-modified polyether-amine cured DGEBA/F epoxies.

## 6.5 Compressive properties

The compressive Young's modulus,  $E_c$ , compressive true yield strength,  $\sigma_{yc}$ , and compressive true yield strain,  $\varepsilon_{yc}$ , were obtained from plane strain compression tests on the unmodified and nanosilica-modified epoxy. With the results summarised in Table 6.4, the value of  $E_c$  was found to increase with nanosilica content, as demonstrated in the true compressive stress versus compressive true strain plot in Figure 6.4. The Young's modulus was measured from compression tests and good agreement with the Young's modulus from tensile tests was found. The magnitude of  $E_c$  ranges from 3.17 GPa for the unmodified epoxy to 3.51 GPa for the 20N formulation. Yield in the epoxy was initiated at 0.07 true strain and was unaffected by the presence of nanosilica in the modified formulations and this was also shown for tensile tests. The value of  $\sigma_{yc}$ , decreases with the addition of nanosilica. This would suggest that the particle-matrix interface is weak, or that nanosilica promotes shear band yielding in the epoxy. Shear band yielding, or strain softening initiated at  $\sigma_{yc}$  and continued until 0.375 true strain in the unmodified formulation. Strain softening was also observed in the nanosilica-modified epoxies. With continued loading, the epoxies were found to work-harden, and this was more pronounced at higher nanosilica contents.

The unmodified epoxy was compressed to failure and a compressive true fracture strain of  $1.06 \pm 0.02$  was obtained. The value is quoted as the von Mises equivalent strain so can be greater than 1 [185, 186].

Table 6.4. Compressive Young's modulus,  $E_c$ , compressive true yield strength,  $\sigma_{yc}$ , and compressive true yield strain,  $\varepsilon_{yc}$ , for the unmodified and nanosilica-modified polyether-amine cured DGEBA/F epoxies.

Formulation	$E_c$ (GPa)		$\sigma_{yc}$ (MPa)		$\varepsilon_{yc}$ (true strain)	
	$\bar{x}$	$\pm$	$\bar{x}$	$\pm$	$\bar{x}$	$\pm$
Unmodified	3.17	0.15	101	0	0.07	0.00
10N	3.40	0.04	96	1	0.08	0.00
20N	3.51	0.16	94	0	0.08	0.00

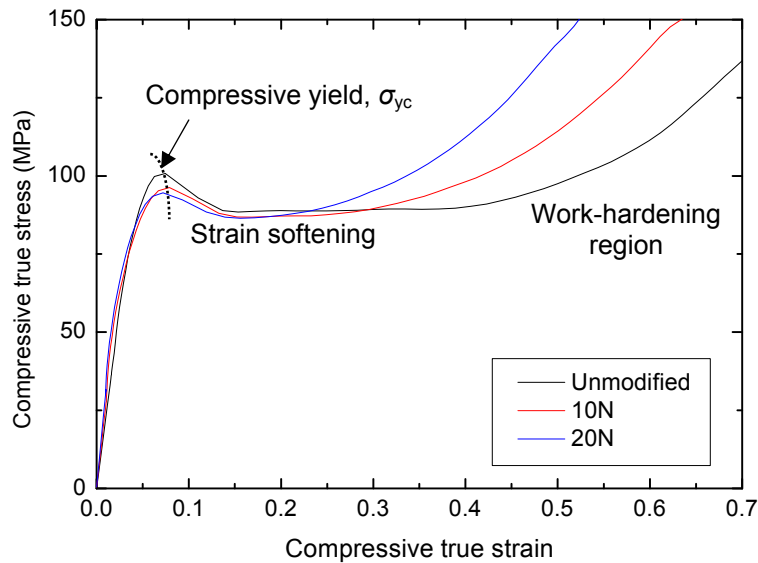


Figure 6.4. Compressive true stress versus compressive true strain for the unmodified and nanosilica-modified polyether-amine cured DGEBA/F epoxies.

A sample of the unmodified epoxy was compressed to 0.375 true strain (within the strain softened region) and was sectioned to find evidence of shear band yielding during strain softening. Shown optically using cross-polarised light microscopy in Figure 6.5, shear band yielding was found to occur in the gauge area of the epoxy. In the image, 0.5 mm wide bands of highly focused shear strain were observed. Bowden [12] showed that strain inhomogeneities can form if the negative slope of the true stress-true strain curve after  $\sigma_{yc}$  is large. From Figure 6.4 shown previously, it is clear that strain softening occurs in all of the formulations, hence the nanosilica-modified formulations are expected to also shear band.

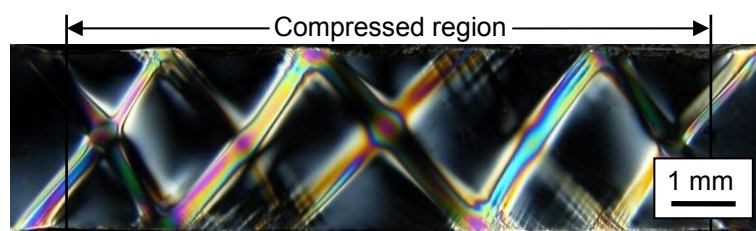


Figure 6.5. Optical section of the unmodified polyether-amine cured DGEBA/F shows extensive shear banding in the compressed region when viewed using cross-polarised light microscopy.

## 6.6 Fracture properties

Single edge notched bend (SENB) tests were conducted on the unmodified and nanosilica-modified polyether-amine cured DGEBA/F. The fracture properties summarised in Table 8.5 show that the fracture toughness,  $K_C$ , and the fracture energy,  $G_C$ , increase with nanosilica content. A 123 % improvement in  $K_C$  was found with the

addition of 20 wt. % nanosilica, as shown in Figure 6.6(a). Similarly, a 185 % improvement in  $G_C$  was found with the addition of 20 wt. % nanosilica, with the trend of  $G_C$  versus nanosilica content, see Figure 6.6(b). The improvements in fracture properties are notably higher in this system, than those observed for other nanosilica-modified systems that are also shown in this study.

Table 6.5. Fracture toughness,  $K_{IC}$ , and fracture energy,  $G_C$ , from SENB tests for unmodified and nanosilica-modified polyether-amine cured DGEBA/F.

Formulation	$K_{IC}$ (MPa $\sqrt{m}$ )		$G_C$ (J/m $^2$ )	
	$\bar{x}$	$\pm$	$\bar{x}$	$\pm$
Unmodified	0.78	0.07	184	23
10N	1.40	0.06	444	37
20N	1.76	0.16	702	125

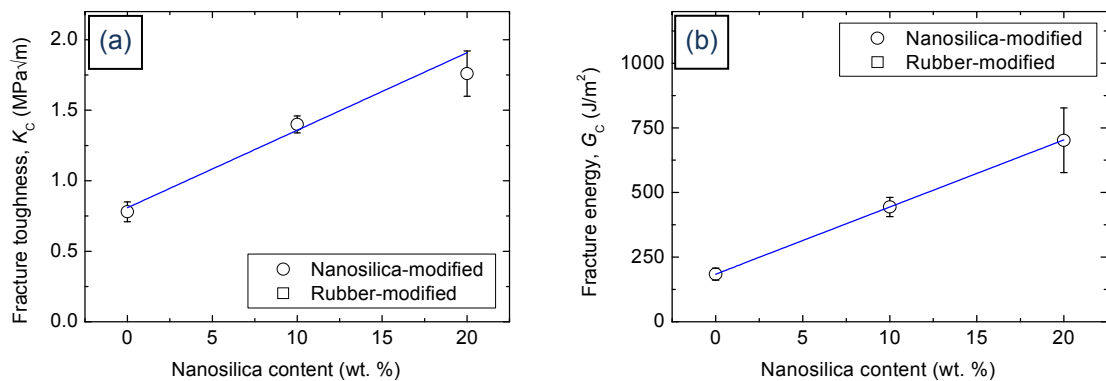


Figure 6.6. The (a) fracture toughness,  $K_{IC}$ , and (b) fracture energy,  $G_C$ , versus nanosilica content for the unmodified and nanosilica-modified polyether-amine cured DGEBA/F epoxies. A linear fit shows the general trend.

### 6.6.1 Toughening mechanisms

Irwin's prediction in plane strain conditions [193] was used to calculate the plastic zone radius,  $r_{pz}$ . The value of  $r_{pz}$  ranges from 8  $\mu\text{m}$  for the unmodified epoxy up to 31  $\mu\text{m}$  for 20N. Field emission gun scanning electron microscopy (FEGSEM) was conducted of the fracture surface, in the process zone region of 20N to find evidence of toughening. Nanosilica particles were seen on the fracture surface shown with the high magnification micrograph in Figure 6.7. Many particles were observed on the surface, and some are identified with arrows. The mean diameter of these particles was found to be 35 nm and shows excellent consistency considering that a 5 nm layer of chromium was used. Larger particles would be expected to debond more readily because the debonding stress at the interface is proportional to  $r_p^{-1/2}$  [34, 47, 49].

Faber and Evans [73, 203] have shown that for crack deflection to occur, a size parity between the nanosilica particles and the crack opening displacement is also required. For the 20N formulation, the crack opening displacement can be calculated as 10  $\mu\text{m}$  [71]. No evidence of pinning or crack deflection was found at lower magnification on the fracture surface and is supported by previous studies [7, 52]. Importantly, debonding and subsequent plastic void growth was found to be present and is shown circled in Figure 6.7.

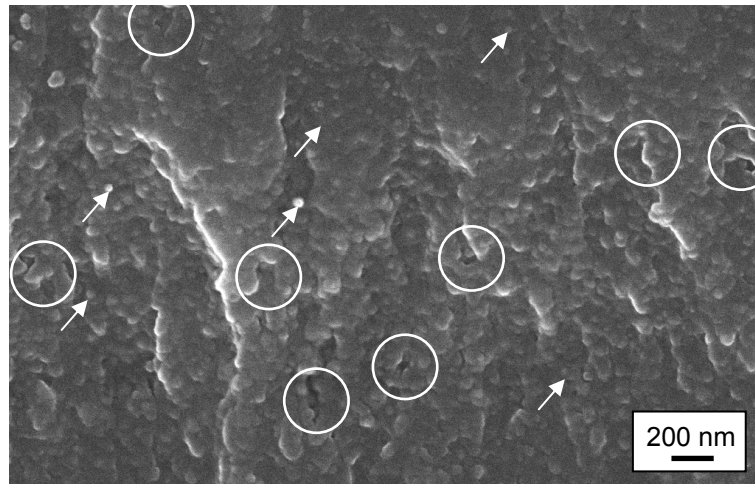


Figure 6.7. A FEGSEM image of the fracture surface for the 20N amine cured polyether-amine cured DGEBA/F epoxy. The nanosilica particles are identified with arrows and evidence of plastic void growth around debonded particles is shown circled.

## 6.7 Chapter summary

Bulk properties for polyether-amine cured DGEBA/F epoxy modified with nanosilica were examined. The  $T_g$  was found to be constant at 69 °C up to 20 wt. % addition of nanosilica. Thus, the cross-link density was reported to remain unchanged when nanosilica was added to this epoxy. The 20 nm particles were found to remain well dispersed when studied up to 20 wt. % nanosilica.

As the nanosilica content was increased, the value of  $E_t$  increased from 3.16 to 3.48 GPa and  $E_c$ , from 3.17 GPa to 3.51 GPa with the addition of 20 wt. % nanosilica. The magnitude of  $\sigma_{yt}$  was found to decrease with increasing nanosilica content from 82 MPa to 73 MPa and similar observations were obtained for values of  $\sigma_{yc}$  (101 MPa to 94 MPa). This would suggest that either the particles may be poorly bonded or that an interphase may be forming around the nanosilica particles.

## Polyether-amine Cured DGEBA Epoxy Properties

### 7.1 Introduction

This chapter presents the morphology and material properties of nanosilica-modified polyether-amine (Jeffamine D 230) cured di-glycidyl ether of bisphenol A (DGEBA) epoxy. Polyether-amine cured epoxies have a history of application as low cost matrices for fibre reinforced composites. They are suited to high toughness and high elongation applications due to their polyether backbone, which allows good chain mobility [205, 206]. Improvement of bulk toughness and interfacial properties with continuous fibre reinforcement is sought. Importantly, the system considered in this chapter is a stoichiometric composition of epoxy and hardener. Chapter 6 has shown properties for a sub-stoichiometric DGEBA/F blend cured with the same polyether-amine. This system was examined with nanosilica modification by Ma et al. [65].

Formulations with different amounts of nanosilica were considered, and are summarised in Table 7.1. The volume fraction was calculated from known weight percentages of the system's constituents. The density of the matrix was measured to be 1,150 kg/m<sup>3</sup>.

Table 7.1. Formulations of the unmodified and nanosilica-modified polyether-amine cured DGEBA epoxies.

Formulation	Nanosilica content	
	wt. %	vol. %
Unmodified	0	0
10N	10	6.6
20N	20	13.8

The effect of nanosilica content on the glass transition temperature and thus, any change in cross-link density is reported. The dispersion of nanosilica in the epoxy was examined at different nanosilica contents. Tensile, plane strain compression and fracture tests are reported to show the effect of adding nanosilica, on the toughenability of the epoxy polymer.

## 7.2 Glass transition temperature

The glass transition temperature,  $T_g$ , of the unmodified epoxy and nanosilica-modified formulations was measured using differential scanning calorimetry (DSC). Table 9.2 shows that there was little variation in  $T_g$ , with a mean value of  $88 \pm 1$  °C. This matches tabulated data from Burton et al. [172] for polyether-amine cured DGEBA epoxies. The addition of nanosilica has no effect on the overall  $T_g$  of the system, and thus the cross-link density is expected to remain unchanged. This was also observed for other nanosilica-modified epoxies that were studied in this work and has been reported previously [7, 52, 65].

Table 7.2. Glass transition temperatures,  $T_g$ , of the unmodified and nanosilica-modified polyether-amine cured DGEBA epoxies.

Formulation	$T_g$ (°C)	
	$\bar{x}$	$\pm$
Unmodified	89	0
10N	89	1
20N	87	3

## 7.3 Morphology

Atomic force microscopy (AFM) was conducted on the unmodified epoxy polymer. Figure 7.1 shows that the planed surface of the sample was flat and devoid of any features, as would be typical for a homogenous thermoset polymer. Some scratches were seen on the height image in Figure 7.1(b) from sample preparation.

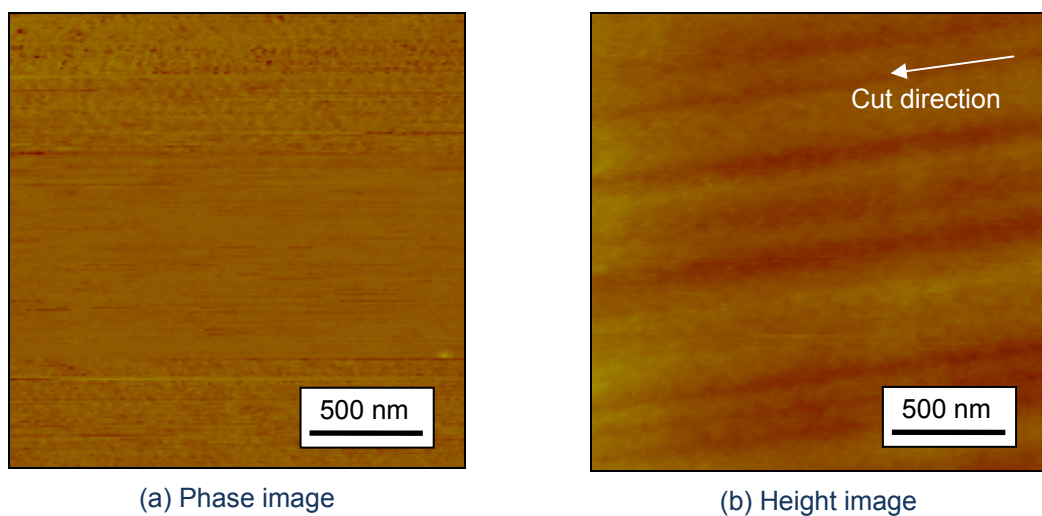


Figure 7.1. Shows (a) phase and (b) height images of the unmodified polyether-amine cured DGEBA. The cut direction is shown in the height image.

Figure 7.2 shows that nanosilica particles are well dispersed in the 10N epoxies. The cut direction is shown in the height image in Figure 7.2(b) and can be used to eliminate scratch lines parallel to this, from being morphological features in the epoxy. The bright, well defined nano-particles that are shown with white arrows in Figure 7.2(c, d) are on the surface of the epoxy. The area fraction of these particles was measured to be 6.6 % using the high magnification images in Figure 7.2(c, d). This agrees very well with the calculated volume fraction of 6.5 % shown previously in Table 7.1. The less defined particles are sub-surface nanosilica particles that have been recognised in the AFM scan because they are much stiffer than the epoxy (identified with blue arrows). The inter-particle distance,  $D_{IP}$ , was calculated as 20 nm using Equation (4.1).

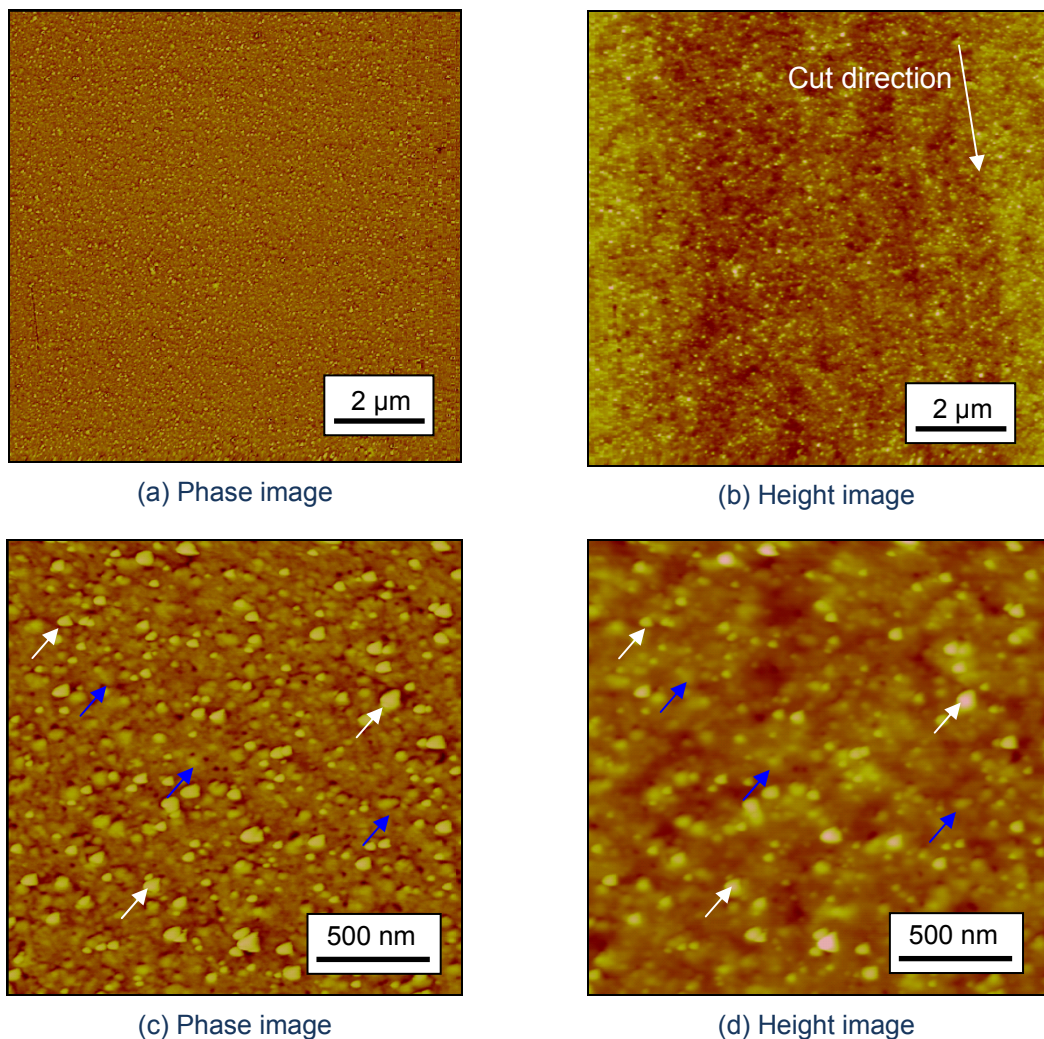


Figure 7.2. Shows (a, c) phase and (b, d) height images of the 10N polyether-amine cured DGEBA epoxy. The white arrows identify the nanosilica on the surface and the blue arrows indicate sub-surface particles.

To verify good particle dispersion at higher contents, AFM was conducted on the epoxy with 20 wt. % nanosilica, shown in Figure 7.3. The 20 nm particles remain dispersed at

this content, and this can be confirmed by reference to the high magnification micrographs in Figure 7.3(c, d). The area fraction was measured as 14.1 % and compares well to the calculated volume fraction (13.8 % from Table 7.1). The value of  $D_{IP}$  was calculated to be 11 nm.

Ma et al. [65] examined this nanosilica dispersion in this system with transmission electron microscopy (TEM) and reported good dispersion of nanosilica particles in the epoxy.

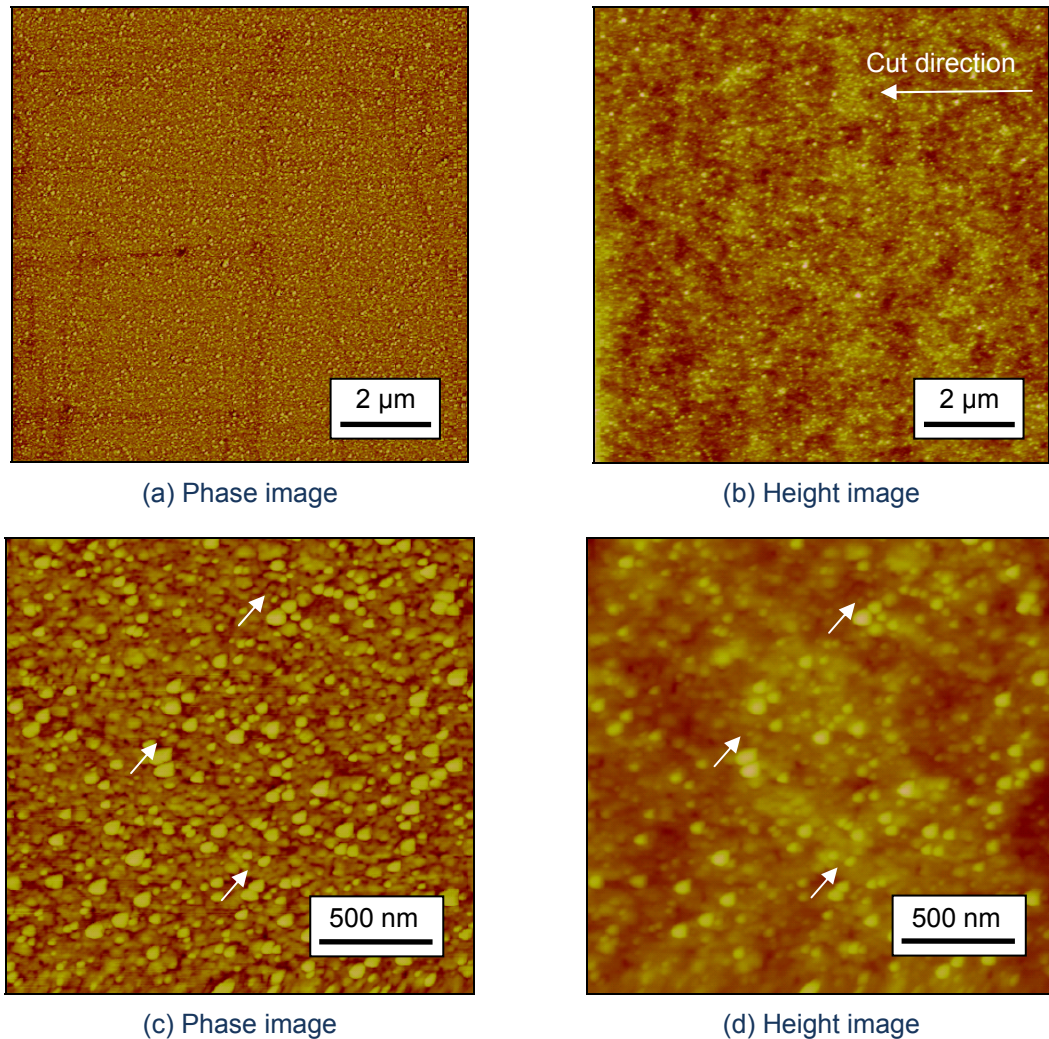


Figure 7.3. Shows (a, c) phase and (b, d) height images of polyether-amine cured DGEBA with 20N. The nanosilica remains dispersed; some of the 20 nm particles are indicated with arrows.

## 7.4 Tensile properties

The tensile Young's modulus,  $E_t$ , tensile true yield strength,  $\sigma_{yt}$ , and tensile true yield strain,  $\epsilon_y$ , are reported for bulk epoxies in Table 7.3. The value of  $\sigma_{yt}$  for the unmodified system was 67 MPa at 0.05 true strain. The plot of tensile true stress versus tensile

true strain in Figure 7.4 shows the effect of nanosilica content on the tensile behaviour of the epoxy polymer. The value of  $E_t$  increases from 2.94 GPa to 3.44 GPa with the addition of 20 wt. % nanosilica. The transition to non-linear behaviour occurred at about 0.014 true strain for both the unmodified and nanosilica-modified systems. Thus, the addition of nanosilica seems to have no effect on the initiation of yield in the epoxy polymer. Thus, it was surmised that plastic deformation initiated before debonding of the nanosilica particles had occurred in this epoxy. The mean value of  $\sigma_{yt}$  increased with the addition of 10 wt. % nanosilica, little increase in the mean was observed with further addition of nanosilica in the 20N epoxy. The true strain and yield strength decreased with increase in nanosilica content. Vollenberg and Heikens showed that intrinsic yield processes dominate the material and hinder global diffuse yield, thus exhibiting lower true strain at yield and failure [26] and could explain the observations in this epoxy.

Table 7.3. Young's modulus,  $E_t$ , tensile true yield strength,  $\sigma_{yt}$ , and tensile true yield strain,  $\epsilon_y$ , for the unmodified and nanosilica-modified polyether-amine cured DGEBA epoxies.

Formulation	$E_t$ (GPa)		$\sigma_{yt}$ (MPa)		$\epsilon_y$ (true strain)	
	$\bar{x}$	$\pm$	$\bar{x}$	$\pm$	$\bar{x}$	$\pm$
Unmodified	2.94	0.11	67	3	0.05	0.00
10N	3.24	0.12	70	1	0.05	0.00
20N	3.44	0.36	72	1	0.04	0.01

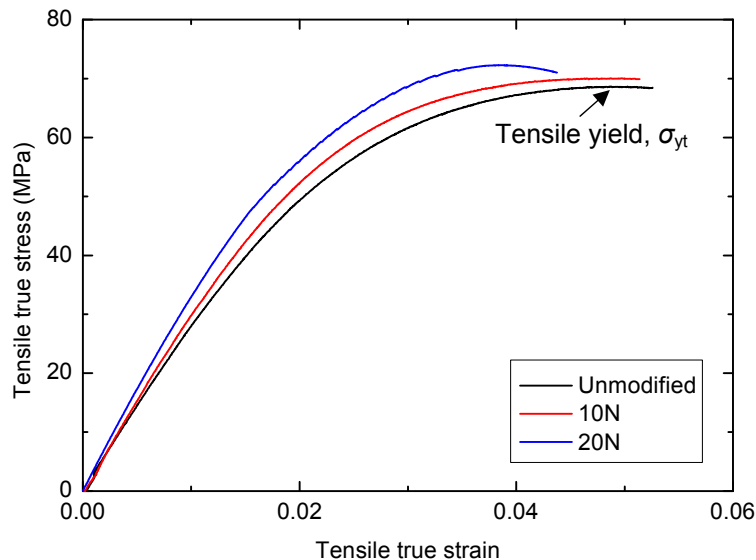


Figure 7.4. Tensile true stress versus tensile true strain for the unmodified and nanosilica-modified polyether-amine cured DGEBA epoxies.

## 7.5 Compressive properties

The compressive Young's modulus,  $E_c$ , compressive true yield strength,  $\sigma_{yc}$ , and compressive true yield strain,  $\epsilon_{yc}$ , from plane strain compression tests are summarised in Table 7.4. The value of  $E_c$  increases with the addition of nanosilica, as demonstrated in the true compressive true stress versus compressive true strain plot in Figure 7.5. Good agreement was found between the values of  $E_t$  and  $E_c$ , with  $E_c$  values in the range 2.80-3.86 GPa for the unmodified-20N epoxies. The value of  $\sigma_{yc}$ , of the 10N formulation increases by 9 % when compared to the unmodified epoxy. Further addition of nanosilica in the 20N epoxy resulted in a 13 % improvement. With further applied displacement, strain softening initiated at  $\sigma_{yc}$  and continued until 0.2 true strain for the unmodified formulation. Strain softening decreased in prevalence with the addition of nanosilica to the epoxy. A sharp drop in the true stress at  $\sigma_{yc}$  was still observable when nanosilica was added to the epoxy. With continued loading, the epoxies were found to work-harden. The effect of work-hardening increased with nanosilica content.

The unmodified epoxy was loaded to failure and a compressive true fracture strain of  $0.91 \pm 0.01$  was obtained.

Table 7.4. Compressive Young's modulus,  $E_c$ , compressive true yield strength,  $\sigma_{yc}$ , and compressive true yield strain,  $\epsilon_{yc}$ , for the unmodified and nanosilica-modified polyether-amine cured DGEBA epoxies.

Formulation	$E_c$ (GPa)		$\sigma_{yc}$ (MPa)		$\epsilon_{yc}$ (true strain)	
	$\bar{x}$	$\pm$	$\bar{x}$	$\pm$	$\bar{x}$	$\pm$
Unmodified	2.80	0.23	96	1	0.09	0.00
10N	3.10	0.37	105	2	0.08	0.00
20N	3.86	0.33	108	1	0.07	0.01

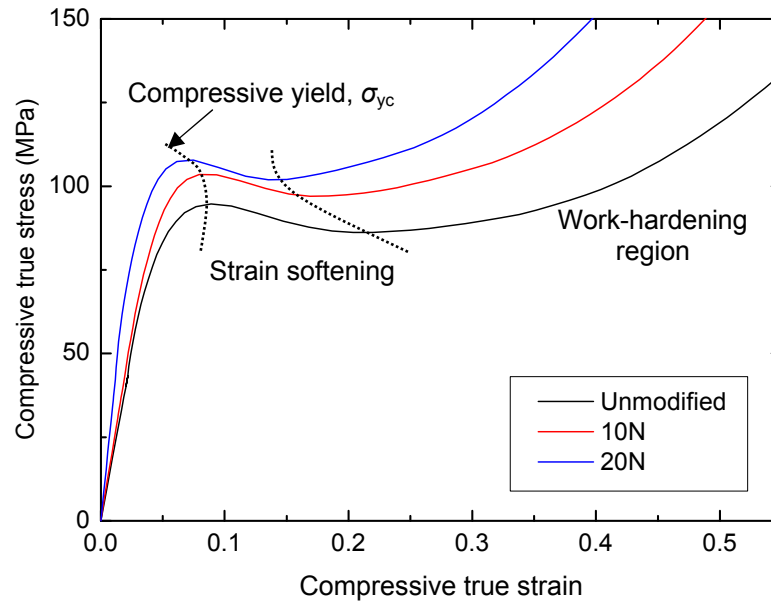


Figure 7.5. Compressive true stress versus compressive true strain for unmodified and nanosilica-modified polyether-amine cured DGEBA epoxies.

A sample of the unmodified epoxy was compressed to the strain softened region (0.21 true strain) and was sectioned to find evidence of shear banding. This is shown optically using cross-polarised light microscopy in Figure 7.6. Extensive shear yielding occurred in the compressed region, and was focused into 0.5 mm wide bands. Bowden [12] showed that strain inhomogeneities tend to form if the negative slope of the true stress-true strain curve after  $\sigma_{yc}$  is large. From the true stress-true strain graph shown previously in Figure 7.5, it is evident that this strain softening occurs to the same extent for all of the formulations since the gradient of the slope remains unchanged. Hence, the nanosilica-modified formulations would be expected to also shear band accordingly.

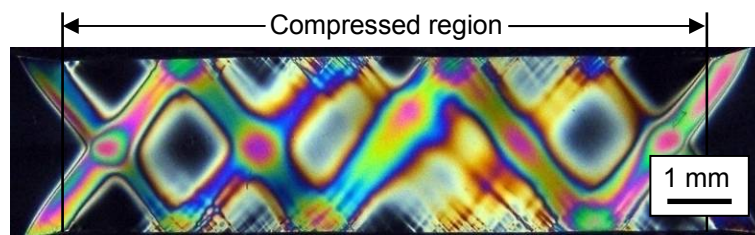


Figure 7.6. Optical section of the unmodified polyether-amine cured DGEBA shows extensive shear banding in the gauge area when viewed with cross-polarised light.

## 7.6 Fracture properties

Single edge notched bend (SENB) tests were conducted on the unmodified and nanosilica-modified polyether-amine cured DGEBA. The results summarised in Table 8.5 show that there is an increase in the fracture toughness,  $K_{IC}$ , (Figure 7.7(a)) and the

fracture energy,  $G_C$ , (Figure 7.7(b)) when nanosilica was added to the epoxy. Brittle fracture occurred at failure, with  $P_{max}/P_Q$  recorded at unity. A 201 % increase was observed in  $G_C$  for epoxy with 10N and a 278 % increase in the value of  $G_C$  for the 20N. Excellent agreement was obtained both with Kim et al.'s [209] unmodified epoxy and Ma et al.'s [65] nanosilica modified epoxies, with both studies having been conducted on this epoxy system.

Table 7.5. Fracture toughness,  $K_C$ , and fracture energy,  $G_C$ , for the unmodified and nanosilica-modified polyether-amine cured DGEBA epoxies.

Formulation	$K_C$ (MPa $\sqrt{m}$ )		$G_C$ (J/m $^2$ )	
	$\bar{x}$	$\pm$	$\bar{x}$	$\pm$
Unmodified	0.73	0.13	163	55
10N	1.38	0.06	490	72
20N	1.45	0.12	616	109

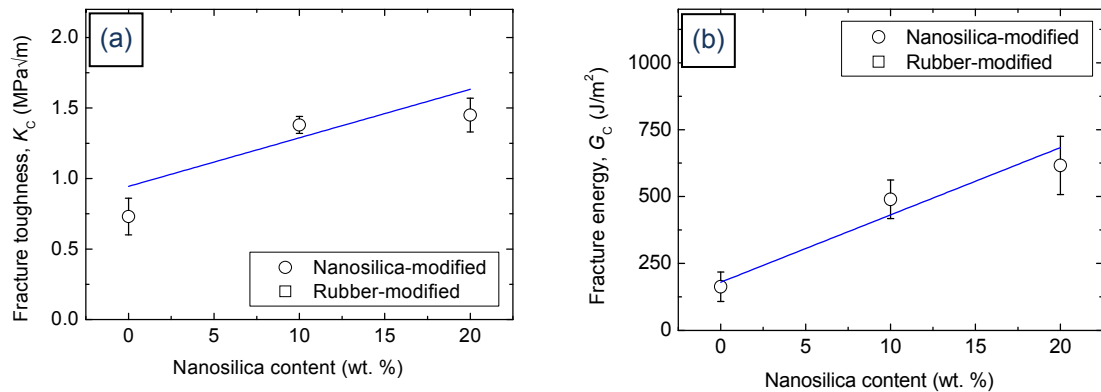


Figure 7.7. The (a) fracture toughness,  $K_C$ , and (b) fracture energy,  $G_C$ , versus nanosilica content for the unmodified and nanosilica-modified polyether-amine cured DGEBA epoxies. A linear fit shows the general trend.

### 7.6.1 Toughening mechanisms

The plastic zone radius,  $r_{pz}$ , was calculated using Irwin's model under plane strain conditions [193] (see Equation (4.12)). The value of  $r_{pz}$  was found to be between 6.5  $\mu\text{m}$  for the unmodified epoxy up to 25  $\mu\text{m}$  for the 20N formulation. Double-notch 4-point bend (DN4PB) tests were used to generate a plastic zone in the 20N specimens. A polished 100  $\mu\text{m}$  section from the mid-plane was examined using cross-polarised light microscopy and is shown in Figure 7.8. The observed plastic zone was half the size of the calculated value of  $r_{pz}$ . This would suggest that the plastic zone was not fully developed in this specimen. This is due to the method being very sensitive to small differences between the two crack-tips. Nevertheless, good evidence is presented to show that shear banding occurs in fracture specimens.

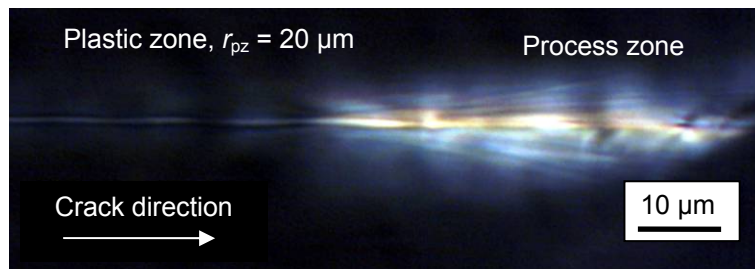


Figure 7.8. Shear bands in the process zone region of the 20N polyether-amine cured DGEBA epoxy.

When Kim et al. [209] examined this system with carbon nanotube reinforcement, they conducted scanning electron microscopy (SEM) on the fracture surface of the unmodified epoxy. It was found to be flat and smooth, with occasional striation marks; very typical for the unmodified epoxy. Hence, SEM was not conducted on the fracture surface for the unmodified polyether-amine cured DGEBA epoxy.

Field emission gun scanning electron microscopy (FEGSEM) was conducted on fractured 20N SENB specimens to find evidence of toughening. Care was taken to image very close to the tapered crack-tip of the fractured specimen in order to remain within the process zone of the epoxy. This is shown by the low magnification micrograph in Figure 7.9 for the 20N sample. Striation marks can be seen in the fast fracture regions of the surface. The process zone was also identified, with evidence of toughening by nature of a rougher surface appearance, indicative of plastic deformation having occurred. This is less apparent in the hackle regions because crack growth occurs quickly. At higher magnifications, the individual nanosilica particles could be identified. Most of the particles are larger than expected, at 40-50 nm in size. Many researchers [34, 47, 49] support that the debonding stress at the interface is proportional to  $r_p^{-1/2}$  and so one would expect the larger particles to debond more readily and could explain why the debonded nanosilica particles on the fracture surface seem larger.

Crack deflection and crack pinning do not contribute to toughening because the particle size is many orders of magnitude smaller than the crack opening displacement [7, 52]. Indeed, no evidence of pinning or crack deflection was observed on the fracture surface in Figure 7.10. Ma et al. [65] proposed a new toughening mechanism of dilation in the epoxy as a result of overlapping stress fields created by the nanosilica particles in this system. There was no evidence to support this by way of voids in the epoxy polymer, away from the nanosilica particles. Very little evidence of particle debonding having occurred, was observed. No plastic void growth was observed, surrounding the debonded nanosilica particles. The particles have remained well bonded and the

dominant mechanism of energy absorption for this system appears to be shear band yielding.

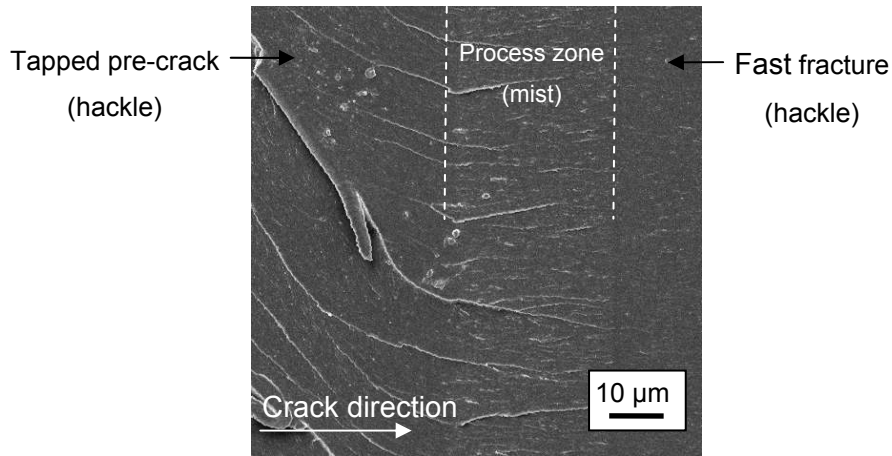


Figure 7.9. A FEGSEM micrograph of the process zone region of a 20N polyether-amine cured DGEBA sample. The hackle and mist regions are identified at low magnification.

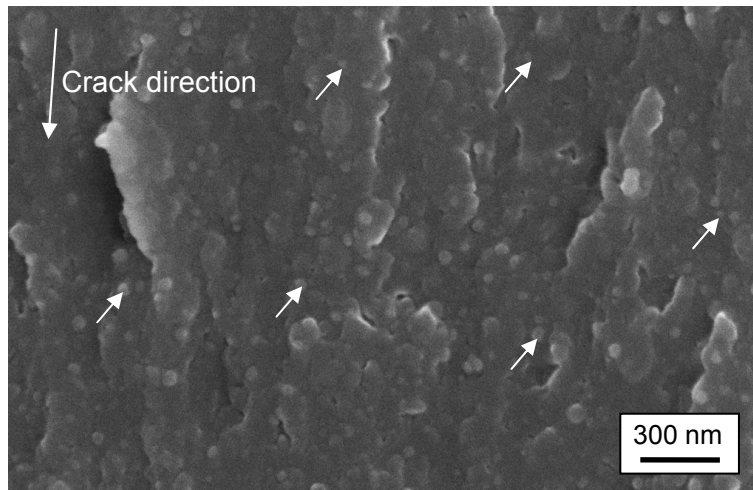


Figure 7.10. A FEGSEM micrograph from the fracture surface of the 20N polyether-amine cured DGEBA. Some debonded nanosilica particles are identified with arrows.

## 7.7 Chapter summary

The bulk properties of a polyether-amine cured DGEBA epoxy, modified with nanosilica particles was examined. The  $T_g$  was found to remain constant at 88 °C for nanosilica modifications up to 20 wt. %, and thus, the cross-link density is expected to remain unchanged when nanosilica is added to this epoxy. The 20 nm particles remain well dispersed at high nanosilica content, and have been studied to do so up to 20 wt. % using AFM.

As the nanosilica content was increased, the value  $E_t$  of the epoxy increases from 2.45 GPa to 3.4 GPa. Small increases in the value of  $\sigma_{yt}$  were observed with a maximum

value of 72 MPa. The increase in extrinsic yield strength would suggest good particle-matrix adhesion. It was postulated that less diffuse yielding occurs and localised shear banding is dominant during yield in the nanosilica-modified epoxies. This was shown to be the case for chalk filled polypropylenes by Vollenberg and Heikens [26]. As a result, lower true strains at yield were observed with increasing nanosilica content.

The values of  $K_C$  and  $G_C$  increase with addition of nanosilica and  $G_C = 616 \text{ J/m}^2$  for the 20N epoxy. Sub-critically loaded crack-tips were used to show that shear banding occurs during the formation of a process zone, prior to fracture. The FEGSEM micrographs from the fracture surface show no real evidence of void growth occurring around the particles. Therefore, it is expected that toughening is achieved by a shear yielding process rather than debonding and plastic void growth mechanisms.

## Amine Cured Multifunctional Epoxy Properties

### 8.1 Introduction

This chapter presents the morphology and material properties of an amine cured multifunctional epoxy. This system comprises of a di-glycidyl ether of bisphenol F (DGEBF) and tri-glycidyl amino-phenol (TGAP) epoxy blend cured with 4,4-methylenebis 3-chloro 2,6-diethylaniline (M-CDEA). Bulk properties were considered for this epoxy modified with different nanosilica contents as summarised in Table 8.1. The volume fraction was calculated from the densities and known weight percentages of the formulation's constituents. The density of the matrix was measured as 1,200 kg/m<sup>3</sup>.

Table 8.1. Formulations of unmodified and nanosilica-modified amine cured multifunctional epoxies.

Formulation	Nanosilica content	
	wt. %	vol. %
Unmodified	0	0.0
5N	5	3.4
10N	10	6.9
15N	15	10.5
20N	20	14.3

Previous work was conducted with this amine-epoxy system by Brooker [79], and is referred to in this chapter. The effect of nanosilica content on the glass transition temperature is reported. Atomic force microscopy (AFM) was used to characterise the morphology, and verify the dispersion of nanosilica in the epoxy. Mechanical properties are examined using tensile, plane strain compression and fracture tests. These are used to make inferences about the interfacial properties between the nanosilica and epoxy, and their effect on the overall toughenability of the epoxy polymer.

### 8.2 Glass transition temperature

The glass transition temperature,  $T_g$ , for the unmodified and nanosilica-modified epoxies was measured using differential scanning calorimetry (DSC). Table 8.2 shows

that the  $T_g$  remains unchanged when nanosilica is added to the epoxy. The mean  $T_g$  was found to be 178 °C. It was concluded that the addition of nanosilica does not affect the cross-link density of this epoxy. Brooker [79] used dynamic mechanical analysis (DMA) and found the mean  $T_g$  to be 194 °C at 1 Hz. The discrepancy in  $T_g$  was attributed to DMA requiring larger specimens and a slower test rate, which results in a lagged response during the temperature sweep [210].

Table 8.2. Glass transition temperatures,  $T_g$ , of the unmodified and nanosilica-modified amine cured multifunctional epoxies.

Formulation	$T_g$ (°C)	
	$\bar{x}$	$\pm$
Unmodified	177	1
2N	178	4
5N	178	3
10N	179	2
20N	178	0

### 8.3 Morphology

The morphology of the unmodified epoxy was examined by [79] and is shown in Figure 8.1. The planed surface was featureless and flat and this was typical of a homogenous thermoset polymer. The cut direction is shown in the height image in Figure 8.1(b) and eliminates scratch marks parallel to the cut direction from being features in the epoxy.

The 15 wt. % nanosilica-modified epoxy was also examined. The nanosilica was supplied by Nanoresins, Germany as a pre-dispersed blend in DGEBF [211]. It was previously thought that the addition of TGAP would cease stable suspension of the nanosilica. Brooker [79], showed that the addition of TGAP did not affect the dispersion, shown in Figure 8.2. The volume fraction was measured from the AFM images to be 10.5 vol. % and agreed with the calculated volume fraction in Table 8.1. The individually dispersed 20 nm particles are shown with arrows in Figure 8.2(c, d). The inter-particle distance was calculated to be of the range 48-11 nm for 2 wt. %-20 wt. % nanosilica-modified epoxies.

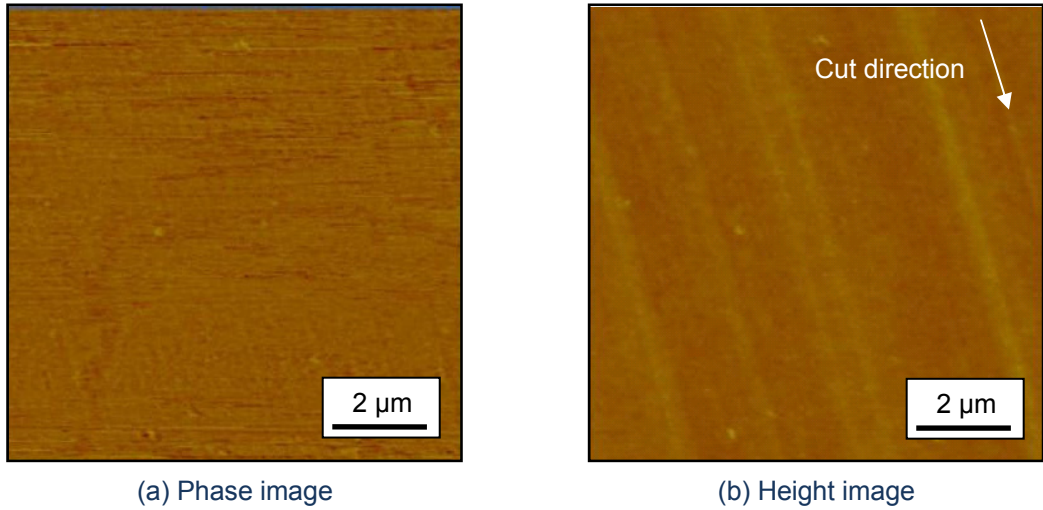


Figure 8.1. Shows (a) phase and (b) height images of the unmodified amine cured multifunctional epoxy [79]. The cut direction is shown in the height image.

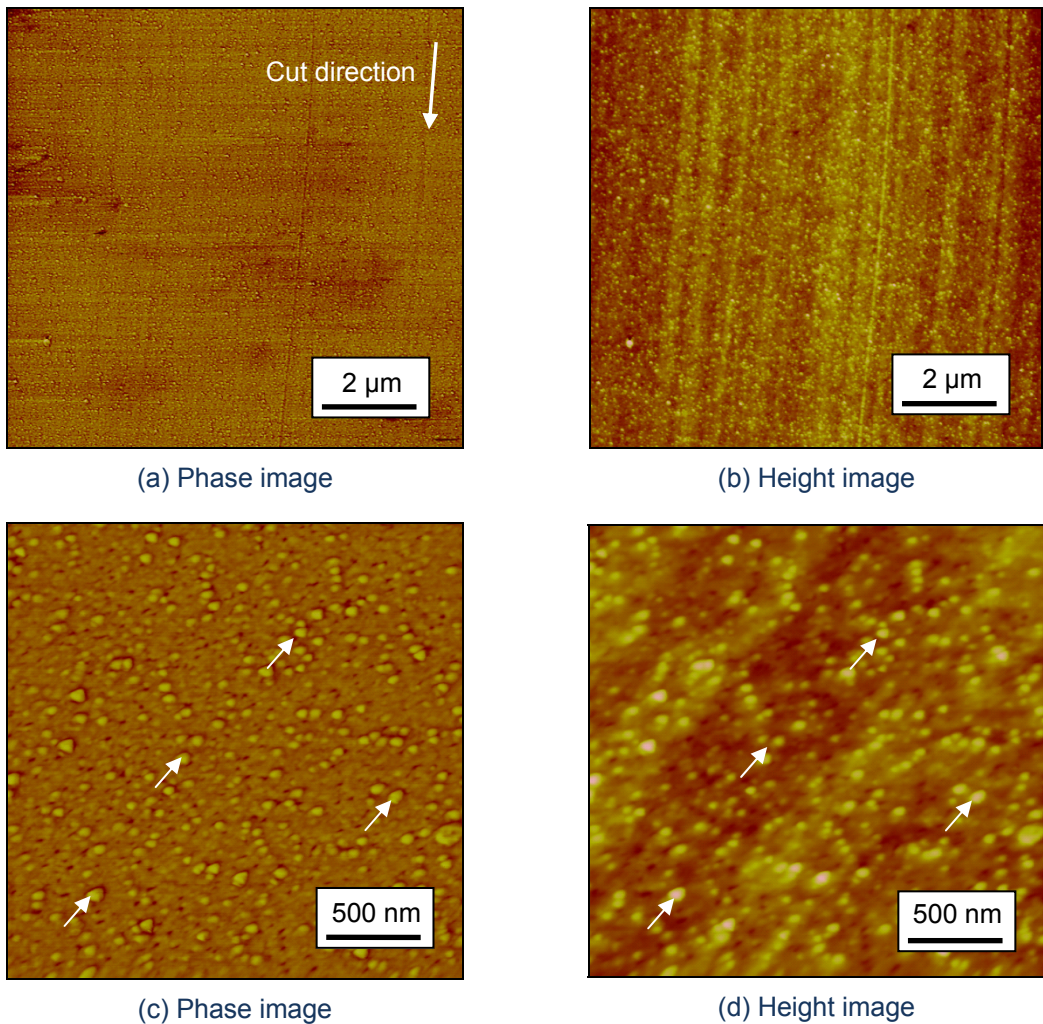


Figure 8.2. Shows (a, c) phase and (b, d) height images of the 15N amine cured multifunctional epoxy [211]. The dispersed 20 nm nanosilica particles are indicated with arrows.

## 8.4 Tensile properties

Tensile tests on bulk polymer samples were reported by Brooker [79]. The tensile Young's modulus,  $E_t$ , ultimate tensile true strength,  $\sigma_{UTS}$ , and ultimate tensile true strain,  $\epsilon_{UTS}$ , for incremental nanosilica contents is shown in Table 8.3. A Plot of tensile true stress versus tensile true strain for the unmodified and 20N samples is shown in Figure 8.3. For the formulations considered, none achieved maximum yield strength, therefore the  $\sigma_{UTS}$  was quoted. For the unmodified epoxy, a transition to non-linear behaviour occurred at 0.015 true strain. The value of  $E_t$  for the unmodified epoxy is 2.55 GPa and failure occurred at 65 MPa and 0.035 true strain. The value of  $E_t$  increased steadily with nanosilica content to a maximum of 3.87 GPa with 20 wt. % nanosilica. With a mean value of 63 MPa, no change in the UTS was reported for the formulations.

Table 8.3. Young's modulus,  $E_t$ , ultimate tensile true strength,  $\sigma_{UTS}$ , and ultimate tensile true strain,  $\epsilon_{UTS}$ , for the unmodified and nanosilica-modified amine cured multifunctional epoxies [79].

Formulation	$E_t$ (GPa)		$\sigma_{UTS}$ (MPa)		$\epsilon_{UTS}$ (true strain)	
	$\bar{x}$	$\pm$	$\bar{x}$	$\pm$	$\bar{x}$	$\pm$
Unmodified	2.55	0.07	65	2	0.04	0.01
2N	3.01	0.03	59	8	0.03	0.01
5N	2.91	0.11	70	1	0.04	0.01
10N	3.34	0.19	63	6	0.02	0.00
15N	3.44	0.34	65	5	0.03	0.00
20N	3.87	0.09	59	3	0.03	0.00

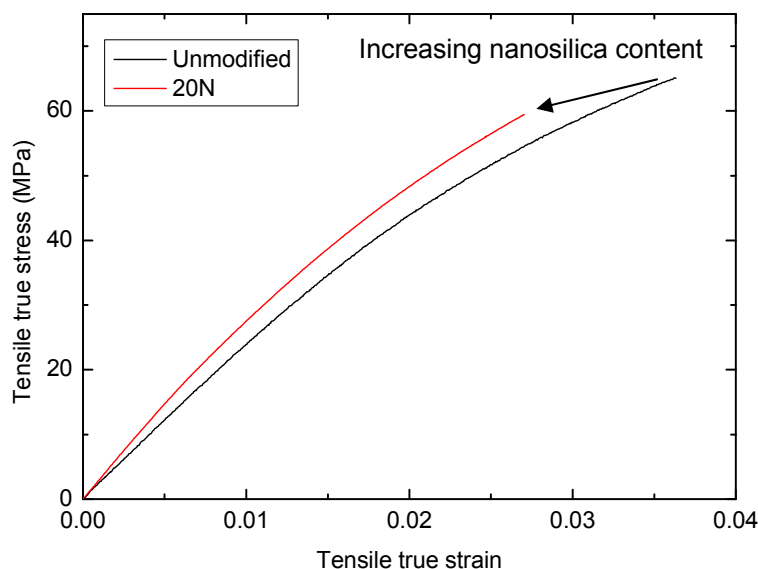


Figure 8.3. Tensile true stress versus tensile true strain for the unmodified and 20N amine cured multifunctional epoxies.

## 8.5 Compressive properties

The compressive Young's modulus,  $E_c$ , compressive true yield strength,  $\sigma_{yc}$ , and compressive true yield strain,  $\varepsilon_{yc}$ , from plane strain compression tests are summarised in Table 8.4. There is an increase in  $E_c$  with increasing nanosilica content. Reasonable agreement was obtained between  $E_c$  and  $E_t$ , shown previously in Table 8.3. The value of  $\sigma_{yc}$  was defined as the first point on the true stress-true strain curve with a zero gradient because strain softening did not occur for this system. The value  $\sigma_{yc}$  was found to increase and the value of  $\varepsilon_{yc}$ , to decrease with increasing nanosilica content, as shown in Figure 8.4. This would suggest good particle-matrix adhesion in this system. With additional applied displacement after  $\sigma_{yc}$ , the lack of strain softening would suggest that this epoxy does not shear band yield [12]. The epoxies showed work-hardened with further applied displacement. This increased in prevalence when more nanosilica was added to the epoxy.

The unmodified epoxy was loaded to failure and a true fracture strain of  $0.64 \pm 0.01$  was obtained.

Table 8.4. Compressive Young's modulus,  $E_c$ , compressive true yield strength,  $\sigma_{yc}$ , and compressive true yield strain,  $\varepsilon_{yc}$ , for the unmodified and nanosilica-modified amine cured multifunctional epoxies.

Formulation	$E_c$ (GPa)		$\sigma_{yc}$ (MPa)		$\varepsilon_{yc}$ (true strain)	
	$\bar{x}$	$\pm$	$\bar{x}$	$\pm$	$\bar{x}$	$\pm$
Unmodified	2.41	0.36	125	0	0.19	0.00
10N	2.83	0.39	130	0	0.17	0.00
20N	3.15	0.38	132	0	0.14	0.01

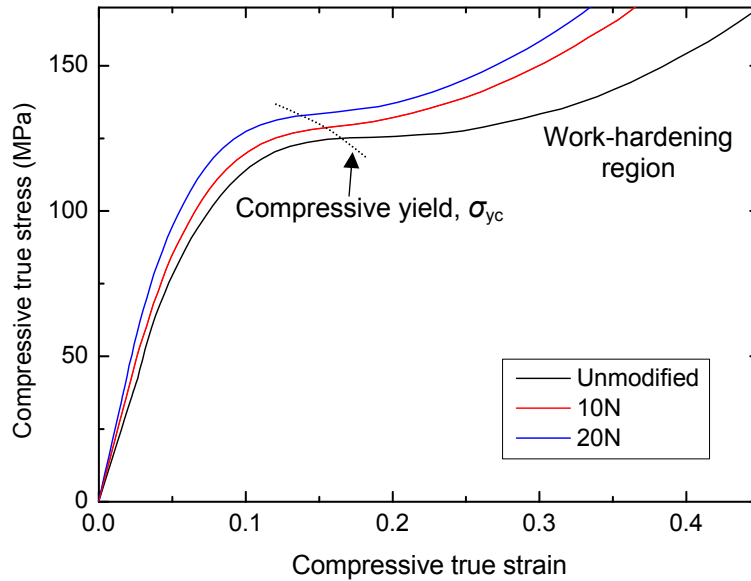


Figure 8.4. Compressive true stress versus compressive true strain for the unmodified and nanosilica-modified amine cured multifunctional epoxies.

A sample of the unmodified epoxy was loaded to  $\sigma_{yc}$  and cut at the mid-plane and polished into a 100  $\mu\text{m}$  section to find evidence of shear banding. It is apparent from the cross-polarised light optical image in Figure 8.5, that shear banding does not readily occur in the gauge area of the amine cured multifunctional epoxy. Large diffuse constraint induced shear bands occur on the boundaries of the indenter. These are a function of pure shear induced by thickness change in the compressed region, rather than inhomogeneous plastic flow in the gauge area [14]. There is no strain softening component to the compressive true stress-compressive true strain curves, and thus shear bands would not be expected to form in the gauge area of the sample.



Figure 8.5. Polished section of the unmodified amine cured multifunctional epoxy shown with cross-polarised light optical microscopy.

## 8.6 Fracture properties

Single edge notched bend (SENB) tests for the unmodified and nanosilica-modified amine cured multifunctional epoxy were reported [79] and results are shown in Table 8.5. There was no statistical difference in the fracture toughness,  $K_C$ , or the fracture energy,  $G_C$ , with increasing nanosilica content, as is evident in the plots  $K_C$  and  $G_C$  in

Figure 8.6. It is noteworthy that the amine cured multifunctional epoxy was the only system considered in the present work that shows no toughening effect with the addition of nanosilica.

Table 8.5. Fracture toughness,  $K_{IC}$ , and fracture energy,  $G_C$ , for the unmodified and nanosilica-modified amine cured multifunctional epoxies [79].

Formulation	$K_{IC}$ (MPa $\sqrt{m}$ )		$G_C$ (J/m $^2$ )	
	$\bar{x}$	$\pm$	$\bar{x}$	$\pm$
Unmodified	0.75	0.01	202	43
2N	0.73	0.04	189	20
5N	0.79	0.10	177	24
10N	0.70	0.10	175	14
20N	0.77	0.10	177	13

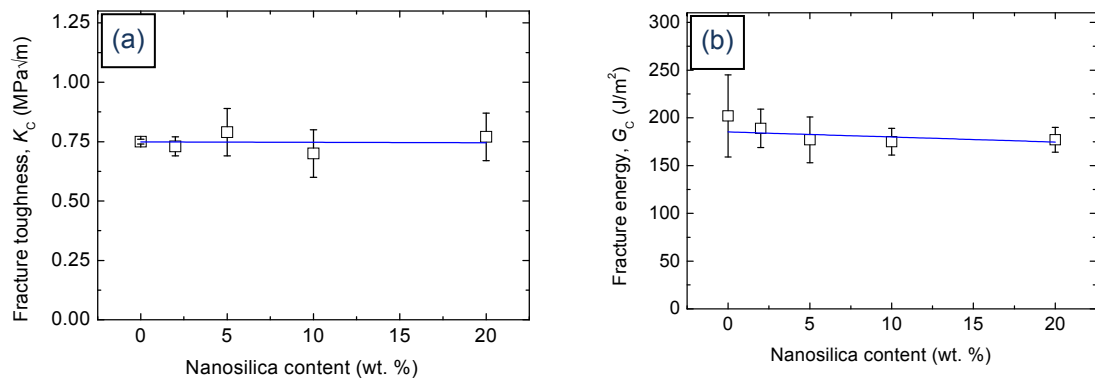


Figure 8.6. The (a) fracture toughness,  $K_{IC}$ , and (b) fracture energy,  $G_C$ , versus nanosilica content for the unmodified and nanosilica-modified amine cured multifunctional epoxies. A linear fits shows the general trend.

### 8.6.1 Toughening mechanisms

The plastic zone radius,  $r_{pz}$ , was calculated using Irwin's prediction in plane strain conditions [193] (see Equation (4.12)). A value for  $\sigma_{yt}$  was not Obtained, so Equation (4.13) from [94] was used to approximate  $\sigma_{yt}$  by using  $\sigma_{yc}$ . The plastic zone radius was of the range 3.2  $\mu\text{m}$  for the unmodified epoxy and 3.8  $\mu\text{m}$  for 20N. Little difference in the calculated plastic zone size is attributable to the lack of any toughening effect when nanosilica was added. Field emission gun scanning electron microscopy (FEGSEM) was conducted in the process zone region of a 20N fracture surface. The nanosilica particles were discernable on the fracture surface as indicated in Figure 8.7. The white lines in the image identify a single particle, measured at 50 nm diameter. Similarly, most of the particles on the fracture surface were larger than expected. The debonding stress at the interface is proportional to  $r_p^{-1/2}$  and so the larger particles would be expected to debond more readily [34, 47, 49] and could explain why the nanosilica

particles appear larger on the fracture surface. Alternatively, this discrepancy in size could also be a result of epoxy remaining on the surface of the particles. Previous studies have shown that crack deflection and crack pinning do not contribute as toughening mechanisms because the particle size is many orders of magnitude smaller than the crack opening displacement [7, 52]. No evidence of pinning or crack deflection was found at lower magnification on the fracture surface. No significant difference in surface roughness was observed. It was deduced that the particles do debond readily. When particle debonding did occur, no evidence of void growth was located.

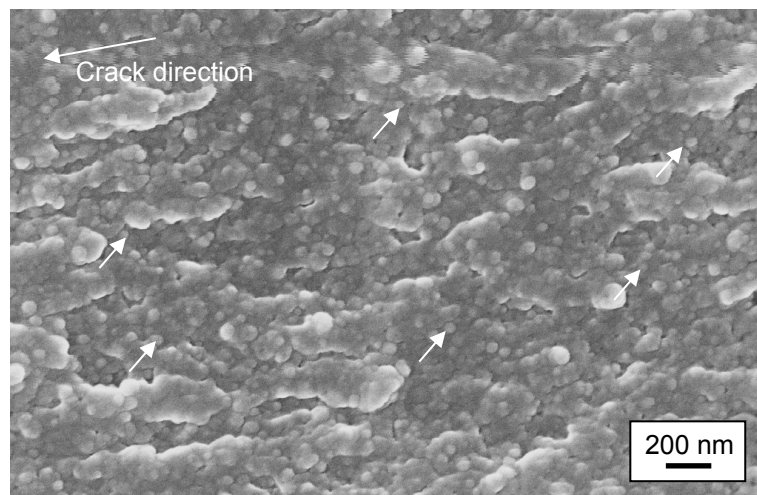


Figure 8.7. Shows a FEGSEM image of the fracture surface for the 20N amine cured multifunctional epoxy. Some nanosilica particles are shown with arrows.

## 8.7 Chapter summary

The bulk properties for an amine cured multifunctional epoxy system modified with nanosilica particles was examined. The  $T_g$  (DSC) was found to be constant at 178 °C for nanosilica modifications up to 20 wt. %. The particles do not impede the formation of a cross-linked and networked structure during curing. The nanosilica particles remain well dispersed in the epoxy at high concentrations.

The value of  $E_t$  increased from 2.55 GPa to 3.87 GPa with the addition of 20 wt. % nanosilica, and this was also observed in compression. The magnitude of  $\sigma_{UTS}$  was unchanged when nanosilica was added to the epoxy (mean  $\sigma_{UTS} = 63$  MPa). The tensile samples failed prior to yield; therefore, no assessment of the quality of the particle-matrix interface could be made from the tensile properties. The value of  $\sigma_{yc}$  was found to increase with nanosilica content. This would suggest a reasonable particle-matrix adhesion. Importantly, no shear band yielding occurred in the amine cured multifunctional epoxy during compressive yield. This was shown with

compressive true stress-compressive true strain curves from the tests and using cross-polarised light microscopy of the unmodified epoxy.

The values of  $K_C$  and  $G_C$  were unchanged with the addition of nanosilica. No evidence of mechanisms indicative of a toughening process were found. Crack pinning, deflection and increased surface roughness have previously been discounted as toughening mechanisms [7, 52]. Therefore, it was postulated the lack of shear yielding in the epoxy has hindered any further mechanisms such as shear band yielding or debonding and plastic void growth that would be initiated by the nanosilica particles.

## Anhydride Cured DGEBA Epoxy Properties

### 9.1 Introduction

The following chapter presents the morphology and material properties of accelerated methylhexahydrophthalic acid anhydride cured diglycidyl ether of bis-phenol A (DGEBA) epoxy system. The anhydride DGEBA system has traditionally been used for electronic device fabrication applications [212] and automotive clearcoats [213]. The low viscosity and ease of processing makes this formulation an ideal candidate for infusion based manufacturing techniques. Such manufacturing techniques are applied heavily in the marine and wind sectors of industry, making continuous glass-fibre a favourable reinforcement in a fibre-composite material.

Various modifications with nanosilica and carboxyl terminated butadiene acrylonitrile (CTBN) rubber and is summarised in Table 9.1. The volume fraction was calculated from the weight fraction. The density of the unmodified epoxy was measured to be 1,140 kg/m<sup>3</sup>. Modifications of up to 20 wt. % with nanosilica have been examined, with the neat resin and a rubber-modified set of formulations with 9 wt. % CTBN. This amount of rubber modifier was found to give optimal fracture properties when normalised by the rubber content, and therefore was set to be constant [59].

Table 9.1. Formulations of anhydride cured DGEBA epoxies that were studied.

Formulation	Nanosilica content		CTBN content	
	wt. %	vol. %	wt. %	vol. %
Unmodified	0	0	0	0
10N	10	6.5	-	-
20N	20	13.7	-	-
9R	-	-	9	10.6
10N9R	10	6.5	9	10.6
15N9R	15	10.1	9	10.6
20N9R	20	13.7	9	10.6

Differential scanning calorimetry (DSC) was conducted to examine changes in glass transition temperature with varying nanosilica and rubber contents. The morphology of the formulations was examined using atomic force microscopy (AFM) and transmission

electron microscopy (TEM). The bulk material properties were characterised using tensile tests, plane strain compression and single edge notched bend (SENB) tests. Field emission gun scanning electron microscopy (FEGSEM) was also conducted on the fractured specimens to gain understanding of the toughening mechanisms that had occurred.

Composite properties were examined for the unmodified, 10N, 9R and 10N9R formulations. The 10N and 10N9R formulations were identified as potential compositions that would provide optimal toughening with minimal inclusion of modifiers in the matrix. The unmodified and 9R formulations were examined to establish baseline properties. Separate glass-fibre reinforced polymer composites (GFRP) with uni-directional (UD) and quasi-isotropic (QI) continuous fibre reinforcement were produced with modified epoxy matrices. A qualitative evaluation of the interfacial adhesion between the fibre and the matrix was examined using single-fibre pull-out tests and short beam shear tests. The mode I composite fracture properties were determined for the infused composites was hoped to provide understanding of how matrix toughness transferred to the fibre-composite.

## 9.2 Glass transition temperature

The glass transition temperature,  $T_g$ , was measured for the unmodified and modified bulk formulations using DSC, and the mean values are summarised in Table 9.2. The  $T_g$  of the unmodified epoxy was measured to be 140 °C. The addition of nanosilica has no affect on the  $T_g$  of this system. Thus, the cross-link density is reported to remain unchanged. The addition of CTBN rubber to the epoxy results in a small reduction in the mean  $T_g$ , and would suggest that some of the rubber remains in solution. With the addition of nanosilica in the hybrid formulations, the  $T_g$  was found to drop steadily. This would suggest that increasing amounts of rubber remain in solution. A quantitative analysis is discussed further when the morphology is examined in section 9.3.2.

Table 9.2. Mean glass transition temperature,  $T_g$ , of unmodified and modified anhydride cured DGEBA epoxies.

Formulation	$T_g$ ( $^{\circ}\text{C}$ )	
	$\bar{x}$	$\pm$
Unmodified	140	2
10N	140	2
20N	142	2
<hr style="border-top: 1px dashed black;"/>		
9R	137	0
10N9R	138	1
15N9R	131	2
20N9R	124	1

### 9.3 Morphology

An atomic force micrograph of a microtome cut surface from the unmodified epoxy is shown in Figure 9.1. The phase and height images in Figure 9.1 show that the sample was featureless and flat, which is typical of the morphology for a homogenous thermoset polymer.

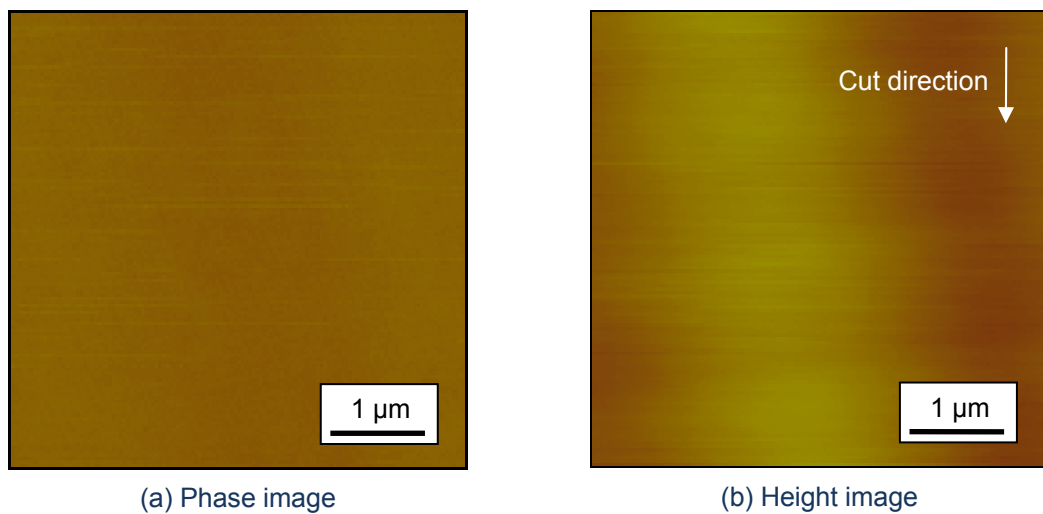


Figure 9.1. Shows (a) phase and (b) height images of the unmodified anhydride cured DGEBA epoxy. The cut direction is shown in the height image.

#### 9.3.1 Nanosilica-modified formulations

Figure 9.2 shows AFM images of the surface of the 10N epoxy. The 20 nm silica particles are dispersed in the epoxy. The area fraction was measured from the high magnification micrographs in (c, d) and a volume fraction of 6.6 % was obtained. This agrees well with the calculated volume fraction shown in Table 9.1 at 6.5 vol. %. Good dispersion is also shown at higher nanosilica content in Figure 9.2 for 20N with a

measured area fraction of 9.8 % (compared to a calculated value of 13.7 vol. %). The inter-particle distance,  $D_{IP}$ , was calculated to be 20 nm and 11 nm for the 10N and 20N formulations respectively. The epoxies were also examined with TEM and good evidence of well dispersed particles shown in Figure 9.4. Notably, the TEM slices are 90 nm in thickness so could contain up to 4-5 particles through the thickness of the specimen. As a result, the apparent volume fraction appears larger than from the AFM images.

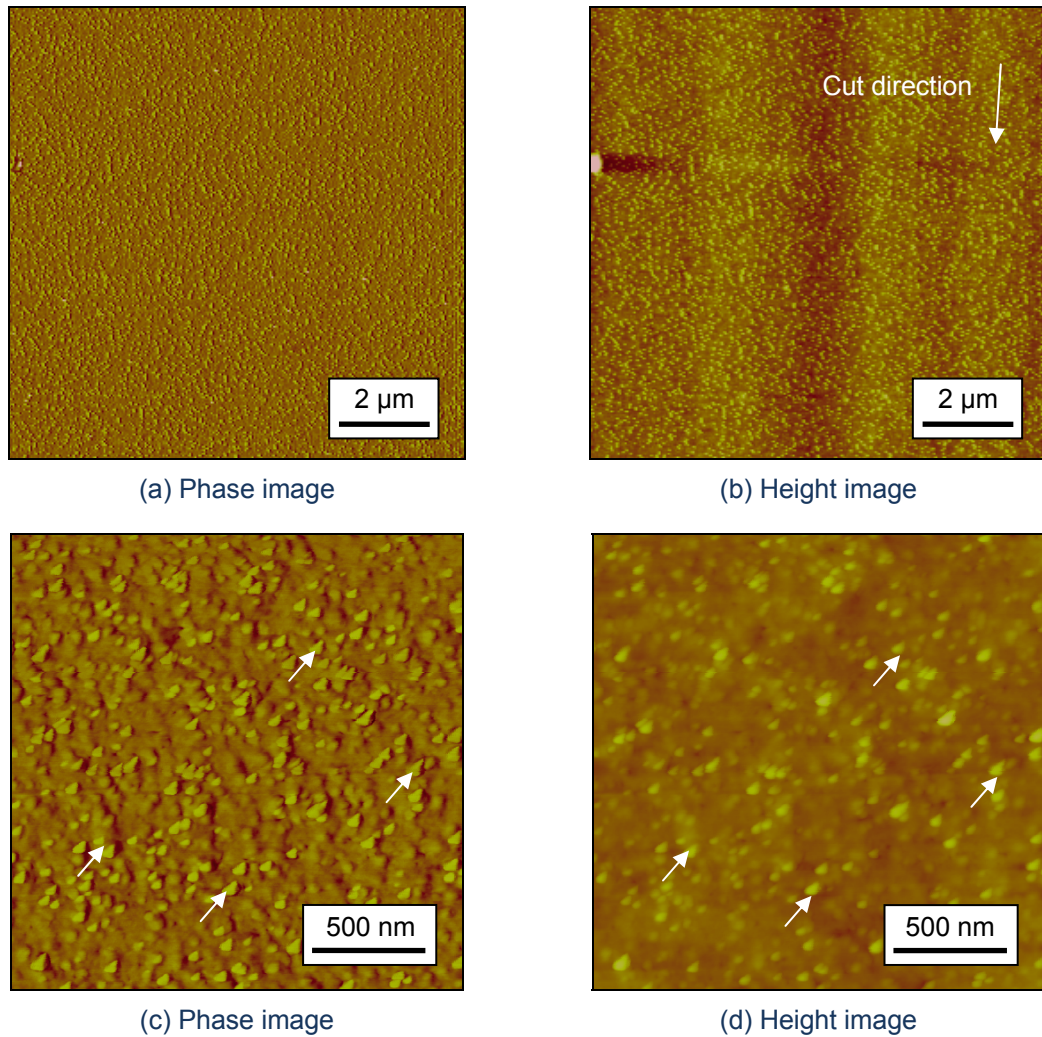


Figure 9.2. Shows (a, c) phase and (b, d) height images of the 10N anhydride cured DGEBA epoxy. Some of the nanosilica particles are identified in (c, d).

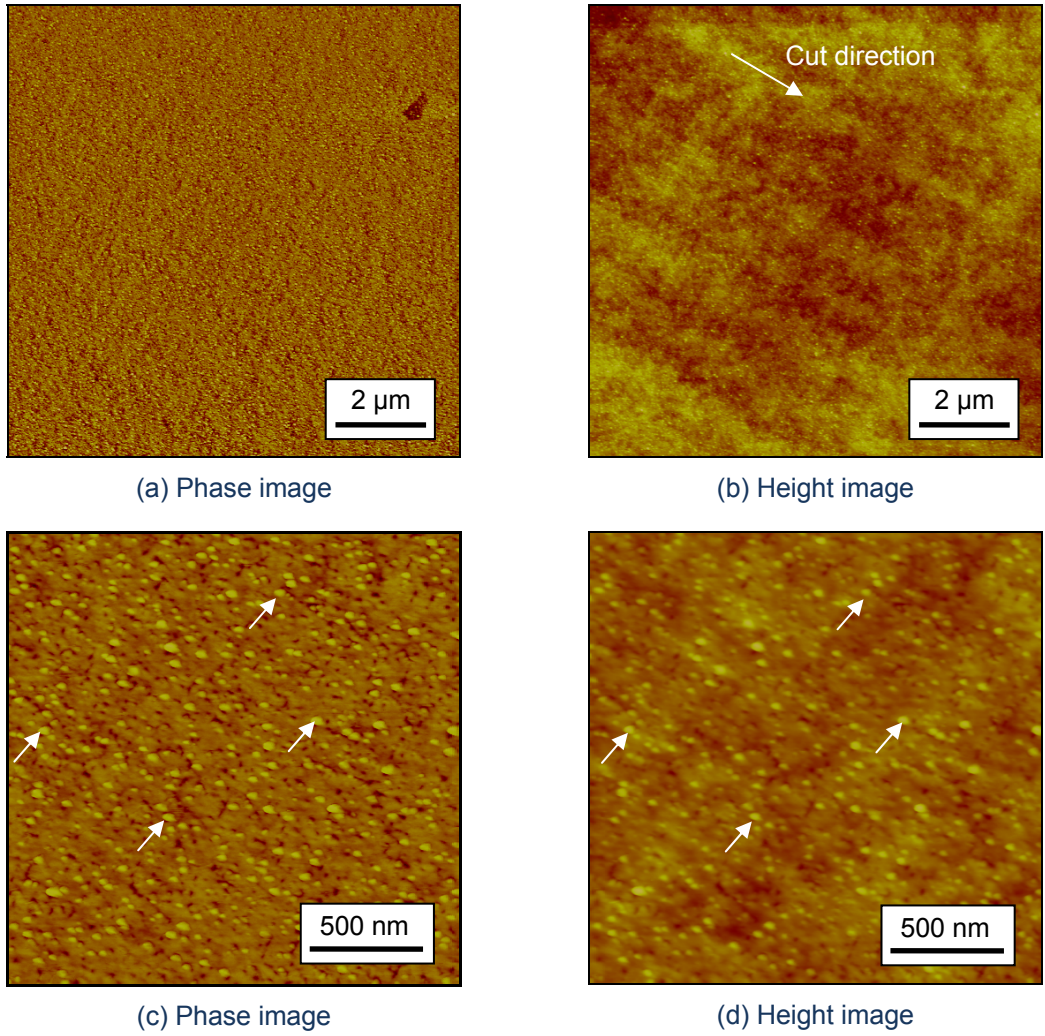


Figure 9.3. Shows (a, c) phase and (b, d) height images of the 20N anhydride cured DGEBA epoxy. Some of the nanosilica particles are identified with arrows in (c, d).

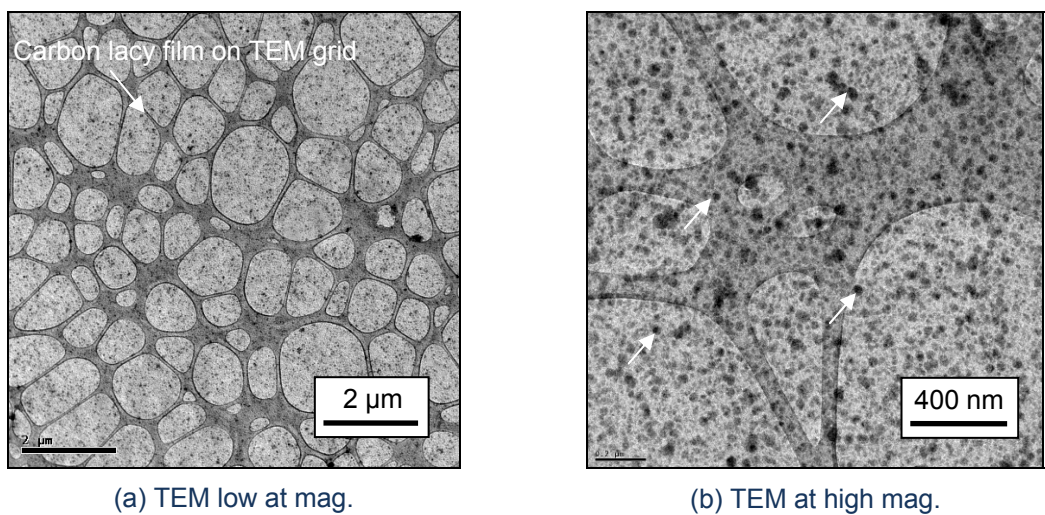


Figure 9.4. Shows TEM images of the (a) 10N anhydride cured DGEBA and (b) 20N anhydride cured DGEBA. Some of the nanosilica particles are identified with arrows.

### 9.3.2 Rubber-modified formulations

The CTBN rubber phase separates out of the epoxy during curing, and can be seen in the AFM micrographs for the 9R epoxy in Figure 9.5. Spherical rubber particles up to 1  $\mu\text{m}$  in size were present and are indicated in the image. The mean rubber particle diameter was measured to be 0.54  $\mu\text{m}$ . The rubber inter-particle distance was calculated to be 0.8  $\mu\text{m}$ . Based on a decrease in the mean  $T_g$  by 3  $^{\circ}\text{C}$ , 1 wt. % of CTBN would be expected to remain in solution (using Fox's equation [201]). The area fraction was measured to be 9.9 % for a selection of AFM images, and provides reasonable agreement to the change in  $T_g$  noted in Table 9.2 and is shown in Table 9.3.

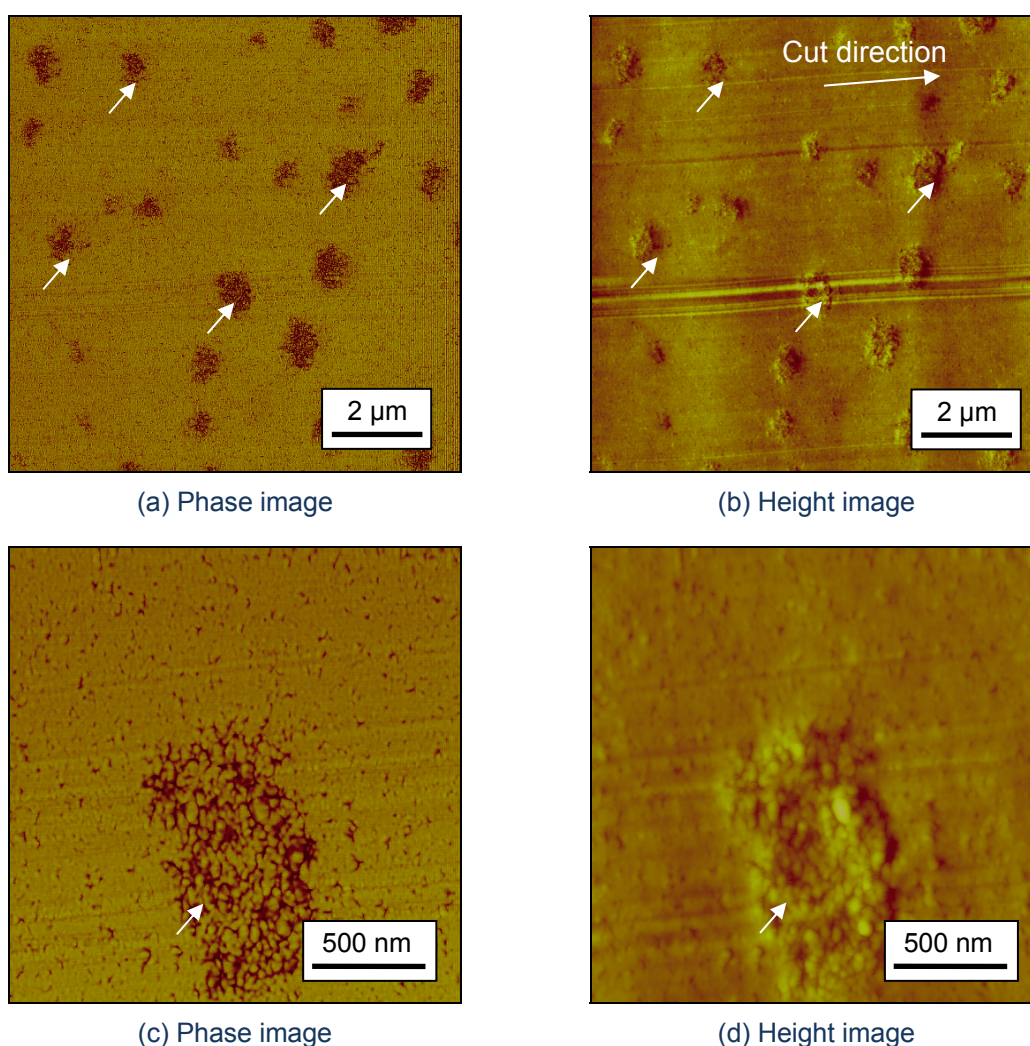


Figure 9.5. Shows (a, c) phase and (b, d) height images of the 9R anhydride cured DGEBA epoxy. Spherical, particles up to 1  $\mu\text{m}$  in diameter are formed in the epoxy (white arrows).

When nanosilica was added to form a hybrid, the rubber particles increased in size, up to 1.5  $\mu\text{m}$ . AFM micrographs for the hybrid epoxy are shown in Figure 9.6. The rubber particles were measured for many images, and mean particle size of 0.75  $\mu\text{m}$  was

obtained. The inter-particle distance between rubber particles is  $1.1\ \mu\text{m}$ . The dispersion of nanosilica was disrupted by the phase separation of the rubber during curing. This resulted in networks of agglomerated necklace-like nanosilica structures which themselves, are well dispersed in the epoxy. Typically, agglomerated nanosilica structures,  $300\ \text{nm}$  by  $1\ \mu\text{m}$  in size were formed in the 10N9R formulation. The mean distance between the nanosilica necklaces was measured to be about  $0.8\ \mu\text{m}$ . The 10N9R hybrid epoxy was also examined with TEM, as shown in Figure 9.7. The morphology in the  $90\ \text{nm}$  TEM slice was found to be the same as the AFM images.

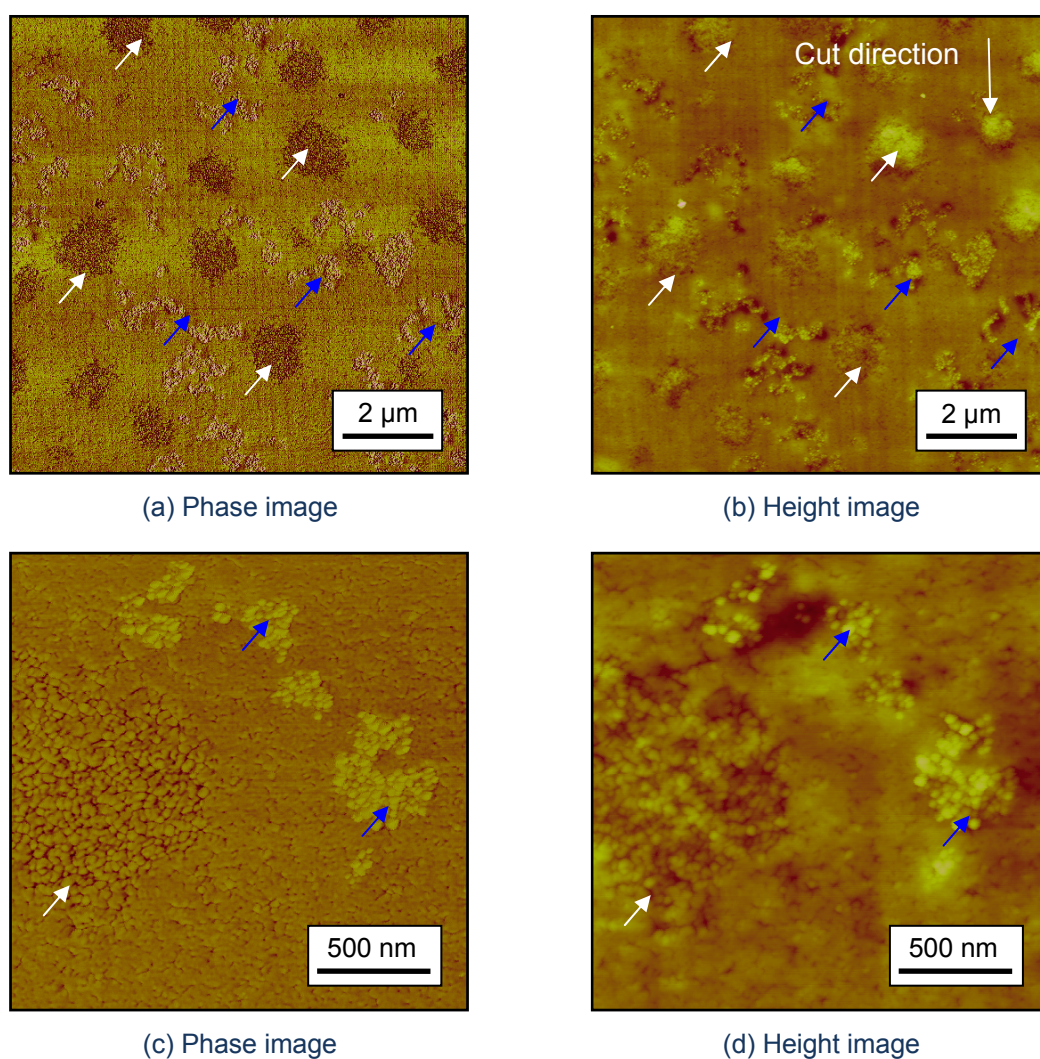


Figure 9.6. Shows (a, c) phase and (b, d) height images of the 10N9R anhydride cured DGEBA epoxy. Some rubber particles are indicated with white arrows and the nanosilica necklace structures are shown with blue.

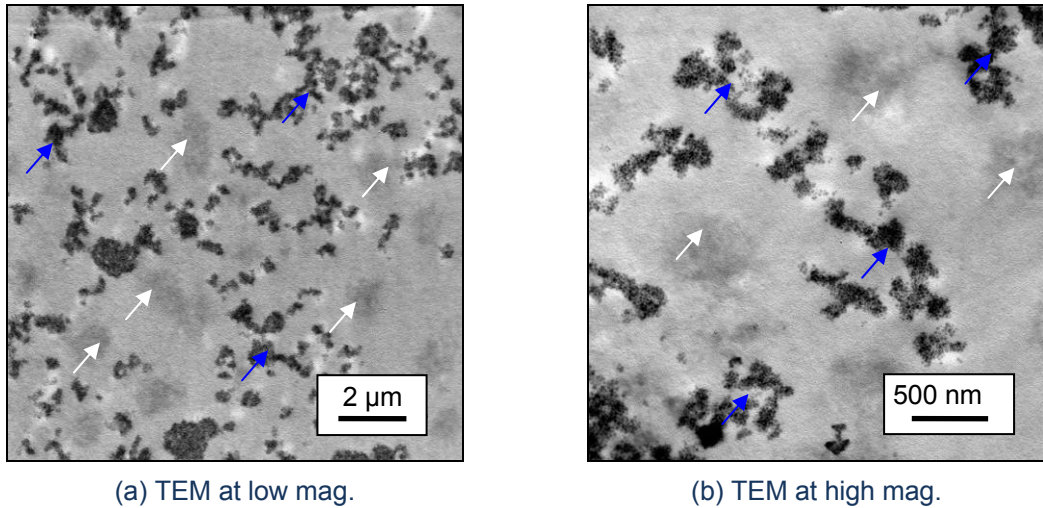


Figure 9.7. Shows TEM images of the 10N9R anhydride cured DGEBA. Some rubber particles are indicated with white arrows and the nanosilica necklaces are shown with blue.

As the nanosilica content was increased in the hybrids, more rubber was found to remain in solution, thus can explain the drop in  $T_g$  noted previously, and a detailed summary shown in Table 9.3. Reasonable agreement was achieved with the calculated volume fraction and the measured area fraction. The rubber particle size was found to remain constant at 1.5  $\mu\text{m}$ , but reduce in area fraction. The agglomerated nanosilica necklaces increased in size to 700 nm by 1.25  $\mu\text{m}$  in the 15N9R and 1  $\mu\text{m}$  by 1.5  $\mu\text{m}$  in the 20N9R. Notably, the nanosilica agglomerates are larger than the rubber micro-particles in the 20N9R, and take the form of large clusters rather than the aforementioned necklace-like structures.

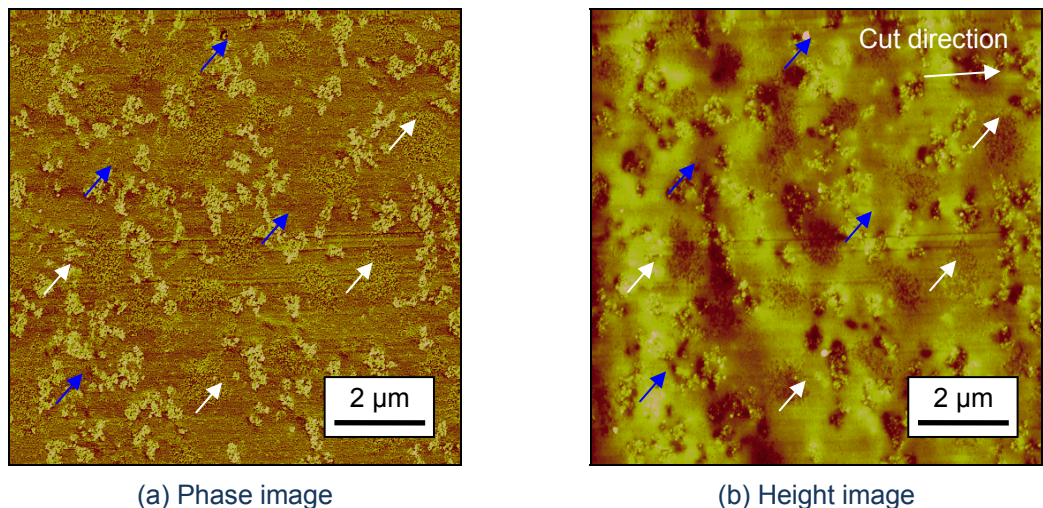


Figure 9.8 Shows (a) phase and (b) height images of the 15N9R anhydride cured DGEBA epoxy [182]. Some rubber particles are indicated with white arrows and the nanosilica necklace structures are shown with blue.

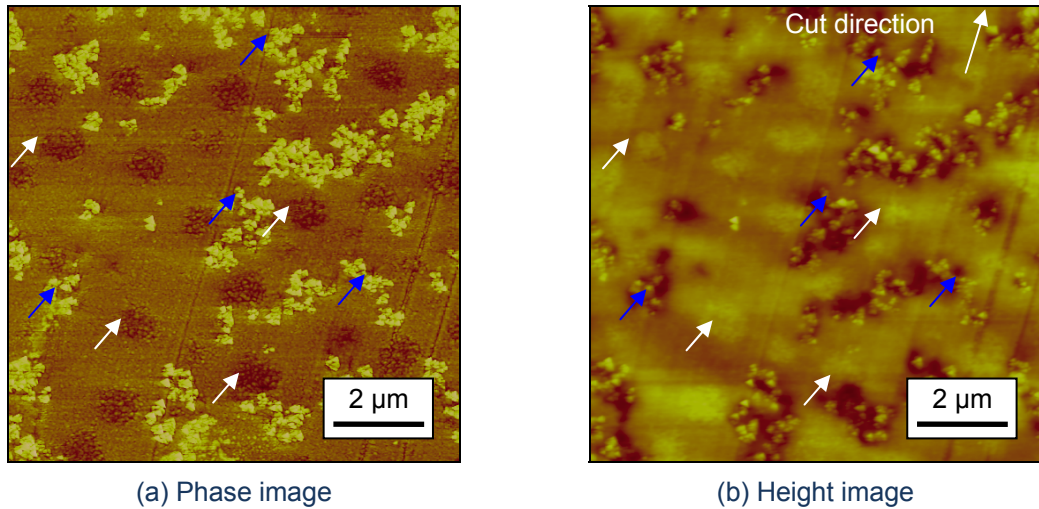


Figure 9.9. Shows (a) phase and (b) height images of the 20N9R anhydride cured DGEBA epoxy. Some rubber particles are indicated with white arrows and the nanosilica necklace structures are shown with blue.

Table 9.3. Morphologies in the rubber- and hybrid-modified anhydride cured DGEBA epoxies.

Formulation	Estimated Vol. % from Fox [201]	Rubber Area % from AFM	CTBN size ( $\mu\text{m}$ )	Nanosilica agglomerate size (nm)	Nanosilica structure
9R	9.4	9.9	1.0	-	-
10N9R	9.4	9.0	1.5	1000 × 500	Necklace
15N9R	7.6	6.9	1.5	1250 × 700	Necklace
20N9R	4.6	6.4	1.5	1500 × 1000	Agglomerate

### 9.3.3 Fibre-reinforced composites

Glass-fibre reinforced polymer composites were produced with two different fibre lay-ups using resin infusion under flexible tooling (RIFT). Firstly, a 7 mm thick, 12 ply uni-directional (UD) composite, was produced with a poly-tetrafluoroethylene (PTFE) insert placed in the mid-plane to initiate a starter crack. Secondly, 4 mm thick, quasi-isotropic (QI) plates were prepared using 8 plies of non-crimp fabric (NCF) in a balanced symmetric lay-up to give a '0/0' interface across the fracture plane. To increase the stiffness of this plate configuration, the plates were backed with 2 plies of uni-directional carbon-fibre in the axial plane. A natural pre-crack was initiated via a PTFE insert film.

Shown in Figure 9.10(a, b) are optical micrographs of the UD GFRP composite. The specimens were very well consolidated and void free with a mean fibre volume fraction calculated to be  $59 \pm 3\%$  from the optical images. The individual glass-fibres are arranged into tows in the warp direction measuring 0.5 mm by 1.5 mm. These are

bound together with polyethylene weft stitching. Figure 9.10(b) shows that the  $24 \pm 3 \mu\text{m}$  glass-fibres are spherical in cross section. The dark streaks in Figure 9.10(a) are polyethylene weft stitches that held the dry perform aligned during infusion. By the nature of the RIFT process, a variable interlaminar region was obtained through the cross-section of the composite as denoted with a dashed blue line. The resin rich region varies in area and also the location with respect to the mid-plane of the beam cross-section. This was due to the highly co-mingled nature of the fibre tows when a vacuum was applied to the fibre stack, and resulted in well dispersed fibres and no clear interlaminar region. Typically, the resin rich region between fibres was found to be  $100 \mu\text{m}$  thick.

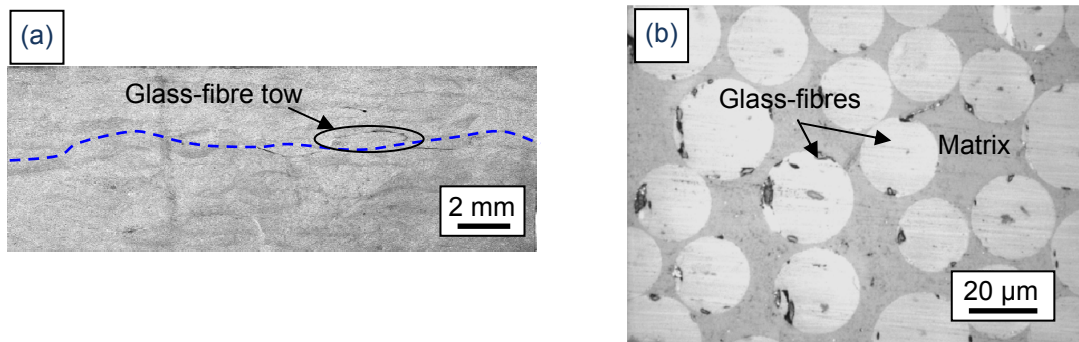


Figure 9.10. Optical cross-sectional micrographs of the UD GFRP show (a) the composite beam, and (b) a high magnification micrograph of the individual glass-fibres in the fracture plane (blue).

Figure 9.11 shows optical micrographs taken for the QI GFRP. Due to the relatively thin, and therefore, low flexural modulus of the quasi-isotropic lay-up, the GFRP was backed with 2 plies of  $0^\circ$  orientation carbon-fibre NCF on each face of the beam in the dry perform lay-up stage, as shown in Figure 9.11(a). This addition stiffness would increase the flexural modulus of the laminate without compromising the fracture properties, [214]. The infused composite was well consolidated and void free, shown in Figure 9.11(a-c). Individual  $17 \pm 1 \mu\text{m}$  glass-fibres are arranged in tows, 2 mm by 0.2 mm. These tows are arranged into biaxial ( $90^\circ$ ) aligned dry preforms, with one on top of the other and bound with polyethylene weft stitching. The perform plies have then been arranged into a quasi-isotropic lay-up with the aforementioned carbon-fibre axial reinforcement. Close examination in Figure 9.11(b) shows that the volume fraction locally in the composite can be variable; the mean volume fraction was calculated as  $57 \pm 3 \%$ . This sample was ground to 1200 grit and explains the poor quality of the surface. The interlaminar region in the composite varied between 1-100 μm in width.

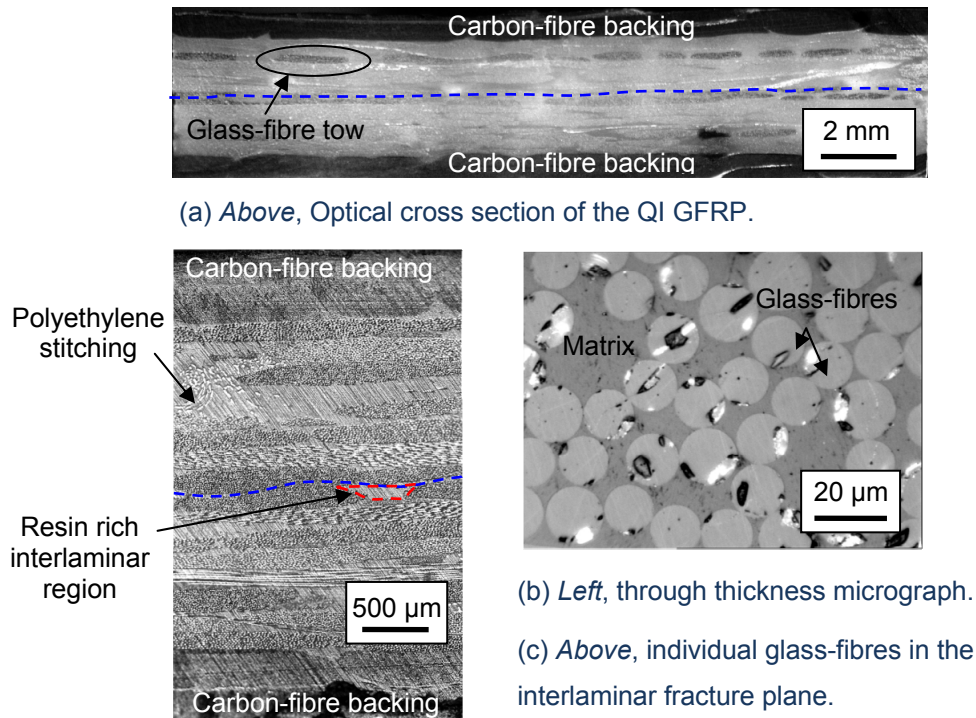


Figure 9.11. Optical cross-sectional micrographs from the QI GFRP showing (a) the composite beam, (b) a micrograph through the thickness of the GFRP and (c) a micrograph of the individual glass-fibres in the interlaminar fracture plane (blue).

It was important to ascertain good dispersion of the nanosilica particles around the fibres. Specimen manufacture was difficult due to the larger disparity in stiffness between the glass-fibres and the matrix. It was not possible to produce flat cross sections in the GFRP perpendicular to the fibre direction using conventional microtomy processes. The cutting process would tend to result in extensive fibre fracture with the surrounding matrix being pulled from the sample. Attempts to cut parallel to the fibre direction resulted in fibre pullout from the surface of the sample and seemed even less likely to produce AFM quality surfaces. The morphology of the fibre-matrix was successfully imaged by micro-potting a sample of the infused glass nanosilica-modified epoxy composite into a parent epoxy. Cutting was conducted perpendicular with only a few fibres cut during the microtome process. This resulted in good quality surfaces and also yielded TEM quality, 90 nm slices of GFRP. Excellent dispersion was obtained in the GFRP. The fibre-matrix interface in the AFM height images for the 10N UD GFRP in Figure 9.12 show individually dispersed nanosilica particles, right up to the fibre-matrix interface.

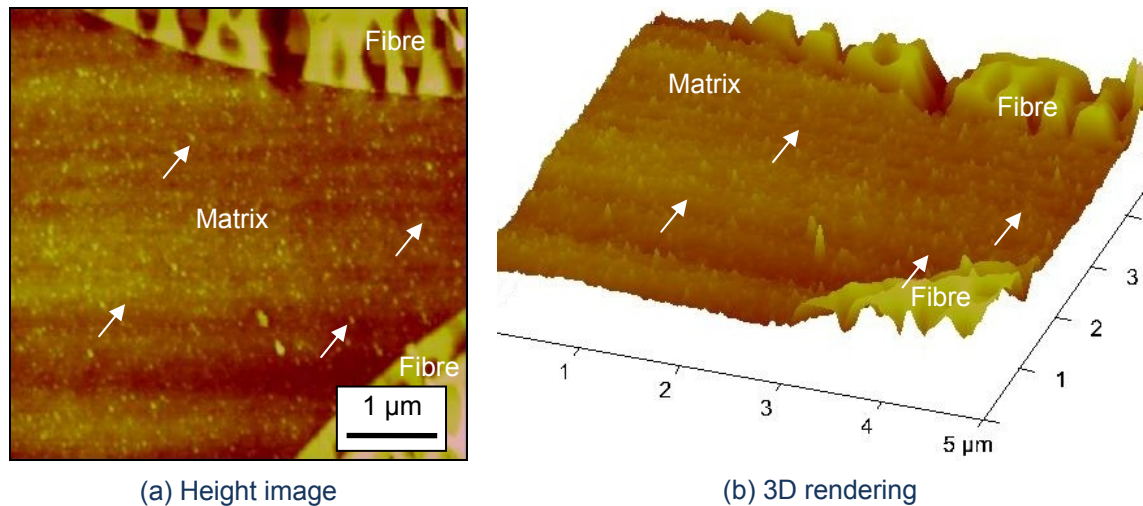


Figure 9.12. Height images (a, b) of the 10N anhydride cured DGEBA UD GFRP. The nanosilica particles (white arrows) are well dispersed up to the fibre-matrix interface.

Due to the added complication of rubber present in the rubber-modified GFRPs, cryo-temperatures or cross-linking of the rubber particles would be required during cutting to obtain such images with the hybrid-modified GFRP. The 10N9R modified QI GFRP was instead sectioned using a focused ion beam (FIB) to obtain a 110 nm slice. This technique was explored as a potential route to examining the morphology of the fibre-matrix interface. The preliminary FIB cut sample was examined with TEM and is shown in Figure 9.13. The sample was cut between two fibres and shows the fibres lying horizontally at the top and bottom of the image with the matrix region in the centre. The slice was machined as thin as possible, and was too thick to obtain excellent TEM images. A thickness change can be seen near the upper fibre in the specimen where the specimen was no longer stable enough to continue machining the thickness of the slice. The nanosilica particles agglomerate close to the interface and are identified in the image. Compared to the TEM images in Figure 9.7, the necklaces appear large. However, this sample is 110 nm thick in comparison to 90 nm slices in Figure 9.7 and could explain why the nanosilica seems to agglomerate more. A single 1.5 µm rubber particle can be identified faintly in the image. The image is a composite of multiple slices and the rubber was seen in separate images, and thus, can be confirmed as a feature in the sample. The rubber can be verified to phase separate into spherical particles from a SEM image of a fractured GFRP 10N9R specimen, see Figure 9.14. The thick nature of the FIB specimen was attributed to the poor appearance of the rubber particle in Figure 9.7. Therefore it was postulated, that either the FIB process had resulted in smearing the rubber or that the TEM sample was too thick to show intricacies in the specimen. To evaluate the interface further, it is recommended to

firstly cross-link the CTBN rubber with osmium tetroxide, and then perform microtomy with micro-potted GFRP specimens for AFM and TEM.

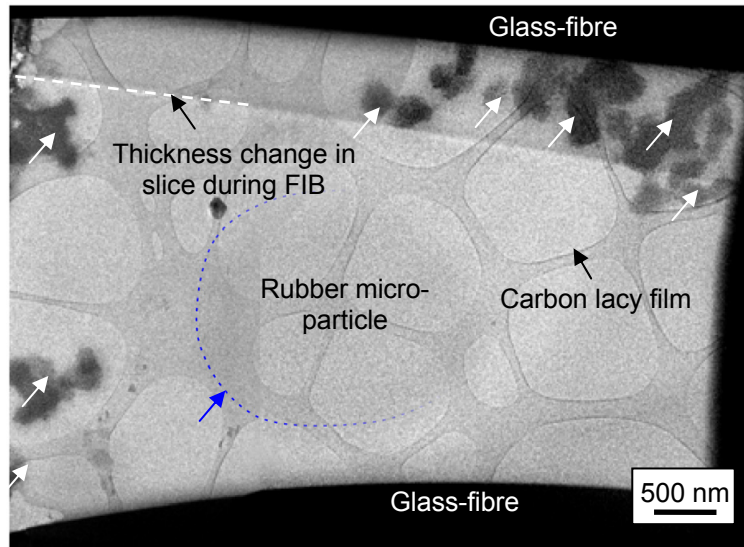


Figure 9.13. A TEM image of the fibre-matrix interface in the 10N9R anhydride cured DGEBA QI GFRP. The nanosilica necklaces are indicated with white arrows and a single rubber particle is identified with blue.

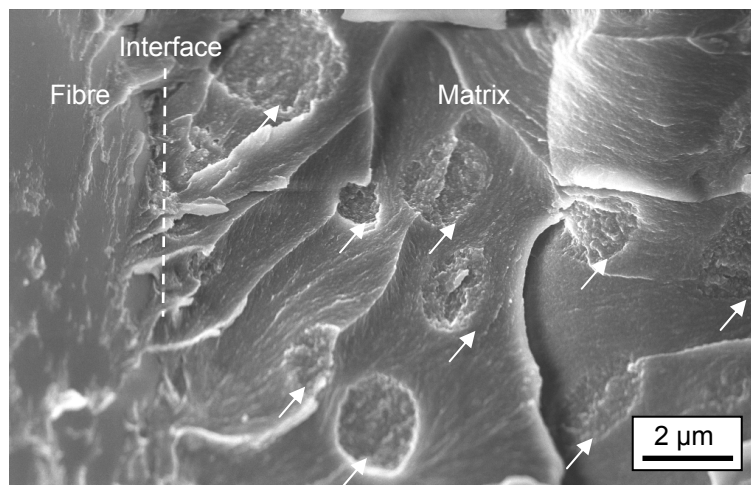


Figure 9.14. A FEGSEM from the fracture surface of the 10N9R anhydride cured DGEBA UD GFRP. The rubber particles are identified with arrows. The nanosilica particles cannot be seen at this magnification.

## 9.4 Rheological properties

Rheological tests were conducted with some of the bulk epoxy polymers to gain understanding of how processing parameters varied with epoxy modification. Rheological properties were examined for the formulations that were made into fibre-reinforced composites. This allowed optimal processing conditions to be identified for RIFT manufacturing of the GFRPs and embedding of single-fibre pull-out specimens.

Shown in Figure 9.15 is a plot of how the viscosity changed through the cure cycle for this system. Similar plots were found in the literature and verify the validity of this data [215]. An initial hold of 30 mins at 60 °C was set to account the time lost due to degassing of the resin and infusion into the fibre composite or steel moulds. Cure was initiated at 60 °C, verified by the increasing viscosity under the isothermal conditions. This was followed by a ramp to 90 °C at 10 °C/min and a 60 min hold, noting the drop in viscosity as the temperature was ramped up. Lastly, a 10 °C/min ramp up to 160 °C was carried out with a 120 min hold for the post cure. Vitrification was achieved quickly as the temperature was ramped up to 160 °C and the test was stopped when the viscosity reached a safe limit for the rheometer. Allowing 5 mins, for the disposable cone plates to be forced cooled back to room temperature, the plates were bonded together and the resin epoxy was cured solid.

At 90 °C, the initial cure temperature is much lower than the glass transition temperature of the cured epoxy. This processing hold provides vital time for reaction induced phase separation to occur in the rubber-modified epoxies, and for the cross linked networks to begin formation. It is necessary for the rubber-modified systems to attain a cloud point and sufficient time for the CTBN to phase separate fully. Previous studies have shown that the inclusion of CTBN can have the effect of decreasing cure time and temperature parameters of the epoxy system [216]. For this system and cure regime, no such increase in cure kinetics was observed.

No notable difference was observed in the cure kinetics for the 10N and 9R formulations apart from the increases in the initial viscosity compared to the unmodified epoxy. Interestingly, the hybrid-modified epoxy undergoes a steep increase in viscosity when the temperature is ramped to 90 °C. This was not noted for the other considered formulations. This would suggest that the nanosilica necklaces when reaction induced phase separation of the rubber initiates in the hybrid-modified epoxy. Agglomeration of the nanosilica has been reported for xN9R modified epoxies at low nanosilica contents (2.3 wt. %) [217], but not for the xN5R epoxies [59], suggesting this was a reasonable explanation, and that careful control of phase separation (i.e. very slow temperature ramp) could lead to well dispersed nanosilica in the xN9R hybrids.

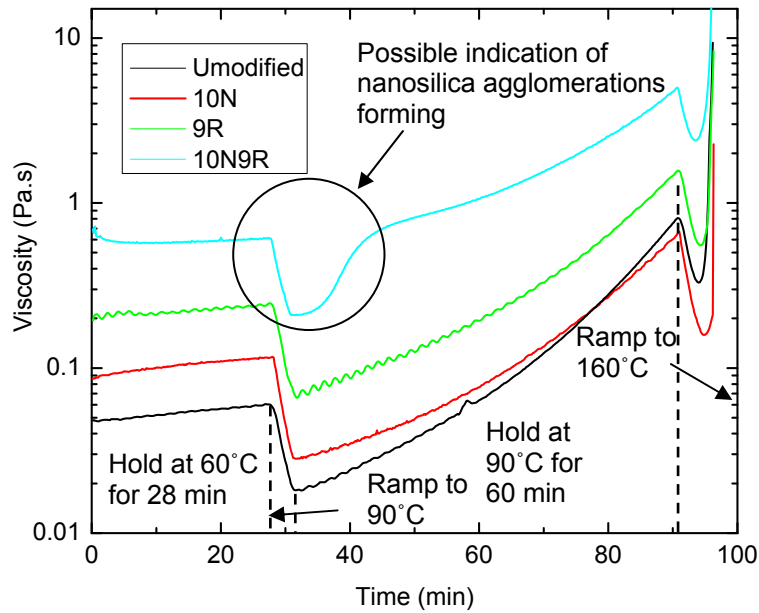


Figure 9.15. Viscosity versus time for the unmodified, 10N, 9R and 10N9R anhydride cured DGEBA epoxies as the samples went through the cure cycle.

## 9.5 Tensile properties

Tensile tests were conducted on bulk polymer samples. The tensile Young's modulus,  $E_t$ , tensile true tensile yield strength,  $\sigma_y$ , and true failure strain,  $\epsilon_y$ , for the unmodified and modified anhydride cured DGEBA are summarised in Table 9.4 and shown in Figure 9.16. The value of  $E_t$  was found to increase steadily with nanosilica content from 2.74 GPa for the unmodified epoxy to 3.47 GPa for the 20N epoxy. The addition of CTBN decreases  $E_t$  to 2.18 GPa, with some stiffness restored when nanosilica was added to the epoxy in the 10N9R hybrid. Good correlation was obtained with previously reported results by Peuch, Mohammed and Sohn Lee [59, 218, 219]. With no change in point of non-linearity for the nanosilica-modified formulations, yield initiates in the epoxy polymer before any debonding or damage associated with the nanosilica particles occurs. Rubber modification resulted in a decrease in the yield strength. This was attributed to internal cavitation and void growth initiating damage in the epoxy polymer. The yield strength was found to remain constant with the addition of nanosilica to the rubber-modified epoxies. Hence, the unmodified formulation was considered as the baseline value for the nanosilica-modified formulations, with the rubber-modified value of  $\sigma_y$  being considered the baseline for the hybrid-modified formulation. The general trend of  $\epsilon_y$  was observed to decrease in true strain with increasing nanosilica content.

Table 9.4. Young's modulus,  $E_t$ , tensile yield strength,  $\sigma_{yt}$ , and tensile fracture strain,  $\epsilon_{yt}$ , for unmodified and modified anhydride cured DGEBA epoxies.

Formulation	$E_t$ (GPa)		$\sigma_y$ (MPa)		$\epsilon_y$ (true strain)	
	$\bar{x}$	$\pm$	$\bar{x}$	$\pm$	$\bar{x}$	$\pm$
Unmodified	2.74	0.08	88.10	0.84	0.07	0.00
10N	3.08	0.06	89.44	0.42	0.06	0.00
20N	3.47	0.11	86.95	4.14	0.05	0.01
9R	2.18	0.06	66.89	2.87	0.05	0.01
10N9R	2.55	0.04	66.35	0.40	0.05	0.01

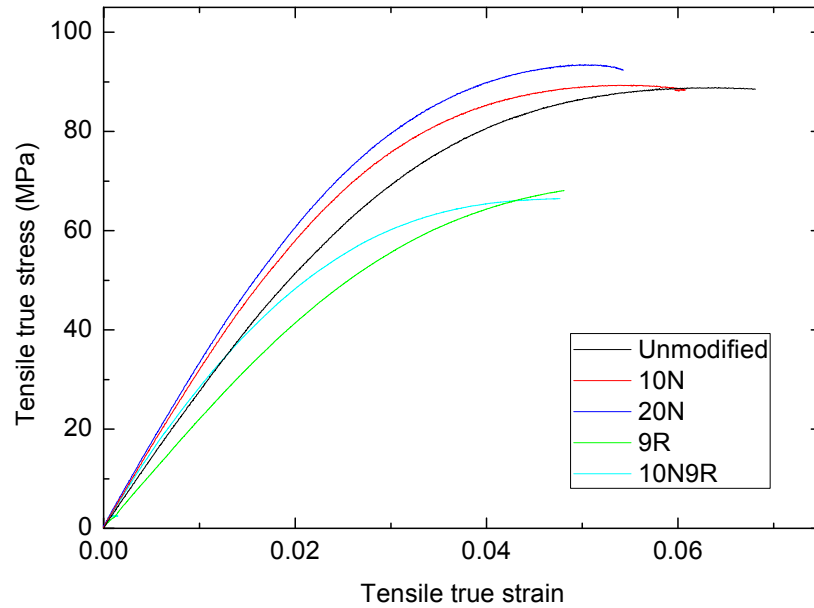


Figure 9.16. Tensile true stress versus tensile true strain for the unmodified and modified anhydride cured DGEBA epoxies.

## 9.6 Compressive properties

Compression tests were conducted on anhydride cured DGEBA modified with nanosilica and rubber micro-particles. The compressive Young's modulus,  $E_c$ , compressive true yield strength,  $\sigma_{yc}$ , and compressive true yield strain,  $\epsilon_{yc}$ , from plane strain compression tests are summarised in Table 9.5 for the unmodified and nanosilica-modified formulations. The value of  $E_c$  for the unmodified epoxy was found to be 2.55 GPa. Good agreement was found between  $E_c$  and  $E_t$ , with  $E_t$  previously being shown as 2.74 GPa. The maximum compressive yield strength for the unmodified epoxy was attained at 126 MPa. With continued loading, the polymer would strain soften suggesting inhomogeneous yield within the polymer [12] and subsequently work-harden until failure. The compressive true fracture strain at failure was recorded as  $0.75 \pm 0.01$ .

### 9.6.1 Nanosilica-modified formulations

The value of  $E_c$  increases with nanosilica content and provides good agreement with  $E_t$  from tensile tests, as shown summarised in Table 9.5. The value of  $\sigma_{yc}$  was also found to remain constant with the addition of nanosilica to the epoxy and is shown in the plot of compressive true stress versus compressive true strain in Figure 9.17. The curves are seen to reach a maximum at  $\sigma_{yc}$  and deform inhomogenously as identified by the negative slope to the true compressive stress-true compressive strain curve [12]. The epoxies are expected to shear band yield during this strain softening phase. With continued compression, the each formulation was found to work-harden and this was more prevalent at higher nanosilica contents.

Table 9.5. Compressive Young's modulus,  $E_c$ , compressive true yield strength,  $\sigma_{yc}$ , and compressive true yield strain,  $\varepsilon_{yc}$ , for the unmodified and nanosilica modified anhydride cured DGEBA epoxies.

Formulation	$E_c$ (GPa)		$\sigma_{yc}$ (MPa)		$\varepsilon_{yc}$ (true strain)	
	$\bar{x}$	$\pm$	$\bar{x}$	$\pm$	$\bar{x}$	$\pm$
unmodified	2.55	0.68	124	2	0.10	0.00
10N	2.68	0.06	133	1	0.10	0.01
20N	3.59	0.59	127	3	0.09	0.01

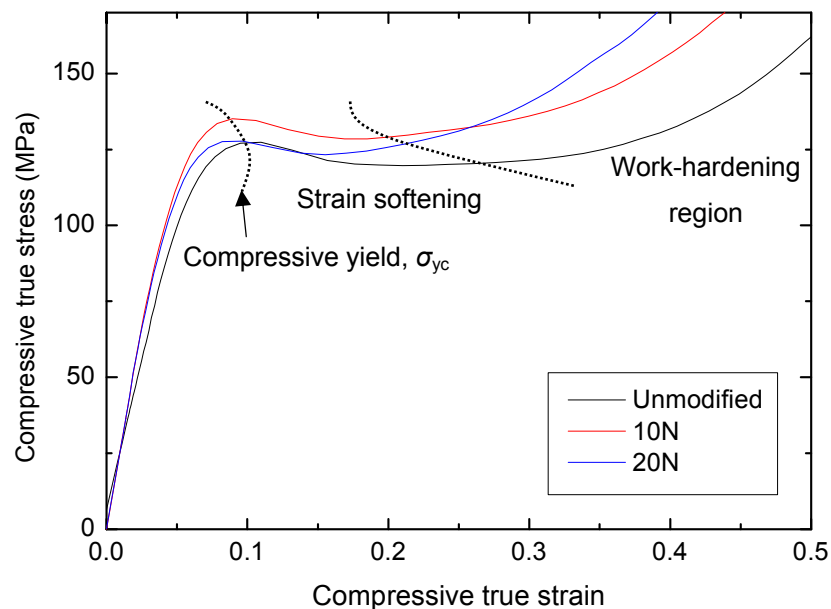


Figure 9.17. Compressive true stress versus compressive true strain for the unmodified and nanosilica-modified anhydride cured DGEBA epoxies.

Samples of the unmodified and nanosilica-modified formulations were loaded to the strain softening limit and sectioned for examination using transmission cross-polarised light microscopy. A sample of the unmodified epoxy is shown Figure 9.18(a). Evidence

of shear band yielding was found in the compressed region. Many focused shear bands constitute the deformed region of the sample. As the nanosilica content was increased, the appearance of shear banding was more diffuse in nature, shown for the 10N in Figure 9.18(b) and 20N in Figure 9.18(c). Therefore, one would expect the presence of nanosilica, to promote and contribute to shear yield banding mechanisms in the epoxy. Vollenberg and Heikens have shown that with increased localised shear deformation, less prominent extrinsic failure strains occur [26] and this was observed for the epoxy with increasing nanosilica content. AFM and TEM was conducted on the shear banded regions of the strain softened 10N and 20N samples but did not yield any useful evidence of toughening via shear band yielding or void growth mechanisms.

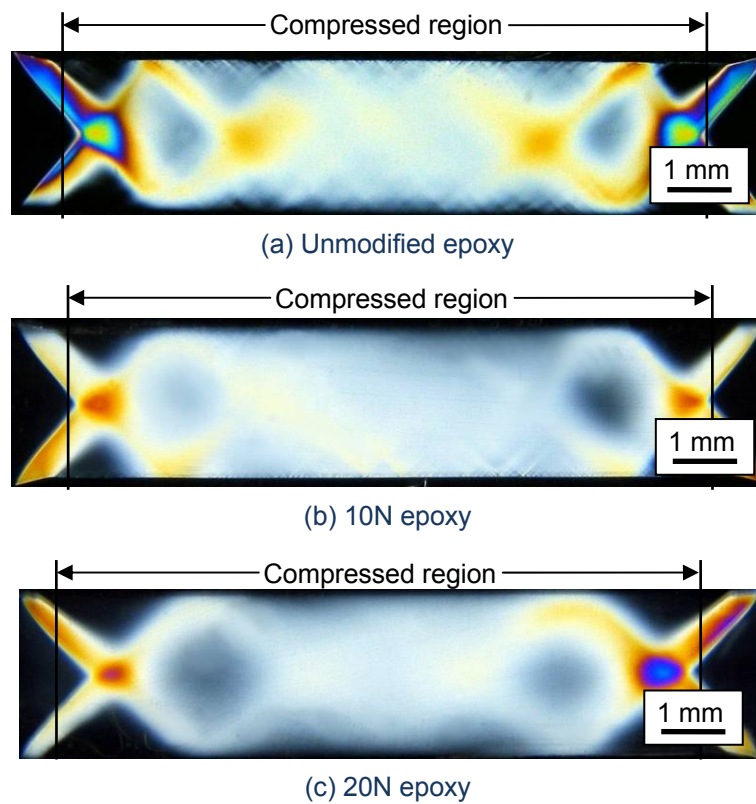


Figure 9.18. Images from compressed samples of the unmodified and modified anhydride cured DGEBA epoxies. The images show extensive shear banding in the compressed region.

### 9.6.2 Rubber-modified formulations

The value of  $E_c$  for the rubber-modified epoxy is 1.93 GPa and compared well to  $E_t$  measured at 2.18 GPa when the experimental error was considered. As with the nanosilica modified formulations, the value of  $E_c$  increases with nanosilica content and provides good agreement with  $E_t$  from tensile tests, as summarised in Table 9.5. The value of  $\sigma_{yc}$  was also found to remain constant for the hybrid-modified epoxies when the experimental error was considered, as shown in the plot of compressive true stress

versus compressive true strain in Figure 9.17. The curves are seen to reach a maximum at  $\sigma_{yc}$  and less strain softening occurs in the 9R epoxy compared to the unmodified epoxy. This would suggest that diffuse shear yielding occurs in the samples. With continued compression, each formulation was found to work-harden and this was more prevalent at higher nanosilica contents. The 9R modified epoxy was loaded to failure and a compressive true fracture strain of  $0.88 \pm 0.01$  was measured.

Table 9.6. Compressive Young's modulus,  $E_c$ , compressive true yield strength,  $\sigma_{yc}$ , and compressive true yield strain,  $\epsilon_{yc}$ , for rubber- and hybrid- modified anhydride cured DGEBA epoxies.

Formulation	$E_c$ (GPa)		$\sigma_{yc}$ (MPa)		$\epsilon_{yc}$ (true strain)	
	$\bar{x}$	$\pm$	$\bar{x}$	$\pm$	$\bar{x}$	$\pm$
9R	1.93	0.33	90	1	0.09	0.01
10N9R	2.59	0.70	85	1	0.09	0.01
15N9R	3.22	0.15	85	2	0.10	0.01
20N9R	3.12	0.10	86	1	0.10	0.01

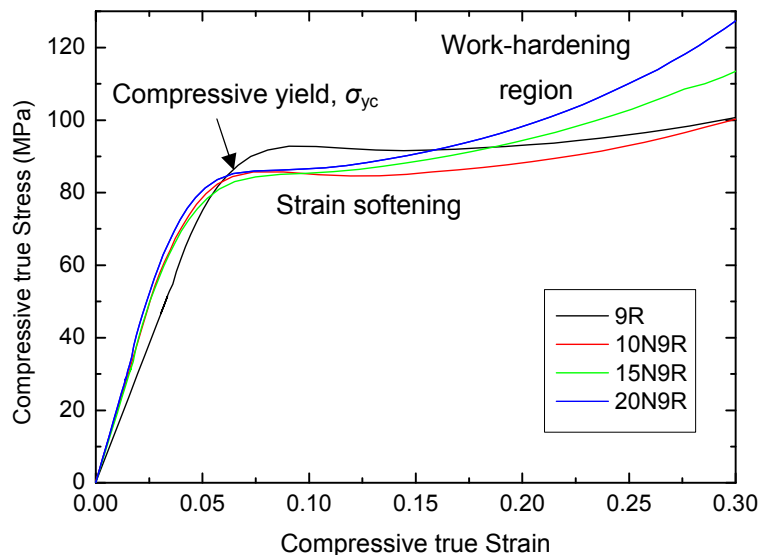


Figure 9.19. Compressive true stress versus compressive true strain for the rubber- and hybrid-modified anhydride cured DGEBA epoxies.

Samples of the rubber-modified formulations were loaded to strain softening and sectioned to be examined with transmission cross-polarised light microscopy. Shown in Figure 9.20(a), in the 9R epoxy, a small drop in stress was observed preceding  $\sigma_{yc}$ , the sample possesses definite shear band yielded regions in the compressed region of the sample. As the nanosilica content was increased, notably more shear band yielding occurred in the compressed region of the samples, shown in Figure 9.20(b) for the 10N9R epoxy. As with the nanosilica-modified formulations examined thus, the appearance of the shear bands was more diffuse in nature, but more prevalent in the

sample cross section and could point to the occurrence of more localised shear yielding [26] in the vicinity of the rubber and nanosilica particles. This was also found in the 15N9R sample shown in Figure 9.20(c).

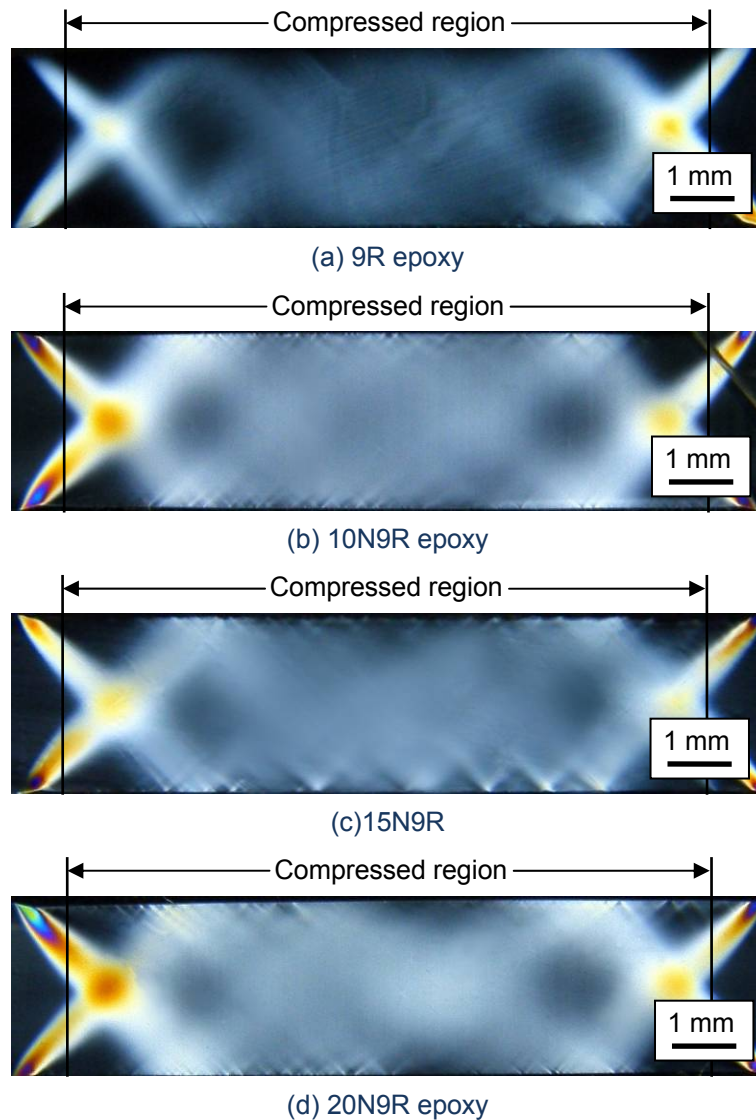


Figure 9.20. Images from compressed samples of the rubber- and hybrid-modified anhydride cured DGEBA epoxies.

Samples within the shear band regions of the 15N9R epoxy were microtome-cut and examined with TEM, shown in Figure 9.21. Evidence of deformation in the rubber was found, and this was parallel to the shear band. Amongst the nanosilica necklaces, debonding had occurred between some of particles, as shown circled. No such stretching of the rubber or debonding in the nanosilica necklaces was found when the morphology was examined previously in Figure 9.7. Therefore these features are a function of deformation and not through specimen preparation. It is unclear as to whether this was an important event, leading to initiation of void growth around the

nanosilica necklaces, however, is a noteworthy observation. AFM was also conducted on the parent epoxy of this section, with no additional information was obtained about the deformation that had occurred.

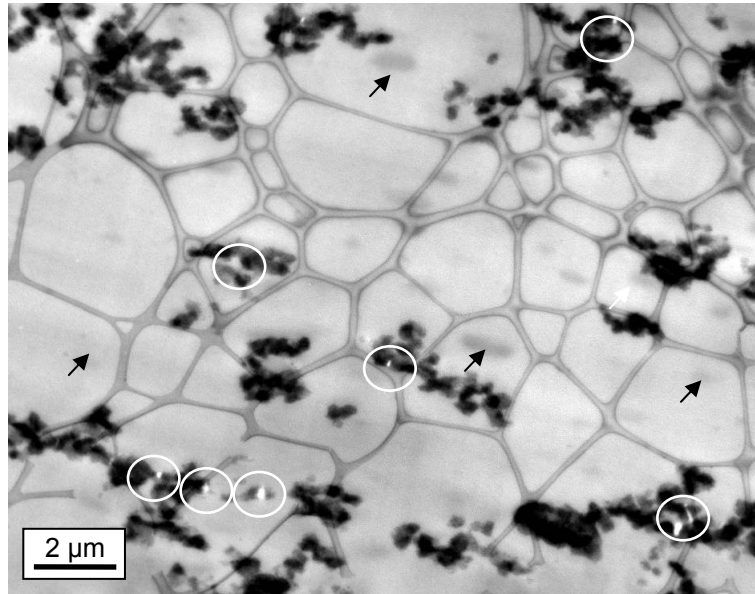


Figure 9.21. A TEM image from the shear band yielded region of the 15N9R anhydride cured DGEBA epoxy. The rubber particles appear elongated (arrows), parallel to the shear direction and the nanosilica necklaces have debonded (circled).

## 9.7 Fracture properties

SENB test were conducted on the unmodified and modified epoxy formulations. The values of fracture toughness,  $K_C$ , and fracture energy,  $G_C$ , are summarised in Table 9.7. For the unmodified epoxy, the values  $K_C = 0.54 \text{ MPa}\sqrt{\text{m}}$  and  $G_C = 83 \text{ J/m}^2$ . Such a system was also reported by Sohn Lee [219]. Good agreement was found for the values of  $K_C$  and  $G_C$  for the unmodified and modified epoxies.

### 9.7.1 Nanosilica-modified formulations

A two fold increase in  $G_C$  was observed with the addition of 20 wt. % nanosilica as shown in Table 9.7. Maximum values of  $K_C = 0.90 \text{ MPa}\sqrt{\text{m}}$  and  $G_C = 204 \text{ J/m}^2$  were observed for the 20N formulation. A steady increase was observed with a linear (blue) correlation in  $K_C$  and  $G_C$  shown in Figure 9.22.

### 9.7.2 Rubber-modified formulations

There are significant gains in  $K_C$  and  $G_C$  with the addition of rubber. A six fold increase in  $G_C$  was found for 9R and such increases have been previously reported in literature

[202, 220]. A steady increase in the fracture properties was observed, with a maximum value of  $G_C$  attained for the 10N9R formulation with  $K_C = 1.79 \text{ MPa}\sqrt{\text{m}}$  and  $G_C = 965 \text{ J/m}^2$ . Further addition of nanosilica in the 20N9R formulation resulted in a decrease in the fracture properties of the epoxy polymer. Figure 9.22 shows the variation of  $K_C$  and  $G_C$  with nanosilica content with quadratic (red) fits given to the data.

### Synergistic effect of hybrid toughening

From the values of  $G_C$  for the hybrid-modified epoxies, it was evident that the presence of both rubber micro-particles and nanosilica gives rise to synergy between the particles and was first reported by Kinloch et al. for this system [4]. This synergistic effect results in values of  $G_C$  that exceed the individual contributions of the constituent particles. For example, the predicted value of the 10N9R would be  $827 \text{ J/m}^2$  by taking the contributions of the unmodified epoxy, 9R and the 10N epoxy. The value of  $G_C$  was measured to be  $1051 \text{ J/m}^2$ , exceeding the individual contributions by some  $224 \text{ J/m}^2$ .

Table 9.7. Fracture toughness,  $K_C$ , and fracture energy,  $G_C$ , for the unmodified and modified anhydride cured DGEBA epoxies.

Formulation	$K_C$ (MPa $\sqrt{\text{m}}$ )		$G_C$ (J/m $^2$ )	
	$\bar{x}$	$\pm$	$\bar{x}$	$\pm$
Unmodified	0.54	0.09	83	15
10N	0.75	0.02	156	8
20N	0.90	0.06	204	5
<hr/>				
9R	1.27	0.08	671	50
10N9R	2.17	0.15	1051	97
15N9R	1.79	0.09	965	145
20N9R	1.50	0.14	665	100

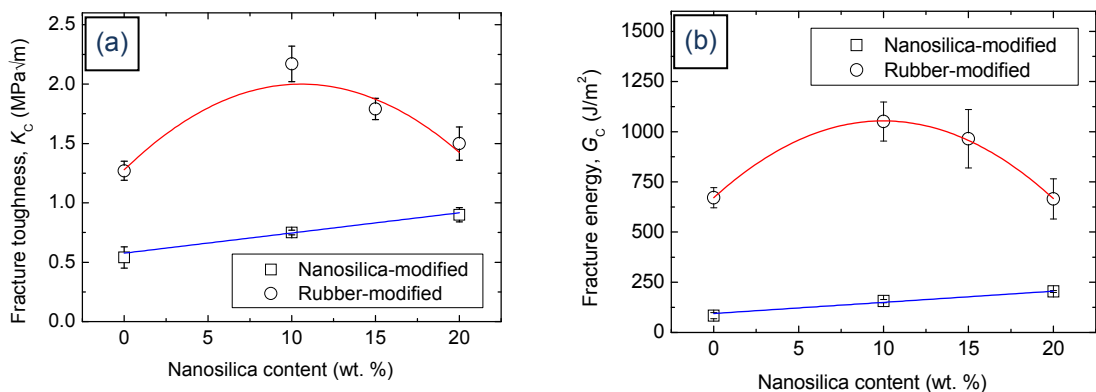


Figure 9.22. The (a) fracture toughness and (b) fracture energy for the unmodified and modified anhydride cured DGEBA. The general trends in the nanosilica-modified epoxies are shown with a linear fit (blue) and the rubber-modified epoxies with a quadratic fit (red).

### 9.7.3 Toughening mechanisms of the nanosilica-modified formulations

The plastic zone radius,  $r_{pz}$ , was calculated for the nanosilica modified formulations using Irwin's prediction in plane strain conditions [193]. The value of  $r_{pz}$  was found to be between 1.8  $\mu\text{m}$  for the unmodified epoxy and up to 5.9  $\mu\text{m}$  for 20N. This would be too small to identify using optical microscopy. Therefore the edge of the specimen of a 10N sample was examined, where the plastic zone radius would be 3 times larger, and would be expected to be 10.9  $\mu\text{m}$ . Shown with cross-polarised light microscopy in Figure 10.11, the measured plane stress plastic zone provides excellent agreement with Irwin's model. Shear band yielding is shown to occur in fracture specimens. Extensive shear band yielding was observed at the crack-tip when viewed with cross-polars. This has been shown by Lee and Yee [66] for micron-sized glass bead filled epoxies. Their extensive microscopy of the deformed fracture surfaces and sub-critically loaded crack-tips showed that shear deformation initiated at the particle-matrix interface. Due to the size limitations of the nanosilica used in this work, this cannot be shown optically. However, it is known that shear band yielding initiates at the strain inhomogeneities in the epoxy [12], thus, shear band yielding is expected to initiate at the particle as with micron-sized glass beads [66]. For the polished sections from compression tests, shear band yielding was found to increase with nanosilica content. Liang and Pearson [52] have shown this to be also true for nanosilica-modified fracture specimens, whilst it is acknowledged that the appearance of the shear bands is different in compression and fracture. They also found that the plastic zone scales up with nanosilica content, thus suggesting that the formation of shear bands provides an important contribution to the toughening that occurs in nanosilica-modified epoxies.

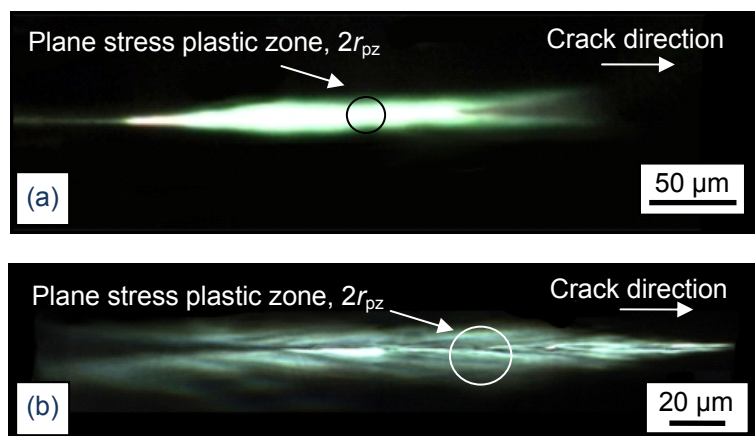


Figure 9.23. Cross-polarised light microscopy images (a, b) of 10N sub-critically loaded crack-tips. The two images are from different samples.

The fracture surface of the unmodified epoxy polymer was examined using FEGSEM. Shown in Figure 9.24, it was found to be smooth with no large-scale plastic deformation and typical of a brittle thermosetting polymer [221]. Step changes of the crack plane were found for all of the formulations that were studied. These are caused by crack forking due to excess stored elastic energy that was released at crack initiation. This forking, and the multi-planar nature of the surface, are ways of absorbing excess energy in brittle materials [222, 223]. The extent of forking or striation marks was found to remain constant for the nanosilica-modified epoxies, [7, 217].

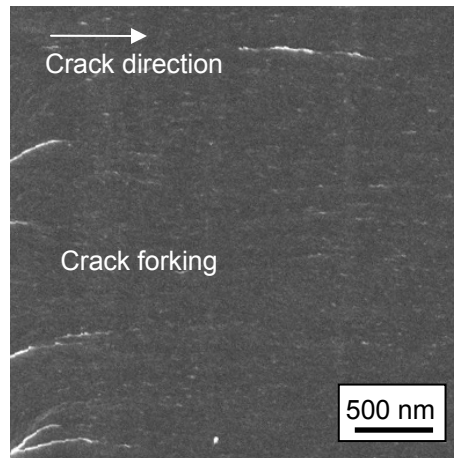


Figure 9.24. A FEGSEM micrograph of the fracture surface for the unmodified anhydride cured DGEBA epoxy [224].

The process zone region from fracture surface of the 20N samples was examined using FEGSEM, see Figure 9.25. Measurement of the identified nanosilica particles (shown with arrows) yielded a mean diameter of 40 nm. The debonding stress at the interface is proportional to  $r_p^{-1/2}$  and so one would expect the larger particles to debond more readily and can explain why the nanosilica particles seem larger on the fracture surface [34, 47, 49]. Due to particle size being many orders of magnitude smaller than the crack opening displacement, crack deflection and crack pinning are discounted as toughening mechanisms [7, 52]. Evidence of particle debonding and subsequent plastic void growth was found, as shown circled in Figure 9.25. The toughening mechanisms for rigid, micron-sized particles have been shown previously [46, 66], to be due to debonding of the particle followed by plastic void growth and shear yielding. The debonding process is generally considered to absorb little energy compared to the plastic deformation of the epoxy polymer [49, 188, 225] and is estimated to be of the order of 0.1 J/m<sup>2</sup> from Chen et al. [49]. However, debonding is essential because this reduces the constraint at the crack-tip and allows the epoxy polymer to deform plastically via a void-growth mechanism. Therefore, it was expected that the main

contributing factors to the improvement in fracture properties are shear band yielding and plastic void growth in the epoxy.

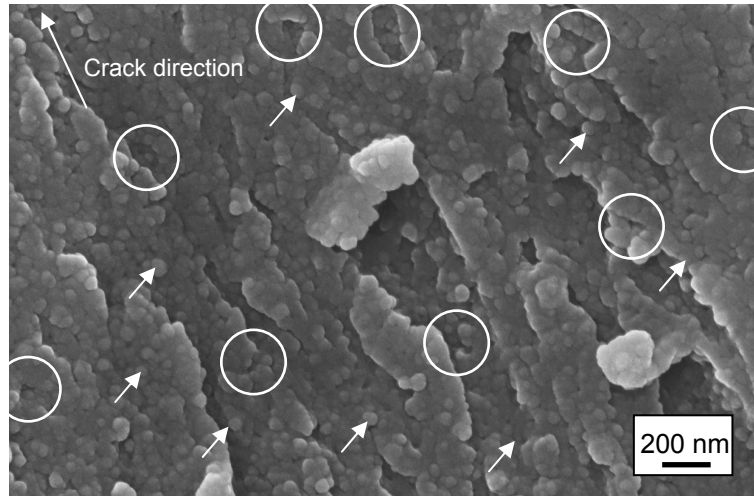


Figure 9.25. A FEGSEM micrograph of 20N anhydride cured DGEBA shows evidence of toughening. Some nanosilica particles are identified with arrows. Void growth was observed around some of the nanosilica particles, shown as circled [224].

A detailed analysis was conducted to quantify the amount of nanosilica particles that debond and then result in plastic void growth, reported in [60, 217] by using the FEGSEM images that had been obtained from the process zone region of the nanosilica-modified epoxies. The diameter of the voids around the nanosilica particles was found to be typically  $30 \pm 5$  nm. The voids were also observed in the fracture surfaces of samples with different concentrations of nanosilica. A detailed analysis to quantify the percentage of particles that debonded with subsequent void growth was conducted in collaboration with Sohn Lee [60] and  $15 \pm 5$  % and was found to be independent of the volume fraction of nanosilica in the epoxy.

#### 9.7.4 Toughening mechanisms of the rubber-modified formulations

The plastic zone radius,  $r_{pz}$ , for the rubber-modified formulations was calculated using Irwin's prediction in plane strain conditions [193] (using (4.12)) and was found to be 16  $\mu\text{m}$  and 20  $\mu\text{m}$  for the 9R and 10N9R epoxies and a maximum of 40  $\mu\text{m}$  for the 15N9R formulation. The plastic zone is thus, sufficiently large, that it would encompass several rubber and agglomerated-nanosilica particles. DN4PB was conducted on the 9R and the 9N9R epoxies to compare Irwin's predictions with the optically measured plastic zone. The optical images for the 9R epoxy show feathering at the crack-tip, as shown in Figure 9.26. This shear deformation is achieved via interactions of the stress fields ahead of the crack-tip, with the rubber particles, ultimately leading to enhanced plastic deformation [226-228]. The observed plastic zone is slightly smaller than the Irwin

prediction and suggests that the crack-tip plastic zone was not fully developed. Notably, shear band yielding was not observed in the feathered region of the cross-polarised image in Figure 9.26(b). Lee and Yee [67] have shown that if the angle of polarised light to shear band is not near zero, then the polarised light can be obscured by the sample. Clearly, shear band yielding does occur in the 9R epoxy.

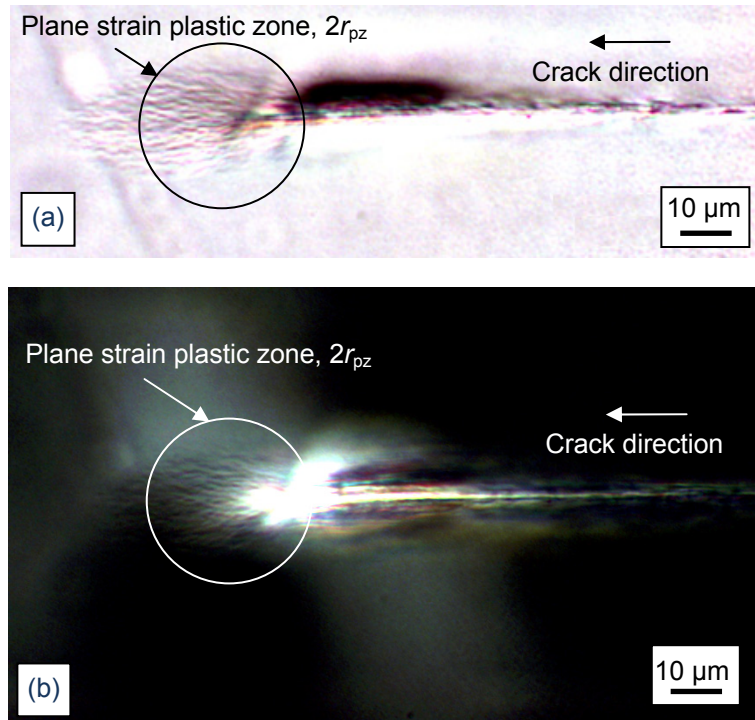


Figure 9.26. Images of a sub-critically loaded crack-tip for the 9R anhydride cured DGEBA.

Shows the crack-tip with (a) transmission light- and (b) cross-polarised light microscopy.

Evidence feathering shear band yielding in the epoxy was obtained.

The DN4PB optical image of the 10N9R epoxy was similar in appearance to the crack-tip of the 9R epoxy. The size of the plastic zone was larger than the 9R epoxy, as reflected by the improved fracture properties for this formulation. Evidence of shear band yielding by way of feathering is shown in Figure 9.27(a-c). The presence of the nanosilica particles has enhanced the toughness of the hybrid-modified epoxy.

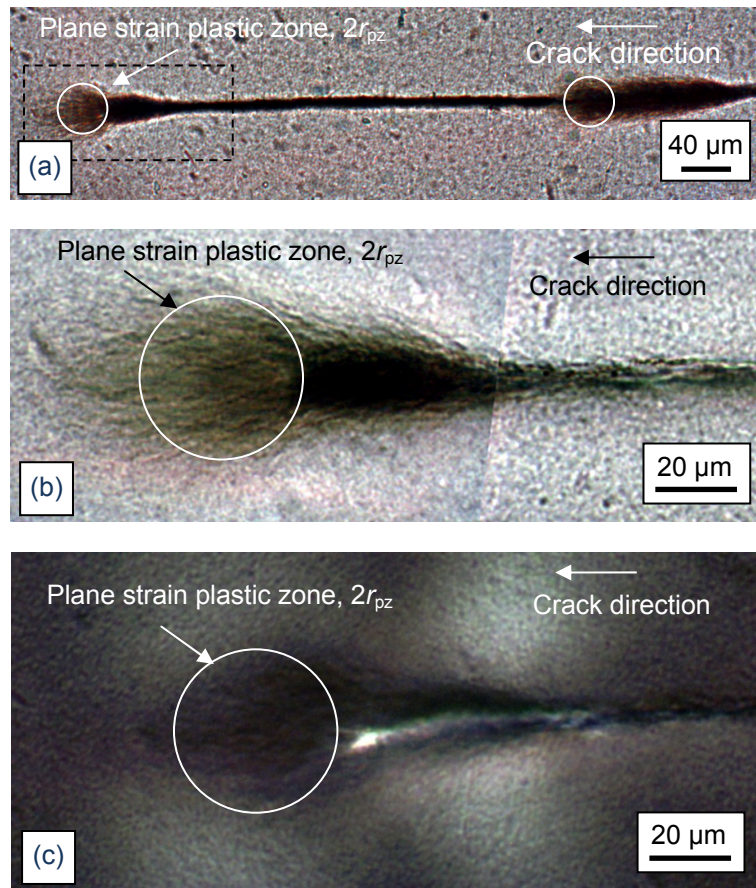


Figure 9.27. Images of a sub-critically loaded crack-tip for the 10N9R anhydride cured DGEBA epoxy. Shows the plane strain plastic zone ahead of the crack-tip with (a, b) transmitted light and (c) cross-polarised light microscopy.

FEGSEM was conducted on the rubber-modified epoxies. Shown in Figure 9.28, the process zone region of the 9R epoxy was found to contain extensive rubber-particle cavitation. This has been well established, as described in [98, 123, 222]. The void sizes were measured and a mean void diameter of  $1.24 \mu\text{m}$  was obtained. When this was compared to the mean rubber-particle size of  $1 \mu\text{m}$  from the AFM images in Figure 9.5, it was evident that the rubber particles internally cavitate and lead to subsequent void growth. The internal structure of a single rubber particle was examined, shown in the inset. Rubber was found to remain in the void and confirms that toughening occurred by internal cavitation and subsequent void growth in the epoxy polymer [99].

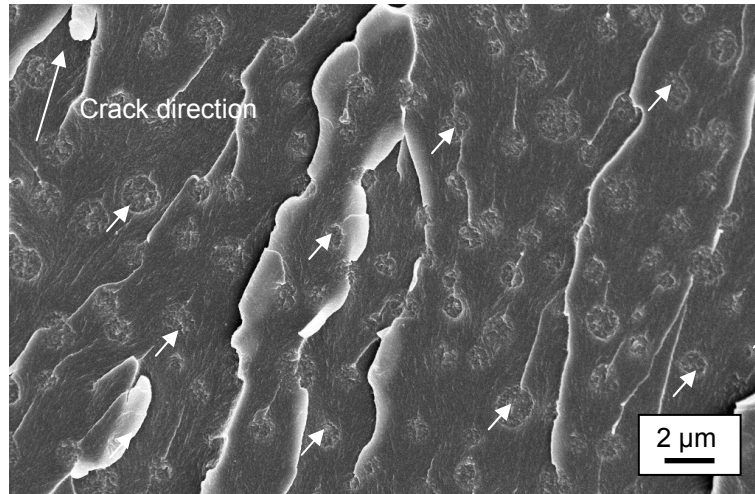


Figure 9.28. A FEGSEM micrograph of the fracture surface for the 9R anhydride cured DGEBA [224]. Some of the voids created by cavitation of the rubber particles are indicated.

A FEGSEM image of the fracture surface for the hybrid-modified (10N9R) epoxy is shown as a composite image in Figure 9.29. Whilst higher resolution images were obtained with the in-lens, it was much easier to identify the individual particles in with the SE2 lens. This technique was employed, when the fracture surfaces were complex in nature. Cavitation and subsequent void growth was identified for the rubber-particles in the hybrid-modified epoxy. Many fracture surface images were examined and a mean void diameter of 1.5-2  $\mu\text{m}$  was observed. High magnification images were obtained between the rubber particles to examine any deformation in the nanosilica necklaces, as shown in Figure 9.30. The image shows the same region of the fracture surface with the two lenses. Extensive epoxy deformation can be seen around the agglomerated nanosilica. The individual necklaces seem to remain well adhered, though it is recognised that the crack has propagated through the agglomerate. Thus, it is expected that the opposing fracture surface would contain an equal and opposite of the agglomerate as would be seen for the rubber micro-particle.

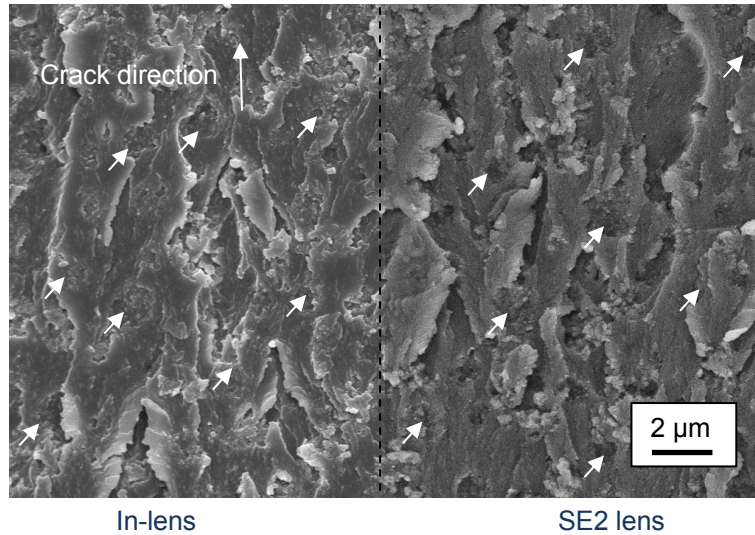


Figure 9.29. A FEGSEM image of the fracture surface for the 10N9R anhydride cured DGEBA epoxy [224]. A composite image shows extensive deformation in the process zone region. The rubber micro-particles are shown with arrows.

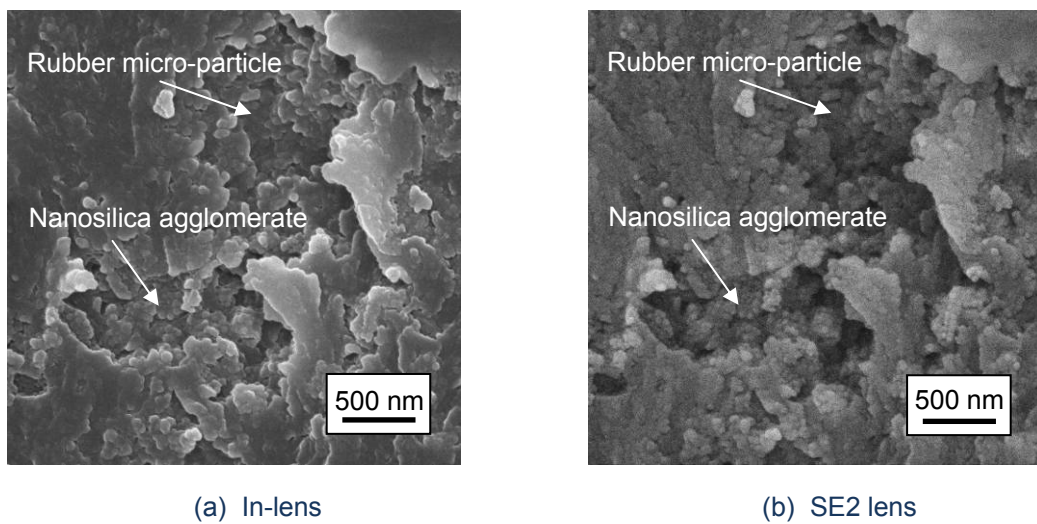


Figure 9.30. High magnification FEGSEM images of the 10N9R epoxy fracture surface [224], showing (a) in-lens and (b) SE2 lens images of a single rubber particle and deformation around the agglomerated nanosilica particles.

Improved properties were also observed for the 15N9R formulations, shown in Figure 9.31 with FEGSEM image taken with the in-lens (*left half*) and switching to SE2 lens (*right half*). Extensive deformation was observed amongst the nanosilica-rich phase of the epoxy. The rubber particles continue to cavitate, with the resulting void growth apparent, however, this starts to become difficult to pick up in the image. Closer examination (Figure 9.32) shows large deformation amongst the nanosilica necklaces, as indicated.

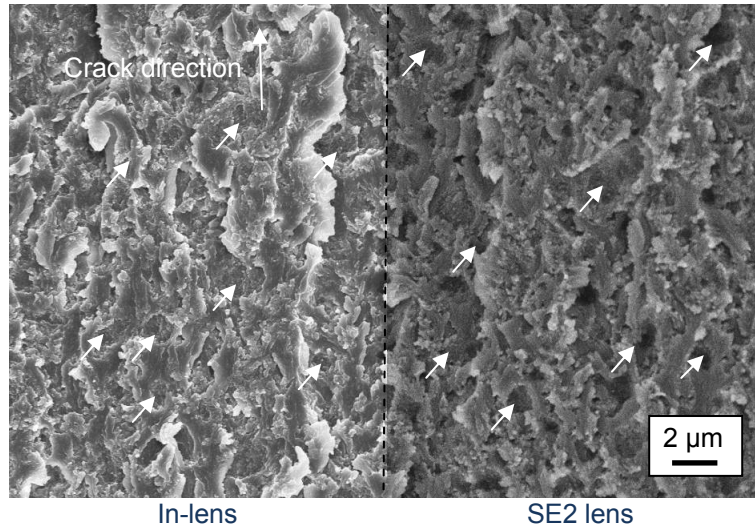


Figure 9.31. A FEGSEM image of the fracture surface for the 15N9R anhydride cured DGEBA epoxy [224]. A composite image identifies some cavitated rubber micro-particles.

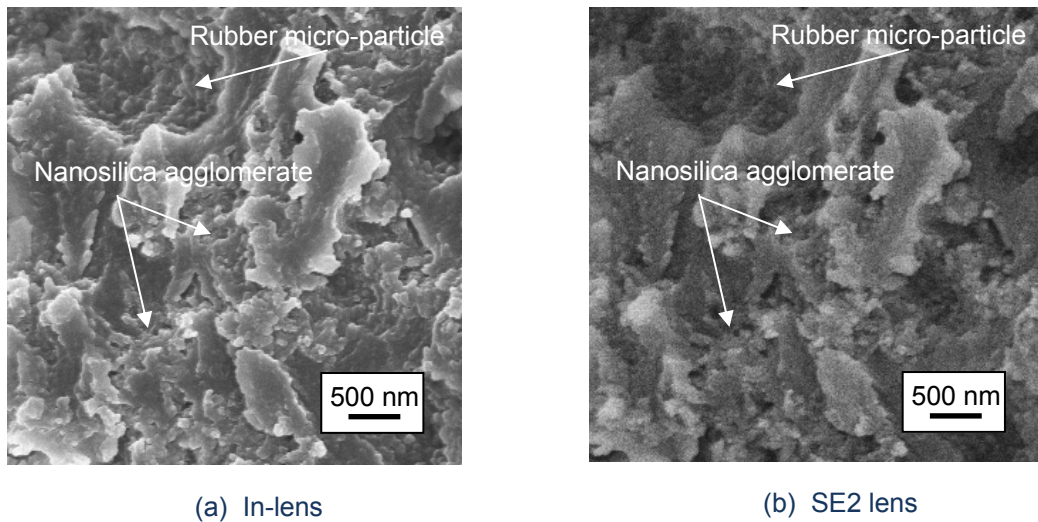


Figure 9.32. High magnification FEGSEM images of the 15N9R epoxy fracture surface [224], showing (a) in-lens and (b) SE2 lens images of a single rubber particle and deformation around the agglomerated nanosilica particles.

## 9.8 Composite properties

This section discusses the analysis of the fibre-matrix interfacial properties using single-fibre pull-out tests and short beam shear tests. The composite fracture properties are then examined in mode I using DCB tests. Finally high rate properties for the GFRP were examined with un-notched Charpy impact tests and ballistic impact tests.

### 9.8.1 Single-fibre properties

Matrix modification has been shown to improve the tensile strength [229] and tensile fatigue [152-154] performance for this composite, suggesting that the fibre-matrix interface was not compromised by the matrix modification with nanosilica. The addition of high modulus nanosilica particles, has improved the stiffness of the matrix compared to the unmodified epoxy. With a reduction in the mismatch of stiffness between the fibre and matrix, improvements in flexural and compressive properties can be achieved [230].

Failure always resulted in a residue meniscus of matrix on the fibre and would suggest a strong interface for the fibre-matrix formulations that were considered [231], and a summary of results is shown in Table 9.8. Shown in Figure 9.33, is the shear strength of the unmodified and modified-fibre matrix GFRPs plotted against embedded fibre length. The strength of the fibre-matrix interface is independent of embedded length, with some error due to the meniscus of epoxy on the fibre at very short embedded lengths [232]. An effort was made to produce a range of embedded lengths to provide accurate data, and all valid test results are shown in the graph. As expected, the value of the mean interfacial shear strength,  $\tau_{\max}$  was found to be independent of embedded length. The general trend of the results would suggest that adding nanosilica to the epoxy improves the value of  $\tau_{\max}$ . For the unmodified epoxy,  $\tau_{\max} = 53$  MPa. The addition of nanosilica increased the interfacial shear strength and the value of  $\tau_{\max}$  approaches the tensile strength for this formulation of bulk matrix, and thus this would be the limit of interfacial properties. No difference was found for the 9R formulation compared to the unmodified epoxy.

Table 9.8. Pull-out shear strength,  $\tau_{\max}$ , from single-fibre pull-out tests for the unmodified and modified anhydride cured DGEBA single-fibre GFRPs.

Formulation	$\tau_{\max}$ (MPa)	
	$\bar{x}$	$\pm$
Unmodified	53	3
10N	75	5
9R	51	4
10N9R	61	7

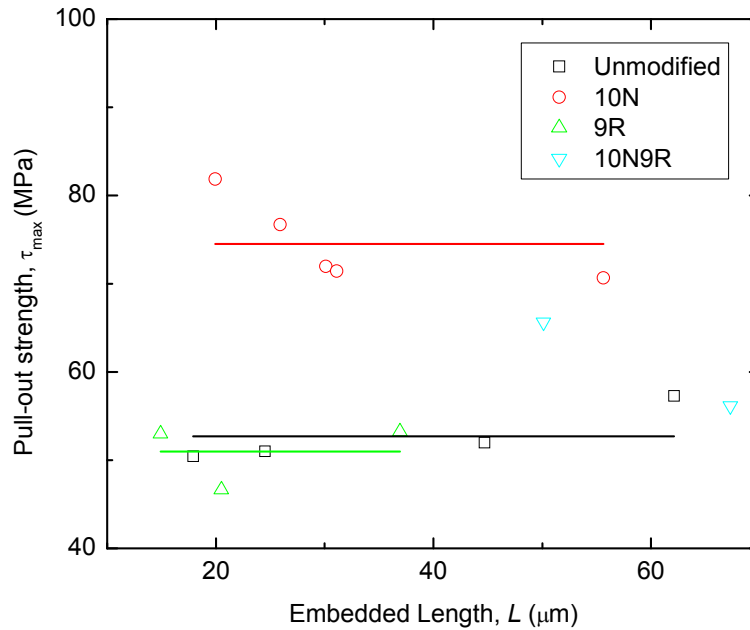


Figure 9.33. Pull-out shear strength versus embedded length for the unmodified and modified anhydride cured DGEBA single-fibre GFRPs.

### 9.8.2 Short beam shear properties

Short beam shear tests were conducted on the UD GFRP and mean values for the interfacial shear strength,  $\sigma_{\text{SBS}}$ , were obtained for the unmodified and modified epoxy formulations. The trends in the short beam shear strength agree qualitatively with the data from single-fibre pull-out tests. Nanosilica-modified epoxy formulations showed the best interlaminar shear strength; over 10% better than the unmodified GFRP. The addition of rubber to the epoxy matrix resulted in a reduction in the mean value of  $\sigma_{\text{SBS}}$ . This is to be expected due to a reduction in the in matrix modulus [230]. A little improvement was found for the hybrid GFRP; however, the presence of rubber in the hybrid formulation reduces the short beam shear strength slightly.

Table 9.9. Interlaminar shear strength,  $\sigma_{\text{SBS}}$ , for the unmodified and modified anhydride cured DGEBA UD GFRPs.

Formulation	Short beam shear strength, $\sigma_{\text{SBS}}$ (MPa)	
	$\bar{x}$	$\pm$
Unmodified	57.2	1.7
10N	64.1	1.6
9R	56.7	1.7
10N9R	61.6	0.4

### 9.8.3 Flexural modulus

The flexural modulus was measured under quasi-static conditions for the UD GFRP (Table 9.10) and QI GFRP (Table 9.11). The results confirm complete consolidation of void-free composite beams, and allow calculation of crack length independent mode I fracture energy,  $G_{IC}$ . The modulus was consistent for each of the different modifications of epoxy. This indicates that the GFRPs were infused to a constant fibre volume fraction [204].

Table 9.10. Flexural Modulus,  $E_f$ , and fracture initiation energy,  $G_{IC\ INT}$ , and fracture propagation energy,  $G_{IC\ PROP}$ , for the unmodified and nanosilica-modified anhydride cured DGEBA UD GFRPs.

Formulation	$E_f$ (GPa)		$G_{IC\ INT}$ (J/m <sup>2</sup> )		$G_{IC\ PROP}$ (J/m <sup>2</sup> )	
	$\bar{x}$	$\pm$	$\bar{x}$	$\pm$	$\bar{x}$	$\pm$
Unmodified	59	6	330	150	1105	57
10N	68	6	1015	195	2009	60
9R	55	8	885	60	1546	47
10N9R	67	4	860	90	1581	51

Table 9.11. Flexural Modulus,  $E_f$ , and fracture initiation energy,  $G_{IC\ INT}$ , and fracture propagation energy,  $G_{IC\ PROP}$ , for the unmodified and nanosilica-modified anhydride cured DGEBA QI GFRPs.

Formulation	$E_f$ (GPa)		$G_{IC\ INT}$ (J/m <sup>2</sup> )		$G_{IC\ PROP}$ (J/m <sup>2</sup> )	
	$\bar{x}$	$\pm$	$\bar{x}$	$\pm$	$\bar{x}$	$\pm$
Unmodified	40	3	718	96	705	36
10N	39	3	626	146	677	28
9R	39	2	1035	61	1231	69
10N9R	41	2	1263	275	1440	60

### 9.8.4 Composite mode I fracture

The unmodified and modified UD and QI GFRPs were fractured in mode I using the double cantilever beam (DCB) test method. Specimens were produced with a 50 mm insert, and fracture was analysed from the region at the end of the insert, until 20 mm of steady state crack propagation was observed in the composites. A summary of values for the initiation fracture energy from the insert,  $G_{IC\ INT}$ , and the mean propagation energy,  $G_{IC\ PROP}$ , are shown in Table 9.10 for the UD GFRPs and in Table 9.11 for the QI GFRPs.

Examining the UD GFRPs, initiation in the unmodified epoxy occurred at a low fracture energy,  $G_{IC\ INT}$ , of  $330 \pm 150$  J/m<sup>2</sup>. A steady state value was taken as the mean value of  $G_{IC\ PROP}$ , and is quoted as 1105 J/m<sup>2</sup>. From examining the R-curves in Figure 9.34, it is apparent that a steady state value was not achieved, and a rising R-curve was visible

for all the formulations. The addition of nanosilica (10N) provides marked improvements in the fracture energy at initiation and propagation conditions. The addition of rubber to the epoxy provided an improvement in the mode I fracture energy, however, no further effect of toughening was found for the hybrid. No trend was observed when the UD GFRP mode I fracture energy was compared to the bulk fracture energy, shown in Figure 9.35. The relative difference between the initiation and propagation values indicates the amount of fibre bridging that occurs in this GFRP architecture.

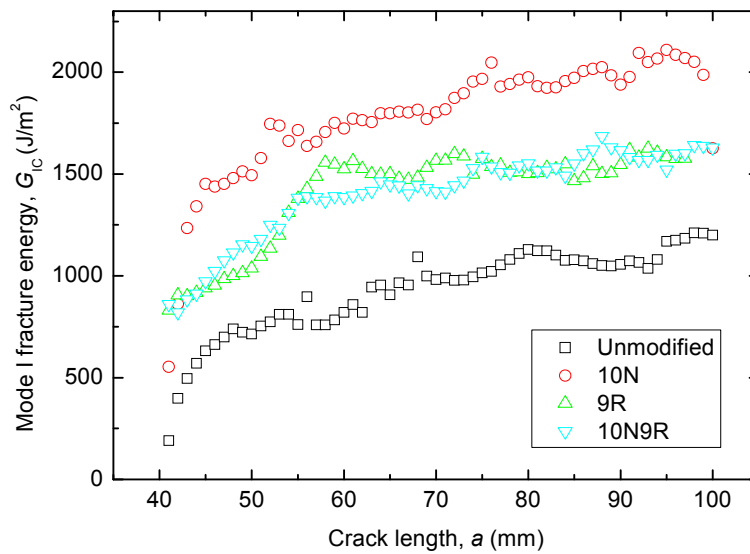


Figure 9.34. Mode I UD GFRP fracture energy versus crack length,  $a$ , for unmodified and modified anhydride cured DGEBA UD GFRPs.

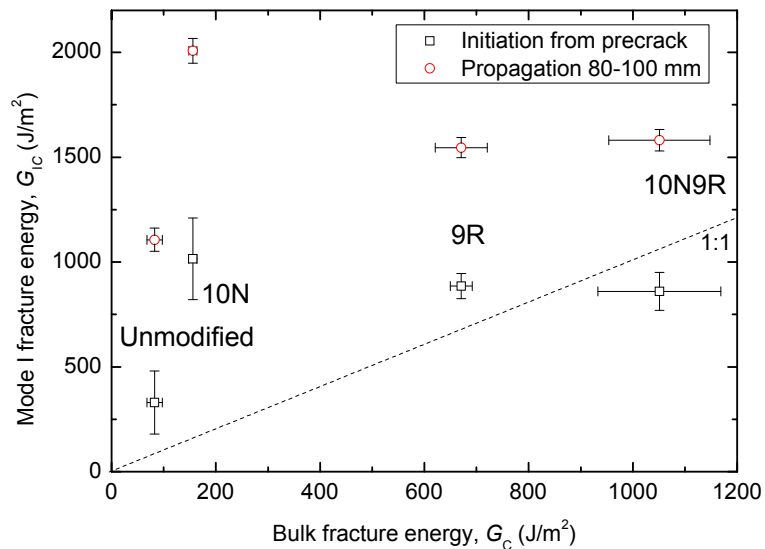


Figure 9.35. Mode I UD GFRP fracture energy versus bulk fracture energy for unmodified and modified anhydride cured DGEBA epoxies.

Due to excessive fibre bridging, it was difficult to draw conclusions on the mode I performance of the composite material. A second fibre morphology was produced with

quasi-isotropic fibre arrangement, although, still with a  $0^\circ/0^\circ$  interface in the fracture plane. Table 9.11 shows a summary of the flexural modulus,  $E_f$ , and mode I fracture initiation,  $G_{IC\ INT}$ , and propagation energies,  $G_{IC\ PROP}$ . With less fibre bridging occurring, a different trend in the mode I fracture properties was observed, as shown by the R-curves in Figure 9.36. The addition of nanosilica provided no improvement the  $G_{IC\ INT}$  or  $G_{IC\ PROP}$  compared to the unmodified epoxy. Steady state values were attained at a shorter crack length, see Figure 9.36, and would suggest better fibre-matrix interfacial adhesion. The addition of rubber resulted in increased mean  $G_{IC}$  values. Similar values for  $G_{IC\ INT}$  were obtained for the 10N9R hybrid GFRP compared to the 9R GFRP, however a notable increase in the value of  $G_{IC\ PROP}$  was obtained for the hybrid, and this value was double that for the unmodified epoxy.

For the QI GFRPs, a roughly 1:1 transfer of toughness was obtained when the mode I fracture initiation and propagation values are compared to their bulk polymer counterparts, shown as a plot in Figure 9.37. The smaller difference between the initiation and propagation values indicates that less fibre bridging occurs in the QI GFRP than in the UD GFRP.

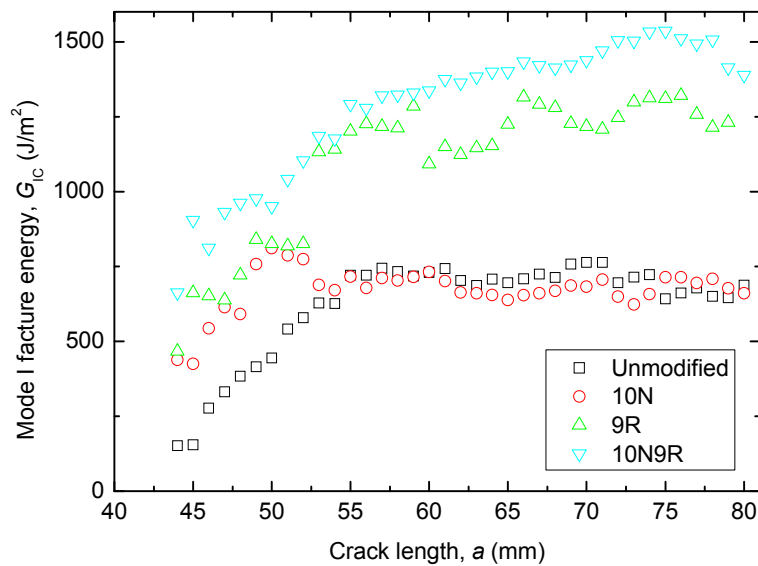


Figure 9.36. Mode I QI GFRP fracture energy versus crack length,  $a$ , for unmodified and modified anhydride cured DGEBA epoxies.

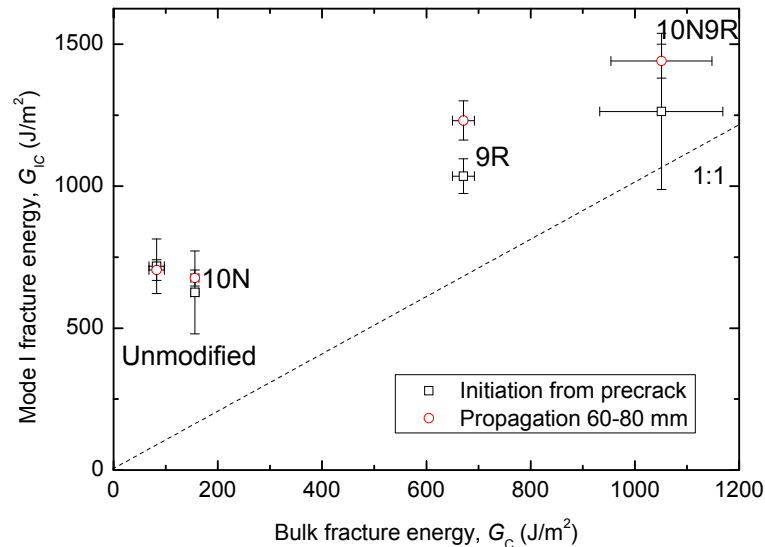


Figure 9.37. Mode I QI GFRP fracture energy versus bulk fracture energy for the unmodified and modified anhydride cured DGEBA epoxies.

### 9.8.5 Composite toughening mechanisms

The plastic zone radius,  $r_{pz}$ , was calculated for the formulations using Irwin's prediction in plane strain conditions [193]. The rule of mixtures was used to obtain a transverse Young's modulus for the QI GFRP [3] and  $G_C$  was assumed to be the bulk fracture energy to provide an estimate of the plastic zone radius. For the unmodified and 10N QI GFRPs,  $r_{pz} = 21\text{-}35 \mu\text{m}$  and for the rubber-modified and hybrid formulations  $r_{pz} = 250\text{-}296 \mu\text{m}$ . This would suggest that the unmodified and 10N plastic zones contain a region equal to two fibres, each side of the crack-tip, where the fibre diameter was measured as  $17 \mu\text{m}$ . The rubber-modified systems would encompass a much larger plastic deformation zone, the order of tens of fibres. The rubber-modified systems attain much improved fracture properties, and this reflects on the larger deformation areas in the epoxy. The fracture surfaces from the mode I QI GFRP specimens were examined using field emission gun scanning electron microscopy (FEGSEM) to find evidence of the toughening mechanisms that have occurred.

The unmodified epoxy GFRP failed with a mixture of cohesive and fibre-matrix interfacial failure, see Figure 9.38(a). Some debonding and fibre pullout was observed on the fracture surface. There was no evidence of excessive plastic deformation and plenty of striation marks on the surface crack propagated through the GFRP [222, 223], as shown for the bulk unmodified epoxy previously in Figure 9.24. Figure 9.38(b) shows the fracture surface at higher magnification. The fibre surface appeared to be bare, with little evidence of epoxy remaining on the surface of the fibre. This suggests that failure occurs at the fibre-matrix interface or very close to the interface.

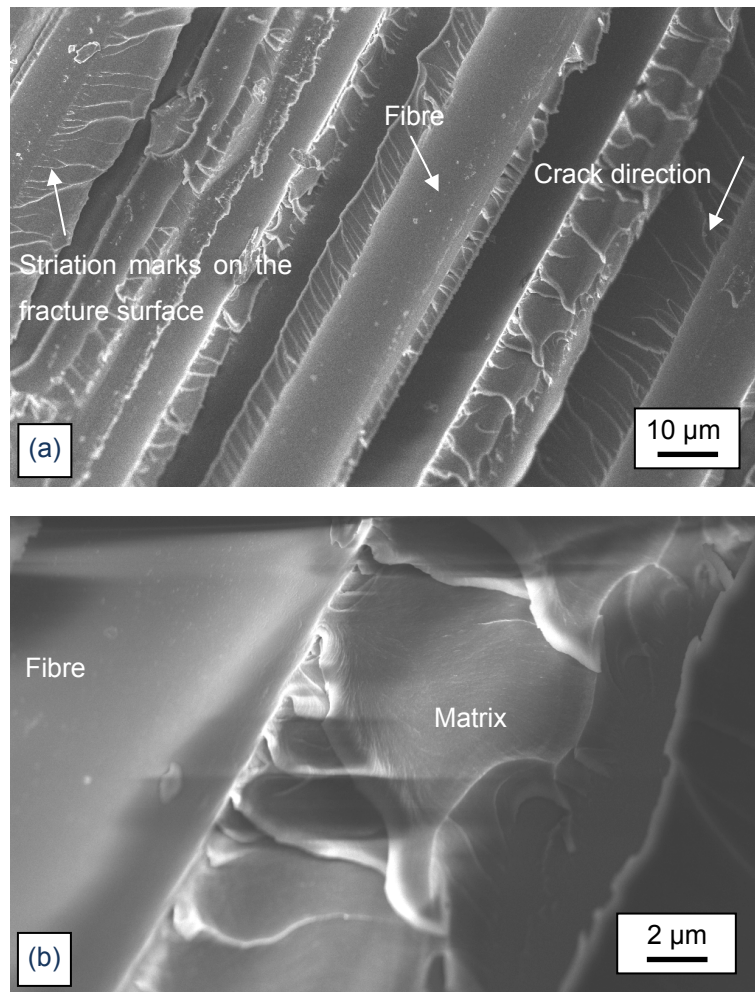


Figure 9.38. Shows (a, b), FEGSEM images of the fracture surface for the anhydride cured DGEBA QI GFRP, taken in the steady state propagation region of crack propagation.

The fracture surface for the 10N modified GFRP, shown at low magnification in Figure 9.39(a), was similar in appearance as the unmodified epoxy. The surface exhibited a relatively brittle appearance, although, a significant amount of debris was observed. However, it is unclear debris whether this was an artefact from sectioning to produce the FEGSEM specimen. A region of the fibre-matrix interface where plastic deformation had occurred was examined. As the magnification was increased, plenty of voids were observed in the epoxy. These were a similar order of magnitude in size as the nanosilica particles, and careful examination showed evidence of void growth around single nanosilica particles in the epoxy. Evidence of plastic void growth around the debonded nanosilica particles are shown circled in Figure 9.39(b) with arrows indicating to some of the nanosilica particles. There was evidence of residual epoxy on the fibre, and this observation agrees well with the findings that the addition of nanosilica results in better interfacial adhesion between the fibre and matrix. Close examination, focusing on some of the epoxy of the fibre showed that amongst the

residue, some nanosilica particles were still bonded to the epoxy, which was bonded to the fibre, shown with arrows in Figure 9.39(c). There were also many crater-like cavities in the epoxy, where the particles had been debonded from the epoxy.

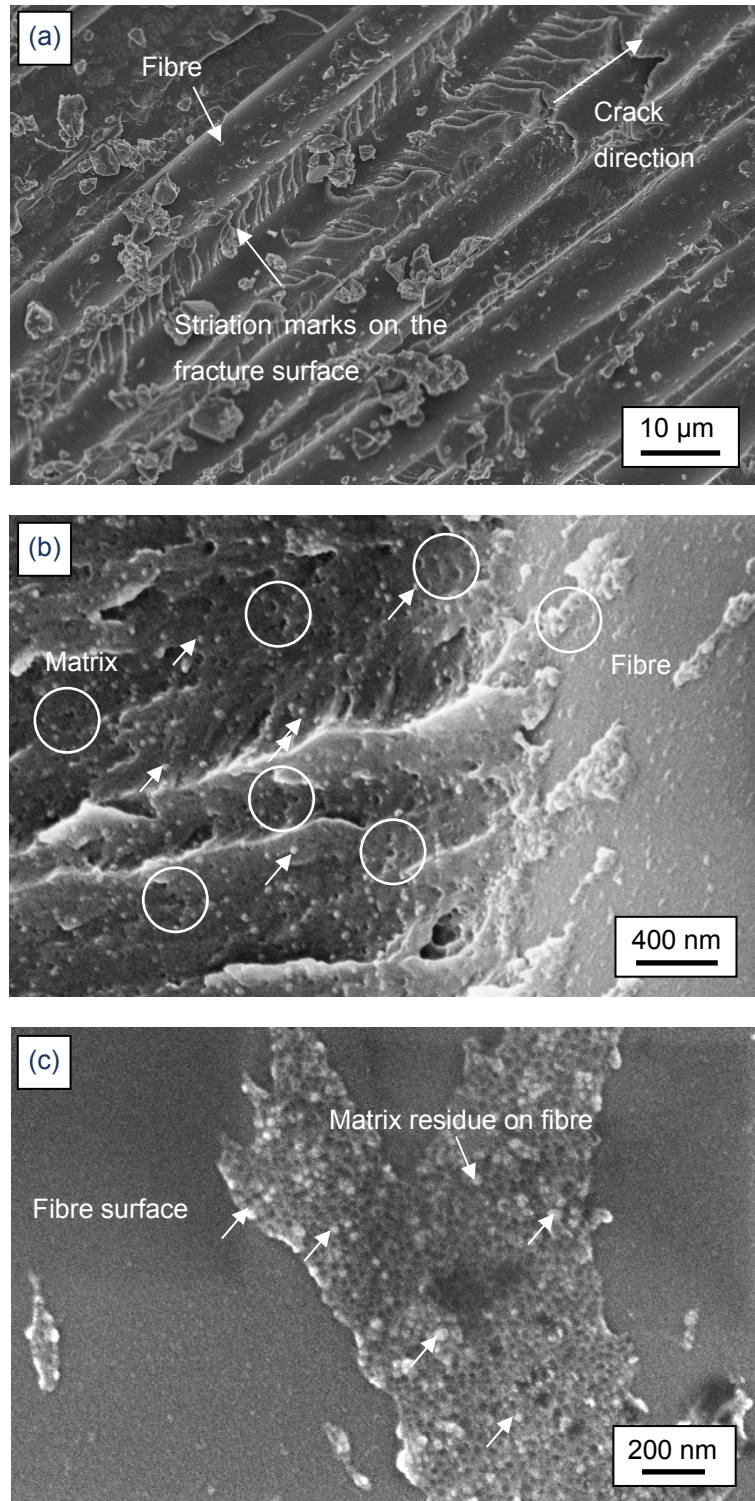


Figure 9.39. Shows (a-c) FEGSEM images of the mode I fracture surface for the 10N anhydride cured DGEBA QI GFRP. The nanosilica particles are indicated in the fracture surface (arrows) and some plastic void growth in the 10N epoxy is shown circled.

When the 9R GFRP was examined, see Figure 9.40(a), plenty of voids were present in the matrix rich regions of the epoxy. These revealed that the rubber particles have cavitated in the epoxy, and subsequent void growth had occurred in the epoxy. The diameter of these voids was measured and cavities up to 2  $\mu\text{m}$  with a mean diameter of  $1.24 \pm 0.46 \mu\text{m}$  were measured. The fibres appeared to be bare, with no epoxy remaining on the surface of the fibres. The fibre-matrix interface region was examined and confirmed that very little epoxy remained on the fibre, shown in Figure 9.40(b). The fibre-matrix adhesion was found to be very comparable to the unmodified epoxy from single-fibre pull-out tests. It was postulated that in the 9R GFRP, the matrix is tougher than the interfacial region of the composite, thus the crack preferentially takes the path of least resistance.

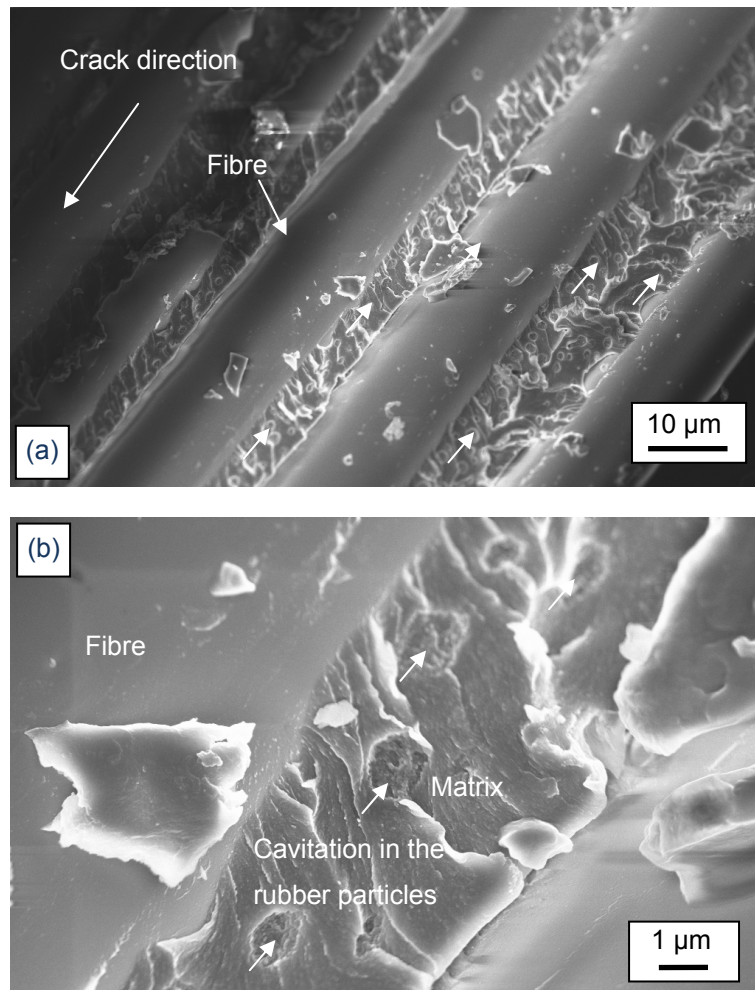
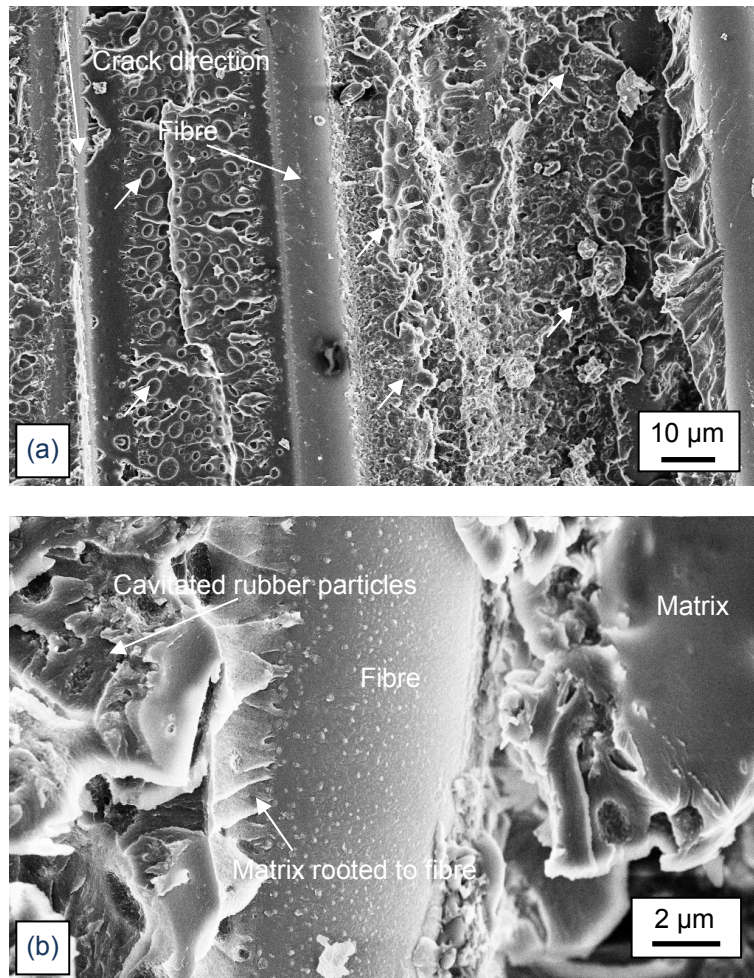


Figure 9.40. Shows (a, b) FEGSEM images of the mode I fracture surface for the 9R anhydride cured DGEBA QI GFRP with some cavitated rubber particles shown with arrows.

The hybrid-modified GFRP fracture surface was very rough in appearance, with extensive plastic deformation having occurred in the epoxy matrix, see Figure 9.41(a). It was possible to identify voids up to 2  $\mu\text{m}$  in diameter in the epoxy from rubber particle

cavitation (arrows) and similar morphologies as the bulk hybrid epoxy as was shown previously in Figure 9.41. Upon closer examination, a significant amount of matrix epoxy was retained on the fibre in small clumps (shown circled in Figure 9.41(b)) and would suggest better fibre-matrix adhesion than in the 9R epoxy GFRP. It was possible to identify evidence of void growth around the nanosilica necklaces in the epoxy, shown circled in Figure 9.41(c) and at high magnification in Figure 9.41(d). It was easier to find such evidence regions where the fibre had debonded from the matrix because the matrix was smooth and secondly because rubber cavitation would not occur in such regions.



*Continues onto next page*

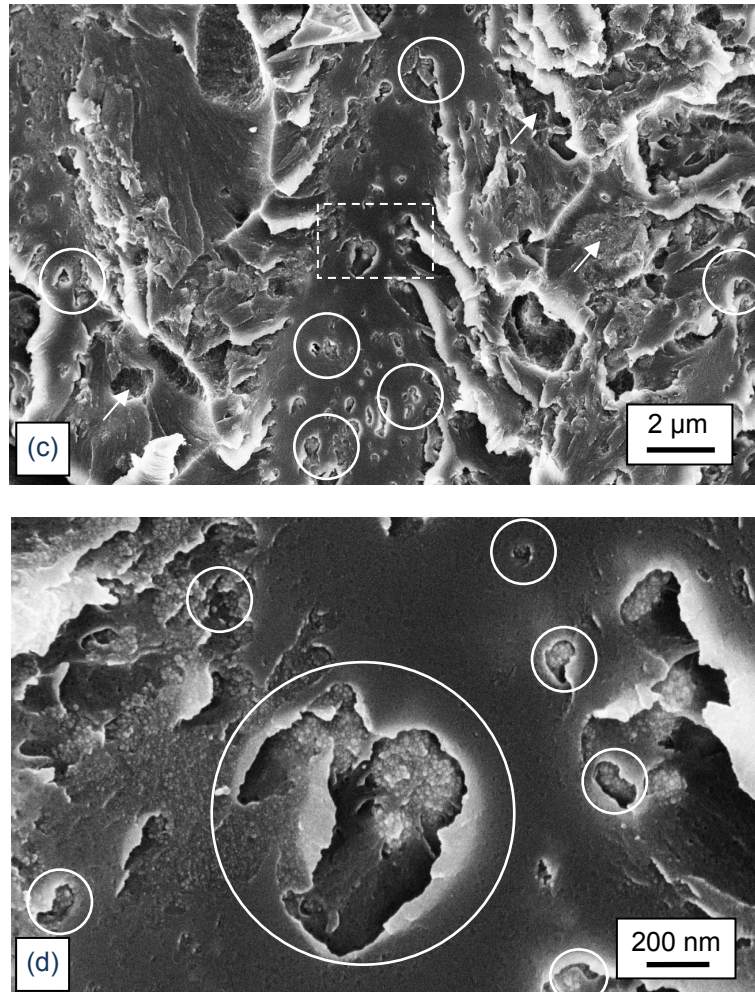


Figure 9.41. Shows (a-d) FEGSEM images of the mode I fracture surface from the steady state propagation region of the 10N9R anhydride cured DGEBA QI GFRP. Some rubber particles are indicated with arrows and plastic void growth around agglomerated nanosilica is circled.

## 9.9 Chapter summary

An anhydride cured DGEBA epoxy modified with nanosilica and rubber micro-particles was examined as a bulk material and glass-reinforced polymer composite. The value of  $T_g$  was found to remain constant at 140 °C for the unmodified epoxy and nanosilica modified up to 20 wt. %. The cross-link density remains unchanged when nanosilica was added to this epoxy. For the rubber-modified formulations, a steady reduction in the mean  $T_g$  occurred with increasing nanosilica content. With a decrease of 16 °C compared to the unmodified epoxy, a maximum of approximately 5 vol. % remains in solution for the 20N9R formulation compared to 1 vol. % for the 9R epoxy.

AFM was used to examine the morphology of the nanosilica and rubber micro-particles in the epoxy. The 20 nm particles have been shown to remain well dispersed up to 20 wt. % in the bulk and GFRP composite. The nanosilica particles are not filtered out

during the infusion process to manufacture the continuous fibre composite. For the rubber-modified formulations, the CTBN phase separates into spherical particles up to 1  $\mu\text{m}$  in diameter in the 9R formulation, and increase slightly in the hybrid epoxies to 1.5  $\mu\text{m}$ . FIB machining and subsequent TEM imaging confirms that similar morphologies are present for the rubber-modified epoxies in the GFRP. This was also verified when SEM was conducted on the composite fracture surfaces.

By running the cure cycle for anhydride cure DGEBA formulations in the rheometer, the viscosity properties under as a function of cure time was examined. The 90 °C temperature hold provided vital time for reaction induced phase separation to occur in the rubber-modified epoxies. Vitrification occurs quickly in the final stage of the cure when the temperature is increased to 160 °C. The nanosilica particles are expected to agglomerate when reaction induced phase separation initiates in the hybrid (10N9R) epoxy.

The tensile Young's modulus was found to increase with nanosilica content up to 3.47 GPa for 20N modification from a baseline value of 2.74 GPa for the unmodified epoxy. The addition of rubber resulted in a reduction in the Young's modulus and a value of 2.18 GPa was measured for the 9R epoxy. The addition of nanosilica restored some of the loss of stiffness in the 10N9R hybrid epoxy (2.55 GPa). The measured Young's modulus from plane strain compression tests yielded similar results for the mean Young's modulus, although the experimental error was larger.

No notable difference in the compressive or tensile yield strength was obtained with the addition of nanosilica to the epoxy. Polished sections were examined for compression specimen cross sections and the appearance of shear banding became more diffuse with increasing nanosilica content. There was a large decrease in the yield strength when rubber was added to the epoxy in tension and compression. The addition of nanosilica to the rubber-modified epoxies increased the yield strength slightly, however, no further change in the yield strength was observed with further addition of nanosilica. The interpretation of the yield strength is complex because with increasing nanosilica content in the hybrid formulations, the amount of rubber that phase separates decreases. It was postulated that the addition of agglomerated nanosilica would be expected to reduce the yield strength since the particles may be loosely bonded together. However, less rubber in the epoxy would increase the yield strength with a roughly equal and opposite magnitude. For the rubber-modified epoxies, a small drop in stress was observed at the yield strength, and would suggest that diffuse and unfocussed shear band yielding occurs in this epoxy. Strain softened samples of the

rubber-modified epoxies were observed with cross polarised light and indeed, diffuse shear yielding was observed in the gauge area of the specimens. As with the nanosilica modified formulations, the appearance of shear banding was notably more obvious for the hybrid epoxies compared to the 9R epoxy. The shear bands also appeared to be more diffuse with increasing nanosilica content.

A two fold increase in the fracture energy was obtained with 20N modification to the epoxy. Fracture surface imaging showed that the primary contribution of toughening in the nanosilica-modified epoxies was obtained from shear band yielding, particle debonding and subsequent void growth. A six fold increase in the fracture properties was obtained in the 9R formulation with the value of  $G_C = 671 \text{ J/m}^2$  and further improvements were found in the hybrid-modified epoxies with a maximum value for 15N9R and the value of  $G_C = 965 \text{ J/m}^2$ . With further addition of nanosilica, the fracture value of the hybrid began to decrease and the value of  $G_C = 665 \text{ J/m}^2$ . Rubber particle cavitation was successfully identified in all of the rubber-modified systems and evidence of plastic void growth around the nanosilica necklaces was also identified.

Single-fibre pull-out tests and short beam shear tests yielded the same trend in the fibre-matrix interfacial properties for the modified matrix GFRPs. The addition of nanosilica improved the interfacial strength in the composite by increasing the modulus of the matrix and decreasing steep change in the stiffness that occurs between the fibre and the matrix at the interface. A maximum value of  $\tau_{\max} = 75 \text{ MPa}$  for the 10N GFRP. The addition of rubber in the 9R GFRP had little effect on the interfacial properties whilst the 10N9R hybrid resulted in an improvement in the mean value of  $\tau_{\max}$  at 61 MPa for 10N9R GFRP.

Continuously reinforced GFRP composites were manufactured using resin infusion under flexible tooling to produce consistent and void-free composites. Polished cross sections show a variable interlaminar region in the UD and QI composites. Results from mode I fracture of the QI GFRP composites show that no difference  $G_{IC}$  occurred with 10N modification. This was attributed to the improvement in fibre-matrix adhesion, and results in less fibre bridging in the composite. A parity in transfer of toughness was achieved for the GFRP with rubber modification and the highest values of  $G_{IC}$  were measured for the hybrid epoxy GFRP. For the unmodified and nanosilica-modified composites, the plastic zone region was estimated to be roughly the two glass-fibres. The rubber-modified formulations had a much larger plastic zone region that was expected to include many tens of fibres in the process zone region of the composite and explain the much larger measured fracture energies. Composite fracture tests

yielded variable results, and show that the interfacial properties of the modified matrix are an important parameter in determining toughenability of the fibre composite. The fracture surfaces were examined and the toughening mechanisms that were observed in the bulk epoxies were also found in the GFRPs. The unmodified epoxies failed in a brittle manner with striation marks that suggest large releases of strain energy during fracture, thus, step changes in the crack path. No evidence of matrix residue was found on the fibres. The 10N and 10N9R modified GFRPs surface had an abundance of voids on the fracture surface and these were the same size as the nanosilica particles. There was evidence of residue in on the fibre surfaces. The 9R and 10N9R epoxies showed evidence of voids from cavitation of the rubber particles in the epoxy.

## **System Comparisons and Toughening Mechanisms**

### **10.1 Introduction**

The reader has been introduced to five systems with nanosilica modification, namely (i) an amine cured tetra-glycidyl methylenedianiline (TGMDA) (Chapter 5), (ii) a polyether-amine cured di-glycidyl ether of bisphenol A & F (DGEBA/F) (Ch. 6), (iii) a polyether-amine cured di-glycidyl ether of bisphenol A (DGEBA) (Ch.7), (iv) an amine cured multifunctional epoxy (Ch. 8) and lastly an anhydride cured DGEBA (Ch. 9).

The purpose of this Chapter is to review the results, and allow detailed comparison of the material properties and stress-strain relationships that were achieved with nanosilica modification. The variation in these properties is compared to nanosilica content with particular emphasis on the fracture energy. Furthermore, the toughening mechanisms of shear band yielding and, given sufficiently low particle-matrix adhesions, debonding with subsequent plastic void growth are postulated [7, 52, 61]. Evidence to support these hypotheses is shown. Once the toughening mechanisms are established, analytical models will be developed in Ch. 11 to examine the relative contributions of each of these mechanisms and their relative importance to the overall toughenability of the epoxies.

This chapter is separated into the various aspects of epoxy modification, being morphology, the effect of cross-link density, stiffness behaviour, yield behaviour, and lastly, fracture behaviour. Each section firstly details the effect of nanosilica-modification compared to the unmodified epoxy, and then hybrid-modification (nanosilica and carboxyl-terminated butadiene-acrylonitrile (CTBN) rubber i.e. xN9R) with respect to the rubber-modified (9R) epoxy. The effect of nanosilica modification on the pure epoxy (i.e. xN) will be the main focus of this Chapter because more data were obtained for such systems. Selected images and experimental results from Ch. 5 to Ch. 9 have been repeated in this Chapter to ease navigation through this thesis as the various theories are developed.

## 10.2 Morphology

The morphology of the nanosilica- and rubber-modified epoxies was determined using atomic force microscopy (AFM) and transmission electron microscopy (TEM).

### 10.2.1 Nanosilica-modified epoxies

For the systems detailed in this study, the nanosilica particles remained well dispersed in the epoxy up to 20 wt. % (i.e. the maximum weight fraction that was examined) as summarised in Table 10.1. With the 20 nm particles being so small, inter-particle distances,  $D_{IP}$ , were calculated to be in the range 20-11 nm. The values of  $D_{IP}$  differ slightly because the densities of the epoxies vary. The postulated toughening mechanisms involve deformation within the epoxy polymer. Therefore, increasing the nanosilica content further would not be expected to result in significant gains in toughening from a morphological viewpoint. This explains why relatively large gains in fracture properties are obtained initially at low nanosilica contents, but then values of fracture energy,  $G_C$ , plateau at higher concentrations. This observation is discussed in Section 10.6.

Table 10.1. Morphologies of the nanosilica-modified epoxies that were studied.

System	Formulation	Nanosilica morphology	
		Structure	$D_{IP}$
Amine cured TGMDA (Ch. 5)	10N, 20N	Dispersed single particles	20-11 nm
Polyether-amine cured DGEBA/F (Ch. 6)	10N, 20N	Dispersed single particles	20-12 nm
Polyether-amine cured DGEBA (Ch. 7)	10N, 20N	Dispersed single particles	20-11 nm
Amine cured multifunctional Epoxy (Ch. 8)	10N, 20N	Dispersed single particles	19-11 nm
Anhydride cured DGEBA (Ch. 9)	10N, 20N	Dispersed single particles	20-11 nm

Figure 10.1 shows AFM (Figure 10.1(a, b)) and TEM (Figure 10.1(c, d)) images of the 20N-modified anhydride cured DGEBA epoxy. The same 20 nm nanosilica particles were used to modify all of the epoxies in this study and so the distribution of particle sizes was the same for the other systems.

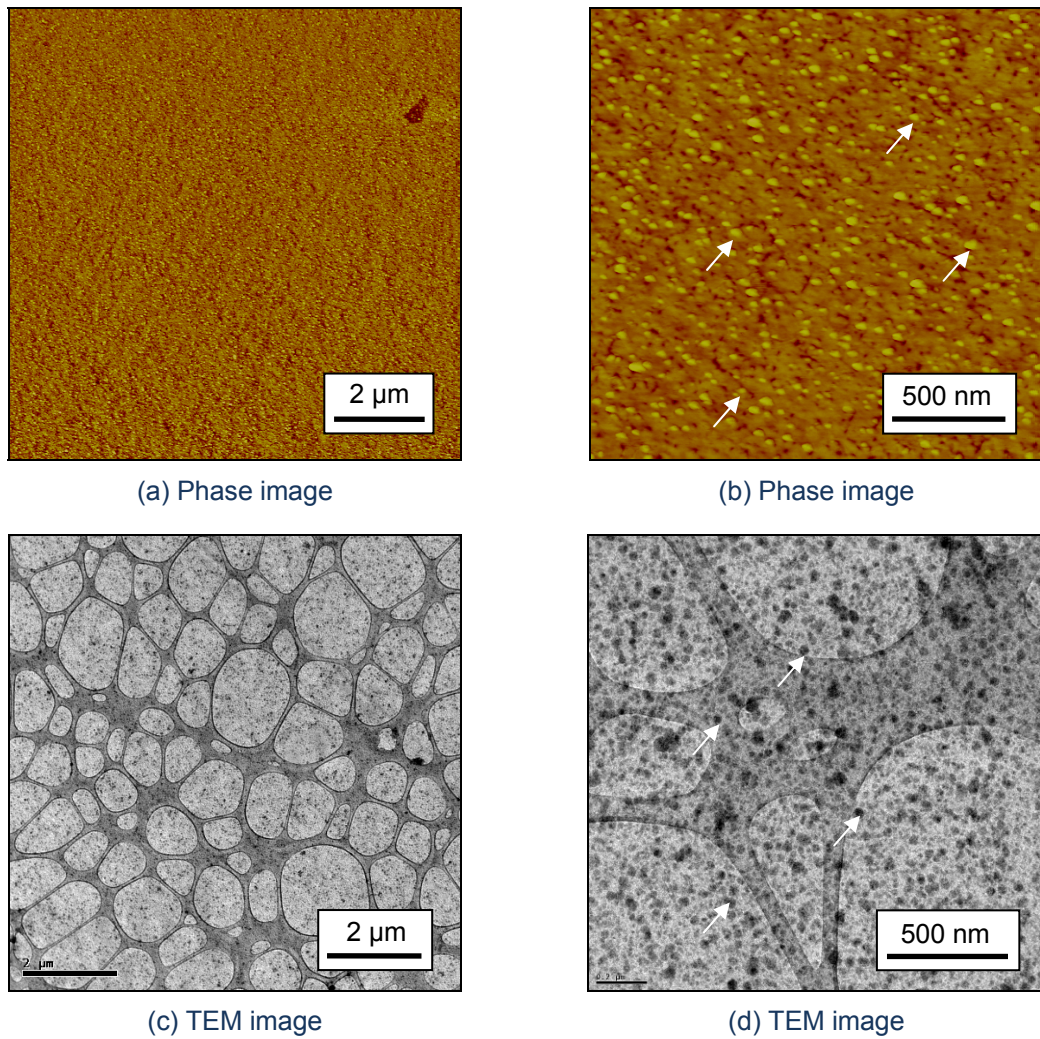


Figure 10.1. Shows (a, b) AFM phase images and (c, d) TEM micrographs of the 20N anhydride cured DGEBA epoxy. The particles remain well dispersed (white arrows) at 20 wt. % addition of nanosilica to the epoxy.

### 10.2.2 Rubber-modified epoxies

The hybrid-modified epoxies formed into more complex morphologies. A summary for the systems is shown in Table 10.2 and selected images from Ch. 9 (the anhydride cured DGEBA) are shown in Figure 10.2(a-d).

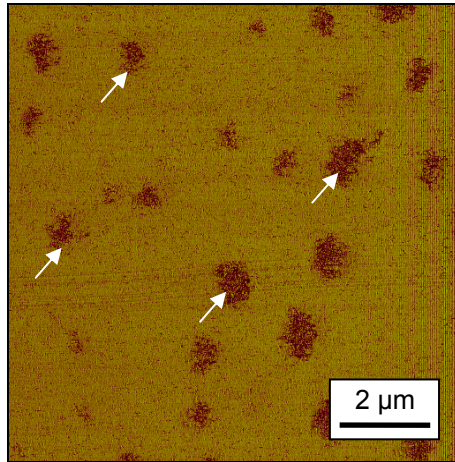
Table 10.2. Morphologies of the rubber- and hybrid-modified epoxies that were studied. The inter-particle distance,  $D_{IP}$  was calculated for the rubber particles and measured for the nanosilica necklaces/agglomerates.

System	Formulation	Nanosilica morphology		CTBN morphology		
		Structure	$D_{IP}$	vol. %	Structure	$D_{IP}$
Amine cured TGMDA (Ch. 5)	9R			9.4	Dispersed spherical particles up to 1 $\mu\text{m}$	1.2 $\mu\text{m}$
	10N9R	1000 by 500 nm necklace structures	0.8 $\mu\text{m}$	9.8	Dispersed spherical particles up to 1.5 $\mu\text{m}$	1.5 $\mu\text{m}$
Anhydride cured DGEBA (Ch. 9)	9R			9.7	Dispersed spherical particles up to 1 $\mu\text{m}$	1.5 $\mu\text{m}$
	10N9R	1000 by 500 nm necklace structure	$\sim 0.8 \mu\text{m}$	9.2	Dispersed spherical particles up to 1.5 $\mu\text{m}$	2.4 $\mu\text{m}$
	15N9R	1250 by 700 nm necklace structure	$\sim 0.7 \mu\text{m}$	7.3	Dispersed spherical particles up to 1.5 $\mu\text{m}$	2.8 $\mu\text{m}$
	20N9R	1500 by 1000 nm agglomerate	$\sim 0.6 \mu\text{m}$	5.5	Dispersed spherical particles up to 1.5 $\mu\text{m}$	3.4 $\mu\text{m}$

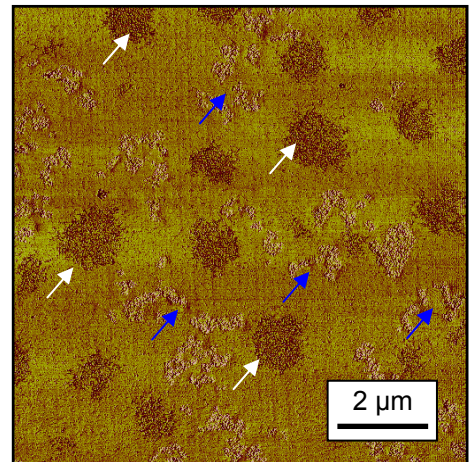
In the 9R epoxies, the rubber particles formed via reaction induced- and nucleation based-phase separation into spherical particles up to 1  $\mu\text{m}$  in diameter. Phase separation of the (CTBN) rubber was hindered by the presence of the nanosilica particles in the hybrid-modified epoxies. This resulted in progressively less rubber phase separating out of the epoxy, and larger nanosilica agglomerates in the epoxy. For the 9R and 10N9R epoxies, approximately 1 vol. % of the CTBN remains in solution in the epoxy. A maximum of 5.5 vol. % remains in solution for the 20N9R epoxy in the anhydride cured DGEBA system. For the hybrid-modified epoxies, the rubber-particle size was found to increase to 1.5  $\mu\text{m}$ . A few possible explanations are speculated at this stage as (i) in the hybrids, the nanosilica particles take up some volume, so effectively, there is less volume of epoxy for 9 wt. % of the CTBN to phase separate into. Alternatively, (ii) the improved thermal conductivity of the nanosilica particles may increase cross-linking reaction rates in the epoxy polymer.

The nanosilica particles formed into necklace-like structures which increased in size at higher nanosilica contents. The agglomerated nanosilica formed in the epoxy and not in the rubber particles, with evidence to show this in Figure 10.2(b-d). The exact

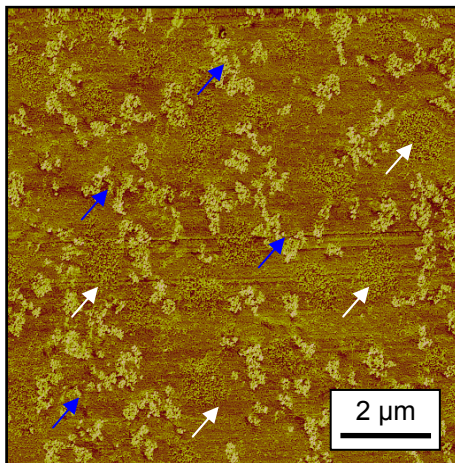
mechanism by which agglomeration occurs in the hybrids is not fully understood. From the rheological tests shown in Ch. 9, during the initial steps of curing; the viscosity rises unexpectedly and could be a result of agglomerates forming.



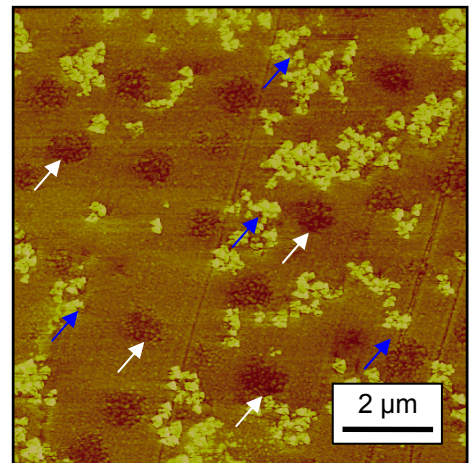
(a) Phase image of the 9R anhydride cured DGEBA epoxy.



(b) AFM phase image of the 9R anhydride cured DGEBA epoxy.



(c) AFM phase image of the 15N9R anhydride cured DGEBA epoxy [182].



(d) AFM phase image of the 20N9R anhydride cured DGEBA epoxy.

Figure 10.2. Shows (a-d) AFM phase images of the rubber- and hybrid-modified anhydride cured DGEBA epoxies. The spherical rubber particles are indicated with white arrows and the nanosilica-necklaces/agglomerates with blue.

Further studies using a heating stage with an optical microscope, and replacing the nanosilica particles with an observable media such as carbon nanotubes may provide more information upon the exact mechanisms by which these agglomerations occur.

### 10.3 The effect of cross-link density

If modifying the epoxy altered the cross-link density, then the glass transition temperature,  $T_g$ , would also be expected to vary with matrix modification. This section reports on how the glass transition temperatures vary, firstly with the addition of nanosilica, and secondly with the addition of nanosilica to the rubber-modified epoxies. The effect of glass transition temperature on the toughenability and yield properties of the epoxy polymers is also discussed.

The cross-link density,  $M_{nc}$ , has been shown by Nielsen [233], (equation (10.1)) to empirically be a function of the  $T_g$  and the glass transition temperature of the linear polymer  $T_{go}$ . The value of  $T_{go}$  is constant for an epoxy system. This expression is widely accepted in the literature [98, 234] and furthermore, with nanosilica-modification [52].

$$M_{nc} = \frac{3.4 \times 10^4}{(T_g - T_{go})} \quad (10.1)$$

Hence, direct comparison between the glass transition temperature and molecular weight between cross-links (cross-link density) can be justified.

#### 10.3.1 Nanosilica-modified epoxies

No difference the value of  $T_g$  was established with the addition of nanosilica to the epoxies. This is shown by the mean values obtained for the unmodified and nanosilica modified epoxies for each system in Table 10.3 (i.e. comparing the standard deviation in the mean). The nanosilica particles are sufficiently small, such that they do not impede polymer chain mobility [52]. Baller et al.'s work [235] agrees with this theory. They reported a 0.7 °C decrease in the  $T_g$  with 40 wt. % nanosilica in epoxy.

Table 10.3. Glass transition temperatures,  $T_g$ , for the unmodified and nanosilica-modified epoxies from this study.

System	Glass transition temperature, $T_g$ ( $^{\circ}\text{C}$ )	
	$\bar{x}$	$\pm$
Amine cured TGMDA (Ch. 5)	185	1
Polyether-amine cured DGEBA/F (Ch. 6)	68	1
Polyether-amine cured DGEBA (Ch. 7)	88	1
Amine cured multifunctional Epoxy (Ch. 8)	178	1
Anhydride cured DGEBA (Ch. 9)	141	1

Studies have been conducted for various rubber-modified epoxies and report that for lower values of  $T_g$ , i.e. high molecular weight between cross-links, the epoxies are more toughenable. This trend is explained as the ability for the epoxy to plastically deform and dissipate more strain energy [84, 86, 236] at lower cross-link density. The postulated mechanisms of shear band yielding and plastic void growth are dependent on deformation in the epoxy polymer. Thus, the lower  $T_g$  systems in this work (the polyether-amine cured epoxies) are expected to provide the largest improvements in  $G_C$  with the addition of nanosilica.

Figure 10.3 shows a plot of  $G_C$  versus  $T_g$  for the unmodified, 10N and 20N modified systems from this study. As expected, there is a general trend of increased toughenability at lower values of  $T_g$  (Note that the effects of particle-matrix adhesion are not yet considered for the different systems). This indicates that yield mechanisms in the epoxy polymer provide the toughening effect with nanosilica particles, and this is much greater for low  $T_g$  epoxies.

Plangsammas et al. [237] have shown that lower values of  $G_C$  tend to be observed for more highly cross-linked epoxies. The purpose of the polyether-amine cure epoxies was to compare the effect of varying the cross-link density. Examination of the mean values would support this theory. Unfortunately the experimental scatter is too large to draw definite conclusions between the two systems.

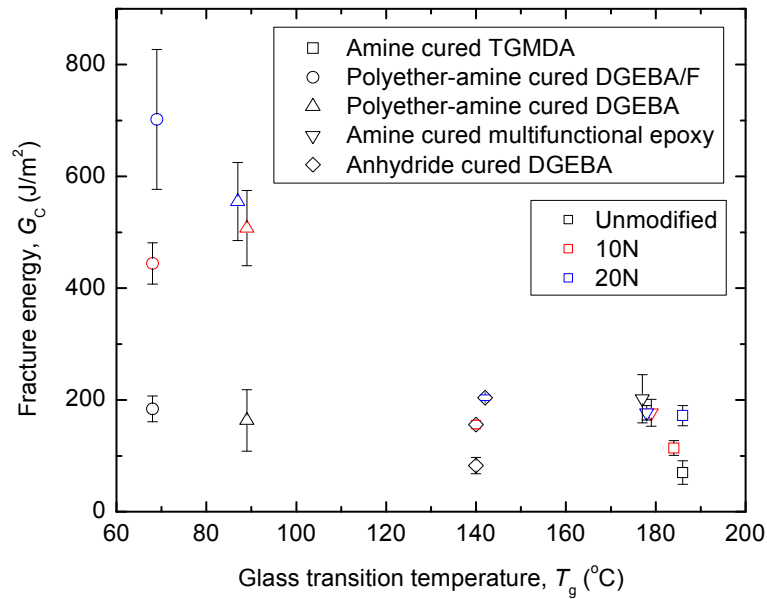


Figure 10.3. Fracture energy versus glass transition temperature,  $T_g$  for the nanosilica-modified epoxies that were studied.

An increased molecular weight between cross-links (decreasing the  $T_g$ ) resulted in a reduction of the compressive yield strength,  $\sigma_{yc}$ , of the various epoxies, as shown in Figure 10.4. No strong correlation was obtained between the magnitude of  $\sigma_{yc}$  and nanosilica content. This is an important observation because it shows that something other than the  $T_g$  (i.e. the interfacial adhesion) plays an important role in the overall toughenability of the nanosilica-modified epoxies, and this is different for the systems in the present study.

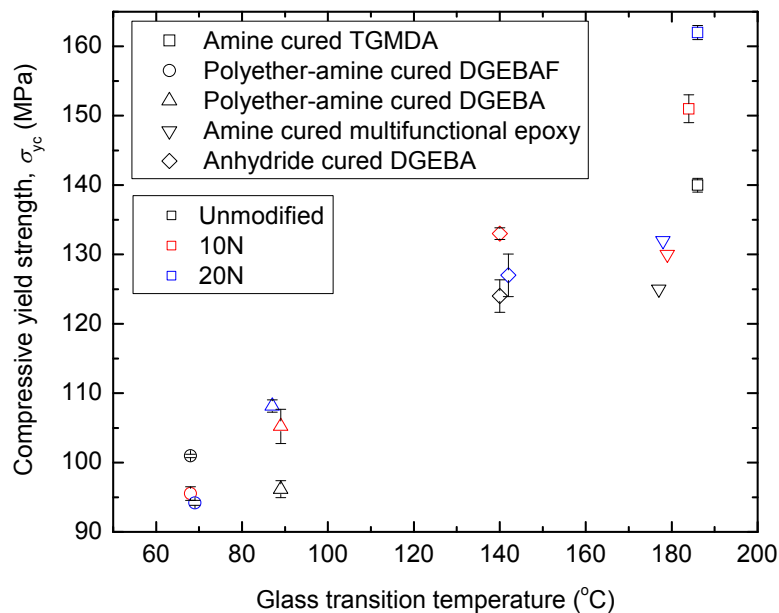


Figure 10.4. Compressive yield strength,  $\sigma_{yc}$ , versus glass transition temperature,  $T_g$  for the unmodified and nanosilica modified epoxies in this study.

The effect of yield strength on the overall toughenability of the epoxies is discussed further in section 10.5 and is shown as a plot of  $\sigma_{yc}$  versus  $G_C$  in Figure 10.8.

### 10.3.2 Rubber-modified epoxies

As shown previously when the morphologies of these formulations was discussed (see Table 10.1), some rubber remains in solution during curing. This results in plasticisation of the epoxy polymer. As a result, small reductions in the magnitude of  $T_g$  were measured for the rubber- and hybrid-modified epoxies, summarised in Table 10.4. This effect of plasticisation is discussed further in the following sections for the rubber-modified epoxy.

Table 10.4. Glass transition temperature,  $T_g$ , for the rubber- and hybrid-modified epoxies from this study.

System	Formulation	Glass transition temperature, $T_g$ (°C)	
		$\bar{x}$	$\pm$
Amine cured TGMDA (Ch. 5)	Unmodified	186	2
	9R	185	2
	10N9R	182	6
Anhydride cured DGEBA (Ch. 9)	Unmodified	140	2
	9R	137	1
	10N9R	138	1
	15N9R	131	3
	20N9R	124	5

## 10.4 Stiffness behaviour

Many material models were reviewed to predict the Young's moduli of particle-modified epoxies [238-244]. The Halpin-Tsai and the Nielsen models were found to be the most pertinent for the present systems and are used to interpret the experimental data from this study.

The Halpin-Tsai model [241, 245] predicts the Young's modulus,  $E$ , of a particle-filled material as a function of the Young's modulus of the unmodified polymer,  $E_u$ , and the Young's modulus of the particles,  $E_p$ . The predicted Young's modulus of the particle-modified epoxy polymer,  $E$ , is given by

$$E = \frac{1 + \zeta \eta v_f}{1 - \eta v_f} E_u \quad (10.2)$$

where  $\zeta$  is the shape factor,  $v_f$  is the volume fraction of particles, and where  $\eta$  is:

$$\eta = \frac{\left(\frac{E_p}{E_u} - 1\right)}{\left(\frac{E_p}{E_u} + \zeta\right)} \quad (10.3)$$

Halpin and Kardos [246] suggested that a shape factor of  $\zeta = \frac{2w}{t}$  should be used,

where  $\frac{w}{t}$  is the aspect ratio of the particles. For spherical nanosilica or rubber particles, the aspect ratio is unity, i.e.  $\zeta = 2$ .

The Lewis-Nielsen model [247] can be modified using the work of McGee & McCullough [248], and gives the Young's modulus,  $E$ , of a particle-modified polymer as

$$E = \frac{1 + (k_E - 1)\beta v_f}{1 - \mu\beta v_f} E_u \quad (10.4)$$

where  $k_E$  is the generalised Einstein coefficient, and  $\beta$  and  $\mu$  are constants. The value of  $\beta$  is given by

$$\beta = \frac{\left(\frac{E_p}{E_u} - 1\right)}{\left(\frac{E_p}{E_u} + (k_E - 1)\right)} \quad (10.5)$$

noting that  $\beta$  is identical to  $\eta$  in the Halpin-Tsai model when a shape factor of  $\zeta = (k_E - 1)$  is used. The value of  $\mu$  depends on the maximum volume fraction of particles,  $v_{\max}$ , that can be incorporated, and is calculated using

$$\mu = 1 + \frac{(1 - v_f)}{v_{\max}} \left[ v_{\max} v_f + (1 - v_{\max})(1 - v_f) \right] \quad (10.6)$$

Nielsen and Landel [249] have published a range of values for  $v_{\max}$  for different particle types and arrangements. The microscopy conducted in this work indicates that the spherical particles are not agglomerated in the nanosilica-modified formulations. Nielsen and Landel quote a value of  $v_{\max} = 0.632$  for random close-packed, non-agglomerated spheres, and this was used to predict the Young's modulus. The magnitude of  $k_E$  varies with the degree of particle-matrix adhesion. For an epoxy polymer with a Poisson's ratio of 0.35 which contains dispersed spherical particles and

no slippage,  $k_E = 2.167$ ; alternatively, if there is slippage at the interface, then  $k_E = 0.867$  [249, 250].

### 10.4.1 Nanosilica-modified epoxies

The Young's modulus of silica,  $E = 70$  GPa [160, 251], is much greater than that of the epoxy polymer. Therefore, as expected, increased Young's moduli were observed for the nanosilica-modified epoxies in tension and compression as summarised in Table 10.5.

The mean value of  $E$  varies from about 2.9 GPa for the unmodified epoxies, to 3.6 GPa with 20N nanosilica-modification. No correlation was identified between the value of  $E$  and  $T_g$  or the fracture energy,  $G_C$ , for the unmodified and nanosilica-modified epoxies that were studied. Moreover,  $E$  is independent of interfacial adhesion (as discussed in Section 10.5).

Table 10.5. Tensile and compressive Young's moduli for the unmodified and nanosilica-modified epoxies.

System	Formulation	Tensile Young's modulus, $E_t$ (GPa)		Compressive Young's modulus, $E_c$ (GPa)	
		$\bar{x}$	$\pm$	$\bar{x}$	$\pm$
Amine cured TGMDA (Ch. 5)	Unmodified	3.14	0.06	2.85	0.52
	10N	3.55	0.03	3.26	0.12
	20N	3.97	0.01	4.11	0.05
Polyether-amine cured DGEBA/F (Ch. 6)	Unmodified	3.16	0.07	3.17	0.15
	10N	3.43	0.10	3.4	0.04
	20N	3.48	0.07	3.51	0.16
Polyether-amine cured DGEBA (Ch. 7)	Unmodified	2.94	0.11	2.80	0.23
	10N	3.24	0.12	3.10	0.37
	20N	3.44	0.36	3.86	0.33
Amine cured multifunctional Epoxy (Ch. 8)	Unmodified	2.55 <sup>1</sup>	0.07 <sup>1</sup>	2.41	0.36
	10N	3.34 <sup>1</sup>	0.19 <sup>1</sup>	2.83	0.39
	20N	3.87 <sup>1</sup>	0.09 <sup>1</sup>	3.15	0.38
Anhydride cured DGEBA (Ch. 9)	Unmodified	2.74	0.08	2.55	0.68
	10N	3.08	0.06	2.68	0.06
	20N	3.47	0.11	3.59	0.59

<sup>1</sup>Taken from Brooker [79]

Figure 10.5 is a plot of the normalised tensile and compressive Young's moduli for all of the nanosilica-modified epoxies from the present study. The Halpin-Tsai and the Nielsen no slip models ( $k_E = 2.167$ ) predict similar Young's modulus values as an upper

bound of predictions. The Nielsen slip model ( $k_E = 0.867$ ) shows the lower bound of Young's modulus values that were measured. Good agreement of moduli was found within this range and also with the lower bound of the rule of mixtures. This may indicate different levels of interfacial adhesion between the nanosilica particles and epoxies; however, any difference is masked in the experimental error in the measurement of  $E$ . Notably, the models are dependent on volume fraction and not particle size, thus, no size effect would be expected for the Young's modulus [28, 51, 239, 247], as was shown by Spanoudakis and Young for glass-particle filled epoxies [23, 24].

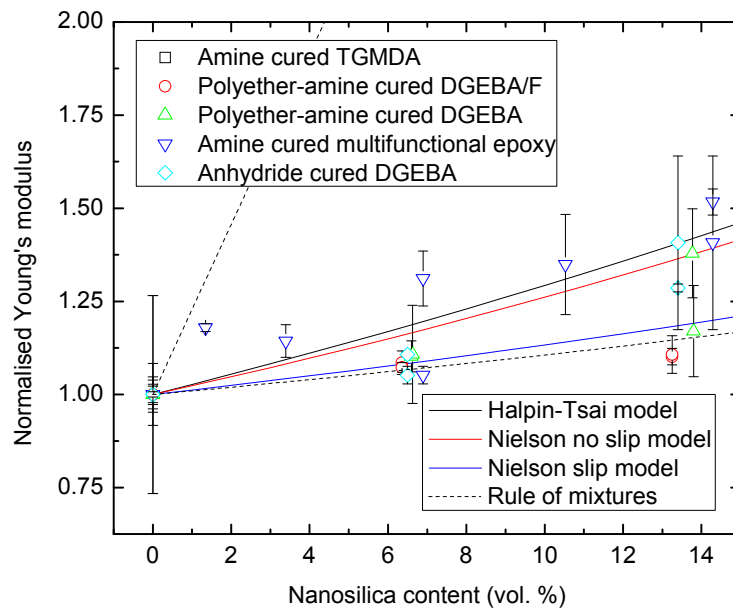


Figure 10.5. Normalised Young's modulus versus nanosilica content for the nanosilica-modified epoxies that were studied are compared to Halpin-Tsai [241, 245] and Nielson [247] and rule of mixtures analytical modulus models.

### 10.4.2 Rubber-modified epoxies

Table 10.6 shows that the addition of nanosilica restores some of the stiffness that was lost due the CTBN rubber. For example, the value of  $E$  for the 20N9R increases to 2.99 GPa from 2.18 GPa for the 9R anhydride cured DGEBA epoxy. The effect the dissolved rubber has no more detrimental effect to the Young's modulus than the phase separated rubber particles do; this is due to the property being volume fraction dominant.

Table 10.6. Tensile and compressive Young's moduli that were measured for the rubber- and hybrid-modified epoxies.

System	Formulation	Tensile Young's modulus, $E_t$ (GPa)		Compressive Young's modulus, $E_c$ (GPa)	
		$\bar{x}$	$\pm$	$\bar{x}$	$\pm$
Amine cured TGMDA (Ch. 5)	9R	2.46	0.03	n/d	
	10N9R	2.66	0.06		
Anhydride cured DGEBA (Ch. 9)	9R	2.18	0.06	1.93	0.33
	10N9R	2.55	0.04	2.59	0.70
	15N9R	2.90 <sup>2</sup>	0.09 <sup>2</sup>	3.22	0.15
	20N9R	2.99 <sup>2</sup>	0.11 <sup>2</sup>	3.12	0.10

<sup>2</sup>Taken from Hsieh et al. [61]

The models assume that the nanosilica particles are randomly dispersed; however, the nanosilica particles in the hybrid epoxies are agglomerated. Figure 10.6 is a plot of the predictive Halpin-Tsai and Nielsen models for the hybrid epoxies from this study and Hsieh et al. [61]. The Halpin-Tsai and Nielsen no slip models provide almost identical values of predicted modulus with close agreement to the lower bound of the rule of mixtures.

The general agreement with the models was good. Initially, the data follows Nielson's no slip model and Halpin-Tsai. At nanosilica contents of above 10 vol. %, the data tends towards Nielson's slip models. The presence of agglomeration increases the value of  $k_E$ , reduces  $v_{max}$  and increases the value of  $\beta$  in Nielson's model. The overall effect of these changes was to increase the predicted modulus. Due to the complications arising from increasing nanosilica agglomeration, with nanosilica content, this would seem fortuitous.

Future work to isolate the effect of nanosilica agglomeration on the Young's modulus for a single-phase modified system may be useful to identify the relative importance to the hybrid-modified Young's modulus.

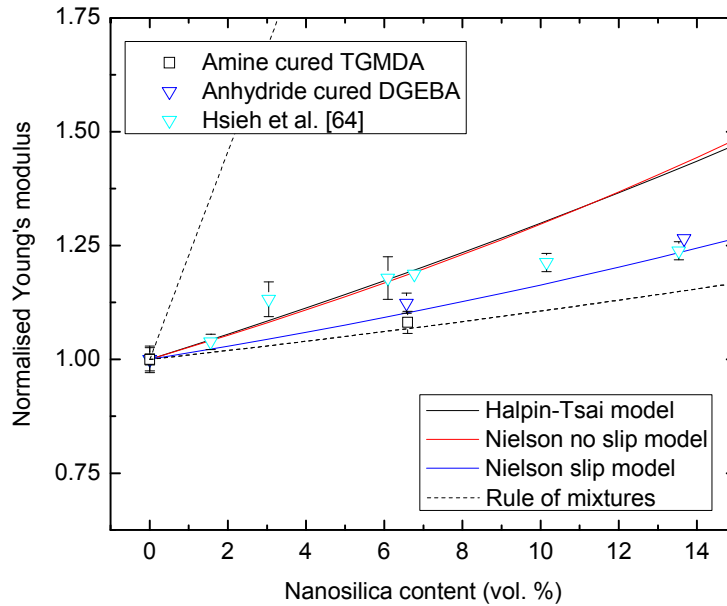


Figure 10.6. Normalised tensile Young's modulus versus nanosilica content for the rubber- and hybrid-modified epoxies. The results from the present study and Hsieh et al. [61] are compared to the Halpin-Tsai [241, 245] and Neilson [247] and Rule of mixtures analytical models.

## 10.5 Yield behaviour

The Young's modulus is measured at low intrinsic strains, where the polymer undergoes insufficient dilation to cause interfacial separation at the particle-matrix interface [29-32]. Therefore, measuring the Young's modulus does not really provide an evaluation of interfacial properties, and so the yield behaviour has been examined. The effect of  $T_g$  on the yield strength of the nanosilica-modified epoxies was shown previously in Figure 10.4, where a linear trend was established between the yield strength and  $T_g$  for the unmodified epoxies.

### 10.5.1 Nanosilica-modified epoxies

Table 10.7 shows a summary of the true yield strengths and corresponding true strains from tensile ( $\sigma_{yt}$  and  $\epsilon_{yt}$ ) and compressive tests ( $\sigma_{yc}$  and  $\epsilon_{yc}$ ). As expected, the trends of  $\sigma_y$  with increasing nanosilica content are the same in tension and compression for each individual system. When tensile tests were conducted, the amine cured TGMDA (Ch. 5) and amine cured multifunctional epoxy (Ch. 8) systems failed prior to attaining maximum yield strength. Huang and Kinloch [94] reported a relationship between the values of  $\sigma_{yt}$  and  $\sigma_{yc}$  as

$$\sigma_{yt} = \sigma_{yc} \frac{(3^{1/2} - \mu_m)}{(3^{1/2} + \mu_m)} \quad (10.7)$$

and  $\mu_m$  was taken as 0.2 [10]. This expression was used to calculate a value of  $\sigma_{yt}$  for the two systems.

Table 10.7. Yield strengths for the unmodified and nanosilica-modified systems. Some values of  $\sigma_{yt}$  were calculated using Equation (10.7) (italicised).

System	Formulation	$\sigma_{yt}$ (MPa)		$\varepsilon_{yt}$ (true strain)		$\sigma_{yc}$ (MPa)		$\varepsilon_{yc}$ (true strain)	
		$\bar{x}$	$\pm$	$\bar{x}$	$\pm$	$\bar{x}$	$\pm$	$\bar{x}$	$\pm$
Amine cured TGMDA (Ch. 5)	Unmodified	111	1	n/d		140	1	0.14	0.01
	10N	120	2			151	2	0.14	0.00
	20N	128	1			162	1	0.13	0.02
Polyether-amine cured DGEBA/F (Ch. 6)	Unmodified	82	1	0.03	0.00	101	0	0.07	0.00
	10N	77	1	0.03	0.00	96	1	0.08	0.00
	20N	73	7	0.03	0.02	94	0	0.08	0.00
Polyether-amine cured DGEBA (Ch. 7)	Unmodified	67	3	0.05	0.00	96	1	0.09	0.00
	10N	70	1	0.05	0.00	105	2	0.08	0.00
	20N	72	1	0.04	0.00	108	1	0.07	0.01
Amine cured multifunctional Epoxy (Ch. 8)	Unmodified	99	0	n/d		125	0	0.19	0.00
	10N	103	0			130	0	0.17	0.00
	20N	105	0			132	0	0.14	0.01
Anhydride cured DGEBA (Ch. 9)	Unmodified	88	1	0.07	0.00	124	2	0.10	0.00
	10N	89	0	0.06	0.00	133	1	0.10	0.01
	20N	87	4	0.05	0.01	127	3	0.09	0.01

The value of  $\sigma_{yt}$  and  $\sigma_{yc}$  varies with nanosilica content for the systems that were studied. For the amine cured TGMDA (Ch. 5) and polyether-amine cured DGEBA (Ch. 7) epoxies, the yield strength increases approximately 16 % with the addition of nanosilica, whilst for the amine cured multifunctional epoxy (Ch. 8) and the anhydride cured DGEBA Ch. 6), the yield strength was virtually unchanged. Notably, for the polyether-amine cured DGEBA/F (Ch. 6) the yield strength decreases with the addition of nanosilica. Clearly then, a difference in the interfacial adhesion exists for the different epoxies. This is expected to be a function of the bonding that occurs between the particles and epoxy, and also perhaps the formation of an inter-phase layer around the particles. The work of Sen et al. [44] has predicted the existence of a thin thermodynamically stable bound layer of polymer surrounding dispersed nanosilica in a thermoplastic polymer using small angle neutron scattering (SANS) and neutron data. Zhang et al [43] also proposed the existence of inter-phase in nanosilica-modified epoxies.

In addition, Table 10.7 shows that the value of yield strain in tension and compression tends to reduce with nanosilica content. Vollenberg and Heikens have shown previously [26] that when intrinsic yield processes (such as shear banding) dominate

the material, they hinder global diffuse yield in the material and result in lower values of  $\epsilon_y$  as the particle content was increased. This provides a useful explanation of why the strain to yield always decreases with nanosilica content and also verifies that intrinsic yield processes such as localised shear band yielding may well be occurring in the nanosilica-modified epoxies.

Further consideration has been given to evaluate the interfacial properties between the nanosilica particles and epoxy to try and quantify the particle-matrix adhesion. The reversible work of adhesion for the various particle-epoxy interfaces is unknown. Therefore a simple model is used to quantify the interfacial strength. Assuming that the particles carry a load proportional to their volume fraction using stress averaging, Pukánszky and Vörös [36, 37] proposed that

$$\sigma_e = v_f k \sigma_e + (1 - v_f) \sigma_m \quad (10.8)$$

where the external stress of the modified polymer,  $\sigma_e$ , is a function of volume fraction,  $v_f$ , proportionality constant for stress transfer between the particles and matrix,  $k$ , and the average stress in the matrix,  $\sigma_m$ . The first term expresses the stress carried by the particles, with the second expressing the stress in the matrix, i.e. if there are no particles present; the external stress is equal to the average matrix stress. This can be simplified further by taking  $\sigma_m$  to occur at the yield strength, expressed for the unmodified epoxy as  $\sigma_{yu}$ . Hence,

$$\sigma_e = \sigma_{yu} \frac{(1 - v_f)}{(1 - k v_f)} \quad (10.9)$$

The magnitude of  $k$  was reported to be greater than 0 for rigid particles and increases with the level of particle-matrix adhesion. No maximum can be given to the value of  $k$  because this is entirely dependent on the inter-phase region that forms between the particles and matrix. The value of  $k = 0$  for the assumption of voids present in the epoxy would provide the lower limit to the model. There is a particle size dependence on the model [36] because there is a size effect associated with the yield strength [34, 36, 37, 47, 49]. This is not considered by the proportionality constant for stress transfer,  $k$ . In the present work, however, the same nanosilica particles were used, and thus size effect does not invalidate this comparison. A more detailed examination could be considered in the future if the adhesion energy between the particles and matrix, and the inter-phase geometry around the particles could be determined [252].

The yield properties were compared for the different epoxies, shown as a plot of normalised compressive true yield strength versus nanosilica content in Figure 10.7. The amine cured TGMDA and amine cured multifunctional epoxy systems failed prior to attaining a yield strength value, so the compressive data were used for comparative purposes. It is noted however, that identical trends in compressive and tensile yield were obtained for the other systems. The nanosilica content is expressed as vol. % due to the epoxies having slightly different densities. Different interfacial parameters were obtained for the systems, and shows that the particle-matrix adhesion does vary between the epoxy systems. The data were expressed with the model shown in Equation (10.9) by varying  $k$  to obtain a sum of least squares fit for each epoxy, as shown in the legend. The values of  $k$  varied between 1.88 with good adhesion, to a minimum value of 0.46 with poor adhesion.

The amine cured TGMDA and polyether-amine cured DGEBA systems possess the best interfacial properties. The values of  $k$  are 1.88 and 1.76 respectively and the yield strength increases with nanosilica content. For the anhydride cured DGEBA and amine cured multifunctional epoxy, the values of  $k$  were calculated to be 1.29 and 1.34, resulting in very small increases in yield strength with the addition of nanosilica. Notably, the polyether-amine cured DGEBA/F is the only system in this study that shows a reduction in the yield strength with increasing nanosilica content and a value of  $k = 0.46$  was obtained. The trends in the value of the interfacial parameter,  $k$ , agree exactly with the observations from FEGSEM of the fracture surfaces from SENB tests, as illustrated in Figure 10.7. No evidence of debonding and subsequent void growth was observed around the nanosilica particles in the amine cured TGMDA and polyether-amine cured DGEBA systems, and the highest values of  $k$  were obtained for these systems.

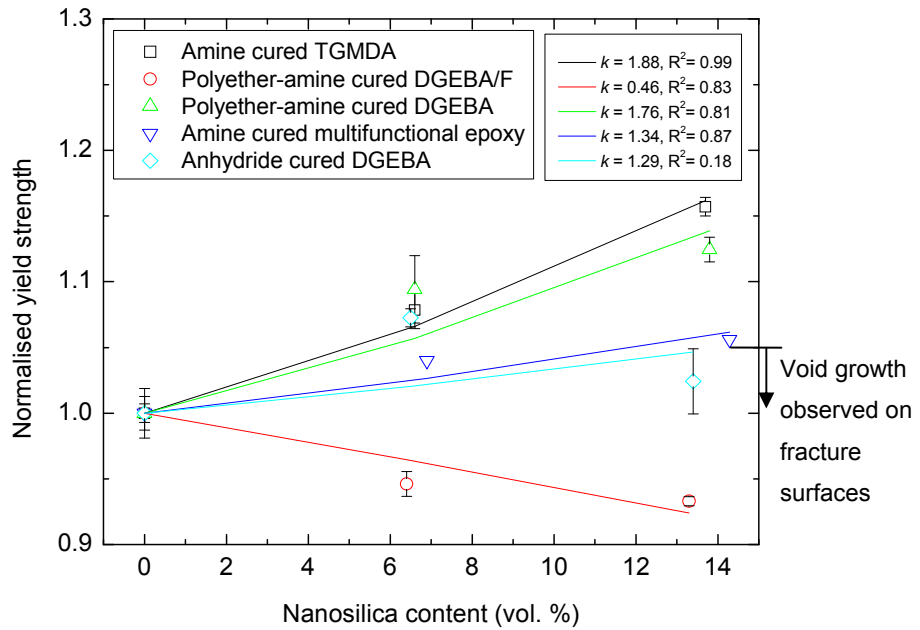


Figure 10.7. Normalised yield strength versus nanosilica content for the nanosilica-modified epoxies. The experimental results are compared to Pukánszky and Vörös’ model [36, 37] in order to quantify the particle-matrix interfacial adhesion.

The yield strength was compared to  $G_C$ , to examine the effect of yield strength on the overall toughenability, as shown in Figure 10.8.

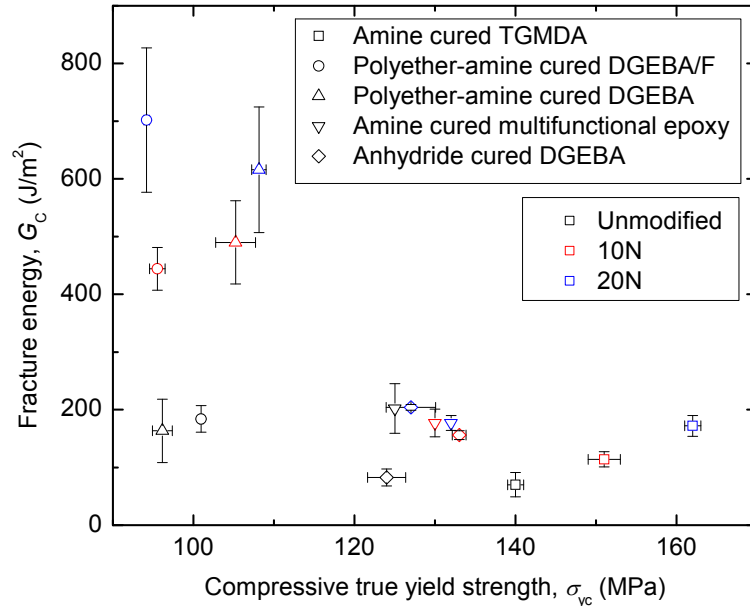


Figure 10.8. Fracture energy,  $G_C$ , versus compressive true yield strength,  $\sigma_{yc}$ , for the nanosilica-modified epoxies.

Disregarding the effect of interfacial adhesion, it is apparent that lower yield strength systems are inherently more toughenable with nanosilica due to their ability to plastically deform. The largest gains in toughness were obtained for the polyether-amine cured DGEBA/F system and the value of  $\sigma_{yc}$  decreases with increasing

nanosilica content. Intuitively, the high  $T_g$  systems generally have higher yield strengths and decreased toughenability with nanosilica.

### 10.5.2 Rubber-modified epoxies

The effect of hybrid-modification on the yield behaviour cannot be explained with averaging stress transfer models. The amount of rubber that phase separates decreases, and the nanosilica particles agglomerate with increasing nanosilica content. Due to the large stress concentrations that would occur between very closely packed particles, the agglomerated particles in the rubber-modified epoxy would be expected to lower the yield strength of the epoxy. The overall effect is shown in Table 10.8 which summarises the true yield strengths and true strains from tensile ( $\sigma_{yt}$  and  $\epsilon_{yt}$ ) and compressive tests ( $\sigma_{yc}$  and  $\epsilon_{yc}$ ) for the rubber- and hybrid-modified formulations. Compressive tests were not conducted on the amine cured TGMDA, and so Table 10.8 focuses on the anhydride cured DGEBA. No difference in the yield properties was ascertained for the hybrid-modified epoxies.

Table 10.8. Yield strengths that were measured for the rubber- and hybrid-modified epoxies.

System	Formulation	$\sigma_{yt}$ (MPa)		$\epsilon_{yt}$ (true strain)		$\sigma_{yc}$ (MPa)		$\epsilon_{yc}$ (true strain)	
		$\bar{x}$	$\pm$	$\bar{x}$	$\pm$	$\bar{x}$	$\pm$	$\bar{x}$	$\pm$
Anhydride cured DGEBA (Ch. 9)	9R	67	3	0.05	0.01	90	1	0.09	0.01
	10N9R	66	0	0.05	0.01	85	1	0.09	0.01
	15N9R					85	2	0.10	0.01
	20N9R					86	1	0.10	0.01

## 10.6 Fracture behaviour

The following section details the fracture properties that were obtained with nanosilica modification and attempts to explain the toughening mechanisms that were observed for modelling considerations in the following chapter.

### 10.6.1 Nanosilica-modified epoxies

For the nanosilica-modified systems, different degrees of toughenability were obtained for the epoxies. Table 10.9 shows a summary of the fracture energy,  $G_C$ , and the toughenability as the percentage difference with respect to the unmodified epoxy. The amine cured multifunctional epoxy did not toughen with the addition of nanosilica. For the 20N amine cured TGMDA and 20N polyether-amine cured DGEBA/F, improvements of 146 % and 282 % were obtained respectively. This would suggest

that toughenability is most definitely a function of the cross-link density, with the low  $T_g$  epoxies providing the highest values of  $G_C$ .

Table 10.9. Fracture energy,  $G_C$ , and  $T_g$  for the unmodified and nanosilica-modified epoxies.

The toughenability is shown as a function of the unmodified epoxy.

System	Formulation	$G_C$ (J/m <sup>2</sup> )		Toughenability (%)	$T_g$ (°C)
		$\bar{x}$	$\pm$		
Amine cured TGMDA (Ch. 5)	Unmodified	70	21	-	185
	10N	114	13	63	
	20N	172	18	146	
Polyether-amine cured DGEBA/F (Ch. 6)	Unmodified	184	23	-	68
	10N	444	37	141	
	20N	702	125	282	
Polyether-amine cured DGEBA (Ch. 7)	Unmodified	163	55	-	88
	10N	490	72	200	
	20N	616	109	277	
Amine cured multifunctional Epoxy (Ch. 8)	Unmodified	202	43	-	178
	10N	177	24	-12	
	20N	177	13	-12	
Anhydride cured DGEBA (Ch. 9)	Unmodified	83	15	-	141
	10N	156	8	89	
	20N	204	5	147	

The toughening mechanisms of crack pinning have been reported for micron-sized glass particles [23, 72]. Pinning mechanisms are identified by the presence of bow shaped lines on the fracture surface. No such evidence was observed for any of the fracture surfaces that were examined. For example, Figure 10.9 shows a low magnification FEGSEM image of the fracture surface from a 20N polyether-amine cured DGEBA epoxy sample.

Crack forking was identified, as a result of the relatively large release of energy at crack initiation. No evidence of crack pinning mechanisms was indentified for this sample or any other nanosilica modified epoxy.

Green et al [70] have suggested that for pinning to occur, the particles need to be much larger than the crack opening displacement. From [71] the crack opening displacement,  $\delta_C$  is given as

$$\delta_C = \frac{G_C}{\sigma_{yt}} \quad (10.10)$$

and  $\delta_C = 9.6 \mu\text{m}$  for 20N polyether-amine cured DGEBA epoxy or  $\delta_C = 2.4 \mu\text{m}$  for the anhydride cured DGEBA 20N formulation. Shown diagrammatically in Figure 10.10, the

nanosilica particles are of the order of hundreds of times smaller than the crack opening displacement and will not impede the crack path in the epoxy matrix.

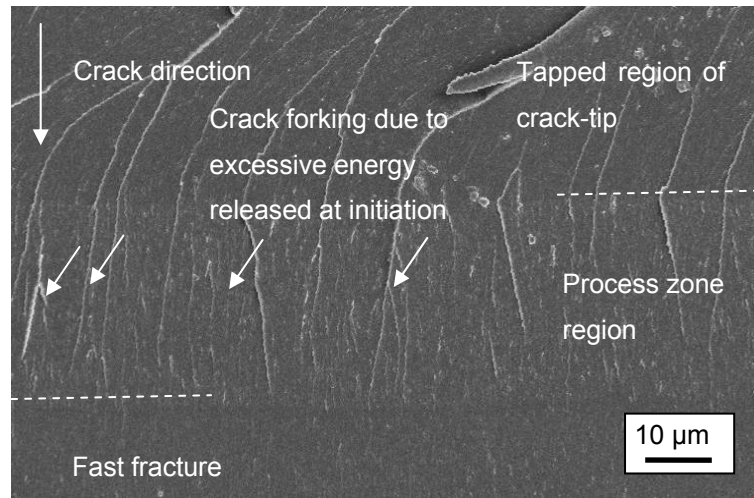


Figure 10.9. Low magnification FEGSEM image of the fracture surface for the 20N polyether-amine cured DGEBA epoxy shows crack forking due to the relatively large release of energy at fracture. No evidence of crack pinning mechanisms were identified.

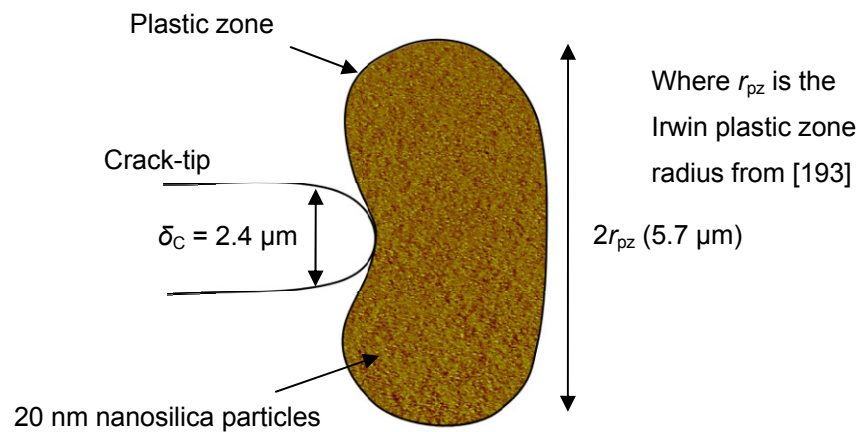


Figure 10.10. The crack opening displacement for the nanosilica-modified epoxies that were studied. The values are shown for the 20N anhydride cured DGEBA epoxy.

Toughening could occur by crack deflection mechanisms, whereby the crack tilts and twists as particles are encountered by the crack-tip. This would increase the surface area of the crack path and induce mix-mode conditions as the crack front negotiates the particles. No such increases in surface roughness were observed with the addition of nanosilica. A detailed study was conducted by Johnsen et al. [7] and concurs with this observation. Moreover, Faber and Evans' model [73, 203] was applied in Johnsen et al.'s study [7] and consistently under-predicted the observed toughening effects. For the 20N anhydride cured DGEBA  $G_C = 204 \pm 5 \text{ J/m}^2$  whereas Faber and Evans' model would predict  $G_C$  as  $126 \text{ J/m}^2$ .

Experimentally from double-notch four-point bend tests (DN4PB) tests, Irwin's model [193] was used to compare a predicted value of the plastic zone radius,  $r_{pz}$ , to the measured plastic zone size. This is shown using polarised light microscopy images of polished cross-sections for sub-critically loaded crack-tips in Figure 10.11(a) and (b) from the 10N anhydride cured DGEBA epoxy (Ch. 9). The value of  $r_{pz}$  in plane stress conditions agrees very well with the observed height of the plastic zone. An inherent characteristic of the DN4PB test is that it is very sensitive to any differences between the two cracks in the sample. Subsequently, the two images appear different although  $r_{pz}$  agrees well for both.

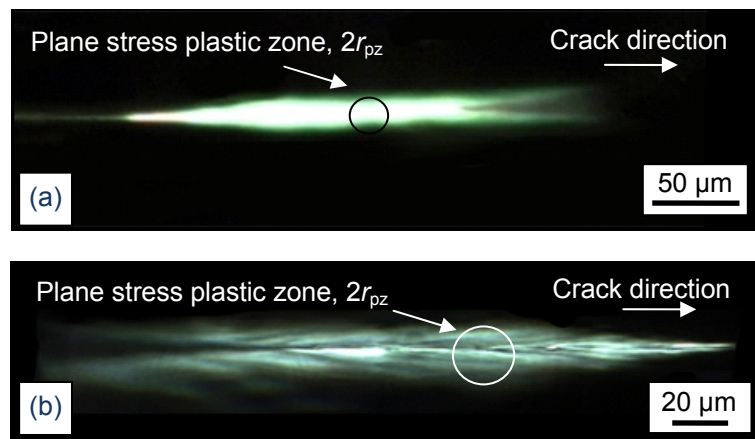


Figure 10.11. Cross-polarised light microscopy images (a, b) of a 10N sub-critically loaded crack-tip. The images are taken of polished sections from the edge of the DN4PB sample, thus under plane stress conditions. (The two images are from different samples)

Such images were not obtained for all systems due to the very small size of the plastic zones and complex procedure required to obtain them. However, a complete system comparison of shear banding in each system can be obtained by examining polished cross-sections of compression specimens that were loaded to within the strain softening region of the unmodified epoxies, as shown in Figure 10.12(a-e). The amine cured multifunctional epoxy showed little evidence of shear banding in the compressed gauge area. The amine cured multifunctional epoxy does not toughen, even though the value of  $k$  (hence the particle-matrix interfacial adhesion) is similar to that for the anhydride cured DGEBA. This suggests that shear band yielding precedes particle debonding and subsequent void growth in the epoxy, and is necessary for void growth to occur.

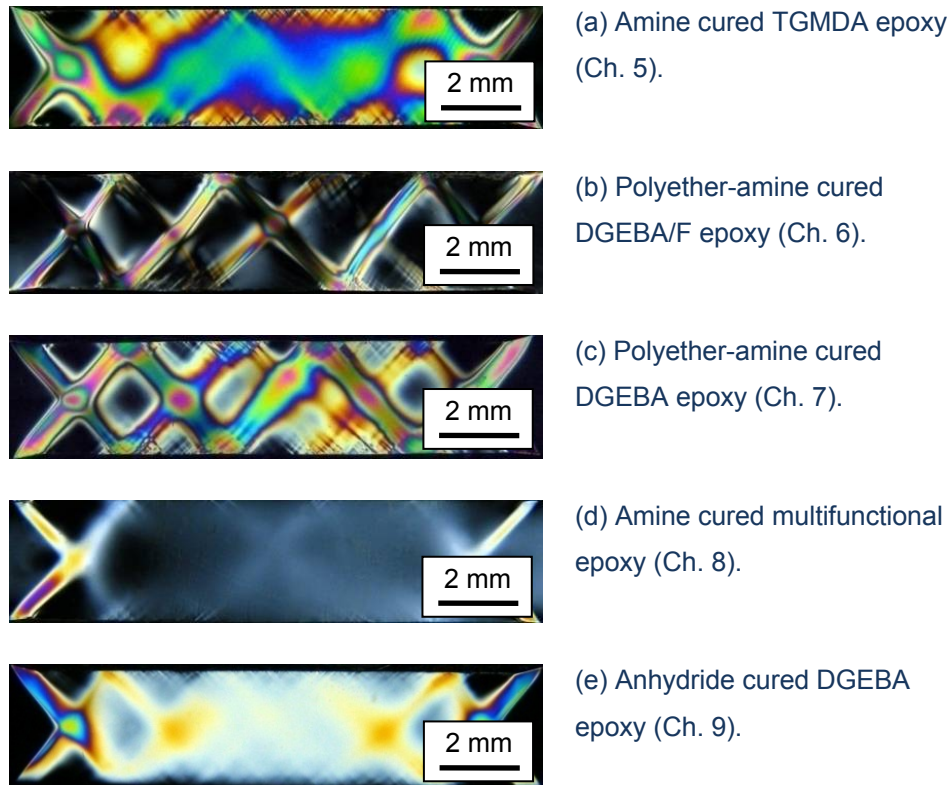


Figure 10.12. Cross-polarised light microscopy images (a-e) of polished cross-sections from unmodified epoxies loaded to within the compressive strain softening region.

Variations in the interfacial parameter  $k$ , which accounts for particle-matrix interfacial adhesion and inter-phase geometry, correlates very well with the toughening mechanisms that were observed on the fracture surfaces of the nanosilica-modified epoxies. Considering the polyether-amine cured DGEBA and polyether-amine cured DGEBA/F systems, where effectively, the cross-link density was varied. Differences in adhesion were obtained and this infers different particle-matrix interfacial chemistries for the two epoxies. For the former system,  $k = 1.76$  and suggests good adhesion between the particles and epoxy. This was apparent in the fracture surfaces, shown in Figure 10.13(a). For the latter, the polyether-amine cured DGEBA/F epoxy with  $k = 0.46$  implied poor adhesion between the particles and epoxy. The SEM image shown in Figure 10.13(b) confirms this and shows particle debonding and plastic void growth in the epoxy.

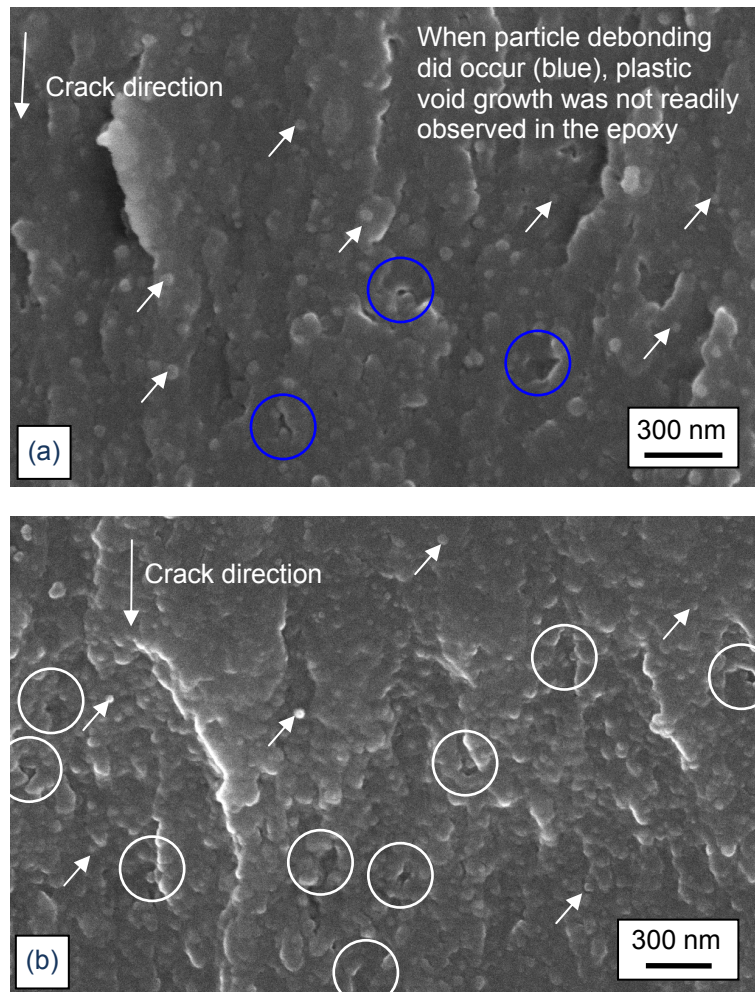


Figure 10.13. Fracture surfaces for the 20N (a) polyether-amine cured DGEBA and (b) the polyether-amine cured DGEBA/F epoxy. The arrows show some nanosilica particles and debonding is circled, (blue) showing no void growth and (white) showing void growth.

The ability for the polymer to yield is dominant in defining the overall toughenability of the epoxies. This is apparent if the fracture energy is compared as a plot of normalised fracture energy  $G_C$  versus nanosilica content in Figure 10.14. Clearly the low  $T_g$  epoxies are the most toughenable. Although the apparent linear fit for the polyether-amine DGEBA epoxy would suggest that it is more toughenable than the polyether-amine DGEBA/F, the experimental scatter in the results shows that there is actually no difference between the magnitudes of  $G_C$  for the two epoxies.

The low  $T_g$  epoxies were found to provide the highest normalised fracture energies. The inter-particle distance was calculated to be very small, at 19-20 nm for the 10N epoxies and 10-11 nm for the 20N epoxies. Due to the very small nature of the particles, much of the free volume of epoxy between them is invoked in toughening. This could explain why for 10 wt. % particles, the toughenability quite high (the order of

2 or 3 times), but then little further improvement is obtained with additional nanosilica in the epoxy.

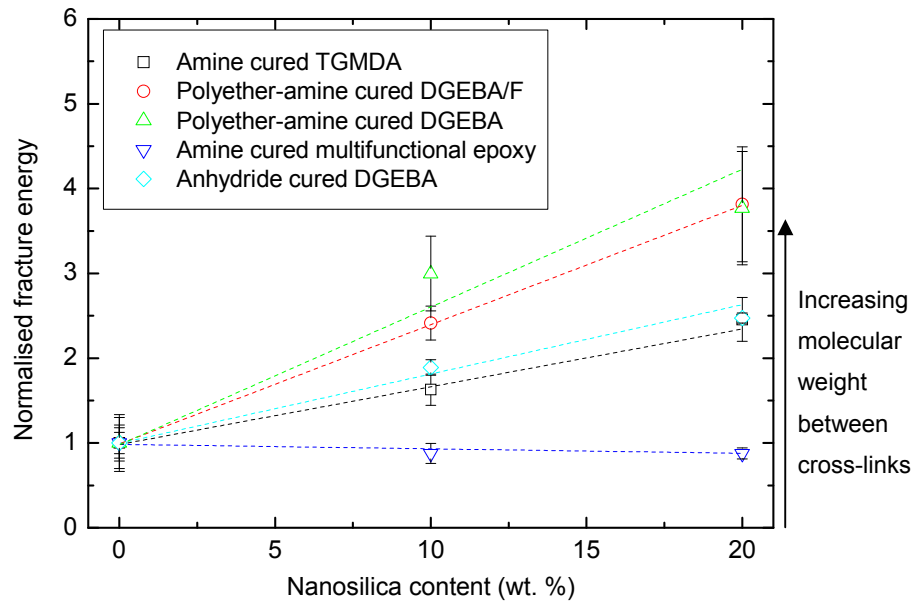


Figure 10.14. Normalised fracture energy versus nanosilica content for the nanosilica-modified epoxies that were studied. The linear fits show the general trend in the fracture energies.

The toughening mechanisms for rigid micron-sized particles have been shown to be shear yielding and plastic void growth in the epoxy [46, 57]. Liang and Pearson have reported the presence of shear band yielding in their nanosilica-modified epoxies with debonding and subsequent plastic void growth [52]. Shear band yielding has been shown for the nanosilica-modified epoxies in this study (except the amine cured multifunctional epoxy from Ch. 8). This has been shown to be dependent on the parent epoxy's ability to strain soften upon yielding. From this study, the polyether-amine cured DGEBA/F (Ch. 6) and anhydride cured DGEBA (Ch. 9) showed evidence of some particle debonding and subsequent plastic void growth in the epoxy. Particular attention is given to the anhydride cured DGEBA, with low particle-matrix interfacial adhesion and evidence of debonding on the fracture surface. The proportion of particles that debond with subsequent void were measured for many FEGSEM images, as reported in Ch. 9 and [60, 61], and found to be  $15 \pm 5$  % of the particles on the fracture surface. The amine cured TGMDA from Ch. 5 showed no evidence of debonded nanosilica particles on the fracture surfaces, and good particle-matrix adhesion was inferred from the yield properties with  $k = 1.88$ .

### 10.6.2 Rubber-modified epoxies

A summary of the measured fracture energies and their relative toughenability are shown in Table 10.10. With no improvement in the value of  $G_C$ , no synergistic behaviour was obtained for the amine cured TGMDA. For the anhydride cured DGEBA, a maximum increase of 57 % was obtained for the 10N9R epoxy with  $G_C = 1051 \text{ J/m}^2$ . With the addition of further nanosilica,  $G_C$  reduces to an equivalent value of the 9R base epoxy.

Table 10.10. Fracture toughness,  $K_{IC}$ , and fracture energy,  $G_C$ , for the rubber- and hybrid-modified epoxies from this study and toughenability with respect to the rubber-modified epoxy.

System	Formulation	$G_C \text{ (J/m}^2\text{)}$		Toughenability (%)
		$\bar{x}$	$\pm$	
Amine cured TGMDA (Ch. 5)	9R	557	21	-
	10N9R	573	52	0
Anhydride cured DGEBA (Ch. 9)	9R	671	50	-
	10N9R	1051	97	57
	15N9R	965 <sup>3</sup>	145 <sup>3</sup>	44
	20N9R	665 <sup>3</sup>	100 <sup>3</sup>	0

<sup>3</sup>Taken from Sohn Lee [60]

The fracture surfaces of the rubber-modified epoxies were examined and particle cavitation was identified. This mechanism is well documented in the literature [98, 123, 222] and shown in Figure 10.15.

Highly triaxial stresses in the rubber-modified epoxy results in internal cavitation of the rubber particles. Subsequent shear band yielding, initiating from the stress concentrations caused by the rubber-voids, is enabled and this absorbs further strain energy and allows the voids to plastically deform.

For the hybrid-modified polymers, it is clear that the presence of both types of particles give rise to a synergistic effect on the fracture energy of the epoxy polymer. Cavitation of the rubber particles still occurs in the hybrid epoxy, shown in Figure 10.16. However, the fracture surface shows evidence of extensive deformation, suggesting that further deformation is occurring and this is resulting in the elevated values of  $G_C$ .

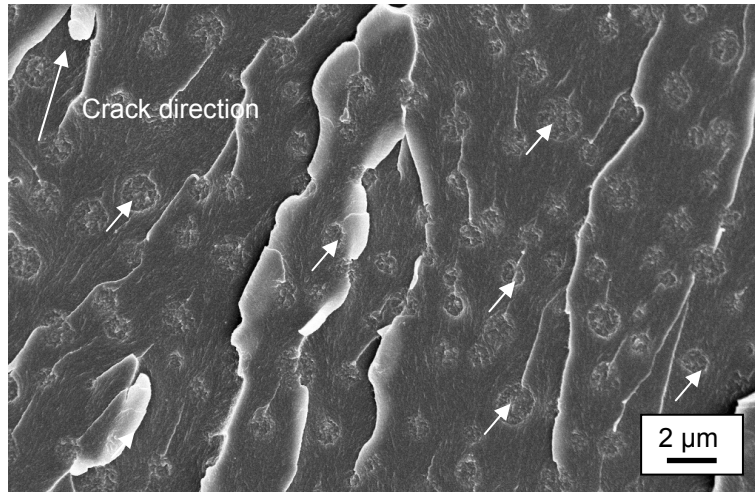


Figure 10.15. Fracture surface of rubber-modified (9R) epoxy. Internal cavitation of the CTBN and subsequent plastic void growth was observed. Some of the rubber particles are indicated with arrows.

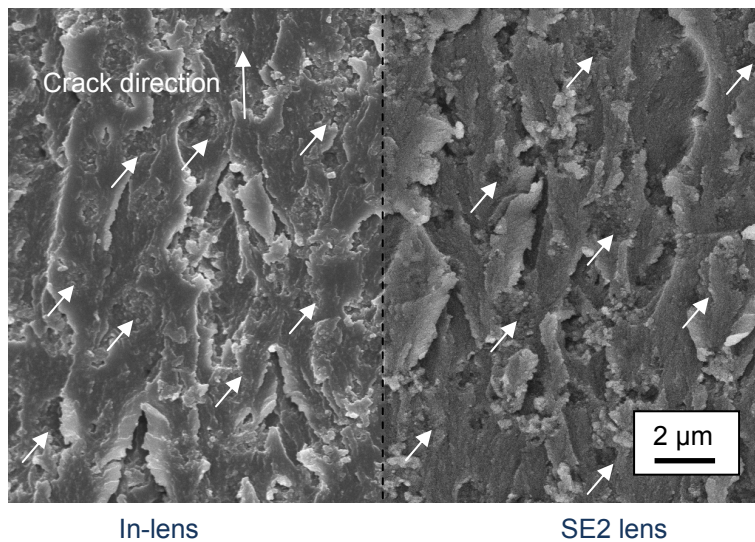


Figure 10.16. A FEGSEM image of the 10N9R anhydride cured DGEBA epoxy fracture surface [224]. A composite shows extensive deformation in the process zone region and the rubber micro-particles are shown identified.

Furthermore, this synergistic effect is shown as a plot of normalised fracture energy versus nanosilica content in Figure 10.17. The quadratic fit shows that a maximum  $G_C$  is obtained for the 10N9R anhydride cured DGEBA. However, the amine cured TGMDA does not toughen further (compared to the 9R epoxy).

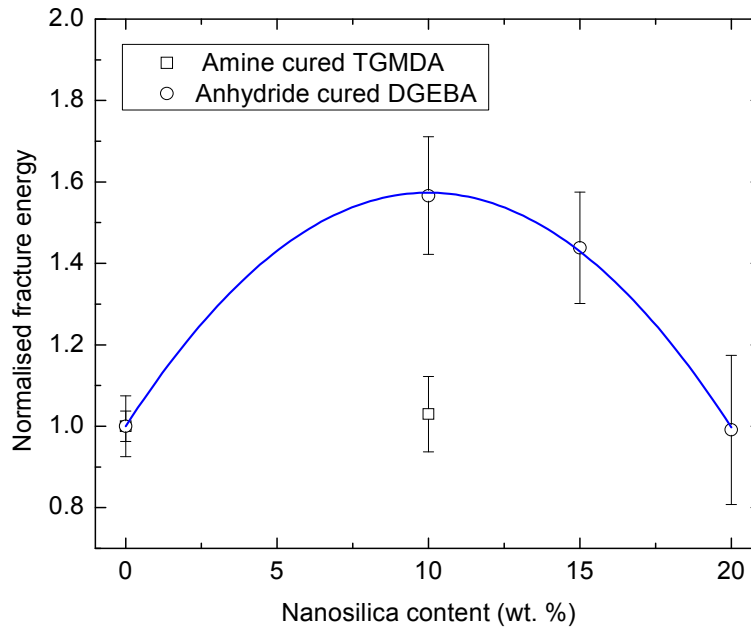


Figure 10.17. Normalised fracture energy versus nanosilica content for the rubber- and hybrid-modified epoxies that were studied. The quadratic fit shows the general trend in the fracture energy for the anhydride cured DGEBA epoxy.

Evidence of plastic void growth around the nanosilica necklaces was also identified in the anhydride cured DGEBA (Figure 10.18), but this was not identified in the 10N9R amine cured TGMDA epoxy. The effect of synergy is well documented in the literature, for example [72, 113, 115]. Of noteworthy observation, is that synergy is not limited to rigid glass particles and CTBN systems although this combination is most widely documented e.g. [72, 89, 113-117, 120, 253]. Synergistic toughening has been reported for many systems in collaboration with micron-sized CTBN rubber e.g. [118, 124, 126, 129, 130, 137, 254, 255] with particles such as bi-modal CTBN, nano-clays and carbon nanotubes, whilst the exact mechanisms may differ slightly. The presence of the CTBN provides some influence to the stress distribution in the plastic zone that gives rise to a synergistic behaviour in  $G_C$ .

One avenue that needs to be discussed is the effect of increased plasticisation of the epoxy due to the CTBN rubber that remains in solution for the hybrid-epoxies. This was found to increase with nanosilica content and was noted to be as high as 5.5 vol. % in the 20N9R anhydride cured DGEBA. Boogh et al. [256] reported the effects of plasticisation and phase separation on the fracture energy for hyperbranched polymer (HBP)-modified epoxies. They found that toughness improvements via plasticisation effects are minimal and amounted to a 2-fold increase in  $G_C$  for 25 % HBP in the epoxy. Moreover, they reported that a 13-fold increase in  $G_C$  was obtained with phase separation induced toughening mechanisms for a less reactive 15 % HBP-modified

epoxy. Hence, increased plasticization is not expected to provide improvements in the value of  $G_C$  in the hybrid-modified epoxies from this study.

A question arises as to why a synergistic effect does not arise for amine cured TGMDA, but does for the anhydride cured DGEBA. An obvious explanation is that the nanosilica particles only provide synergistic toughening via plastic void growth mechanisms, i.e. Figure 10.18, and no synergy arises for systems with well bonded nanosilica particles in a hybrid-epoxy system. Tsai et al. [135] reported nanosilica-modified epoxy with only modest improvements in  $G_C$  and no synergy in a hybrid formulation, and complies with this argument. This would infer that plastic void growth from the secondary phase (i.e. nanosilica) is the mechanism that offers this synergistic effect with the primary CTBN phase. The stress to debond glass particles may be relatively low due to their large size [47, 48], thus they will readily debond with subsequent plastic void growth in the epoxy. This could explain why the CTBN-glass combination is well documented in the literature, and provides general agreement with the theory that void growth from the rigid phase offers a synergistic behaviour.

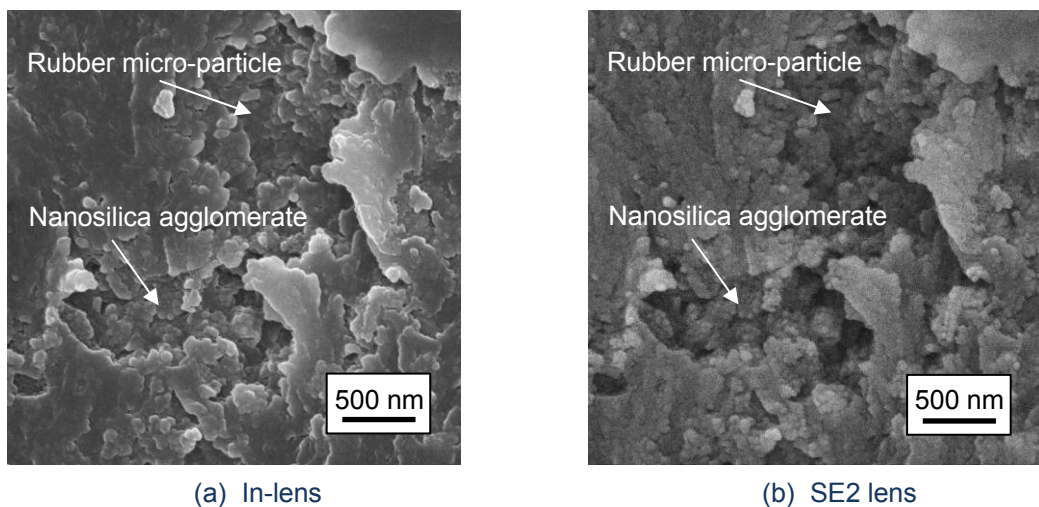


Figure 10.18. High magnification FEGSEM images of the 10N9R epoxy fracture surface [224], show (a) in-lens and (b) SE2 lens images of a single rubber particle and deformation around the agglomerated nanosilica particles.

Due to their co-operative nature of toughening i.e. synergy, an order of precedence needs to be established in order to understand their relative contributions. From the tensile and compressive stress-strain behaviour of the epoxies, the addition of rubber significantly reduces the yield strength of the epoxy polymer; and this was not observed readily for the nanosilica-modified epoxies. Zhang and Berglund [89], Young et al. [115] and Liu et al. [137] have also reported yield data for hybrid-modified epoxies and showed no increase in yield strength from the value of the rubber-modified epoxy as

observed in this study. Thus, it is argued that yielding initiates with the rubber micro-particles i.e. internal cavitation and shear banding. Then the nanosilica particles (notably always agglomerated for the hybrids considered in the present work) provide a co-operative role to toughening via only void growth mechanisms. Shown in Figure 10.19 is a schematic representation of the toughening mechanisms in the hybrid epoxy.

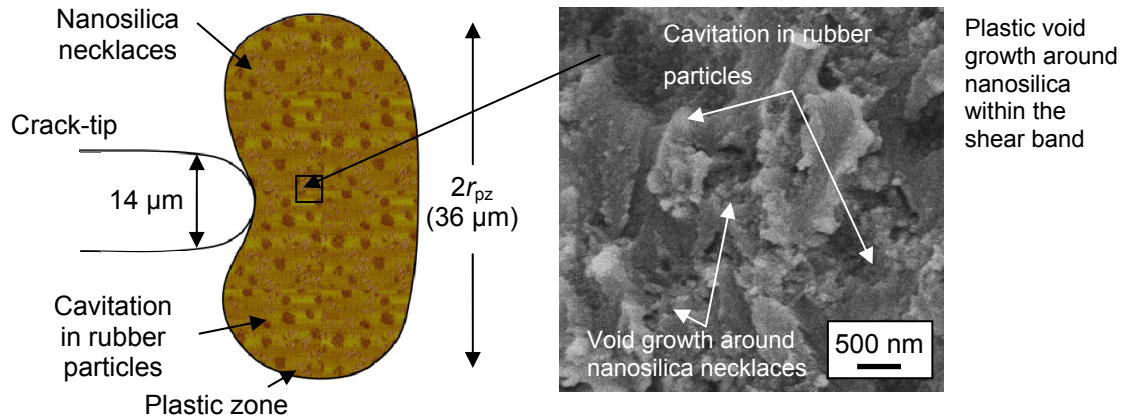


Figure 10.19. Schematic representation of the mechanisms that are expected to occur in the 10N9R anhydride cured DGEBA hybrid-toughened epoxy.

## 10.7 Chapter summary

The nanosilica particles were observed to remain well dispersed in the different epoxies. Values of  $D_{IP} = 20-11$  nm were obtained for 10-20 wt. % nanosilica. When rubber was added to the epoxy, it was found to phase separate into spherical 1  $\mu\text{m}$  particles in the rubber-modified epoxies and into 1.5  $\mu\text{m}$  particles in the hybrid-modified epoxies. Increasing amounts of rubber remained in solution as the nanosilica content was increased in the hybrid epoxies.

Direct comparison was made between the value of  $T_g$  and molecular weight between cross-links. The addition of nanosilica has no effect on the  $T_g$ , hence the cross-link density is reported to remain unchanged. The general trend would suggest that higher molecular weight between cross-links seems to provide increased toughenability with nanosilica. This confirms that toughening mechanisms are via deformation processes in the matrix, as is well documented for rubber toughened epoxies.

For the hybrid epoxies, the addition of nanosilica resulted in increasing amounts of rubber remaining in solution. However, this is not generally regarded as a method of increasing the fracture toughness compared to the mechanisms obtained from phase separated rubbers.

The Young's moduli were obtained for the epoxies using tensile and compressive tests. Reasonable values were obtained from compressive tests however the tensile values were much more precise. Typically values of  $E$  were in the range 3-4 GPa for the epoxies. Since the stiffness properties are predominantly volume fraction controlled, Halpin-Tsai and Neilson models predicted the Young's modulus for both the nanosilica-modified and hybrid-modified epoxies.

The yield behaviour was considered in some detail for the nanosilica-modified epoxies. Different interfacial adhesions were obtained for the different epoxies, although the same nanosilica particles had been used. Either the chemistry or the formation of an inter-phase layer in the particle-matrix interface are postulated to be contributing to the differences are being observed. Interestingly, the best adhesion was obtained in the polyether-amine cured DGEBA whilst the worst was obtained in the polyether-amine cured DGEBA/F and further work needs to be conducted to understand this effect. Such a study was not conducted on the hybrid-modified epoxies due to the complex morphologies that were present.

Roughly linear increases in the fracture energy were obtained for the range of volume fractions that were examined in the nanosilica-modified epoxies. They seem to scale in magnitude with the molecular weight between cross-links, i.e. the polyether-amine cured DGEBA/F was the most toughenable, with the lowest value of  $T_g$ . The toughening mechanisms that are presented in the nanosilica-modified epoxies are shear band yielding and debonding with subsequent plastic void growth.

No difference in the fracture energy was obtained with nanosilica content in the amine cure TGMDA epoxy. For the hybrid-modified anhydride cured DGEBA epoxies, maximum fracture energy was obtained for the 10N9R epoxy with a synergistic behaviour noted. This is postulated as plastic void growth processes around the nanosilica particles, which are enhanced by the presence of the much larger rubber particles.

The following chapter now looks to analytically model the observed toughening mechanisms and compares the models to the experimental data from this work and the literature.

## Analytical Modelling of Toughening Mechanisms

### 11.1 Introduction

The two major toughening mechanisms in nanosilica-modified epoxies have been identified as (i) the formation of localised plastic shear yielding, initiated by stress concentrations around the high modulus nanosilica particles, and (ii) debonding of nanosilica particles which occurs when the particle-matrix adhesion is sufficiently low. This then enables plastic void growth of the epoxy, which absorbs further strain energy.

These toughening mechanisms are very similar to well established mechanisms for rubber micro-particle inclusion in epoxies [98]. For rubber toughened epoxies, stress concentrations form in the epoxy and result in internal cavitation of the rubber particles, this initiates shear band yielding and plastic void growth of the epoxy [222, 257]. This dissipates strain energy, improving the fracture properties of the rubber-modified epoxy.

The nanosilica particles are rigid, thus the order of these mechanisms is different. Firstly shear band yielding initiates at stress concentrations (the particles) when the epoxy polymer begins to yield. Then the nanosilica particles debond, followed by plastic void growth in the epoxy.

Previous modelling studies by Huang and Kinloch [85, 94] for rubber-particle toughened epoxy polymers are relevant to modelling the nanosilica modified-epoxy polymers. Their work was used as an initial theory from which models were developed to predict toughening effects due to nanosilica- and hybrid-modification. In this chapter, the mathematical models are developed and then compared to the experimental data from this study and from literature. Huang and Kinloch [94] proposed a generalised solution to examine incremental increases in  $G_C$  as

$$G_C = G_{Cu} + \psi \quad (11.1)$$

where  $G_{Cu}$  is the fracture energy of the unmodified epoxy polymer and  $\Psi$  represents the overall toughening contributions provided by the presence of the particulate phase. The toughening increment due to nanosilica, termed  $\Psi_N$ , is a combination of three mechanisms, as identified from the experimental studies, and can be separated into their relative toughening contributions. These are (i) plastic shear band yielding in the epoxy,  $\Delta G_s$ , (ii) nanosilica-particle debonding,  $\Delta G_{db}$ , and (iii) plastic void growth in the epoxy polymer,  $\Delta G_v$ .

$$\Psi_N = \Delta G_s + \Delta G_{db} + \Delta G_v \quad (11.2)$$

These three terms are expanded upon and considered in further detail below.

## 11.2 Shear band yielding due to nanosilica, $\Delta G_s$

The energy contribution from localised plastic shear band yielding,  $\Delta G_s$ , initiated by the presence of the nanosilica particles is related to the size of the plastic zone and was calculated from [94] as

$$\Delta G_s = 2 \int_0^{r_y} U_s(r) dr \quad (11.3)$$

where  $r_y$  is the radius of the plastic zone ahead of the crack-tip and  $U_s(r)$  is the dissipated strain-energy density for the shear band yielding mechanism. Evans et al. [258] have proposed that the lower limit of the integral should be the minimum distance from the crack plane at which the epoxy polymer between the particles experiences plastic shear band yielding. This distance was proposed to be of the order of the particle radius [217] i.e. incorporation of a particle-size dependence to the shear term. Thus, Equation (11.3) now becomes

$$\Delta G_s = 2 \int_{r_p}^{r_y} U_s(r) dr \quad (11.4)$$

where  $r_p$  is the radius of the particle. With the lower integration limit of  $r_p$ , instead of zero, the expression for the term  $\Delta G_s$  was evaluated as per [94]. Four shear bands were allowed to form from each particle, and these were allowed to scale with the value of  $r_p$  and distance from the crack-tip. The work of Dekkers and Heikens [76, 77] has shown that shear bands will initiate from all of the particles and the dissipated strain energy density function,  $U_s(r)$ , can be given as

$$U_s(r) = v_{sb}(r)w_d(r) \quad (11.5)$$

The  $v_{sb}(r)$  is the volume fraction of shear yielded matrix material and  $w_d(r)$  is the plastic strain energy density. The magnitude of  $v_{sb}(r)$  as a function of the radial distance from the crack-tip was given from [94] as

$$v_{sb}(r) = N_v v_{sb/p} = 0.5v_f \left\{ 3 \left( \frac{4\pi}{3v_f} \right)^{1/3} \alpha(r) + 4[1 - \alpha(r)]^{3/2} - 4 \right\} \quad (11.6)$$

The magnitude of  $v_{sb}(r)$  was calculated as the product of the number of particles,  $N_v$ , i.e.  $\left( \frac{3v_f}{4\pi r_p^3} \right)$  and  $v_{sb/p}$ , where  $v_f$  is the volume fraction of particles and  $v_{sb/p}$  is the volume fraction of shear yielded material per particle. A scaling factor for the strain field in the process zone,  $\alpha(r)$ , was proposed by Kinloch [82] to be

$$\alpha(r) = 1 - \frac{r}{r_y} \quad (11.7)$$

The strain field for the process zone is considered to be  $0 \leq \alpha(r) \leq 1$ , where close to the crack-tip,  $\alpha(r) \rightarrow 1$  and when the strain approaches the elastic limit,  $\alpha(r) \rightarrow 0$ . Hence shear band yielding is more intense closer to the crack-tip.

The second term,  $w_d(r)$  is the plastic strain energy density of the matrix and assumes that the epoxy is perfectly elastic-plastic,

$$w_d(r) = 0.5\sigma_{ycu}\gamma_{fu}\alpha(r) \quad (11.8)$$

and is a function of the radial distance from the crack-tip. The variables  $\sigma_{ycu}$  and  $\gamma_{fu}$  are the plane-strain compressive true yield stress and true fracture strain for the unmodified epoxy.

Returning to Equation (11.4) and integrating with respect to  $\alpha$  (from Equation (11.7)) between  $r_p$  and  $r_y$  gives

$$\Delta G_s = 2 \int_{r_p}^{r_y} U_s(r) dr = 0.5\sigma_{ycu}\gamma_{fu} F'(r_y) \quad (11.9)$$

when the value of  $r_p$  exceeds, roughly the plastic zone radius,  $r_{pzu}$  of the unmodified epoxy, the value of  $\Delta G_s$  becomes negative. This cannot be the case from an

experimental viewpoint and a simple modification is introduced to eliminate  $\Delta G_s$  when it is negative. The toughening contribution due to shear band yielding in the epoxy is now,

$$\Delta G_s = 0.5v_f \sigma_{ycu} \gamma_{fu} \left( \frac{F'(r_y) + |F'(r_y)|}{2} \right) \quad (11.10)$$

the  $F'(r_y)$  term takes a modified form of the original formulation of the model [94], to be

$$F'(r_y) = r_y \left[ \left( \frac{4\pi}{3v_f} \right)^{1/3} \left( 1 - \frac{r_p}{r_y} \right)^3 - \frac{40}{35} \left( \frac{r_p}{r_y} - 1 \right)^{3/2} \left( \frac{r_p}{r_y} \right) \left( \frac{7}{5} - \frac{r_p}{r_y} \right) - 2 \left( 1 - \frac{r_p}{r_y} \right)^2 + \frac{16}{35} \right] \quad (11.11)$$

The value of  $r_y$  is defined as

$$r_y = K_p^2 \left( 1 + \frac{\mu_m}{3^{1/2}} \right)^2 r_{pzu} \quad (11.12)$$

where  $K_p$  is the maximum stress concentration for the von Mises stresses around a rigid particle,  $\mu_m$  is a material constant which allows for the pressure-dependency of the yield stress and was shown by Sultan and McGarry [10] to be in the range from 0.175-0.225 (taken as 0.2). The value of  $K_p$  is dependent on the volume fraction of particles, and was calculated by linear regression of the data von Mises stress concentration versus volume fraction from Guild and Young [259] for glass particles in an epoxy matrix (noting that  $E_p \gg E_m$ ). The value of  $K_p$  varies from approximately 1.65-1.73 for the range of volume fractions used in the present work (see Equation (11.13)).

$$K_p = 0.59v_f + 1.65 \quad (11.13)$$

The value of  $r_{pzu}$ , the Irwin prediction of plane strain plastic zone radius for the unmodified epoxy at fracture, was calculated from [193] as

$$r_{pzu} = \frac{1}{6\pi} \frac{K_{Cu}^2}{\sigma_{ytu}^2} \quad (11.14)$$

where  $K_{Cu}$  is the fracture toughness and  $\sigma_{ytu}$  is the tensile true yield strength for the unmodified epoxy polymer.

### 11.3 Debonding of nanosilica, $\Delta G_{db}$

The contribution due to particle debonding is widely considered to be negligible [188, 225, 235]. The value of the specific energy contribution due to particle debonding,  $\Delta G_{db}$ , for the 10N anhydride DGEBA epoxy was calculated as  $0.05 \text{ J/m}^2$  using work by Chen [49]. However, particle debonding is essential because this reduces the constraint at the crack-tip, and allows the epoxy polymer to deform plastically via void growth mechanisms. For the studied systems, some have shown no evidence of debonding from the matrix, (namely the amine cured TGMDA and polyether-amine cured DGEBA epoxies) and these epoxies would not be expected to contribute with void growth mechanisms.

### 11.4 Plastic void growth in the epoxy, $\Delta G_v$

The contribution of  $\Delta G_v$  via the plastic void growth mechanism was also taken from [94] and is expressed as

$$\Delta G_v = \left( 1 - \frac{\mu_m}{3^{1/2}} \right) (v_{fv} - v_f) \sigma_{ycu} r_{pzu} K_v^2 \quad (11.15)$$

where  $\mu_m$  is a material constant which allows for the pressure-dependency of the yield stress [10] as before,  $v_{fv}$  and  $v_f$  are the volume fraction of voids and the volume fraction of particles which debond. The value of  $v_{fv}$  was measured directly from the field emission gun scanning microscopy (FEGSEM) images, and was also calculated from the maximum hoop strain that a shell void could form as  $(1+\gamma_{fu})r_p$  in radius as shown schematically in Figure 11.1. The two were found to correlate very closely. For example, in the anhydride cured DGEBA,  $\gamma_{fu} = 0.75$ , thus the predicted diameter of the void is 35 nm. Johnsen et al. [7] reported the diameter of the void for this system as ~30 nm using atomic force microscopy and voids of 30-35 nm in diameter were measured from the FEGSEM images of the fracture surfaces.

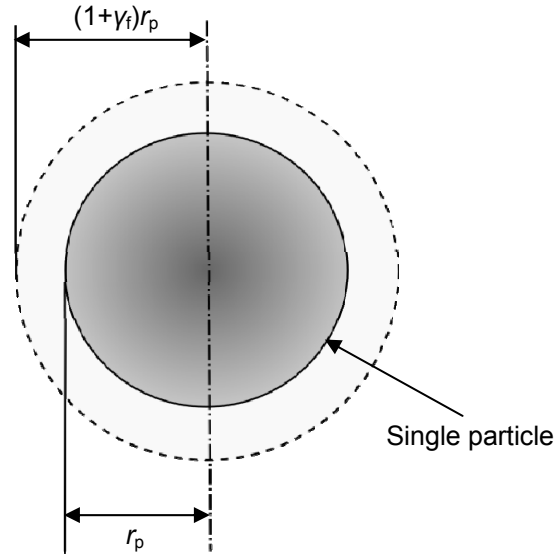


Figure 11.1. Schematic representation of a single particle with the maximum void size that can form in the epoxy.

Note that  $K_v$  is taken as the von Mises stress concentration factor for voids from Guild and Young's work [260] and varies between 2.11 and 2.12 for the volume fractions considered in this study. The value of  $K_v$  was allowed to vary linearly with volume fraction, see Equation (11.16).

$$K_v = 0.918v_f + 2.11 \quad (11.16)$$

An effort was made to derive a new equation for  $\Delta G_v$  with particle size dependence by defining new integrals between  $r_p$  and  $r_y$ . However, the  $\Delta G_v$  was found to be independent of particle size.

## 11.5 Modelling nanosilica toughening

A generalised expression for  $\Psi_N$  may be evaluated by combining Equations (11.10) and (11.15) into (11.2) to give

$$\Psi_N = 0.5v_f\sigma_{ycu}Y_{fu} \left( \frac{F'(r_y) + |F'(r_y)|}{2} \right) + \left( 1 - \left( \frac{\mu_m}{3} \right)^2 \right) (v_{fv} - v_f)\sigma_{ycu}r_{pzu}K_v^2 \quad (11.17)$$

where  $F'(r_y)$  and  $r_{pzu}$  were specified in Equations (11.11) and (11.14) respectively. The first part is the shear yielding term,  $\Delta G_s$ , and the second part is the plastic void growth term,  $\Delta G_v$ . For this model, stochastic variation in the material properties or particle size distribution is not considered. It is worth noting that no back-calculated fitting terms exist in the model and all the parameters are values from experimental tests.

The analytical model was applied to the systems from this study and Liang and Pearson's data [52]. Table 11.1 summarises the systems and the material properties for unmodified epoxies that were used to generate the mathematical models. A value for  $\sigma_{yt}$  was not obtained experimentally for the amine cured TGMDA or the amine cured multifunctional epoxies, and Equation (10.7) was used from Huang and Kinloch's work [94] to obtain values for  $\sigma_{yt}$  (shown italicised). The observations from compressive and fracture studies, as discussed in Ch. 10, are also summarised.

Table 11.1. The epoxy systems that were analytically modelled. The material properties for the unmodified epoxies are listed, and the individual contributions of shear band yielding and plastic void growth are identified as toughening observations for each epoxy polymer.

System	$G_{Cu}$ (J/m <sup>2</sup> )	$K_{Cu}$ (MPa√m)	$\sigma_{ytu}$ (MPa)	$\sigma_{ycu}$ (MPa)	$\gamma_{fu}$ (true strain)	Toughening observations	
						$\Delta G_s$	$\Delta G_v$
Amine cured TGMDA (Ch. 5)	70	0.78	111	140	0.75	✓	×
Polyether-amine cured DGEBA/F (Ch. 6)	184	0.54	82	101	1.06	✓	✓
Polyether-amine cured DGEBA (Ch. 7)	163	0.90	67	96	0.86	✓	×
Amine cured multifunctional Epoxy (Ch. 8)	202	0.75	99	125	0.64	×	×
Anhydride cured DGEBA (Ch. 9)	83	0.51	88	120	0.75	✓	✓
Piperidine cured DGEBA/F [52], [94]	450	1.1	74	94	0.71	✓	✓
Piperidine cured DGEBA [52, 94]	450	1.1	74	94	0.71	✓	✓

The amine cured TGMDA system was presented in Ch. 5. The polished sections from compressive strain softening tests showed that the unmodified epoxy for this system does shear band yield. Thus the nanosilica-modified formulations would also be expected to shear band yield, justifying the inclusion of a  $\Delta G_s$  term for the toughening increment,  $\Psi_N$ . When the fracture surfaces were examined, no evidence of plastic void growth around the debonded nanosilica particles could be readily identified. An interfacial parameter,  $k$ , was obtained to quantify the particle-matrix adhesion. With a value of  $k = 1.88$ , this suggests that the particles are well bonded to the epoxy; hence the measured  $\sigma_{yc}$  increases with nanosilica content. The  $\Delta G_s$  term was applied to  $\Psi_N$  and the resulting model was compared to the measured fracture energy,  $G_C$ , in Figure

11.2. The individual contribution of  $\Delta G_s$  is shown in the inset. Excellent correlation was obtained with the experimental data. The fit was less good for the 20N epoxy but this can be explained by the experimental error for  $G_C$  for the unmodified epoxy.

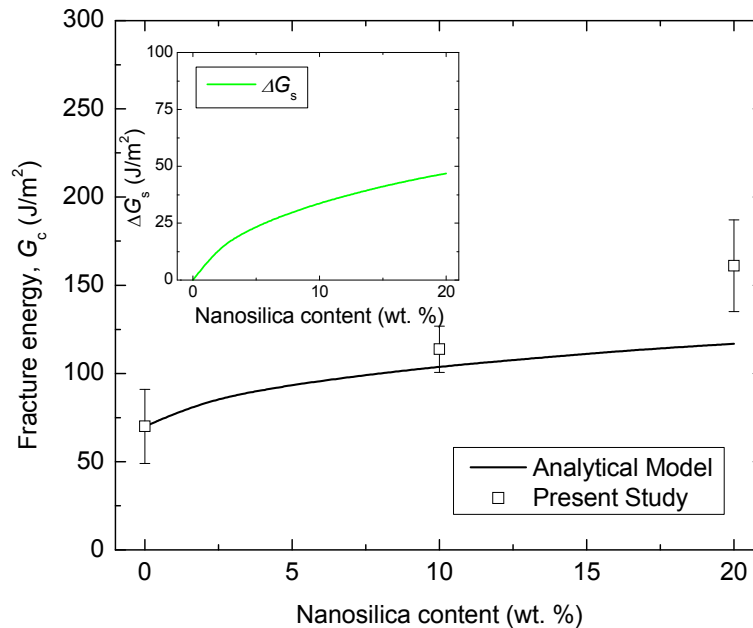


Figure 11.2. Fracture energy and  $\Delta G_s$  (inset) for the amine cured TGMDA epoxy versus nanosilica content. The experimental results from the present study are compared to the predicted fracture energy.

The polyether-amine cured DGEBA/F epoxy was presented in Ch. 6. Polished sections from compressive strain softening tests showed that this system was capable of shear band yielding. The particle-matrix interface was shown to be relatively weak. Notably, this was the only system in this study that showed a reduction in the value of  $\sigma_{yc}$  with increasing nanosilica content. A value of 0.46 was obtained for the interfacial parameter  $k$  (where  $k = 0$  would represent no stress carried by the particle) and suggests low interfacial adhesion. The fracture surfaces showed evidence of debonding with subsequent plastic void growth around the nanosilica particles. Thus, the inclusion of terms for  $\Delta G_s$  and  $0.15\Delta G_v$  in  $\Psi_N$  are justified. No analysis was conducted to estimate the proportion of particles that debond with subsequent void growth for this system. However, a value of  $15 \pm 5\%$  of debonded particles was obtained for the anhydride cured DGEBA, and was assumed to be the case for this system. The actual proportion of particles that debond with resulting plastic void growth may be larger because the particle-matrix adhesion is lower in this system compared to the anhydride system. Equation (11.1) was applied and describes how  $G_C$  varies with nanosilica content in Figure 11.3. The inset shows that the individual contributions of  $\Delta G_s$  and  $0.15\Delta G_v$  to the overall toughening are roughly equal in magnitude. Shear

band yielding of the epoxy provided a larger toughening effect at low nanosilica contents, and plastic void growth from debonded particles became the more significant in contribution of the two mechanisms above about 16 wt. % content of nanosilica. Noting that the assumption of 15 % of the debonding particles debonding seems reasonable despite the comparatively low interfacial adhesion, which is somewhat surprising. The analytical description of the experimental data seems very good.

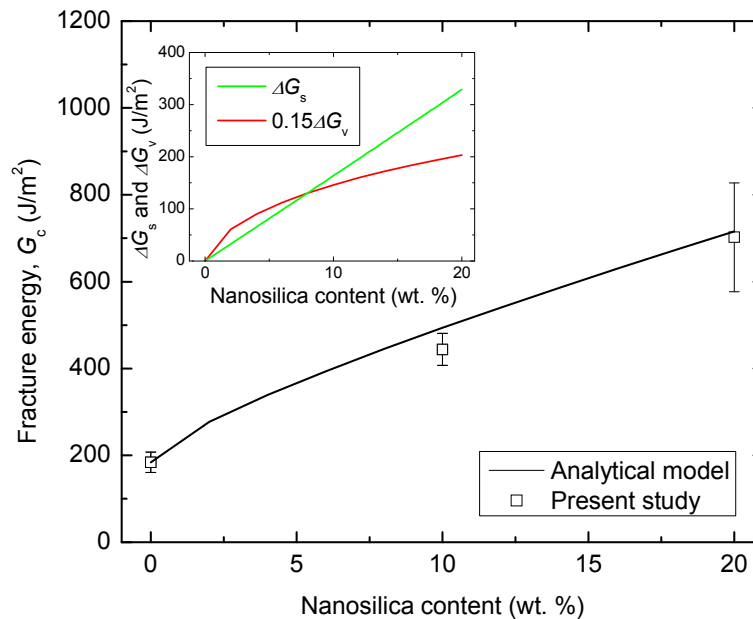


Figure 11.3. Fracture energy for the polyether-amine cured DGEBA/F epoxy versus nanosilica content for is compared to the predictive model. The individual contributions  $\Delta G_s$  and  $0.15\Delta G_v$  are shown in the inset.

The polyether-amine cured DGEBA system was discussed in Ch. 7 and was separately reported by Ma et al. [65]. With an interfacial parameter value of 1.76, good interfacial adhesion was exhibited between the epoxy and nanosilica particles, also noted in [65]. The values of  $\sigma_{yt}$  and  $\sigma_{yc}$  were found to increase with nanosilica content. Polished cross-sections from compressive strain-softening tests showed the formation of shear bands in the epoxy. Moreover, double-notched four-point bend (DN4PB) tests were conducted and the resulting images of sub-critically loaded crack-tips showed shear banding in the process zone region. The FEGSEM images of fracture surfaces were examined and no evidence of plastic void growth within the epoxy was observed. Thus,  $\Psi_N = \Delta G_s$  was modelled and compared to the values of  $G_c$  as shown in Figure 11.4. The resulting comparison also provides a very good fit for the experimental data from this study and Ma et al.'s values of  $G_c$  [65]. The individual contribution of  $\Delta G_s$  to the fracture energy is shown in the inset.

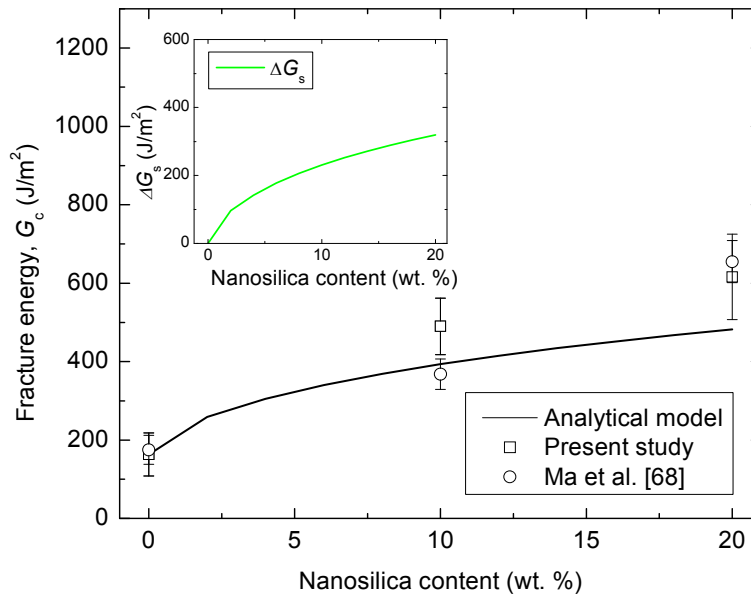


Figure 11.4. Fracture energy for the polyether-amine cured DGEBA versus nanosilica content. The experimental results and [65] are compared to the predicted fracture energy and  $\Delta G_s$  is shown in the inset.

The amine cured multifunctional epoxy system (Ch. 8) was unique to the studied epoxies in that no variation in  $G_C$  was found with nanosilica content. Small improvements in  $\sigma_{yc}$  were obtained from compressive tests and this suggests reasonable stress transfer through the particle-matrix interface with  $k = 1.34$ . No evidence of shear band yielding was readily obtained from optical sections of the strain softened compressive samples. Therefore, little shear band yielding would be expected in the plastic zone region of this epoxy.

Interestingly, the anhydride cured DGEBA epoxy possesses similar particle-matrix adhesion ( $k = 1.29$ ) and plastic void growth surrounding the debonded nanosilica particles was observed in the fracture surfaces of the nanosilica-modified epoxies. Therefore, shear band yielding seems to be vital for plastic void growth in the epoxy to occur around debonded nanosilica particles. Moreover, shear band yielding is confirmed to take mechanistic precedence in the failure process. A predictive model is compared to the experimental data obtained from Brooker [79] in Figure 11.5. Although, with no shear band yielding or debonding with subsequent void growth in the epoxy,  $\Psi_N = 0$ , and  $G_C = G_{Cu}$  for all nanosilica contents.

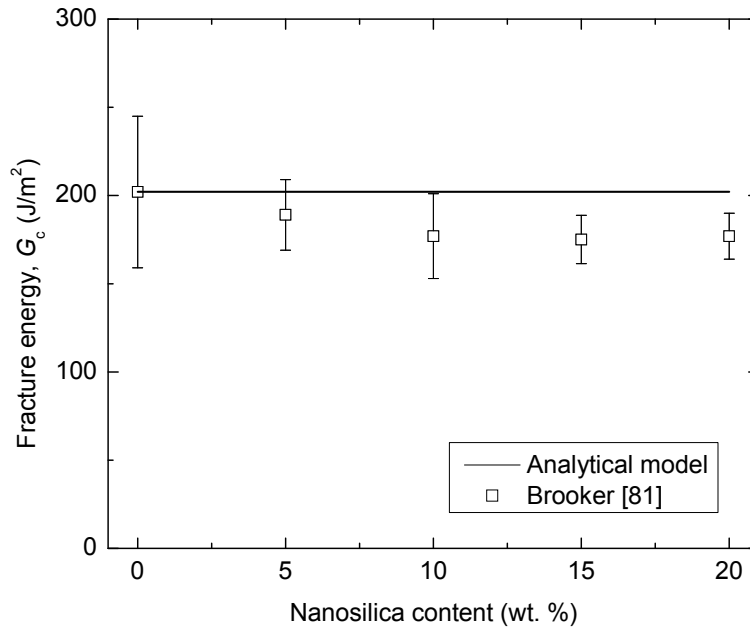


Figure 11.5. Fracture energy for the amine cured multifunctional epoxy versus nanosilica content. The experimental results from [79] did not vary with nanosilica content.

The anhydride cured DGEBA epoxy was studied in Ch. 9 and has been reported in [61]. The particle-matrix interfacial adhesion was quantified to be a value of  $k = 1.29$  and suggests reasonable stress transfer through the interface. Polished optical sections from DN4PB and compressive strain softening tests showed that this system was capable of shear band yielding. Moreover, this was found to occur for increasing nanosilica contents (as inferred for the other epoxies). FEGSEM images were taken from the process zone region of the fracture surfaces and evidence of  $15 \pm 5\%$  of the particles debonding with subsequent void growth was obtained. Thus  $\Psi_N = \Delta G_s + 0.15\Delta G_v$  was used to predict how  $G_c$  varies with nanosilica content. Shown in Figure 11.6, the predictive model provides excellent correlation with the values of  $G_c$  from this work and from [61]. The contribution of shear yielding is the predominant contributor to improvement in fracture energy for this system.

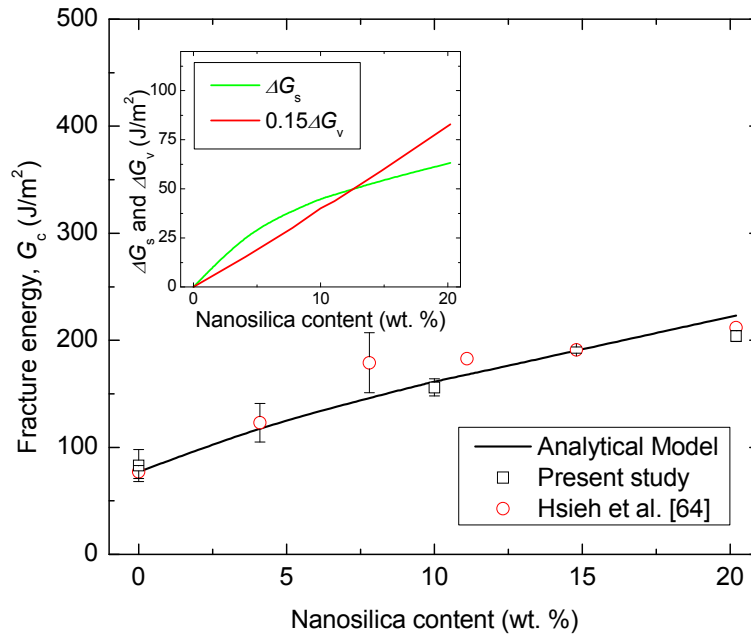


Figure 11.6. Fracture energy for the anhydride cured DGEBA epoxy versus nanosilica content. The contributions  $\Delta G_s$  and  $0.15\Delta G_v$  are shown inset. The experimental data from this study and [61] compare very well to the predictive model.

Liang and Pearson reported data for a piperidine cured DGEBA/F with 20 nm nanosilica particles in [52]. No change in  $\sigma_{yc}$  was reported for the nanosilica-modified epoxies and infers a similar particle-matrix adhesion to the anhydride cured DGEBA. Liang and Pearson [52] did report shear band yielding and debonding with plastic void growth as a toughening mechanisms. Thus  $\Psi_N = \Delta G_s + 0.15\Delta G_v$  was used to model  $G_c$ . These contributions were implemented and compared to the experimental results from [52] in Figure 11.7. Good general agreement was found between the analytical model and fracture results, especially considering the experimental error from the FEGSEMs is 5 %. At low nanosilica contents, the fit is poor, but does improve as the nanosilica content reaches 6.5 vol. % and further confirms the validity of this predictive model, noting again that taking  $\Delta G_v$  for 15 % of the particles seems very reasonable. A rationale for the poor quality of the fit could be because  $\gamma_{fu}$  was taken as 0.71, which is for a piperidine cured DGEBA from [95] and not for a piperidine cured DGEBA/F.

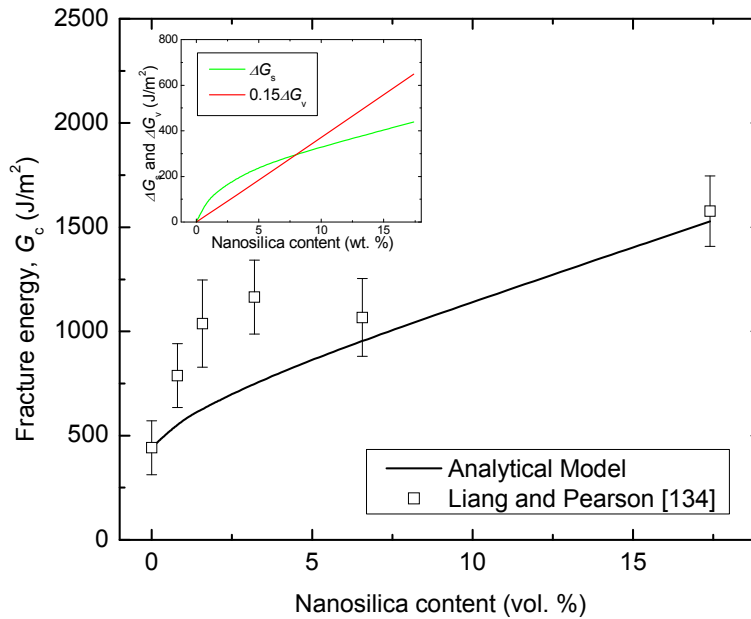


Figure 11.7. Fracture energy versus nanosilica content for piperidine cured DGEBA/F epoxy from [52] (20 nm silica particles) is compared to the predictive model. The inset shows contributions  $\Delta G_s$  and  $0.15\Delta G_v$ .

### 11.5.1 The effect of particle size

For the nanosilica-modified systems, a trend has developed with regard to particle debonding and subsequent plastic void growth for the 20 nm nanosilica-modified epoxies. A question arises as to why there is an apparent limit at  $15 \pm 5\%$  void growth which seems to be independent of particle-matrix adhesion, if debonding occurs, i.e.  $k < 1.3$ . Even with only 15% particle debonding and plastic void growth, the magnitudes of  $0.15\Delta G_v$  and  $\Delta G_s$  are in parity with one another. Much greater toughening could be invoked with a larger degree of debonding and plastic void growth.

Liang and Pearson [52] reported a second system, with 80 nm nanosilica particles in a piperidine cured DGEBA system. Shear band yielding was observed and no change in  $\sigma_{yc}$  was reported with the addition of nanosilica. Thus,  $\Psi_N = \Delta G_s + 0.15\Delta G_v$  was assumed. This analytical solution was compared to the experimental data in Figure 11.8 and a poor agreement was found. The obvious reasoning would be that the effect of larger particle size is that more particles debond and contribute via plastic void growth mechanisms. Because the fracture surfaces could not be examined to quantify the amount of void growth that occurs, a least squares regression was performed and it was estimated that 30% of the nanosilica particles would need to debond with subsequent plastic void growth in order to obtain good agreement with Liang and Pearson's values of  $G_c$ . The goodness of fit would suggest that an enhanced contribution from  $\Delta G_v$  (i.e.  $0.3\Delta G_v$ ) was obtained with a small increase in particle size.

Further thought has been given to obtaining the optimal particle size for toughening with epoxies in the future.

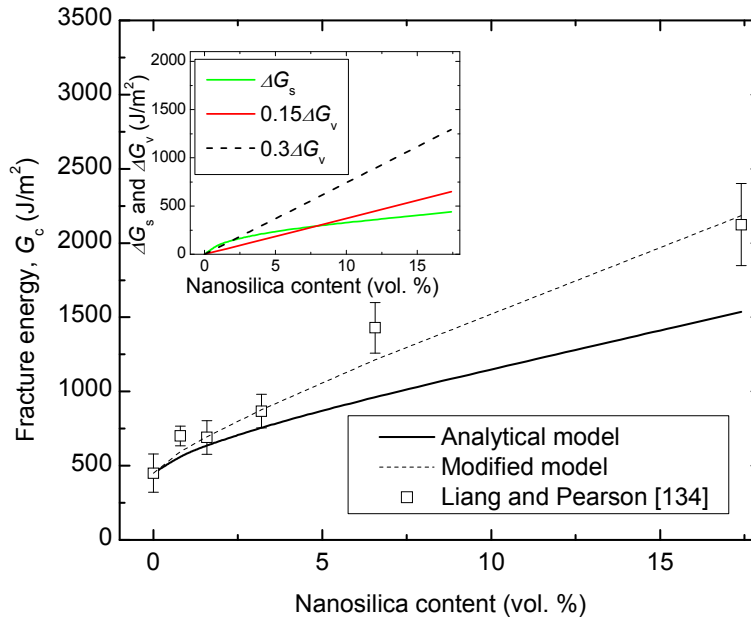


Figure 11.8. Fracture energy for piperidine cured DGEBA epoxy versus nanosilica content from [52] (80 nm silica particles) is compared to the predictive model. The contributions of  $\Delta G_s$ ,  $0.15\Delta G_v$  and  $0.3\Delta G_v$  shown in the inset.

### 11.5.2 Optimal particle size for rigid particle toughening

A plot of the shear banding term,  $\Delta G_s$ , versus particle radius,  $r_p$ , is shown in Figure 11.9 for the anhydride cured DGEBA epoxy. Smaller particles provide the largest values of  $\Delta G_s$ , and the value of  $\Delta G_s$  tends to zero for large particles ( $\Delta G_s = 0$  when  $r_p = 6 \mu\text{m}$ ). For small variations in  $r_p$ , as shown in the inset, little variation was found in the value of  $\Delta G_s$ . For small particles, the contribution of  $\Delta G_s$  is maximised. However, the actual contribution is relatively small in magnitude (70-90 J/m<sup>2</sup>). At higher volume fractions, little additional improvements are obtained. This would suggest that with such small particle sizes, even at relatively low nanosilica contents, maximum volumes for shear deformation are induced (the inter-particle distance is 11 nm for 20N) and there is little free-volume matrix epoxy to shear band yield at higher nanosilica concentrations.

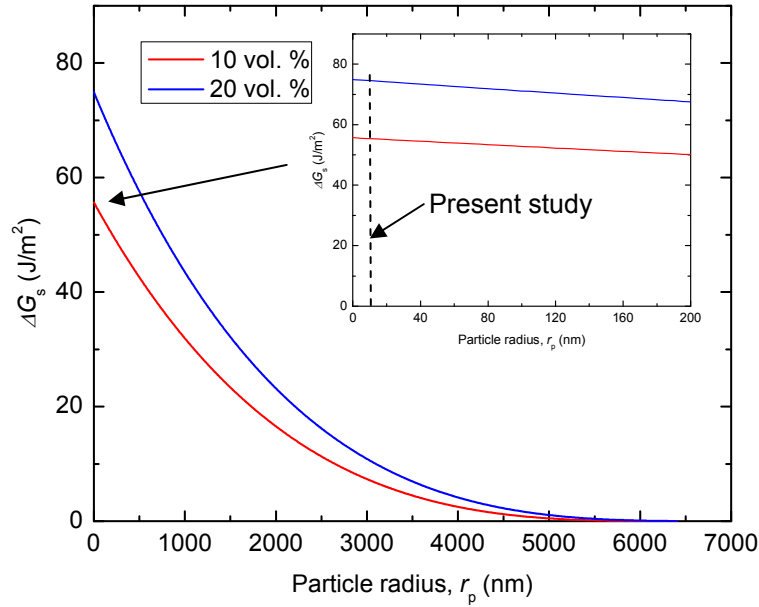


Figure 11.9. The shear band yielding term,  $\Delta G_s$  versus nanosilica-particle radius (at 10 and 20 vol. %) for the anhydride cured DGEBA epoxy. There is little variation for small changes in particle size (inset).

The critical debonding stress,  $\sigma_{db}$ , at the particle-matrix interface was proposed by Nicholson [48] and modified by Lauke [33] to show that  $\sigma_{db}$  can be given as

$$\sigma_{db} = \frac{1}{3(1-\nu)} \sqrt{\frac{16\gamma_d E_m (1+\nu)}{r_p}} \quad (11.18)$$

where  $\gamma_d$  is the specific debonding energy for two newly created surfaces and  $E_m$  is the Young's modulus of the matrix. Chen et al. [49, 261] and Williams [51] have also derived similar equations. The value of  $\gamma_d$  was calculated as 0.01 J/m<sup>2</sup> from Chen et al.'s work [49]. A plot of Equation (11.18) is shown in Figure 11.10 for varying values of  $r_p$ . The reduction in the critical debonding stress,  $\sigma_{db}$ , is very steep as the value of  $r_p$  increases initially from zero. The curve flattens when  $r_p \approx 50 \pm 10$  nm as demonstrated in the inset. Plastic void growth was previously shown to be independent of particle size. However, debonding is critical in providing relief of the crack-tip constraint, hence allowing the epoxy to plastically deform, and  $\sigma_{db}$  is sensitive to particle size. From Figure 11.10, when  $r_p = 10$  nm (for the nanosilica particles from this work) then  $\sigma_{db}$  is relatively high, calculated as 122 MPa for the anhydride cured DGEBA from Ch. 9 ( $\nu_f = 0.1$ ). For large values of  $r_p$ , such as 1  $\mu$ m,  $\sigma_{db} = 12$  MPa, so debonding would occur more readily. However, this would result in the reduction of strength in the particle-epoxy composite [36]. Hence, to provide a maximum toughening effect without compromising the strength of the epoxy, optimal values of  $r_p$  are expected to be of the range  $r_p = 50 \pm 10$  nm (i.e. 100 nm particles) in an attempt to maximise  $\Delta G_s$  and

minimise  $\sigma_{db}$  without altering the yield strength of the silica particle-epoxy composite significantly. Hence the value of the critical debonding stress,  $\sigma_{db}$ , and tensile yield strength of the polymer,  $\sigma_{yt}$ , should be roughly equal for optimal debonding without altering the yield strength of the particle-modified epoxy.

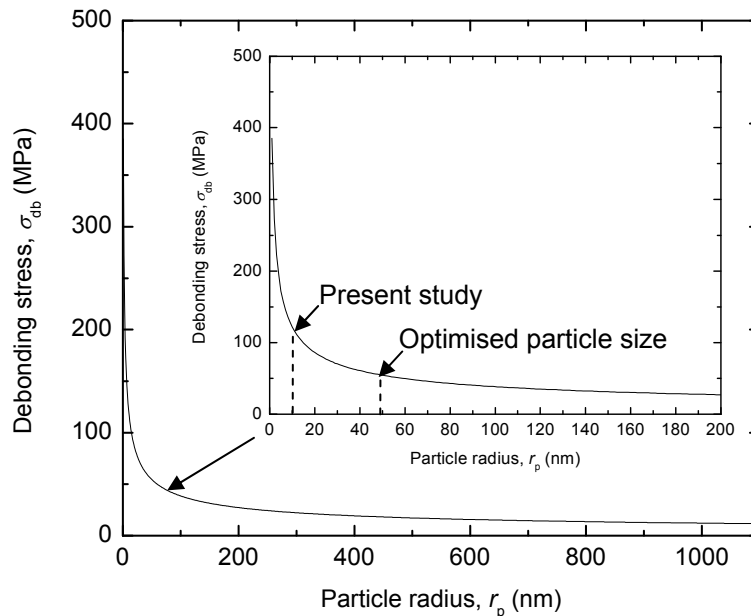


Figure 11.10. The debonding stress,  $\sigma_{db}$ , as a function of particle radius at the particle-matrix interface. The inset focuses on small particle radii in the range 0-200 nm.

## 11.6 Modelling coreshell particle toughening

One solution to fulfilling the criterion of small particles sizes that are capable of readily debonding into voids would be to use sub-micron sized coreshell particles in the epoxy. Such particles can be applied to the epoxies without altering their  $T_g$ , because the rubber centres are encapsulated in a hard shell. Coreshell particles can be used in an epoxy matrix without altering the monomer viscosity as large glass beads would. Giannakopoulos [262] has reported coreshell (CSR) particles as modifiers in the anhydride cured DGEBA epoxy from this study. Experimental values of  $G_C$  were reported for two compositions; a 100 nm particle with a poly-butadiene core and a 300 nm particle with a styrene core at increasing CSR contents up to 15 wt. %. When the fracture surfaces were examined, evidence of coreshell separation and plastic void growth was clearly identified for all the CSR particles in the epoxy, as shown in Figure 11.11.

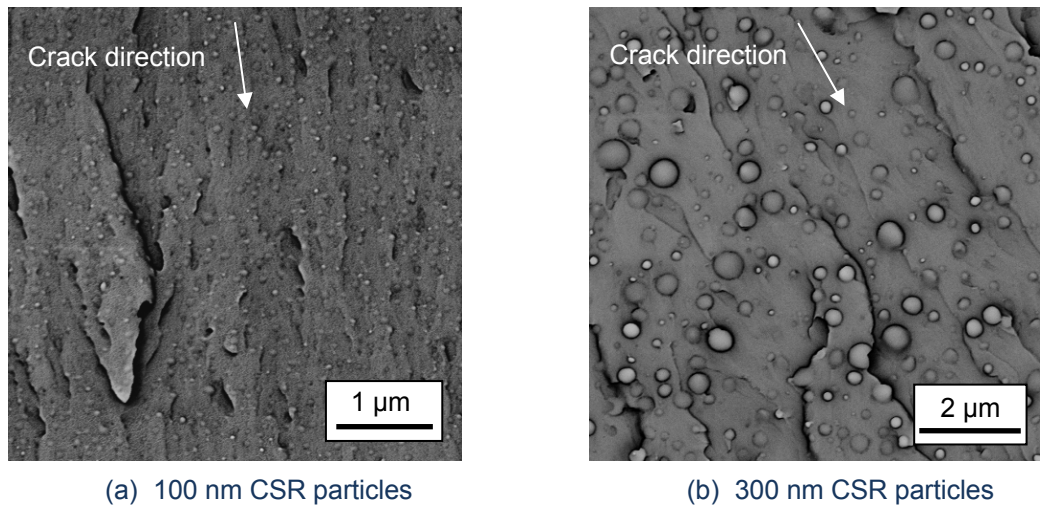


Figure 11.11. The fracture surfaces for 9 wt. % coreshell particle-modified anhydride cured DGEBA epoxies with (a) 100 nm particles and (b) 300 nm particles.

Thus  $\Psi_N = \Delta G_s + \Delta G_v$  was used, as before (noting now 100%  $\Delta G_v$  is used as all the particles show void growth) and the predictive model was compared to the experimental data in Figure 11.12. Two individual models were produced for the two types of CSR particle. However, there was little difference between the two predictions as they overlaid one another, and so only the model for 100 nm coreshell particles is shown. The insets show the individual contributions of  $\Delta G_s$  and  $\Delta G_v$  to the overall fracture energy of the epoxy polymer. The difference between the values of  $\Delta G_s$  is minimal, as mentioned previously. Though now, the contribution of  $\Delta G_v$  is large, a factor 7 times larger than  $\Delta G_s$  for the 15 wt. %, 300 nm CSR-epoxy. The predictive model agrees very well with the experimental data that was reported. For the 10N nanosilica-modified epoxy, a 140 % improvement in  $G_C$  was obtained. For these formulations, an improvement of about 560 % was obtained; roughly equivalent to the  $G_C$  for a rubber toughened epoxy without reductions in  $T_g$ ,  $E_m$  and  $\sigma_y$ . Based on toughening by shear band yielding and plastic void growth mechanisms, these formulations fulfil the limit of toughening that can be achieved by the two mechanisms.

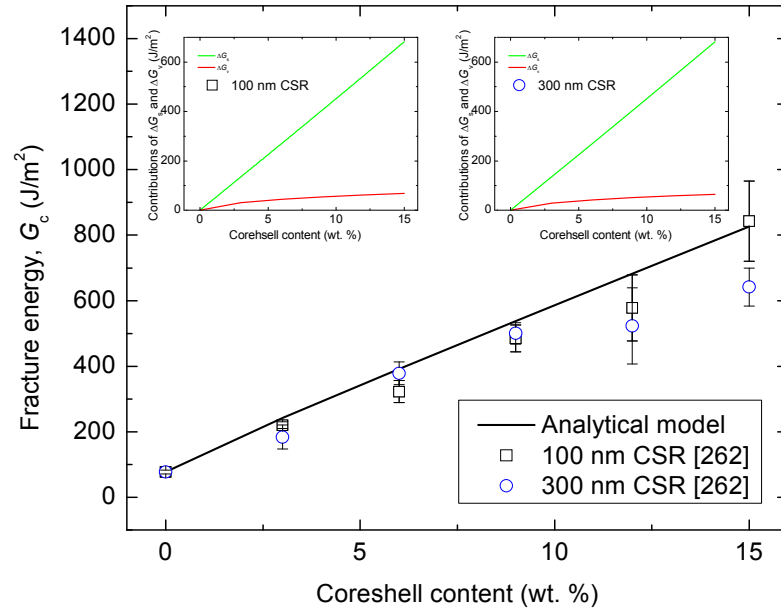


Figure 11.12. Fracture energy for anhydride cured DGEBA epoxy versus CSR content from [262]. The experimental values of  $G_c$  are compared to the predictive models for 100 nm and 300 nm particles. The contributions of  $\Delta G_s$  and  $\Delta G_v$  are shown in the inset.

## 11.7 Modelling rubber toughening

This section describes modelling of the rubber toughened epoxies. Then the proceeding section aims to predict the toughening of the hybrid-modified epoxies.

For analytical modelling of rubber toughening, the toughening increment,  $\psi_R$ , was calculated using Huang and Kinloch's [94] modified equations shown previously, noting that  $K_v$  varies between 2.11 and 2.12 for the von Mises stress concentration at a soft inclusion, and incorporating a rubber bridging term  $\Delta G_b$ , from [105] as

$$\psi_R = \Delta G_b + \Delta G_s + \Delta G_v \quad (11.19)$$

where  $\Delta G_b$  is defined as

$$\Delta G_b = 4\Gamma(T)v_f \quad (11.20)$$

and  $\Gamma(T)$  is the tearing energy as a function of temperature. The value of  $\Gamma(T)$  was taken as 460 J/m<sup>2</sup> [263]. Shown in Figure 11.13 is the prediction for rubber toughening of the anhydride cured DGEBA, noting that the content of rubber is for the phase separated weight fraction and not the formulation weight fraction.

The good agreement between the predicted fracture energy and experimental value (Figure 11.13) would imply that the hypothesis for the rubber that remains in solution, not contributing to toughening is valid. As shown in the inset, the contribution due to rubber bridging is greater than the contribution of shear band yielding. It is worth noting that in reality, the particles that bridge the crack will not also cavitate, whilst the model assumes this to occur, hence the model over predicts the fracture energy.

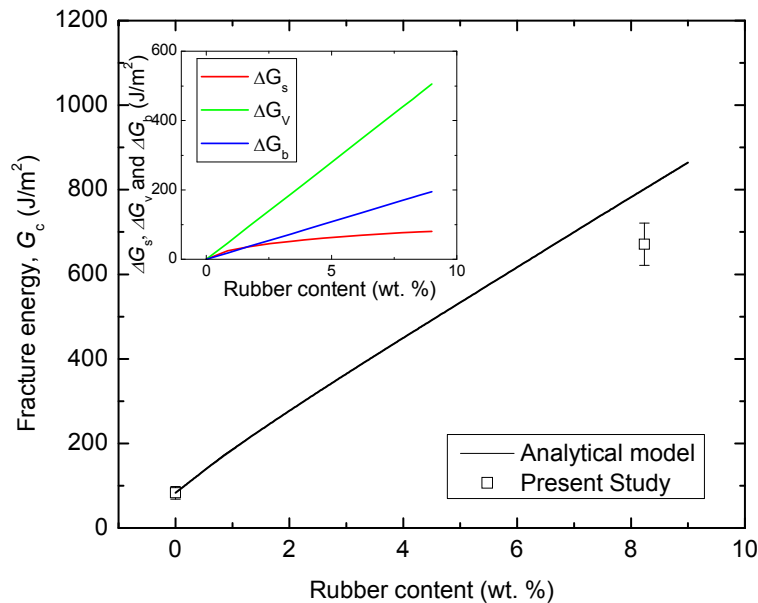


Figure 11.13. Fracture energy for the rubber-modified anhydride cured DGEBA epoxy versus phase separated rubber content. The present work is compared to the predicted fracture energy. The individual contributions of  $\Delta G_s$ ,  $\Delta G_v$  and  $\Delta G_b$  are shown (inset).

## 11.8 Modelling hybrid toughening

Fracture surface examination of the hybrid-modified epoxies identified plastic void growth to surround the nanosilica particles in Section 10.6.2. A sequence of mechanisms was identified for the failure process as firstly internal cavitation of the rubber particles due to high stress triaxiality at the crack-tip to form voids in the epoxy, which occurs at relatively low stresses before the epoxy yields [91, 98]. Secondly these voids increase the stress concentration factor of the rubber phase and dilatational shear band yielding initiates as the epoxy yields. This is highly constrained to the regions between the rubber particles and debonding occurs in the nanosilica particles. Thirdly plastic void growth within the cavitated rubber- and nanosilica-particles now occurs and this dissipates further strain energy. Importantly, the combination of the two dissipates more strain energy than the rubber-modified epoxy alone.

The stress concentration is higher for the cavitated rubber particles (von Mises stress concentration factor  $\approx 3$ ), and thus shear band yielding is not induced from the nanosilica particles ( $K_p \approx 1.7$ ). This seems reasonable and can explain why  $G_C$  for the hybrid-epoxy is no greater than  $G_C$  for the rubber-modified epoxy in the amine cured TGMDA epoxy (Ch. 5), where only shear band yielding induced toughening was achieved in the nanosilica-only epoxies.

This section tackles shear band yielding in the rubber and plastic void growth from both particles as a potential mechanism by which the synergistic behaviour of toughening in the hybrid multi-phase polymers arises.

Modelling considerations for the hybrid epoxy are more complex due to the presence of the soft and rigid particulate phases in the epoxy. A second complication arises from the fact that as the nanosilica content is increased, a larger amount of rubber remains in solution. A summary of the volume fraction of phase separated rubber in the epoxies was shown previously in Table 10.2. Effectively, the contribution due to rubber toughening decreases due to a lower volume fraction of phase separated rubber in the epoxy, even though the amount added to the formulations is constant at 10.6 vol. %. The rubber that remains in solution plasticises the epoxy matrix a little. This was previously discounted from being a significant toughening mechanism [256] in Section 10.6.2 and will be assumed to provide no additional toughening effect.

Measurements from FEGSEM images of the nanosilica-modified epoxy fracture surfaces were discussed previously. It is recognised that  $15 \pm 5$  % void growth was measured for well dispersed particles in the epoxy. The hybrid epoxy contains agglomerated particles. Furthermore, the quality of the particle-particle and particle-matrix adhesion is not known for the agglomerate nanosilica formulation. Therefore, 15 % particle debonding cannot be assumed. Thus, separate models for ( $k' =$ ) 5, 10 and 15 % debonding with void growth are included to gain an overview of the synergistic behaviour in the hybrid epoxy and understand exactly how much void growth is occurring. It is noteworthy to mention that  $\Delta G_v$  is independent of particle size and thus, no description of the size of the nanosilica agglomerates is necessary to model the hybrids.

The synergistic toughening increment,  $\psi_H$ , takes the form

$$\psi_H = \psi_R + \psi_N = [\Delta G_b + \Delta G_s + \Delta G_v]_u + [k' \Delta G_v]_R \quad (11.21)$$

using  $\Delta G_b$ ,  $\Delta G_s$ , and  $\Delta G_v$  from the material properties for the unmodified epoxy for the first term and for the second term, taking,  $k'\Delta G_v$  from the material properties for the (phase separated vol. %) rubber-modified epoxy. For this term, the material properties should to be dependent on the volume fraction of phase separated rubber in the hybrid-modified epoxy since these provide the toughening effect ( $\sigma_{yc}$ ,  $\sigma_{yt}$  and  $\gamma_f$  are assumed to remain unchanged as a first approximation). The values of  $G_C$  and  $K_C$  were allowed to vary with volume fraction of phase separated rubber. Those that were not measured experimentally were obtained via linear interpolation between the material properties of the unmodified epoxy and 9R epoxy. The toughening contribution was then calculated as before.

The contribution to the fracture energy due to the secondary nanosilica phase was described as  $k'\Delta G_v$ . This was obtained by taking the rubber-modified base properties for each of the hybrid formulations and letting the phase separated rubber content vary with nanosilica content as in Table 10.1. A good interpretation of toughening in the hybrid epoxies was obtained in Figure 11.14. The graph shows the effect of different percentages of plastic void growth, on the overall fracture energy of the hybrid epoxies. The predictive value for 20N9R over-estimates the fracture energy. This is probably because the effects of the large agglomerated nanosilica particles now cause such large stress concentrations in the epoxy such that they cause failure in the epoxy. From TEM imaging of the shear banded region for the 15N9R hybrid anhydride cured DGEBA (Ch. 9), evidence of debonding at the nanosilica particle-particle interface was identified. This would suggest that this interface may be relatively weak. Liang and Pearson [134] have reported that high concentrations of nanosilica in the hybrid epoxies results in values of  $G_C$  which are lower than the rubber-modified base value for that epoxy and would provide general agreement with this work.

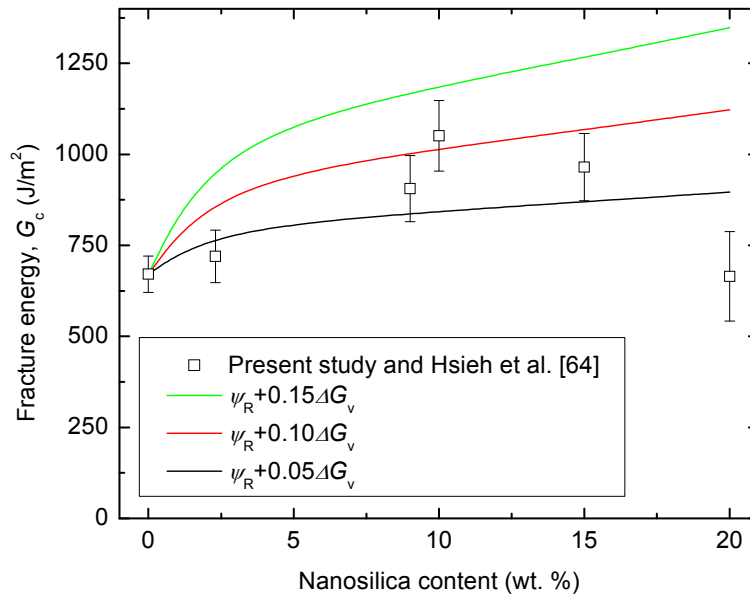


Figure 11.14. Fracture energy for the rubber- and hybrid-modified epoxies anhydride cured DGEBA epoxy versus nanosilica content. The experimental study from [61] is compared to the predicted fracture energy for different degrees of void growth.

Unfortunately, a detailed understanding of microstructures is required to model hybrid toughening, and this was not available for any other systems in order to validate this model further. Examination using TEM of osmium tetroxide stained DN4PB samples would be an excellent technique to confirm the mechanistic behaviour of this synergistic toughening. The model shows that even the smallest contribution via plastic void growth from the secondary phase is enough to account for a synergistic effect in a rubber-modified epoxy and may explain why a synergistic behaviour with CTBN rubber is well documented in the literature i.e. [72, 89, 113-118, 120, 124, 126, 129, 130, 137, 253-255]. With the addition of 10 wt. % nanosilica to the rubber-modified epoxy (10N9R), a maximum toughening effect is achieved and no further toughening is predicted with the model for higher nanosilica contents. This was also the case for the experimental values of  $G_C$ . This system could potentially provide a much greater synergistic effect on the toughening with better tailoring of the cure (or reactive chemistry of the CTBN) since the amount of phase separated rubber decreases dramatically with nanosilica content. Secondly, only about 10 % of the nanosilica particles seem to be invoked in debonding and plastic void growth processes, hence the synergistic behaviour is relatively low.

## Concluding Remarks and Future Work

### 12.1 Conclusions

The aim of this work was to investigate and identify the toughening mechanisms that operate in silica nanoparticle-modified epoxies. Five epoxy systems were studied in this work, and these were compared to some nanosilica-modified epoxy systems from literature. The structure, property relationships were considered with respect to the overall toughenability of the epoxy polymer. This was extended to examine the effects of (i) hybrid modification with nanosilica particles and carboxyl-terminated butadiene-acrylonitrile (CTBN), and (ii) using the modified systems as matrices in a continuous-fibre composite material. This section summarises the main findings of this study with regard to morphology, yield behaviour and toughenability.

#### 12.1.1 Nanosilica-modified epoxies

The 20 nm nanosilica particles were received from Nanoresins pre-dispersed in a master batch of the monomer epoxy and blended to the required concentration prior to curing. There was some size variation in the particles; in the range 5-35 nm with a peak number density of 15 nm and mean particle diameter of 20 nm. Consistent, dispersed morphologies of the nanosilica particles were obtained in the epoxies in all cases (i.e. up to 20 wt. % addition). Typical inter-particle distances were determined to be of the range 20-11 nm for 10-20 wt. % modifications.

The addition of nanosilica had no effect on the glass transition temperature,  $T_g$ , of the epoxy system; hence a direct comparison could be made between the  $T_g$  and the cross-link density. The value of the fracture energy,  $G_C$ , was found to scale inversely with the cross-link density. Thus, the low  $T_g$  epoxies had the highest toughenability, indicating that the toughening mechanisms in the nanosilica-modified epoxies are dependent on the ability of the epoxy system to plastically deform; just as for rubber-toughening. For example, with the 20N polyether-amine cured di-glycidyl ether of bisphenol A/F (DGEBA/F) from Chapter 6,  $T_g = 68$  °C and a 282 % increase in  $G_C$  was reported. Whilst for the 20N amine cured tetra-glycidyl methylenedianiline (TGMDA)

epoxy from Ch. 5,  $T_g = 185$  °C and a 146 % increase in  $G_C$  was obtained by the addition of nanosilica.

The ability for the epoxy to plastically deform was shown to be vital in obtaining toughening with the nanosilica particles. The compressive yield strength,  $\sigma_{yc}$  was found to scale linearly with  $T_g$  for the epoxies that were considered in this study. Furthermore, toughening was only obtained for epoxies that strain softened upon yielding ( $\sigma_{yc}$ ) during compressive tests. This is supported by referring to Ch. 8; an amine cured multifunctional epoxy was examined. Strain softening was not identified from the true stress-true strain curves, or from the presence of shear bands on the polished cross-sections of the compressive samples were examined for this epoxy polymer. This behaviour was unlike the other epoxies that were studied. For this epoxy, no change in  $G_C$  was recorded with increasing nanosilica content and  $G_C = 202$  J/m<sup>2</sup> for the unmodified formulation.

The Young's modulus,  $E$ , increased with the addition of nanosilica. This is to be expected as the particles that are much stiffer than the epoxy polymer (70 GPa compared to ~3 GPa). Both the Halpin-Tsai and Nielsen models were found to accurately represent the increase in Young's modulus with the addition of nanosilica. There was no effect on the strain at which yielding initiated. Hence, it was surmised that yielding initiates in the epoxy and is enhanced by the presence of the nanosilica particles in the epoxy, as opposed to initiating due to the presence of the nanosilica particles. From studying the literature, the latter is case for micron-sized, poorly bonded glass beads.

No correlation was obtained between the effect of interfacial adhesion and Young's modulus of the nanosilica-modified epoxies, with  $E$  measured in the range 3-4 GPa. A simple model was used to quantify the particle-matrix adhesion between the nanosilica particles and the epoxy as an interfacial parameter,  $k$ . This was achieved by least squares regression to the experimental data of  $\sigma_{yc}$  at varying nanosilica contents in each epoxy polymer. Different particle-matrix interfacial adhesions were inferred for the nanosilica-modified epoxy systems, some showed an increase in the value of  $\sigma_{yc}$ . For example, the polyether-amine cured di-glycidyl ether of bisphenol A (DGEBA) a 13 % increase in  $\sigma_{yc}$  was obtained for the 20N epoxy. Alternatively a decrease in  $\sigma_{yc}$  was recorded. For the polyether-amine cured DGEBA/F, a 7 % decrease in  $\sigma_{yc}$  for the 20N compared to the unmodified epoxy. This difference in particle-matrix properties suggested that a different interfacial chemistry or inter-phase region may exist for the different epoxies. The interfacial properties were found to be a controlling parameter for

the exact mechanisms that occurred in the plastic zone ahead of the crack-tip during fracture.

For the 'well adhered' particle-epoxy systems, only shear band yielding was observed, i.e. the amine cured TGMDA epoxy (Ch. 5) and the polyether-amine cured DGEBA (Ch. 7). The values of  $G_C$  for the amine cured TGMDA was of the range 70-172 J/m<sup>2</sup> with a maximum value obtained for the 20 wt. % nanosilica-modified epoxy. In the polyether-amine cured DGEBA epoxies, values for  $G_C$  in the 163-616 J/m<sup>2</sup> range were obtained with the addition of 20 wt. % nanosilica.

For the 'poorly adhered' particle-epoxy systems, shear band yielding and debonding with subsequent void growth were identified as noted for the polyether-amine cured DGEBA/F (Ch. 6) and the anhydride cured DGEBA (Ch. 9) epoxies. For the polyether-amine cured DGEBA/F epoxy,  $G_C = 184-702$  J/m<sup>2</sup> with the addition of nanosilica up to 20 wt. %. The values of  $G_C$  were in the range 83-204 J/m<sup>2</sup> with the addition of 20 wt. % nanosilica for the anhydride cured DGEBA.

A maximum  $G_C$  was obtained when both shear band yielding and debonding with plastic void growth toughening mechanisms occurred. Shear band yielding was observed for sub critically loaded crack-tips and polished compression samples using cross-polarised light microscopy. Debonding and plastic void growth were observed on the fracture surfaces of the 20N epoxies using field-emission gun scanning electron microscopy (FEGSEM). Evidence of plastic hole growth surrounding debonded particles was visible at very high magnifications. A quantitative analysis was conducted on the anhydride cured DGEBA epoxies and 15 ± 5 % of the particles on the fracture surface were found to debond with subsequent void growth processes occurring.

Mechanisms such as crack deflection or pinning were shown to be only relevant for cases where the crack opening displacement and particle size are relatively similar. For the systems considered in the present study, there is a size disparity to the order of a hundred between the crack opening displacement and particle size. Thus, the nanosilica particles will not impede the crack path.

### 12.1.2 Rubber-modified epoxies

The addition of phase separating CTBN to the epoxies resulted in spherical 1 µm sized disperse particles of rubber in the epoxy. In the hybrid epoxies, increasing amounts of the rubber remained in solution (i.e. did not phase separate) with increasing nanosilica content. From the rubber that was added, about 1 vol. % of the 10.6 vol. % that was

added remained in solution for the 9R and 10N9R epoxies. This resulted in a decrease in the  $T_g$  by about 3 °C for the epoxies. The nanosilica particles formed into  $1 \times 0.5 \mu\text{m}$  necklace structures which themselves were well dispersed in the epoxy. The amount of rubber that remained in solution and the size of the nanosilica agglomerates increased with nanosilica content.

For the 20N9R anhydride cured DGEBA epoxy, (i.e. the highest nanosilica content in the hybrid epoxies that were studied) the  $T_g$  decreased by 17 °C to a minimum of  $T_g = 124 \text{ °C}$ . Spherical  $1.5 \mu\text{m}$  sized rubber particles were formed (5.5 vol. %) with agglomerates of nanosilica particles in the epoxy. These formed into  $1.5 \times 1 \mu\text{m}$  agglomerates that appeared to have a detrimental effect on  $G_C$ .

The addition of rubber decreased the Young's modulus of the epoxy to 2.18 GPa for the 9R anhydride cured DGEBA. The addition of nanosilica had the effect of steadily increasing the Young's modulus. Just as with the single component systems, the Halpin-Tsai and Nielsen models represented the increase in Young's modulus with reasonable accuracy. A maximum value of 2.99 GPa was obtained for the 20N9R epoxy.

The value of  $\sigma_{yc}$  reduced dramatically from 124 MPa for the unmodified epoxy to 90 MPa for the 9R anhydride cured DGEBA epoxy. Hence, yielding was confirmed to initiate due to the rubber particles in the epoxy. This showed mechanistic precedence over the nanosilica particles during the failure process as plastic deformation developed ahead of the crack-tip. A mean value of 85 MPa was measured for the hybrid-modified anhydride cured DGEBA epoxies. As the effects of (i) increasing amounts of rubber remaining in solution and (ii) increasing sizes of nanosilica necklaces/agglomerates on the yield behaviour could not be examined as single component systems, no firm conclusions on the effects that these morphologies had on the yield behaviour of the hybrid epoxies could be drawn.

Interesting synergistic behaviours in  $G_C$  were observed with the combination of the two types of particles, providing greater toughening than the sum of the two single-system epoxies. For the 9R anhydride cured DGEBA of  $G_C = 671 \text{ J/m}^2$ . A maximum of  $G_C = 1051 \text{ J/m}^2$  was measured for the 10N9R anhydride cured DGEBA whilst the sum of the toughening increments from the two single-phase systems is  $744 \text{ J/m}^2$ . It was postulated that shear band yielding and void growth in the rubber micro-particles occurs (as for the rubber-modified epoxy), with nanosilica debonding and plastic void growth (without shear band yielding due to the nanosilica particles). Conversely, the anhydride cured DGEBA presented evidence of low particle-matrix adhesion. The

amine cured TGMDA, with 'well adhered' particles showed no effect of synergy and  $G_C$  remained the same as that for the rubber-modified epoxy. The fracture surfaces of the two hybrid-modified systems were examined and confirmed these hypotheses. Rubber particle cavitation was still visible in both hybrid-modified epoxy systems. Closer examination revealed that void growth had occurred surrounding debonded nanosilica necklaces only in the anhydride cured DGEBA epoxy. The particles within the necklaces seemed to remain well adhered to one another. Thus, evidence to support that the rubber particles cavitate and the nanosilica particles debond with void growth can be presented.

### 12.1.3 Fibre-Composites

Continuous fibre-reinforced polymer composites were manufactured using resin infusion under flexible tooling (RIFT) with the nanosilica- and rubber-modified matrices. The particles were sufficiently small that they were not filtered by the fibres during the infusion process. Microscopy of the composites revealed that the same morphologies as the bulk epoxy were obtained in the fibre-composites. The amine cured TGMDA was examined as a carbon-fibre reinforced polymer (CFRP) and the anhydride cured DGEBA was examined as a glass-fibre reinforced polymer (GFRP) composite.

A one-to-one transfer of toughness was measured for the rubber- and hybrid-modified fibre-composites. A maximum fracture energy of  $1500 \text{ J/m}^2$  was measured for the 10N9R anhydride cured DGEBA GFRP. For the nanosilica-modified composites, the composite fracture energy was found vary dramatically depending on the exact fibre architecture that was examined due to varying amounts of fibre bridging. The improvements in fibre-matrix adhesion and the reduction in the stiffness mismatch between the fibres and matrix for the nanosilica-modified epoxies also contributed to the improved fracture properties of the nanosilica- and hybrid-modified composites. Moreover, this hypothesis was supported by single-fibre and short beam shear fibre-matrix interfacial tests. A 42 % increase in the pull-out shear strength and 12 % increase in the short beam shear strength were obtained for the nanosilica-modified composite when compared to the unmodified epoxy.

The fracture surfaces of the modified matrix composites were also examined. The same toughening mechanisms as those for the bulk epoxies were present. In addition, fibre-specific mechanisms such as fibre bridging and pull-out also contributed to the elevated fracture energies that were measured. For the nanosilica-modified composites, evidence was obtained for extensive matrix retention on the fibres, indicative of good

stress transfer between the fibres and matrix, with some cohesive failure. Evidence of particle debonding and plastic void growth was readily observed on the fracture surfaces of the 10N anhydride cured GFRP. For the rubber-modified epoxies, the fibre surfaces appeared to be smooth and free of epoxy residue. This was supported by the observation that extensive fibre bridging occurred, and contributed significantly to the elevated fracture energies that were measured. Rubber particle cavitation was also found to occur in both the rubber-modified and hybrid-modified composites and evidence of plastic void growth around the debonded nanosilica necklaces was obtained.

The elimination of the large stiffness mismatch between the fibres and epoxy, even locally at the fibre-matrix interface, seems to produce fibre-composites with better interfaces and improved stress transfer capability.

#### **12.1.4 Analytical Modelling**

Analytical models were extended from those for modelling the toughening mechanisms for rubber-modified epoxies. The relative contributions of shear band yielding and debonding with plastic void growth, to the overall value of  $G_C$  for the modified epoxy were examined. Toughening observations were made regarding (i) the ability for the epoxy to plastically deform and strain soften and (ii) particle-matrix interfacial adhesion; thus whether or not the nanosilica particles would debond and result in plastic void growth mechanisms. The models were able to provide an excellent correlation with the experimental values of fracture energies for the epoxies from this study and the literature. This would suggest that the arguments that were presented in this study appear to be reasonable.

The developed models were also used to examine toughening mechanisms of coreshell (CSR) particles. Such particles are attractive because they are relatively simple to disperse, and can provide comparable improvements in the fracture properties to rubber particles without the loss of modulus and reduction in  $T_g$ . Accurate predictions were obtained to describe the effect of 100 nm and 300 nm diameter CSR particles on the value of  $G_C$  with shear band yielding and debonding with plastic void growth toughening mechanisms. The value of  $G_C \approx 800 \text{ J/m}^2$  for the 15 wt. % CSR-modified anhydride cured DGEBA epoxies. A maximum toughening effect was obtained for the toughening mechanisms of shear band yielding and plastic void growth in the epoxy. These values provide the upper limit for what is mathematically possible with the two toughening mechanisms.

Analytical models were also developed to explain hybrid-toughening as a two-part process. The failure process was postulated as firstly cavitation of the rubber particles resulting in plastic void growth and shear band yielding of the epoxy polymer. This was accompanied by debonding and plastic void growth of the necklace particles. For the first part, the material properties were required as a function of phase separated rubber content and hence were interpolated for data that were not measured experimentally. Secondly, the nanosilica particles were modelled to debond with plastic void growth in the epoxy polymer (by taking the base properties of the rubber-modified epoxy). When modelled, this combination of mechanisms seemed to be reasonable, when somewhere close to 10 % of the particle debond.

This hypothesis of processes was able to explain the toughening mechanisms that were present in the studied systems and those from the literature. This shows that synergistic toughening can be achieved relatively simply by introducing a second phase into a rubber-modified epoxy that is capable of debonding or inducing void growth processes. Further to this, even relatively low amounts of debonding (~10 % in this study) may lead to large improvements in  $G_C$ . Many researchers have reported synergistic toughening with various particles with CTBN rubber and would provide general agreement with this theory.

## **12.2 Recommendations for future work**

The closing remarks look to make recommendations for potential areas of research, or interesting avenues that have been identified and require further investigation in the future.

### **12.2.1 Nanosilica toughening**

The lack of toughening for the nanosilica-modified amine cured multifunctional epoxy could be attributed to the inability for the matrix to shear yield. A possible way of testing this theory would be to attempt to toughen this system with phase separated CTBN rubber. For shear band yielding to dominate over plastic void growth processes, large improvements in toughening should not be achieved (some contribution may arise from rubber bridging and plasticisation, resulting in a more compliant, strain softening epoxy). From examination of the literature, this system has only been reported to be toughened with thermoplastic additives [264] and would agree with this hypothesis.

Currently, small angle neutron scattering (SANS) data from the manufacturers is being interpreted as the particle size distribution for the nanosilica particles. A simple method

of obtaining an accurate particle size distribution may be to conduct image analysis on low volume fraction TEM images. This would be useful for future work in dispersion analyses and provide a suitable curve for the modelling analyses.

This work has suggested that different inter-phase geometries may form around the nanosilica particles, giving rise to the different interfacial adhesions that were measured. To verify this, SANS could be conducted to measure such inter-phases in the different epoxies. Deuterium enriched epoxies would be required to provide a good contrast with the nanosilica particles. This may be done at the constituent phase of manufacture for the nanosilica epoxies and will require enriched monomers.

Determination of how sensitive the process of debonding is to (i) particle-matrix adhesion (ii) particle size (iii) inter-phase geometry to toughening would be useful to determine the controlling parameters that result in 15 % of the particles debonding. This may be done by (i) introducing a silane coupling agent such as aminopropyltrimethoxysilane to see if the adhesion can be changed, and if so, the effect this has on the toughenability (i.e. compared to the shear contribution to toughening only from the modelling studies). A preliminary examination of the surface free energies of the different epoxies may be worth examining (e.g. [252]) to see if subtle changes in the work of adhesion is causing the effect of different interfacial adhesion, although the surface free energy is known to vary very little for epoxies [100]. Alternatively (ii) varying the particle size may be relatively simple to examine, ensuring that similar adhesion is obtained through the scale of size ranges.

A low shrinkage potting resin formulation [265] may be utilised to embed sub-critically loaded crack-tips from double notch four point bend (DN4PB) tests, whilst in an elastically loaded state. This may provide better samples for further TEM or small angle X-ray scattering (SAXS) type studies.

The stress distribution at the crack-tip could be identified by combining finite element methods and the micrographs that have been obtained in this work. With the stress distribution ahead of the crack-tip, the degree of debonding and void growth may be identified, independently of the fracture surfaces images. The theory that that debonding is limited by the particle size distribution for particle-matrix adhesions may be tested.

Extension of analytical modelling to incorporate rate effects using time-temperature superposition methods to adjust the material properties of the unmodified epoxy with respect to temperature or strain rate may be relatively simple to do, whilst providing

valuable insight into the variation of properties under various conditions. Whilst current predictions are very good and favourable due to their simplistic nature, the effect of stochastic variation in the material properties and the particle size should be examined.

### **12.2.2 Hybrid toughening**

The toughening mechanisms the hybrid-modified epoxies was postulated as rubber-particle cavitation, shear band yielding and void growth and debonding and plastic void growth of the nanosilica necklaces.

The rubber that remains in solution makes it difficult to draw firm conclusions on the exact behaviour of the hybrid epoxies which contributes to toughening. It would be interesting to isolate the effects of (i) rubber that remains in solution and (ii) agglomeration of the nanosilica. Manzione et al. [266, 267] were able to form a variety of different morphologies of their rubber-modified epoxies from a single epoxy by varying the cure temperature and this may be worth examining as a first consideration.

Since increasing amounts of rubber stay in solution as nanosilica is added, it may be worth running the cure cycles in a differential scanning calorimeter, as the solution of improving phase separation in the high nanosilica contents may be as simple as prolonging the temperature step at 90 °C in the anhydride cured DGEBA epoxies. For visualising the formation of nanosilica, replacing the nanosilica particles with more observable particles such as carbon nanotubes may provide a useful insight to the exact processes using an optical microscope hot stage.

The mechanistic behaviour of failure in the hybrid-modified epoxies needs to be examined, perhaps using the DN4PB technique. It was postulated that the CTBN particles cavitate, then the nanosilica particles debond with void growth and this may be verified with such experiments at incremental stress intensity factors.

There is scope for this technique to be extended in to examination of complex epoxy systems (i.e. many types of toughening particles). It may be of interest to examine high toughness adhesives, extend mechanistic understanding of the failure processes and then analytically model them.

### **12.2.3 Continuous-fibre composites**

The incorporation of nanosilica seems to provide better fibre-matrix interfacial properties. A suitable method of introducing these particles could be by adding the nanosilica particles in as a sizing on the fibres. Upon curing, these would diffuse out,

yet remain close to the fibre-matrix interface [268]. This would have to effect of providing a transition in stiffness to the matrix epoxy. Introduction in such a constituent phase may also tackle the issue of nanosilica agglomeration in the hybrid epoxies.

Impact and high rate properties were not reported in this work, but have been reported in [269, 270]. The nanosilica modified epoxy seems to increase the dynamic stiffness of the composite, and result in more delamination. More work required to understand this behaviour, for example impact tests at the ballistic limit, and secondly using compression after impact to monitor the strength of these composites once damaged.

## References

1. *Epoxy resins: Chemistry and Technology*. Second edition, revised and expanded. Ed. C.A. May. 1988, New York: Marcel Dekker.
2. Kinloch, A.J., *Theme Article - Toughening Epoxy Adhesives to Meet Today's Challenges*. Materials Research Society Bulletin, 2003. 28(6): p. 445-448.
3. Matthews, F.L. and R. Rawlings, *Composite materials: Engineering and science*. 1994, Cambridge: Woodhead Publishing.
4. Kinloch, A.J., R. Mohammed, A.C. Taylor, C. Eger, S. Sprenger and D. Egan, *The effect of silica nano particles and rubber particles on the toughness of multiphase thermosetting epoxy polymers*. Journal of Materials Science, 2005. 40(18): p. 5083-5086.
5. Kinloch, A.J., R.D. Mohammed, A.C. Taylor, S. Sprenger and D. Egan, *The interlaminar toughness of carbon-fibre reinforced plastic composites using 'hybrid-toughened' matrices*. Journal of Materials Science, 2006. 41(15): p. 5043-5046.
6. Kinloch, A.J., K. Masania, A.C. Taylor, S. Sprenger and D. Egan, *The Fracture of glass-fibre reinforced epoxy composites using nanoparticle-modified matrices*. Journal of Materials Science, 2008. 43(3): p. 1151-1154.
7. Johnsen, B.B., A.J. Kinloch, R.D. Mohammed, A.C. Taylor and S. Sprenger, *Toughening mechanisms of nanoparticle-modified epoxy polymers*. Polymer, 2007. 48(2): p. 530-541.
8. Sprenger, S., A.J. Kinloch and A.C. Taylor, *Silica nanoparticles and rubber toughening, a synergy in adhesives and composites* in Proceedings of Thermoset Resin Formulators Association 2008, Chicago, IL,
9. Vinson, J.R., *Adhesive bonding of polymer composites*. Polymer Engineering and Science, 1989. 29(19): p. 1325-1331.
10. Sultan, J.N. and F.J. McGarry, *Effect of rubber particle size on deformation mechanisms in glassy epoxy*. Polymer Engineering and Science, 1973. 13(1): p. 29-34.
11. Ward, I.M., *The yield behavior of polymers*. Journal of Polymer Science Part C: Polymer Symposia, 1971. 32(1): p. 195-218.
12. Bowden, P.B., *A criterion for inhomogeneous plastic deformation*. Philosophical Magazine. A, Physics of Condensed Matter, Defects and Mechanical Properties, 1970. 22(177): p. 455-462.
13. Bowden, P.B. and S. Raha, *Formation of micro shear bands in polystyrene and polymethylmethacrylate*. Philosophical Magazine, 1970. 22(177): p. 463-482.
14. Bowden, P.B. and J.A. Jukes, *The plastic flow of isotropic polymers*. Journal of Material Science, 1972. 7(1): p. 52-63.
15. Bowden, P.B., *The yield behaviour of glassy polymers*, in *The Physics of Glassy Polymers*, R.N. Haward, Editor Applied Science Publishers: 1973, London.

16. Vakil, U.M., *Yield and fracture behaviour of cross-linked epoxies*. Journal of Materials Science, 1993. 28(16): p. 4442-4450.
17. Kinloch, A.J. and J.G. Williams, *Crack blunting mechanisms in polymers*. Journal of Materials Science, 1980. 15(4): p. 987-996.
18. Yamini, S. and R.J. Young, *Stability of crack propagation in epoxy resins*. Polymer, 1977. 18(10): p. 1075-1080.
19. Moloney, A.C., H.H. Kausch and H.R. Stieger, *The fracture of particulate-filled epoxide resins: Part 1*. Journal of Materials Science, 1983. 18(1): p. 208-216.
20. Garg, A.C. and Y.W. Mai, *Failure prediction in toughened epoxy resins: A review*. Composites Science and Technology, 1988. 31(3): p. 225-242.
21. Griffiths, R. and D. Holloway, *The fracture energy of some epoxy resin materials*. Journal of Materials Science, 1970. 5(4): p. 302-307.
22. Broutman, L.J. and S. Sahu, *Effect of Interfacial Bonding on Toughness of Glass Filled Polymers*. Materials Science and Engineering, 1971. 8(2): p. 98-107.
23. Spanoudakis, J. and R. Young, *Crack propagation in a glass particle-filled epoxy resin: Part 2 Effect of particle-matrix adhesion*. Journal of Materials Science, 1984. 19(2): p. 487-496.
24. Spanoudakis, J. and R.J. Young, *Crack propagation in a glass particle-filled epoxy resin: Part 1 Effect of particle volume fraction and size*. Journal of Materials Science, 1984. 19(2): p. 473-486.
25. McGrath, L.M., R.S. Parnas, S.H. King, J.L. Schroeder, D.A. Fischer and J.L. Lenhart, *Investigation of the thermal, mechanical, and fracture properties of alumina-epoxy composites*. Polymer, 2008. 49(4): p. 999-1014.
26. Vollenberg, P.H.T. and D. Heikens, *The mechanical properties of chalk-filled polypropylene: a preliminary investigation*. Journal of Materials Science, 1990. 25(7): p. 3089-3095.
27. Vollenberg, P.H.T., J.W. Dehaan, L.J.M. Vandeven and D. Heikens, *Particle-size dependence of the Young's modulus of filled polymers 2. Annealing and solid-state nuclear magnetic-resonance experiments*. Polymer, 1989. 30(9): p. 1663-1668.
28. Vollenberg, P.H.T. and D. Heikens, *Particle-size dependence of the Young's modulus of filled polymers 1. Preliminary experiments*. Polymer, 1989. 30(9): p. 1656-1662.
29. DiBenedetto, A.T. and A.D. Wambach, *The fracture toughness of epoxy-glass bead composites*. International Journal of Polymeric Materials, 1972. 1(2): p. 159-173.
30. Sahu, S. and L.J. Broutman, *Mechanical properties of particulate composites*. Polymer Engineering and Science, 1972. 12(2): p. 91-100.
31. Dekkers, M.E.J. and D. Heikens, *The effect of interfacial adhesion on the mechanism for craze formation in polystyrene-glass bead composites*. Journal of Materials Science, 1983. 18(11): p. 3281-3287.

32. Levita, G., A. Marchetti and A. Lazzeri, *Fracture of ultrafine calcium carbonate/polypropylene composites*. *Polymer Composites*, 1989. 10(1): p. 39-43.
33. Lauke, B., *On the effect of particle size on fracture toughness of polymer composites*. *Composites Science and Technology*, 2008. 68(15-16): p. 3365-3372.
34. Fu, S., X. Feng, B. Lauke and Y. Mai, *Effects of particle size, particle/matrix interface adhesion and particle loading on mechanical properties of particulate-polymer composites*. *Composites Part B: Engineering*, 2008. 39(6): p. 933-961.
35. Wang, K., J. Wu, L. Ye and H. Zeng, *Mechanical properties and toughening mechanisms of polypropylene/barium sulfate composites*. *Composites Part A: Applied Science and Manufacturing*, 2003. 34(12): p. 1199-1205.
36. Vörös, G. and B. Pukánszky, *Stress distribution in particulate filled composites and its effect on micromechanical deformation*. *Journal of Materials Science*, 1995. 30(16): p. 4171-4178.
37. Pukánszky, B. and G. Vörös, *Stress distribution around inclusions, interaction, and mechanical properties of particulate-filled composites*. *Polymer Composites*, 1996. 17(3): p. 384-392.
38. Vörös, G., E. Fekete and B. Pukánszky, *An interphase with changing properties and the mechanism of deformation in particulate-filled polymers*. *Journal of Adhesion*, 1997. 64(1-4): p. 229-250.
39. Dekkers, M.E.J. and D. Heikens, *The Effect of Interfacial Adhesion on the Tensile Behavior of Polystyrene Glass-Bead Composites*. *Journal of Applied Polymer Science*, 1983. 28(12): p. 3809-3815.
40. Vollenberg, P., D. Heikens and H.C.B. Ladan, *Experimental-Determination of thermal and adhesion stress in particle filled thermoplasts*. *Polymer Composites*, 1988. 9(6): p. 382-388.
41. Vörös, G. and B. Pukánszky, *Prediction of the yield stress of composites containing particles with an interlayer of changing properties*. *Composites Part A: Applied Science and Manufacturing*, 2002. 33(10): p. 1317-1322.
42. Pukánszky, B., *Interfaces and interphases in multicomponent materials: past, present, future*. *European Polymer Journal*, 2005. 41(4): p. 645.
43. Zhang, H., Z. Zhang, K. Friedrich and C. Eger, *Property improvements of in situ epoxy nanocomposites with reduced interparticle distance at high nanosilica content*. *Acta Materialia*, 2006. 54(7): p. 1833-1842.
44. Sen, S., Y. Xie, S. Kumar, H. Yang, D. Ho, L. Hall, J. Hooper and K. Schwizer, *Chain conformations and bound-layer correlations in polymer nanocomposites*. *Physical review letters*, 2007. 98(128302): p. 1-4.
45. Kawaguchi, T. and R.A. Pearson, *The effect of particle-matrix adhesion on the mechanical behavior of glass filled epoxies: Part 1. A study on yield behavior and cohesive strength*. *Polymer*, 2003. 44(15): p. 4229-4238.
46. Kawaguchi, T. and R.A. Pearson, *The effect of particle-matrix adhesion on the mechanical behavior of glass filled epoxies. Part 2. A study on fracture toughness*. *Polymer*, 2003. 44(15): p. 4239-4247.

47. Gent, A.N., *Detachment of an elastic matrix from a rigid spherical inclusion*. Journal of Materials Science, 1980. 15(11): p. 2884-2888.
48. Nicholson, D.W., *On the detachment of a rigid inclusion from an elastic matrix*. Journal of Adhesion, 1979. 10(3): p. 255-260.
49. Chen, J., Z. Huang and J. Zhu, *Size effect of particles on the damage dissipation in nanocomposites*. Composites Science and Technology, 2007. 67(14): p. 2990-2996.
50. Chen, J.-K., G.-T. Wang, Z.-Z. Yu, Z. Huang and Y.-W. Mai, *Critical particle size for interfacial debonding in polymer/nanoparticle composites*. Composites Science and Technology, 2010. 70(5): p. 861-872.
51. Williams, J.G., *Particle toughening of polymers by plastic void growth*. Composites Science and Technology, 2010. 70(6): p. 885-891.
52. Liang, Y.L. and R.A. Pearson, *Toughening mechanisms in epoxy-silica nanocomposites (ESNs)*. Polymer, 2009. 50(20): p. 4895-4905.
53. Dittanet, P. and R.A. Pearson, *Fracture Behaviour of silica filled epoxies: effect of bimodal particle size distributions* in Proceedings of 33<sup>rd</sup> Annual meeting of the Adhesion Society. 2010, Daytona, FL, Adhesion Society.
54. Jordan, J., K.I. Jacob, R. Tannenbaum, M.A. Sharaf and I. Jasiuk, *Experimental trends in polymer nanocomposites-a review*. Materials Science and Engineering A, 2005. 393(1-2): p. 1-11.
55. Sun, L., R.F. Gibson, F. Gordaninejad and J. Suhr, *Energy absorption capability of nanocomposites: A review*. Composites Science and Technology, 2009. 69(14): p. 2392-2409.
56. Srivastava, I. and N. Koratkar, *Fatigue and fracture toughness of epoxy nanocomposites*. Journal of Minerals, Metals and Materials Society, 2010. 62(2): p. 50-57.
57. Lee, J. and A.F. Yee, *Role of Inherent Matrix Toughness on Fracture of Glass Bead Filled Epoxies*. Polymer, 2000. 41: p. 8375-8385.
58. Lee, J.H. *Fracture behaviour of nano toughened epoxy adhesives*, PhD Thesis, Department of Mechanical Engineering, Imperial College London, 2006.
59. Mohammed, R.D. *Material properties and fracture mechanisms of epoxy nano composites*, PhD Thesis, Department of Mechanical Engineering, Imperial College London, London, 2007.
60. Sohn Lee, J. *The fatigue of nano-modified epoxy polymers*, PhD Thesis, Department of Mechanical Engineering, Imperial College London, London, 2009.
61. Hsieh, T.H., A.J. Kinloch, K. Masania, J. Sohn Lee, A.C. Taylor and S. Sprenger, *The toughness of epoxy polymers and fibre composites modified with rubber microparticles and silica nanoparticles*. Journal of Materials Science, 2010. 45(5): p. 1193-1210.
62. Kinloch, A.J., J.H. Lee, A.C. Taylor, S. Sprenger, C. Eger and D. Egan, *Toughening Structural Adhesives via Nano- and Micro-phase Inclusions*. Journal of Adhesion, 2003. 79(8-9): p. 867-873.

63. Blackman, B.R.K., A.J. Kinloch, J. Sohn Lee, A.C. Taylor, R. Agarwal, G. Schueneman and S. Sprenger, *The fracture and fatigue behaviour of nano-modified epoxy polymers*. Journal of Materials Science, 2007. 42(16): p. 7049-7051.
64. Zhang, H., L.-C. Tang, Z. Zhang, K. Friedrich and S. Sprenger, *Fracture behaviours of in situ silica nanoparticle-filled epoxy at different temperatures*. Polymer, 2008. 49(17): p. 3816-3825.
65. Ma, J., M. Mo, X. Du, P. Rosso, K. Friedrich and H. Kuan, *Effect of inorganic nanoparticles on mechanical property, fracture toughness and toughening mechanism of two epoxy systems*. Polymer, 2008. 49(16): p. 3510-3523.
66. Lee, J., *Fracture of glass bead/epoxy composites: on micro-mechanical deformations*. Polymer, 2000. 41(23): p. 8363-8373.
67. Lee, J. and A.F. Yee, *Inorganic particle toughening I: micro-mechanical deformations in the fracture of glass bead filled epoxies*. Polymer, 2001. 42(2): p. 577-588.
68. Lange, F.F., *Interaction of a Crack Front with a Second-Phase Dispersion*. Philosophical Magazine, 1970. 22(179): p. 983-992.
69. Evans, A.G., *The Strength of Brittle Materials Containing Second Phase Dispersions*. Philosophical Magazine, 1972. 26(6): p. 1327-1344.
70. Green, D.J., P.S. Nicholson and J.D. Embury, *Fracture of a brittle particulate composite. Part 1 Experimental aspects*. Journal of Materials Science, 1979. 14(6): p. 1413-1420.
71. Kinloch, A.J. and R.J. Young, *Fracture behaviour of polymers*. 1983, London: Elsevier Applied Sciences.
72. Kinloch, A.J., D.L. Maxwell and R.J. Young, *The fracture of hybrid-particulate composites*. Journal of Materials Science, 1985. 20(11): p. 4169-4184.
73. Faber, K.T. and A.G. Evans, *Crack deflection processes - I. Theory*. Acta Metallurgica, 1983. 31(4): p. 565-576.
74. Kinloch, A.J., *The toughening of cyanate-ester polymers: Part 1 physical modification using particles, fibres and woven-mats*. Journal of Materials Science, 2002. 37(3): p. 433-460.
75. Amdouni, N., H. Sautereau, J.F. Gerard, F. Fernagut, G. Coulon and J.M. Lefebvre, *Coated glass beads epoxy composites: influence of the interlayer thickness on pre-yielding and fracture properties*. Journal of Materials Science, 1990. 25(2): p. 1435-1443.
76. Dekkers, M.E.J. and D. Heikens, *Crazing and shear deformation in glass bead-filled glassy polymers*. Journal of Materials Science, 1985. 20(11): p. 3873-3880.
77. Dekkers, M.E.J. and D. Heikens, *Shear band formation in polycarbonate-glass bead composites*. Journal of Materials Science, 1984. 19(10): p. 3271-3275.
78. Bucknall, C.B., *Toughened plastics*. 1977, London: Applied Science Publishers Ltd.

79. Brooker, R.D. *The morphology and toughness of thermoplastic-modified epoxy polymer with carbon nanotubes or silica nanoparticles*, PhD Thesis, Department of Mechanical Engineering, Imperial College London, London, 2009.
80. Ratna, D. and A.K. Banthia, *Rubber toughened epoxy*. *Macromolecular Research*, 2004. 12(1): p. 11-21.
81. Bagheri, R., B.T. Marouf and R.A. Pearson, *Rubber-Toughened Epoxies: A Critical Review*. *Polymer Reviews*, 2009. 49(3): p. 201-225.
82. Kinloch, A.J., *Relationships between the Microstructure and Fracture Behavior of Rubber-Toughened Thermosetting Polymers*. *Rubber-Toughened Plastics*, Ed. C.K. Riew. 1989: American Chemical Society
83. Huang, Y., A.J. Kinloch, R.J. Bertsch and A.R. Siebert, *Particle-matrix interfacial bonding: Effect on the fracture properties of rubber-modified epoxy polymers*. *Advances in Chemistry Series 233. Toughened plastics I - Science and Engineering*, Ed. C.K. Riew and A.J. Kinloch. 1993, Washington: American Chemical Society.
84. Kinloch, A.J., C.A. Finch and S. Hashemi, *Effect of Segmental Molecular Mass between Cross-Links of the Matrix Phase on the Toughness of Rubber-Modified Epoxies*. *Polymer Communications*, 1987. 28(12): p. 322-325.
85. Huang, Y. and A.J. Kinloch, *Modelling of the toughening mechanisms in rubber-modified epoxy polymers: Part I: Finite element analysis and studies*. *Journal of materials science*, 1992. 27(10): p. 2753.
86. Pearson, R.A. and A.F. Yee, *Toughening Mechanisms in Elastomer-Modified Epoxies. 3. The Effect of Cross-Link Density*. *Journal of Materials Science*, 1989. 24(7): p. 2571-2580.
87. Meeks, A.C., *Fracture and mechanical properties of epoxy resins and rubber-modified epoxy resins*. *Polymer*, 1974. 15(10): p. 675.
88. Arias, M.L., P.M. Frontini and R.J.J. Williams, *Analysis of the damage zone around the crack tip for two rubber-modified epoxy matrices exhibiting different toughenability*. *Polymer*, 2003. 44(5): p. 1537-1546.
89. Zhang, H. and L.A. Berglund, *Deformation and fracture of glass bead CTBN-rubber epoxy composites*. *Polymer Engineering and Science*, 1993. 33(2): p. 100-107.
90. Bascom, W.D., R.L. Cottingham, R.L. Jones and P. Peyser, *The fracture of epoxy- and elastomer-modified epoxy polymers in bulk and as adhesives*. *Journal of Applied Polymer Science*, 1975. 19(9): p. 2545-2562.
91. Yee, A.F. and R.A. Pearson, *Toughening Mechanisms in Elastomer-Modified Epoxies. Part 1 Mechanical studies*. *Journal of Materials Science*, 1986. 21(7): p. 2462-2474.
92. Kinloch, A.J. and D.L. Hunston, *Effect of volume fraction of dispersed rubbery phase on the toughness of rubber-toughened epoxy polymers*. *Journal of Materials Science Letters*, 1986. 5(9): p. 909-911.
93. Guild, F.J., A.C. Taylor and A.J. Kinloch, *The role of particle cavitation in the toughening of rubber-modified epoxy adhesives* in *Proceedings of 32<sup>nd</sup> Annual Meeting of the Adhesion Society*. 2008, Savannah, GA.

94. Huang, Y. and A.J. Kinloch, *Modelling of the toughening mechanisms in rubber-modified epoxy polymers. Part II: A quantitative description of the microstructure-fracture property relationships*. Journal of Materials Science, 1992. 27(10): p. 2763-2769.
95. Huang, Y. and A.J. Kinloch, *The toughness of epoxy polymers containing microvoids*. Polymer, 1992. 33(6): p. 1330-1332.
96. Guild, F.J. and A.J. Kinloch, *Modelling the properties of rubber-modified epoxy polymers*. Journal of Materials Science, 1995. 30(7): p. 1689-1697.
97. Bagheri, R., M.A. Williams and R.A. Pearson, *Use of surface modified recycled rubber particles for toughening of epoxy polymers*. Polymer Engineering & Science, 1997. 37(2): p. 245-251.
98. Pearson, R.A. and A.F. Yee, *Toughening Mechanisms in Elastomer-Modified Epoxies. 2. Microscopy Studies*. Journal of Materials Science, 1986. 21(7): p. 2475-2488.
99. Huang, Y. and A.J. Kinloch, *The sequence of initiation of the toughening micromechanisms in rubber-modified epoxy polymers*. Polymer, 1992. 33(24): p. 5338.
100. Guild, F.J., *The mechanistic processes that lead to toughening in rubber-modified epoxies*. Department of Mechanical Engineering. Personal Communication. 2010, Imperial College London.
101. Huang, Y. and A.J. Kinloch, *The role of plastic void growth in the fracture of rubber-toughened epoxy polymers*. Journal of Materials Science Letters, 1992. 11(8): p. 484-487.
102. Bagheri, R. and R.A. Pearson, *Role of particle cavitation in rubber-toughened epoxies: 1. Microvoid toughening*. Polymer, 1996. 37(20): p. 4529-4538.
103. Bagheri, R. and R.A. Pearson, *The use of microvoids to toughen polymers*. Polymer, 1995. 36(25): p. 4883-4885.
104. Sue, H.-J. and A.F. Yee, *Micromechanical modelling of crack-tip rubber particle cavitation process in polymer toughening*. Polymer Engineering & Science, 1996. 36(18): p. 2320-2326.
105. Kunz-Douglass, S.C., P.W.R. Beaumont and M.F. Ashby, *A model for the toughness of epoxy-rubber particulate composites*. Journal of Materials Science, 1980. 15(5): p. 1109-1123.
106. Guild, F.J. and A.J. Kinloch, *Predictive modelling of the mechanical properties of rubber-toughened epoxy*. Journal of Materials Science Letters, 1994. 13(9): p. 629-632.
107. Pearson, R.A., H.-J. Sue and A.F. Yee, *Toughening of Plastics: Advances in Modelling and Experiments*. 2000, Washington: ACS Symposium Series 759. American Chemical Society.
108. Yan, C., K. Xiao, L. Ye and Y.-W. Mai, *Numerical and experimental studies on the fracture behavior of rubber-toughened epoxy in bulk specimen and laminated composites*. Journal of Materials Science, 2002. 37(5): p. 921-927.

109. Wang, X., F.J. Guild, A.J. Kinloch, A.C. Taylor and H. Hadavinia, *Modelling the mechanical behaviour of rubber toughened epoxies* in Proceedings of 28th Annual Meeting of the Adhesion Society. 2005, Mobile, Alabama, USA, The Adhesion Society.
110. Wang, X., F.J. Guild, A.J. Kinloch, A.C. Taylor and H. Hadavinia, *Modelling of rubber toughened adhesives: the effect of particle cavitation* in Proceedings of Adhesion '05. 2005, Oxford, IOM communications Ltd.
111. Wang, X., F.J. Guild, A.J. Kinloch and A.C. Taylor, *Modelling the Fracture Toughness of Rubber Toughened Epoxies: the Role of Particle Size* in Proceedings of 29<sup>th</sup> Annual Meeting of the Adhesion Society. 2006, Jacksonville, USA, Adhesion Society.
112. Guild, F.J., A.C. Taylor and A.J. Kinloch, *An extended model for rubber particle cavitation in epoxy adhesives* in Proceedings of 31st Annual Meeting of the Adhesion Society. 2007, Austin, TX,
113. Maxwell, D., R.J. Young and A.J. Kinloch, *Hybrid particulate-filled epoxy-polymers*. Journal of Materials Science Letters, 1984. 3(1): p. 9-12.
114. Kinloch, A.J., D.L. Maxwell and R.J. Young, *Micromechanisms of Crack propagation in Hybrid-Particulate Composites*. Journal of Materials Science Letters, 1985. 4(10): p. 1276-1279.
115. Young, R.J., D.L. Maxwell and A.J. Kinloch, *The deformation of hybrid-particulate composites*. Journal of Materials Science, 1986. 21(2): p. 380-388.
116. Maazouz, A., H. Sautereau and J.F. Gerard, *Hybrid-particulate composites based on an epoxy matrix, a reactive rubber, and glass beads: Morphology, viscoelastic, and mechanical properties*. Journal of Applied Polymer Science, 1993. 50(4): p. 615-626.
117. Geisler, B. and F. Kelley, *Rubbery and rigid particle toughening of epoxy resins*. Journal of Applied Polymer Science, 1994. 54(2): p. 177-189.
118. Vallo, C.I., L. Hu, P.M. Frontini and R.J.J. Williams, *Toughened-Hybrid Epoxies - Influence of the Rubber-Phase Morphology on Mechanical-Properties*. Journal of Materials Science, 1994. 29(9): p. 2481-2486.
119. Azimi, H.R., R.A. Pearson and R.W. Hertzberg, *Role of crack tip shielding mechanisms in fatigue of hybrid epoxy composites containing rubber and solid glass spheres*. Journal of Applied Polymer Science, 1995. 58(2): p. 449-463.
120. Azimi, H.R., R.A. Pearson and R.W. Hertzberg, *Fatigue of hybrid epoxy composites: Epoxies containing rubber and hollow glass spheres*. Polymer Engineering and Science, 1996. 36(18): p. 2352-2365.
121. Karger-Kocsis, J. and K. Friedrich, *Fatigue crack-propagation and related failure in modified, anhydride-cured epoxy-resins*. Colloid and Polymer Science, 1992. 270(6): p. 549-562.
122. Low, I.M., S. Bandyopadhyay and Y.W. Mai, *On hybrid toughened DGEBA epoxy resins*. Polymer International, 1992. 27(2): p. 131-137.
123. Karger-Kocsis, J. and K. Friedrich, *Microstructure-related fracture toughness and fatigue crack growth behaviour in toughened, anhydride-cured epoxy resins*. Composites Science and Technology, 1993. 48(1-4): p. 263-272.

124. Boynton, M.J. and A. Lee, *Fracture of an epoxy polymer containing recycled elastomeric particles*. Journal of Applied Polymer Science, 1997. 66(2): p. 271-277.
125. DiBerardino, M.F. and R.A. Pearson, *The effect of particle size on synergistic toughening of boron nitride-rubber hybrid epoxy composites*, in *Toughening of Plastics: Advances in Modeling and Experiments*, R.A. Pearson, H.J. Sue, and A.F. Yee, Editors. American Chemical Society: 2000, Washington DC.
126. Gilbert, E.N., B.S. Hayes and J.C. Seferis, *Nano-alumina modified epoxy based film adhesives*. Polymer Engineering and Science, 2003. 43(5): p. 1096-1104.
127. Liu, W.P., S.V. Hoa and M. Pugh, *Morphology and performance of epoxy nanocomposites modified with organoclay and rubber*. Polymer Engineering and Science, 2004. 44(6): p. 1178-1186.
128. Lee, H.B., H.G. Kim, K.B. Yoon, D.H. Lee and K.E. Min, *The effect of CTBN rubber on mechanical properties of epoxy-clay nanocomposite*. Polymer-Korea, 2008. 32(1): p. 31-37.
129. Marouf, B.T., R.A. Pearson and R. Bagheri, *Anomalous fracture behavior in an epoxy-based hybrid composite*. Materials Science and Engineering: A, 2009. 515(1-2): p. 49-58.
130. Salinas-Ruiz, M., A. Skordos and I.K. Partridge, *Rubber-toughened epoxy loaded with carbon nanotubes: structure–property relationships* Journal of Materials Science, 2010. 45(10): p. 2633-2639.
131. Barsotti, R., *The synergetic behaviour of block co-polymer and CTBN modified hybrid epoxies*. Arkema, Inc. Personal Communication. 2010, Tampa, FL.
132. Lee, J.W. and A.F. Yee, *Micro-mechanical deformation mechanisms in the fracture of hybrid-particulate composites based on glass beads, rubber and epoxies*. Polymer Engineering and Science, 2000. 40(12): p. 2457-2470.
133. Caccavale, V., M.H.G. Wichmann, M. Quaresimin and K. Schulte, *Nanoparticle/Rubber Modified Epoxy Matrix Systems: Mechanical Performance in CFRPs* in Proceedings of Italian Association for Stress Analysis (AIAS) 2007, Naples, Italy, University of Naples.
134. Liang, Y.L. and R.A. Pearson, *The Role of Nanosilica Dispersion and Particle Size in Hybrid Epoxy-Silica Nanocomposites Toughening Mechanism* in Proceedings of 31<sup>st</sup> Annual meeting of the Adhesion Society. 2008, Austin, TX, Adhesion Society.
135. Tsai, J.-L., B.-H. Huang and Y.-L. Cheng, *Enhancing fracture toughness of glass/epoxy composites by using rubber particles together with silica nanoparticles*. Journal of Composite Materials, 2009. 43(25): p. 3107-3123.
136. Zeng, M.F., X.D. Sun, X.D. Yao, G.Z. Ji, N. Chen, B.Y. Wang and C.Z. Qi, *Effects of SiO<sub>2</sub> nanoparticles on the performance of carboxyl-randomized liquid butadiene-acrylonitrile rubber modified epoxy nanocomposites*. Journal of Applied Polymer Science, 2007. 106(2): p. 1347-1352.
137. Liu, W., S.V. Hoa and M. Pugh, *Morphology and performance of epoxy nanocomposites modified with organoclay and rubber*. Polymer Engineering and Science, 2004. 44(6): p. 1178-1186.

138. Cripps, D. *Polymer composites*; Accessed (01/04/10), 2010. Available from: <http://www.netcomposites.com/EducationIntro.asp>
139. Azom.com. *Composites - An basic introduction*; Accessed (12/01/10), 2010. Available from: <http://www.azom.com/details.asp?articleID=962>
140. Hughes, J.D.H., *The carbon fibre/epoxy interface--A review*. Composites Science and Technology, 1991. 41(1): p. 13-45.
141. Scott, J.M. and C. Phillips, *Carbon fibre composites with rubber toughened matrices*. Journal of Materials Science, 1975. 10(4): p. 551-562.
142. Day, R.J., P.A. Lovell and A.A. Wazzan, *Toughened carbon/epoxy composites made by using core/shell particles*. Composites Science and Technology, 2001. 61(1): p. 41-56.
143. Sprenger, S., A.J. Kinloch, A.C. Taylor and R.D. Mohammed, *Rubber-toughened GFRCs optimised by nanoparticles - Part I*. JEC Composites, 2005. 2005(21): p. 66-69.
144. Bozkurt, E., E. Kaya and M. Tanoglu, *Mechanical and thermal behavior of non-crimp glass fiber reinforced layered clay/epoxy nanocomposites*. Composites Science and Technology, 2007. 67(15-16): p. 3394-3403.
145. Wichmann, M.H.G., J. Sumfleth, F.H. Gojny, M. Quaresimin, B. Fiedler and K. Schulte, *Glass-fibre-reinforced composites with enhanced mechanical and electrical properties - Benefits and limitations of a nanoparticle modified matrix*. Engineering Fracture Mechanics, 2006. 73(16): p. 2346-2359.
146. Vlasveld, D.P.N., P.P. Parlevliet, H.E.N. Bersee and S.J. Picken, *Fibre-matrix adhesion in glass-fibre reinforced polyamide-6 silicate nanocomposites*. Composites Part A: Applied Science and Manufacturing, 2005. 36(1): p. 1-11.
147. Tran, M.Q., K.K.C. Ho, G. Kalinka, M.S.P. Shaffer and A. Bismarck, *Carbon fibre reinforced poly(vinylidene fluoride): Impact of matrix modification on fibre/polymer adhesion*. Composites Science and Technology, 2008. 68(7-8): p. 1766-1776.
148. Hussain, M., A. Nakahira and K. Niihara, *Mechanical property improvement of carbon fiber reinforced epoxy composites by Al<sub>2</sub>O<sub>3</sub> filler dispersion*. Materials Letters, 1996. 26(3): p. 185-191.
149. Sprenger, S., A.J. Kinloch, A.C. Taylor and R.D. Mohammed, *Rubber-toughened CFRCs optimised by nanoparticles - Part III*. JEC Composites, 2007. 2007(30): p. 54-57.
150. Sprenger, S., A.J. Kinloch, A.C. Taylor and R.D. Mohammed, *Rubber-toughened FRCs optimised by nanoparticles - Part IV*. JEC Composites, 2008. 2008(38): p. 60-63.
151. Sprenger, S., A.J. Kinloch, A.C. Taylor, R.D. Mohammed and C. Eger, *Rubber-toughened FRCs optimised by nanoparticles - Part II*. JEC Composites, 2005. 2005(19): p. 73-76.
152. Manjunatha, C.M., A.J. Kinloch, A.C. Taylor and S. Sprenger, *The effect of rubber micro-particles and silica nano-particles on the tensile fatigue behaviour of a glass-fibre epoxy composite*. Journal of Materials Science, 2009. 44(1): p. 342-345.

153. Manjunatha, C.M., A.J. Kinloch, A.C. Taylor and S. Sprenger, *The tensile fatigue behaviour of a silica nanoparticle-modified glass fibre reinforced epoxy composite*. Composites Science and Technology, 2009. 70(1): p. 193-199.
154. Manjunatha, C.M., A.C. Taylor, A.J. Kinloch and S. Sprenger, *The effect of rubber micro-particles and silica nano-particles on the tensile fatigue behaviour of a glass-fibre epoxy composite*. Journal of Materials Science, 2009. 44(1): p. 342-345.
155. Compston, P., *The Transfer of Matrix Toughness to Composite Mode I Interlaminar Fracture Toughness in Glass-Fibre/vinyl Ester Composites*. Applied Composite Materials, 2002. 9(5): p. 291-314.
156. Bradley, W.L., *Relationship of Matrix Toughness to Interlaminar Fracture Toughness*. Applications of Fracture Mechanics to Composite Materials Ed. K. Fredrich. 1989, Amsterdam: Elsevier.
157. Hull, D. and T.W. Clyne, *An Introduction to Composite Materials*, in *Cambridge Solid State Science Series*, Cambridge University Press: 1981, Cambridge.
158. Hunston, D., R. Moulton, N. Johnston and W.D. Bascom, *Matrix Resin Effects in Composite Delamination: Mode I Fracture Aspects*, in *Symposium on Toughened Composites*, N.J. Johnston, Editor ASTM Special Technical Publications: 1987, Houston, TX.
159. Huang, X.N. and D. Hull, *Effects of fibre bridging on  $G_{IC}$  of a unidirectional glass/epoxy composite*. Composites Science and Technology, 1989. 35(3): p. 283-299.
160. *Goodfellow Product Catalogue*. 2005, Huntingdon: Goodfellow.
161. *Hycar® Reactive Liquid Polymers CTBN 1300X8 & CTBN 1300X8F Datasheet*, Noveon, 2001, Cleveland, Ohio.
162. Nanoresins. *Modifying epoxy resins with nanocomposites* Accessed (12/1/06), 2005. Available from: <http://www.nanoresins.ag/content/view/52/55/lang/en/>
163. Verchere, D., H. Sautereau, J.P. Pascault, S.M. Moschiar, C.C. Riccardi and R.J.J. Williams, *Rubber-modified epoxies. I. Influence of carboxyl-terminated butadiene-acrylonitrile random copolymers (CTBN) on the polymerization and phase separation processes*. Journal of Applied Polymer Science, 1990. 41(3-4): p. 467-485.
164. Verchere, D., J.P. Pascault, H. Sautereau, S.M. Moschiar, C.C. Riccardi and R.J.J. Williams, *Rubber-Modified epoxies. IV. Influence of morphology on mechanical properties*. Journal of Applied Polymer Science, 1991. 43(2): p. 293-304.
165. Verchere, D., *Rubber-modified epoxies. II. Influence of the cure schedule and rubber concentration on the generated morphology*. Journal of Applied Polymer Science, 1991. 42(3): p. 701-716.
166. Moschiar, S.M., C.C. Riccardi, R.J.J. Williams, D. Verchere, H. Sautereau and J.P. Pascault, *Rubber-modified epoxies. III. Analysis of experimental trends through a phase separation model*. Journal of Applied Polymer Science, 1991. 42(3): p. 717-735.

167. Wise, C.W., W.D. Cook and A.A. Goodwin, *CTBN rubber phase precipitation in model epoxy resins*. *Polymer*, 2000. 41(12): p. 4625-4633.
168. Yamanaka, K., *Phase separation mechanism of rubber-modified epoxy*. *Journal of Materials Science*, 1990. 25(1): p. 241-245.
169. Ratna, D. and A.K. Banthia, *Toughened epoxy adhesive modified with acrylate based liquid rubber*. *Polymer International*, 2000. 49(3): p. 281-287.
170. Sprenger, S., *Formulation of the amine cured TGMDA epoxy*. Nanoresins AG. Personal Communication. 2009, via E-mail.
171. Mazumdar, S.K., *Composites Manufacturing: Materials Product and Process Engineering*. 2002, London, New York, Washington: CRC Press.
172. Burton, B., D. Alexander, H. Klein, A. Garibay-Vasquez, A. Alan Pekarik and C. Henkee, *Epoxy formulations using Jeffamine polyether-amines*. 2005, Huntsman: TX.
173. Williams, C., J. Summerscales and S. Grove, *Resin Infusion under Flexible Tooling (RIFT): a review*. *Composites Part A: Applied Science and Manufacturing*, 1996. 27(7): p. 517-524.
174. Chen, F. *Impact behaviour of composites in different fibre architectures*, MSc Thesis, Department of Aeronautics, Imperial College London, London, 2007.
175. Patel, D. *Impact on Laminated Composites*, MEng Thesis, Department of Aeronautics, Imperial College London, London, 2005.
176. ISO-1183, *Plastics - Methods for determining the density of non-cellular plastics, in Part 1: Immersion method, liquid pycnometer method and titration method*. 2004, British Standards Institute.
177. ISO-11357, *Plastics - Differential scanning calorimetry (DSC). Determination of glass transition temperature*. 1999, British Standards Institute.
178. ASTM-D7426, *Standard Test Method for Assignment of the DSC Procedure for Determining Tg of a Polymer or an Elastomeric Compound*. 2008, American Society for Testing and Materials: West Conshohocken.
179. *GNU image manipulation program (GIMP v2.6)*; Accessed (01/10/09), 2010. Available from: <http://www.gimp.org/>
180. *ImageJ v1.43r*; Accessed (1/10/09), 2010. Available from: <http://rsbweb.nih.gov/ij/>
181. *Hugin Panorama Stitcher GUI v.2009.4.0*; Accessed (1/10/10), 2010. Available from: <http://hugin.sourceforge.net/>
182. Johnsen, B.B., *FEGSEM and AFM imaging of nanosilica modified epoxies*. Department of Mechanical Engineering. Personal Communication. 2006, Imperial College London.
183. ISO-527-1, *Plastics - Determination of tensile properties - Part 1: General principles*. 1993, International Standards Organisation: Geneva.

184. ISO-527-2, *Plastics - Determination of tensile properties - Part 2: Test conditions for moulding and extrusion plastics*. 1996, International Standards Organisation: Geneva.
185. Williams, J.G. and H. Ford, *Stress-strain relationships for some unreinforced plastics* *Journal of Mechanical Engineering Science*, 1964. 6(4): p. 405-417.
186. Williams, J.G., *Calculation of the true stress and true strain from plane strain compression tests*. Department of Mechanical Engineering. Personal Communication. 2009, Imperial College London.
187. ISO-13586, *Plastics - Determination of fracture toughness ( $G_{IC}$  and  $K_{IC}$ ) - Linear elastic fracture mechanics (LEFM) approach*. 2000, International Standards Organisation: Geneva.
188. Kinloch, A.J., *Adhesion and Adhesives : Science and Technology*. 1987, London: Chapman & Hall.
189. Sue, H.J., *Study of rubber-modified brittle epoxy systems. Part I: Fracture toughness measurements using the double-notch four-point-bend method*. 1991. p. 270-274.
190. Sue, H.-J., *Study of rubber-modified brittle epoxy systems. Part II: Toughening mechanisms under mode-I fracture*. *Polymer Engineering & Science*, 1991. 31(4): p. 275-288.
191. Pearson, R.A. and A.F. Yee, *Influence of particle size and particle size distribution on toughening mechanisms in rubber-modified epoxies*. *Journal of Materials Science*, 1991. 26(14): p. 3828-3844.
192. Sue, H.J. and A.F. Yee, *Study of fracture mechanisms of multiphase polymers using the double-notch four-point-bending method*. *Journal of materials science*, 1993. 28(11): p. 2975-2980.
193. Caddell, R.M., *Deformation and fracture of solids*. 1980, Englewood Cliffs, New Jersey: Prentice-Hall.
194. Azom.com. *E-Glass fibre*; Accessed (18/04/10), 2010. Available from: <http://www.azom.com/Details.asp?ArticleID=764>
195. ASTM-D2344, *Standard test method for short beam shear strength of polymer matrix composite materials and their laminates*. 2000, American Society for Testing and Materials: West Conshohocken.
196. ASTM-D790, *Standard test methods for flexural properties of unreinforced and reinforced plastics and electrical insulating materials*. 2003, American Society for Testing and Materials: West Conshohocken.
197. ASTM-D5528, *Standard Test Method for Mode I interlaminar fracture toughness of unidirectional fiber-reinforced polymer matrix composites*. 2002, American Society for Testing and Materials: West Conshohocken.
198. ISO-25217, *Adhesives - determination of the mode 1 adhesive fracture energy of structural adhesive joints using double cantilever beam and tapered double cantilever beam specimens*. 2009, International Standards Organisation: Geneva.

199. Williams, J.G., *Large displacement and end block effects in the DCB interlaminar test in mode I and mode II*. Journal of Composite Materials, 1987. 21: p. 330-347.
200. *Hexaflow RTM 6 Product Data*. 2007, Hexcel Composites.
201. Fox, T.G., *Influence of diluent and of copolymer composition on the glass temperature of a polymer*. Bulletin of the American Physical Society, 1956 1.
202. Pearce, P.J., C.E.M. Morris and B.C. Ennis, *Rubber toughening of practical tetraglycidyl methylenedianiline-piperidine adduct systems*. Polymer, 1996. 37(7): p. 1137-1150.
203. Faber, K.T. and A.G. Evans, *Crack deflection processes - II. Experiment*. Acta Metallurgica, 1983. 31(4): p. 577-584.
204. Hagstrand, P.O., F. Bonjour and J.A.E. Månson, *The influence of void content on the structural flexural performance of unidirectional glass fibre reinforced polypropylene composites*. Composites Part A: Applied Science and Manufacturing, 2005. 36(5): p. 705-714.
205. Morgan, R.J., *Structure-property relations of polyethertriamine-cured bisphenol-A-diglycidyl ether epoxies*. Polymer, 1984. 25(1): p. 375-386
206. Morgan, R.J., *Epoxy matrices for filament-wound carbon fiber composites*. Journal of Applied Polymer Science, 1987. 34(1): p. 37-46.
207. Stewart, A. *Tensile and fracture properties of particulate composites*, MEng Thesis, Department of Mechanical Engineering, Imperial College London, London, 2004.
208. Kinloch, A.J. and A.C. Taylor, *Mechanical and fracture properties of epoxy/inorganic micro- and nano-composites*. Journal of Materials Science Letters, 2003. 22(20): p. 1439-1441.
209. Kim, B.C., S.W. Park and D.G. Lee, *Fracture toughness of the nano-particle reinforced epoxy composite*. Composite Structures, 2008. 86(1-3): p. 69-77.
210. Chekanov, Y., D. Arrington, G. Brust and J.A. Pojman, *Frontal curing of epoxy resins: Comparison of mechanical and thermal properties to batch-cured materials*. Journal of Applied Polymer Science, 1997. 66(6): p. 1209-1216.
211. Brooker, R.D., *The material properties and toughening mechanisms of amine cured multi-functional epoxies modified with nanosilica*. Personal Communication. 2009, Imperial College London.
212. Nanoresins AG, *Albidur HE 600 Datasheet*, 2006, Geesthacht, Germany.
213. Gould, M.L., *New epoxy/anhydride chemistry for durable, high solids coatings*. 1994, The Dow Chemical Company: Freeport, TX.
214. Reeder, J.R., *The use of doubler reinforcement in delamination toughness testing*. Composites. Part A, Applied science and manufacturing, 2004. 35(11): p. 1337-1344.
215. Franck, A.J., *Understanding rheology of thermosets*. 2004, TA Instruments: Germany.

216. Calabrese, L. and A. Valenza, *The effect of a liquid CTBN rubber modifier on the thermo-kinetic parameters of an epoxy resin during a pultrusion process*. Composites Science and Technology, 2003. 63(6): p. 851-860.
217. Kinloch, A.J., T. Hsieh, K. Masania, J. Sohn Lee, A.C. Taylor and S. Sprenger, *The toughness of epoxy polymers and fibre composites modified with rubber microparticles and silica nanoparticles* in Proceedings of European Conference on Fracture 18. 2010, Dresden, Germany, European Conference on Fracture 18.
218. Puech, B. *Structure and Property relationships of hybrid organic / inorganic composites*, UROP Thesis, Department of Mechanical Engineering, Imperial College London, London, 2006.
219. Sohn Lee, J. *The Fatigue Behaviour of Nano-modified Epoxy Adhesives*, PhD Thesis, Department of Mechanical Engineering, Imperial College London, London, 2009.
220. Moloney, A.C., H.H. Kausch, T. Kaiser and H.R. Beer, *Parameters determining the strength and toughness of particulate filled epoxide resins*. Journal of Materials Science, 1987. 22(2): p. 381-393.
221. Kinloch, A.J. and A.C. Taylor, *The toughening of cyanate-ester polymers Part I Physical modification using particles, fibres and woven-mats*. Journal of Materials Science, 2002. 37(3): p. 433-460.
222. Kinloch, A.J., ed. *Structural Adhesives - Developments in Resins and Primers*. Applied Science Publishers, 1986: London.
223. Andrews, E.H., *Fracture in Polymers*. 1st. 1968, Edinburgh: Oliver & Boyd.
224. Sohn Lee, J., *Toughening mechanisms and morphologies of nanosilica-modified epoxies*. Department of Mechanical Engineering. Personal Communication. 2009, Imperial College London.
225. Norman, D.A. and R.E. Robertson, *Rigid-particle toughening of glassy polymers*. Polymer, 2003. 44(8): p. 2351-2362.
226. Cheng, C., A. Hiltner, E. Baer, P.R. Soskey and S.G. Mylonakis, *Cooperative cavitation in rubber-toughened polycarbonate*. Journal of Materials Science, 1995. 30(3): p. 587.
227. Azimi, H.R., R.A. Pearson and R.W. Hertzberg, *Fatigue of rubber-modified epoxies: effect of particle size and volume fraction*. Journal of Materials Science, 1996. 31(14): p. 3777-3789.
228. Chen, T.K. and H.J. Shy, *Effects of Matrix Ductility on Rubber/Matrix Interfacially Modified Epoxy Resins*. Polymer, 1992. 33(8): p. 1656-1663.
229. Manjunatha, C.M., *Quasi-static tensile properties of unmodified and modified anhydride cured DGEBA epoxy GFRP*. Department of Mechanical Engineering. Personal Communication. 2009, Imperial College London.
230. Marissen, R. and H.R. Brouwer, *The significance of fibre microbuckling for the flexural strength of a composite*. Composites Science and Technology, 1999. 59(3): p. 327-330.

231. Piggott, M.R., *Load Bearing Fibre Composites*. Second Edition. 2002, Massachusetts, USA: Kluwer Academic Publishers
232. Broughton, W.R., L.E. Crocker and M.J. Lodeiro, *Characterising Micro and Nanoscale Interfaces in Advanced Composites: A Review*. NPL Report, 2006.
233. Nielson, L.E., *Cross-linking effect on physical properties of polymers*. Journal of Macromolecular Science, Part C: Polymer Reviews, 1969. 3(1): p. 69-103.
234. Kishi, H., *Shear ductility and toughenability study of highly cross-linked epoxy/polyethersulphone*. Journal of Materials Science, 1997. 32(3): p. 761-771.
235. Baller, J., N. Becker, M. Ziehmer, M. Thomassey, B. Zielinski, U. Müller and R. Sanctuary, *Interactions between silica nanoparticles and an epoxy resin before and during network formation*. Polymer, 2009. 50(14): p. 3211-3219.
236. Bos, H.L. and J.J.H. Nusselder, *Toughness of model polymeric networks in the glassy state: effect of crosslink density*. Polymer, 1994. 35(13): p. 2793-2799.
237. Plangsangmas, L., J.J. Mecholsky and A.B. Brennan, *Determination of fracture toughness of epoxy using fractography*. Journal of Applied Polymer Science, 1999. 72(2): p. 257-268.
238. Ahmed, S. and F.R. Jones, *A review of particulate reinforcement theories for polymer composites*. Journal of Materials Science, 1990. 25(12): p. 4933-4942.
239. Kerner, E.H., *The Elastic and Thermo-elastic Properties of Composite Media*. Proceedings of the Physical Society, 1956. 69(8): p. 808-813.
240. Nielsen, L.E., *Simple Theory of Stress-Strain Properties of Filled Polymers*. Journal of Applied Polymer Science, 1966. 10: p. 97-103.
241. Halpin, J.C. and N.J. Pagano, *The Laminate Approximation for Randomly Oriented Fibrous Composites*. Journal of Composite Materials, 1969. 3(4): p. 720-724.
242. Chow, T.S., *The effect of particle shape on the mechanical properties of filled polymers*. Journal of materials science, 1980. 15(8): p. 1873-1888.
243. Einstein, A., *Investigation on theory of Brownian motion*. (English translation). 1956, New York: Dover.
244. Guth, E., *Theory of Filler Reinforcement*. Journal of Applied Physics, 1945. 16(1): p. 20-25.
245. Halpin, J.C., *Stiffness and Expansion Estimates for Oriented Short Fiber Composites*. Journal of Composite Materials, 1969. 3: p. 732-734.
246. Halpin, J.C. and J.L. Kardos, *The Halpin-Tsai Equations: A Review*. Polymer Engineering and Science, 1976. 186(5): p. 344-352.
247. Lewis, T.B. and L.E. Nielsen, *Dynamic mechanical properties of particulate-filled composites*. Journal of Applied Polymer Science, 1970. 14(6): p. 1449-1471.

248. McGee, S. and R.L. McCullough, *Combining rules for predicting the thermoelastic properties of particulate filled polymers, polymers, polyblends, and foams*. Polymer Composites, 1981. 2(4): p. 149-161.
249. Nielsen, L.E. and R.F. Landel, *Mechanical properties of polymers and composites*. 2nd. 1994, New York: Marcel Dekker.
250. Nielsen, L.E., *The relation between viscosity and moduli of filled systems*. Journal of Composite Materials, 1968. 2(1): p. 120-123.
251. Pascoe, K.J., *An introduction to the properties of engineering materials*. 3rd. 1978, London: Van Nostrand Reinhold.
252. Lehmann, B., A.K. Schlarb, K. Fredrich, M.Q. Zhang and M.Z. Rong, *Modelling of Mechanical Properties of Nanoparticle Filled Polyethylene*. International Journal of Polymeric Materials, 2007. 56(9): p. 945-964.
253. Lee, J. and A.F. Yee, *Micro-mechanical deformation mechanisms in the fracture of hybrid-particulate composites based on glass beads, rubber and epoxies*. Polymer Engineering & Science, 2000. 40(12): p. 2457-2470.
254. Chen, T.K. and Y.H. Jan, *Fracture mechanism of toughened epoxy-resin with bimodal rubber-particle size distribution*. Journal of Materials Science, 1992. 27(1): p. 111-121.
255. Ramos, V.D., H.M. da Costa, V.L.P. Soares and R.S.V. Nascimento, *Modification of epoxy resin: a comparison of different types of elastomer*. Polymer Testing, 2005. 24(3): p. 387-394.
256. Boogh, L., B. Pettersson and J.-A.E. Månson, *Dendritic hyperbranched polymers as tougheners for epoxy resins*. Polymer, 1999. 40(9): p. 2249-2261.
257. Kinloch, A.J., S.J. Shaw, D.A. Tod and D.L. Hunston, *Deformation and fracture behaviour of a rubber-toughened epoxy: 1. Microstructure and fracture studies*. Polymer, 1983. 24(10): p. 1341-1354.
258. Evans, A.G., S. Williams and P.W.R. Beaumont, *On the Toughness of Particulate Filled Polymers*. Journal of Materials Science, 1985. 20(10): p. 3668-3674.
259. Guild, F.J. and R.J. Young, *A predictive model for particulate-filled composite-materials .1. Hard Particles*. Journal of Materials Science, 1989. 24(1): p. 298-306.
260. Guild, F.J. and R.J. Young, *A predictive model for particulate-filled composite-materials .2. Soft particles*. Journal of Materials Science, 1989. 24(1): p. 2454-2460.
261. Chen, J., Z. Huang, S. Bai and Y. Lui, *Theoretical analysis on the local critical stress and size effect for interfacial debonding in particle reinforced rheological materials*. Acta Mechanica Soldia Sinica. Chinese Edition, 1999. 20(1): p. 1-7.
262. Giannakopoulos, I. *Manufacture and properties of hybrid particle-modified fibre composites by RIFT*, MSc Thesis, Department of Mechanical Engineering and Department of Aeronautics, Imperial College London, London, 2008.

263. Kunz, S.C. and P.W.R. Beaumont, *Low-Temperature Behaviour of Epoxy-Rubber Particulate Composites*. Journal of Materials Science, 1981. 16(11): p. 3141-3152.
264. Kinloch, A.J., M.L. Yuen and S.D. Jenkins, *Thermoplastic-toughened epoxy polymers*. Journal of Materials Science, 1994. 29(14): p. 3781.
265. Bishopp, J., *Formulation of a room temperature cure, low shrinkage epoxy resin*. Star Adhesion Ltd. Personal Communication. 2009, 32<sup>nd</sup> Annual Meeting of the Adhesion Society.
266. Manzione, L.T., J.K. Gillham and C.A. McPherson, *Rubber-modified epoxies. I. Transitions and morphology*. Journal of Applied Polymer Science, 1981. 26(3): p. 889-905.
267. Manzione, L.T., *Rubber-modified epoxies. II. Morphology and mechanical properties*. Journal of Applied Polymer Science, 1981. 26(3): p. 907.
268. Bismarck, A., *Discussions regarding removal and replacing of sizing from NCF glass-fibre fabrics*. PaCE group, Department of Chemical Engineering. Personal Communication. 2009, Imperial College London.
269. Taylor, A.C., K. Masania, A.J. Kinloch and S. Sprenger, *Fibre-reinforced composites optimised by the synergy between rubber-toughening and SiO<sub>2</sub>-Nanoparticles* in Proceedings of 17<sup>th</sup> International Conference on Composite Materials (ICCM-17). 2009, Edinburgh, UK, 17<sup>th</sup> International Conference on Composite Materials (ICCM-17).
270. Masania, K., A.C. Taylor, A.J. Kinloch and S. Sprenger, *The fracture of nanosilica and rubber toughened epoxy fibre composites* in Proceedings of American Composites Manufacturing Association (ACMA) Composites and POLYCON '09. 2009, Tampa, FL., American Composites Manufacturing Association (ACMA).

# Appendix I. List of Publications

## Conference Papers

Taylor, A.C., A.J. Kinloch, K. Masania, R.D. Mohammed and S. Sprenger, *Toughness of nanoparticle-modified epoxy and fibre composites* in Proceedings of 31st Annual Meeting of the Adhesion Society. 2007, Austin, TX, the Adhesion Society.

Masania, K., A.C. Taylor, A.J. Kinloch and S. Sprenger, *The fracture of nanosilica and rubber toughened epoxy fibre composites* in Proceedings of American Composites Manufacturing Association (ACMA) Composites and POLYCON '09. 2009, Tampa, FL, American Composites Manufacturing Association (ACMA).

Masania, K., A.J. Kinloch, A.C. Taylor and S. Sprenger, *The fracture of nanosilica and rubber toughened epoxy fibre composites* in Proceedings of 32nd Annual Meeting of the Adhesion Society. 2009, Savannah, GA, the Adhesion Society.

Masania, K., A.J. Kinloch, A.C. Taylor and S. Sprenger, *The fracture of nanosilica and rubber toughened epoxy fibre composites* in Proceedings of 17th International Conference on Composite Materials (ICCM-17). 2009, Edinburgh, UK, International Conference on Composite Materials (ICCM-17).

Sprenger, S., A.J. Kinloch, A.C. Taylor, K. Masania, C.M. Manjunatha and R.D. Mohammed, *Tough and stiff: The Synergy Between rubber-toughening and SiO<sub>2</sub>-nanoparticles in gfrc and cfrc* in Proceedings of SAMPE EUROPE 30th International Conference and Forum: Composites - Innovative Materials for Smarter Solutions. 2009, Paris: SAMPE, Covina, USA.

Taylor, A.C., A.J. Kinloch, K. Masania and S. Sprenger, *Toughening mechanisms of nanosilica modified epoxy polymers* in Proceedings of 32nd Annual Meeting of the Adhesion Society. 2009, Savannah, GA, the Adhesion Society.

Taylor, A.C., K. Masania, A.J. Kinloch and S. Sprenger, *Fibre-reinforced composites optimised by the synergy between rubber-toughening and SiO<sub>2</sub>-Nanoparticles* in Proceedings of 17th International Conference on Composite Materials (ICCM-17). 2009, Edinburgh, UK, International Conference on Composite Materials (ICCM-17).

Taylor, A.C., A.J. Kinloch, K. Masania, J. Sohn Lee and S. Sprenger, *Predicting the toughness of nanoparticle-modified epoxies* in Proceedings of 33rd Annual Meeting of the Adhesion Society. 2010, Daytona Beach, FL, the Adhesion Society.

Kinloch, A.J., T. Hsieh, K. Masania, J. Sohn Lee, A.C. Taylor and S. Sprenger, *The toughness of epoxy polymers and fibre composites modified with rubber microparticles and silica nanoparticles* in Proceedings of European Conference on Fracture 18. 2010, Dresden, Germany, European Conference on Fracture 18.

Kinloch, A.J., T. Hsieh, K. Masania, J. Sohn Lee, A.C. Taylor and S. Sprenger, *The toughness of epoxy polymers and fibre composites modified with rubber microparticles and silica nanoparticles* in Proceedings of 4th World Congress on Adhesion and Related Phenomena. 2010, Arcachon, France, French Adhesion Society.

## Journal Papers

Kinloch, A.J., K. Masania, A.C. Taylor, S. Sprenger and D. Egan, *The Fracture of glass-fibre reinforced epoxy composites using nanoparticle-modified matrices*. Journal of Materials Science, 2008. 43(3) p. 1151-1154.

Hsieh, T.H., A.J. Kinloch, K. Masania, J. Sohn Lee, A.C. Taylor and S. Sprenger, *The toughness of epoxy polymers and fibre composites modified with rubber microparticles and silica nanoparticles*, Journal of Materials Science, 2010. 45(5) p. 1193-1210.

Giannakopoulos, G., Masania, K. and Taylor, A.C., *Toughening of epoxy using core-shell rubber particles and silica nanoparticles*, submitted to Journal of Materials Science, 2010.